ADAM MICKIEWICZ UNIVERSITY IN POZNAŃ
FACULTY OF PHYSICS
NANOBIOMEDICAL CENTER IN POZNAŃ

Optimization of charge separation in organic dye-sensitized solar cells (DSSCs) with different nanostructure films and redox mediators.

PhD Thesis based on original publications.

M. Sc. Eng. Jan Sobuś
2016-01-13

Supervisor: dr hab. Marcin Ziółek, prof. UAM

Optimization of charge separation in organic dye-sensitized solar cells (DSSCs) with different nanostructure films and redox mediators.

I wish to express my gratitude towards:

- My supervisor dr hab. Marcin Ziółek for introducing me to the subject, scientific patronage and everlasting stream of advice.
- Prof. Anders Hagfeldt for invitation to EPFL, where I honed my skills and perfected the knowledge of DSSC's manufacturing as well as other people I met there for the vast amount of knowledge they shared wih me.
- Members of the research group, both at ZEK and CNBM for everyday help and positive work environment.
- Co-authors of the publications for for their commitment and fruitful cooperation.

Work was partially financed from the project "Rozwój środowiskowych interdyscyplinarnych studiów doktoranckich w zakresie nanotechnologii-elektroniki i fotowoltaiki w Instytucie Fizyki Molekularnej PAN w Poznaniu i na Wydziale Fizyki UAM" UDA-POKL.04.03.00-00-015/12-00 in the frame of Human Capital Operational Program funded fromEuropean Social Fund and by National Science Centre OPUS grant no. 2012/05/B/ST3/03284 named „Badanie elementarnych procesów separacji ładunku w fotoogniwach barwnikowych metodami czasowo-rozdzielczej spektroskopii optycznej”.

HUMAN CAPITAL
NATIONAL COHESION STRATEGY

EUROPEAN UNION
EUROPEAN
SOCIAL FUND

NARODOWE CENTRUM NAUKI

Optimization of charge separation in organic dye-sensitized solar cells (DSSCs) with different nanostructure films and redox mediators.

Table of contents

Abstract

The main aim of the study in the series of publications constituting my Ph.D. thesis was to understand the group of processes undergoing during the operation of Dye Sensitized Solar Cells (DSSCs), in order to unveil their nature and find ways of tuning device properties in a desired way. The attention was focused on how selected properties of different building elements of DSSC (especially those related to the nanostructure of the photoanode, redox mediators in the electrolyte and dyes used for sensitization) affect the charge separation efficiency and, consequently, how they can be optimized.

Popular organic dyes were chosen as the basis of the study (indoline dyes D149, D358 and carbazole dyes MK2 and ADEKA-1) because of their high efficiency, lower cost compared to other dye families (e.g. ruthenium ones) and potential applicability. Cells were prepared using the most common "sandwich" setup with conducting glass used as substrates for both electrodes. For the photoanode, number of oxides (titanium dioxide, zinc oxide, aluminium oxide) of different morphologies (mesoporous layers, nanowires, core-shell structures etc.) were used. The counter electrodes were prepared by deposition of a thin platinum or carbon layer on the substrate. After dipping of the photoanode in the dye solution (with or without co-adsorbent) both electrodes were sealed together with the polymer binder and filled with appropriate electrolyte (iodide or cobalt based). Additional effect of surface treatment (from solution or by Atomic Layer Deposition) and of electrolyte additives (4-tert-butylpyridine, lithium salts) was investigated as well.

Ready devices were subjected to a range of measuring techniques in order to confirm their desired structure and to pinpoint the impact of the processes ongoing on the timescales, ranging from femtoseconds to seconds (injection, different types of recombination, regeneration and charge transport and collection). Those techniques included: stationary and transient absorption spectroscopy, current-voltage measurements, electrochemical impedance spectroscopy, scanning electron microscopy and transmission electron microscopy.

Some of the modifications were found to be unambiguously beneficial, like for example $TiCl_4$ surface treatment, addition of 4-tert-butylpyridine or better performance of TiO_2 based cells, in comparison to their counterparts base on ZnO. In most cases, however, situation was far more complex with the changes in parameters affecting some processes in a positive way, while hindering others. One of the prime examples is switching from iodide to cobalt based electrolyte, which improves the voltage of the cell at the expense of increase in the transport recombination. Molecular capping treatment, creation of alumina shell and co-adsorbent addition all fall into this category as well.

Experimental work was supplemented by numerical analysis of the optimal parameters of the dyes with different types of redox mediators, including the use of them in tandem devices, which are inevitably to dominate the future of solar cells. Theoretical research resulted in creation of algorithm able to model optimal parameters for the tandem devices consisting of up to ten junctions and formed of different types of cells. It can also help in matching additional modules to already existing solutions.

All this work is expected to help the global understanding of DSSCs and related photo-electrochemical devices and enable them to reach previously unattainable efficiencies.

Streszczenie

Głównym celem badań w cyklu publikacji naukowych tworzących moją rozprawę doktorską było zrozumienie szeregu procesów zachodzących w trakcie działania Ogniw Słonecznych Sensybilizowanych Barwnikiem (DSSC) w celu odkrycia ich natury oraz możliwości dostrajania właściwości ogniwa w pożądany sposób. Główny nacisk położony był na zrozumieniu, w jaki sposób poszczególne elementy DSSC (w szczególności te związane z nanostrukturą fotoanody, parą redoks w elektrolicie i barwnikiem użytym do sensybilizacji) wpływają na skuteczność separacji ładunku, oraz jak te procesy mogą być zoptymalizowane.

Jako baza do badań zostały wybrane popularne barwniki organiczne (barwniki indolinowe D149, D358 oraz barwniki karbazolowe MK2 i ADEKA-1) ze względu na ich wysoką wydajność, niski koszt w porównaniu do innych typów barwników (na przykład rutenowych) i szeroki potencjał zastosowań. Ogniwa zostały przygotowane w oparciu o najpopularniejszy model "kanapki", w którym podłożem dla obu elektrod jest szkło z warstwą przewodzącą. W celu przygotowanie fotoanody były użyte różnorakie tlenki metali (tlenek tytanu, tlenek cynku i tlenek glinu) o różnych morfologiach (warstwa mezoporowata, nanodruty, struktury rdzeń-powłoka itd.). Katody były przygotowane przez osadzenie na podłożu cienkiej warstwy platyny bądź węgla. Po zanurzeniu fotoanody w roztworze barwnika (z opcjonalnym dodatkiem koadsorbentu) obie elektrody były sklejane za pomocą polimerowej uszczelki, a przestrzeń między nimi wypełniana elektrolitem (na bazie jodu bądź kobaltu). Sprawdzony został również wpływ modyfikacji powierzchniowych (z roztworu lub osadzanych metodą ALD) oraz dodatków do elektrolitu (4-tert-butylpirydyny oraz soli litu).

Gotowe ogniwa zostały poddane badaniom za pomocą szeregu technik badawczych w celu potwierdzenia otrzymania zakładanej struktury oraz analizy procesów zachodzących w skalach czasowych od femtosekund do sekund (wstrzykiwanie elektronu, różne typy rekombinacji, regeneracja barwnika oraz transport i zbieranie ładunku). Do tych technik należały: stacjonarna i przejściowa spektroskopia optyczna, pomiary prądowo-napięciowe, elektrochemiczna spektroskopia impedancyjna, skaningowa i transmisyjna mikroskopia elektronowa.

Pewne modyfikacje okazały się w pełni korzystne, jak modyfikacja powierzchniowa przy użyciu czterochlorku tytanu, dodatek 4-tert-butylpirydyny lub użycie tlenku tytanu zamiast tlenku cynku jako materiału fotoanody. Dużo częściej jednak modyfikacje sprawiały, że część parametrów ogniw ulegała polepszeniu kosztem pogorszenia innych parametrów. Jednym z przykładów może być zamiana elektrolitu z jodkowego na kobaltowy, która skutkuje wzrostem uzyskanego napięcia, ale za cenę wzrostu rekombinacji transportowej. Tworzenie ochronnej warstwy organicznej (capping), powłoki z tlenku glinu bądź dodanie koadsorbentu owocują podobnymi skutkami.

Badania eksperymentalne zostały wsparte analizą numeryczną optymalnych barwników i elektrolitów dla ogniw tandemowych, które nieuchronnie zdominują rynek ogniw słonecznych w przyszłości. Posłużyła ona do stworzenia algorytmu odnajdującego parametry ogniw tandemowych skutkujące najwyższą wydajnością (w urządzeniach zawierających aż do dziesięciu ogniw i zbudowanych z ogniw różnego typu). Może on też pomóc w prawidłowym dobieraniu dodatkowych elementów do już istniejących urządzeń.

Spodziewam się, że efekty tej pracy pomogą pogłębić zrozumienie fundamentalnych zasad działania ogniw słonecznych sensybilizowanych barwnikiem i innych pokrewnych urządzeń i pozwolą im osiągnąć wyższe niż dotychczas spotykane wydajności.

List of publications constituting the thesis

In chronological order:

[Sob -A] *Comparison of TiO_2 and ZnO Solar Cells Sensitized with an Indoline Dye: Time-Resolved Laser Spectroscopy Studies of Partial Charge Separation Processes*

Jan Sobuś, Gotard Burdziński, Jerzy Karolczak, Jesus Idígoras, Juan A. Anta and Marcin Ziółek,

Langmuir,**30** (2014) 2505–2512

[Sob -B] *Optimization of absorption bands of dye-sensitized and perovskite tandem solar cells based on loss-in-potential values*

Jan Sobuś and Marcin Ziółek,

Phys. Chem. Chem. Phys., **16** (2014) 14116-14126

[Sob -C] *Transient states and the role of excited state self-quenching of indoline dyes in complete dye-sensitized solar cells*

Jan Sobuś, Jerzy Karolczak, Dariusz Komar, Juan A. Anta and Marcin Ziółek,

Dyes and Pigments, **113** (2015) 692-701

[Sob -D] *Carbazole Dye- Sensitized Solar Cells Studied from Femtoseconds to Seconds —Effect of Additives in Cobalt and Iodide-Based Electrolytes*

Jan Sobuś, Jacek Kubicki, Gotard Burdziński and Marcin Ziółek,

ChemSusChem, **8** (2015) 3118–3128

[Sob -E] *Effect of different photoanode nanostructures on the initial charge separation and electron injection process in dye sensitized solar cells: a photophysical study with indoline dyes*

Jesús Idígoras, **Jan Sobuś**, Mariusz Jancelewicz, Eneko Azaceta, Ramon Tena-Zaera, Juan A. Anta and Marcin Ziółek

Materials Chemistry and Physics, **170** (2016) 218-228

[Sob-F] *Factors affecting the performance of champion silyl-anchor carbazole dye revealed in the femtosecond to second studies of complete ADEKA-1 sensitized solar cells.*

Jan Sobuś, Błażej Gierczyk, Gotard Burdziński, Mariusz Jancelewicz, Anders Hagfeldt and Marcin Ziółek

Paper in preparation: finalized and sent to co-authors for corrections.

Commentary

1. Introduction and motivation

In the face of ever-growing global energy consumption and shrinking fossil fuels deposits, humanity is searching for means of obtaining clear and environmentally friendly energy. Solar radiation, being the most abundant natural renewable energy source, quickly attracted the attention of scientists. Together with the advent of semiconductor technology, first commercial solar cells started to appear as early as in the late 1950s. Nowadays, semiconductor based solar cells (mainly silicon ones, with CdTe, CdSe and CIGS to lesser extent) are still dominant on the market, mostly because of well defined and widely adopted manufacturing process and their prices have dropped as low as $\$0.6/W_p$ (which is a measure of the cost efficiency of a photovoltaic device, being its total cost divided by its peak power). Yet, the limitations of semiconductor technology (high energy and purity needed for the manufacturing process and expensive materials in the case of thin film photovoltaics) led to search for alternative paths of turning sunlight energy into electricity.

Dye sensitized solar cells (DSSCs) were the first member of the group, which later started to be called emerging photovoltaics or the 3^{rd} generation photovoltaics (with organic solar cells, quantum dot solar cells and recently perovskite solar cells as well). Introduced in 1991, this generation broke with the dogma of devices based solely on p-n junction and offered the perspective of cheap, easy to manufacture and eco-friendly devices. Today, they are the member of the emerging photovoltaics group, which achieved biggest commercial success.

Yet, despite initially reported high efficiency of 7%[1], which was rapidly increased to 10% [2], further development over the years was much slower and hit the “glass ceiling” of around 12-13% efficiency. In this work dye sensitized solar cells utilizing various popular dyes (D149, D358 from indoline family, MK2 and ADEKA-1 from carbazole family), electrolytes (iodide and cobalt based), photoanode materials (ZnO and TiO_2) and morphologies (mesoporous nanoparticle network, nanowires) were analyzed in order to find general rules and guidelines for constructing efficient devices, providing identification of unwanted processes at the same time. DSSCs are very sophisticated photo-electrochemical systems, where energy levels and surface

properties of individual components need to be finely tuned in order to achieve maximum performance (which will be described in detail in further chapters). In this thesis, such tuning was achieved by the direct surface modification of the oxide ($TiCl_4$ treatment, core-shell structures) or electrolytes additives: 4-tert-butylpyridine(TBP) and lithium salts. In order to fully understand undergoing mechanisms, whose characteristic timescales span from femtoseconds to seconds, series of methods were applied in order to analyze them separately and verify their impact on the final performance of the device.

In parallel with experimental work, theoretical numeric analysis was performed as well with two main areas of interest. The first was to find the optimal parameters for materials to be used in already existing devices. Second led to definition of optimized characteristics of the tandem devices that are to be produced.

In the subsequent chapters of this commentary the main aims of the thesis are presented, the basic principles of the operation of DSSCs and importance of individual components are unveiled. There are also included short descriptions of the experimental methods used, brief description of the experimental work done (together with obtained results) and the short reviews of the publications forming the backbone of the thesis. Finally, a short summary is added, followed by the full texts of the aforementioned publications and co-author statements.

2. Aims of the thesis

Charge separation in DSSC determines its performance and consists of several partial charge separation processes taking place on different time scales and at interfaces of different elements forming DSSC. The main aim of the thesis was to study how selected properties of these building blocks of DSSC (especially those related to the nanostructure of the photoanode and redox mediators in the electrolyte) affect the charge separation efficiency and, consequently, how they can be optimized. The particular aims of the thesis were the following:

i) Optimization of the nanostructure film:

i.i) effect of different semiconductor material (TiO_2, ZnO and Al_2O_3);

i.ii) effect of different nanostructure morphology (ZnO nanoparticles vs. ZnO nanowires);

i.iii) effect of various surface treatment ($TiCl_4$, core-shell, molecular capping);

ii) Optimization of the electrolyte composition:

ii.i) electrolyte redox couple (cobalt vs. iodide);

ii.ii) different electrolyte additives (TBP and Li^+);

iii) Optimization of the dye:

iii.i) determination of the best dye absorption band, including multi-dyes sets for tandem devices (an algorithm for calculation the optimal bandgaps);

iii.ii) different families of all-organic dyes (indoline vs. carbazole family);

iii.iii) effect of dye anchoring unit (carboxyl vs. silyl);

iii.iv) effect of co-adsorbent.

3. Dye Sensitized Solar Cells

3.1 Principles of operation

Dye sensitized solar cell is a novel type of photovoltaic device which instead of utilizing p-n junction like most solar cells do, has different working principle. It consists of several distinctive elements listed below, with their common arrangement shown in Fig. 1 :

- **Mesoporous photoanode** which is typically made of the oxide nanoparticles sintered together to form a layer several µm thick, yet possessing high porosity and specific surface area. The substrate on which this layer is deposited is most commonly glass plate with thin layer of transparent conductive oxide (TCO), which is usually fluorine-doped tin oxide (FTO).
- **Photoabsorbing dye molecules** deposited on the surface of the photoanode, utilizing its high specific surface area.
- **Electrolyte with redox couple** which fills the space between both electrodes and penetrates the mesoporous network.
- **Counter electrode** composed of the glass substrate with thin TCO layer covered with thin layer of platinum or carbon.

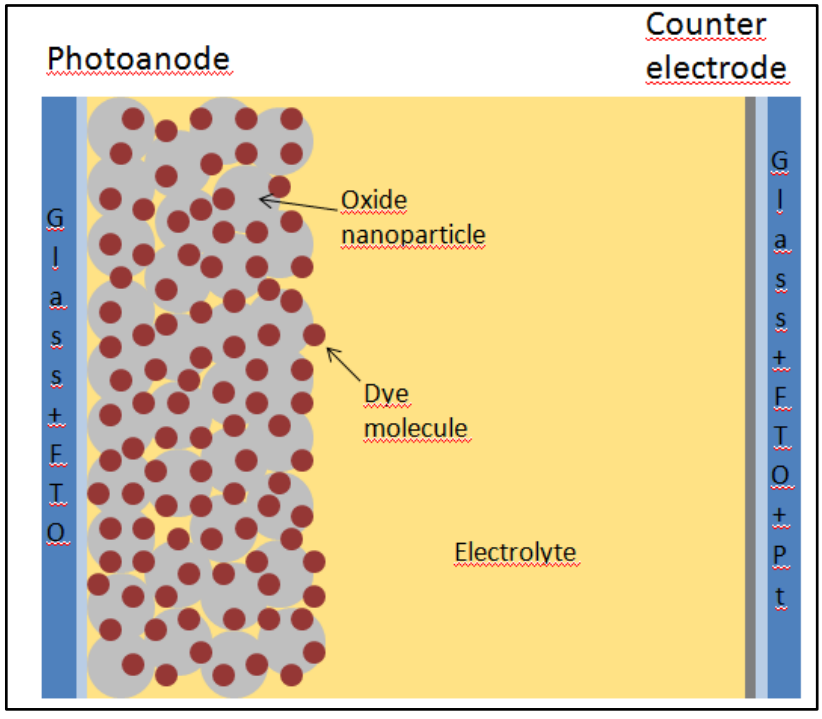

Figure 1. Schematic view of the construction of dye sensitized solar cell.

The main difference in operation between these cells and p-n based devices is that in DSSCs different medium is responsible for the light absorption (dye), separation of charge (dye/oxide interface) and transport of obtained charge carriers (oxide network). The energy diagram of DSSC with the operation cycle is presented in Fig. 2. First, photon is absorbed by a dye molecule, which excites electron from the HOMO (highest occupied molecular orbital) to the LUMO (lowest unoccupied molecular orbital) level. Then the electron is injected to the conduction band of the oxide the dye molecule is attached to. It travels through the mesoporous oxide layer until it reaches the FTO contact. After travelling through the external load it reaches the counter electrode. Shortly after, the oxidized dye is regenerated by the redox couple in the electrolyte, which in turn is fed by the carriers form the counter electrode. In this way the full cycle is completed. It should be noted that in order to achieve working cell the energy levels of each component must be well aligned to provide necessary driving force for the aforementioned processes. LUMO level of the dye must lie above (higher energy) the conduction band of the oxide for successful injection, its HOMO potential must lie below the redox potential of the electrolyte redox couple used. Similarly the redox potential of the electrolyte should lie well below the conduction band of the oxide. The thing of note is that these processes occur in the wide range of timescales: injection typically takes from a fraction to single picoseconds, dye regeneration is done in microsecond scale, while charge transport and collection occurs on the scale from milliseconds to seconds. Therefore various experimental methods have to be used in order to probe those processes independently. One cannot forget about unwanted, competing processes of dye relaxation and charge recombination (marked with dashed arrows) that need to be minimized in order to develop a successful device.

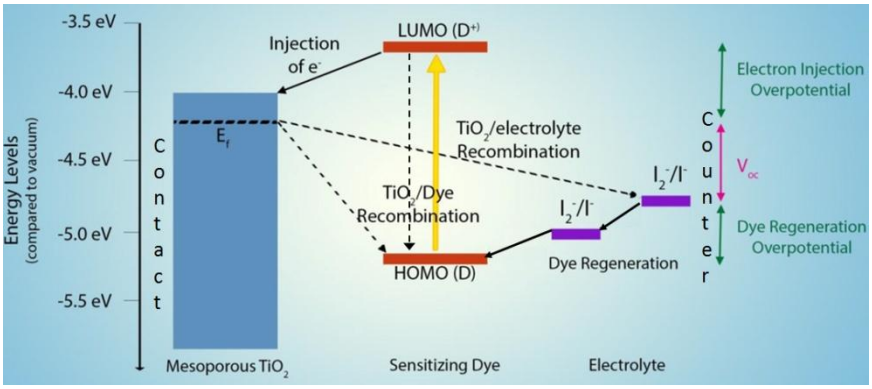

Figure 2. Operating cycle of DSSC with the energy levels of individual components.

From the electrical viewpoint DSSC can be considered as a reverse biased diode and described by the diode equation with additional photocurrent term:

$$I_{diode} = I_{ph} - I_0(exp(q(V + I_{diode} * R_s)/mkT) - 1) - (V + I_{diode} * R_s)/R_{sh}$$

Here R_s is the series resistance of the device, m is the diode's ideality factor and R_{sh} is the shunt resistance. With the desirable, yet unobtainable R_s equal to 0, m of 1 and infinite R_{sh} one would obtain the equation of ideal diode. The equation above yields the current-voltage characteristic presented in Fig. 3 with the characteristic values of short circuit current (J_{sc}), open circuit voltage (V_{oc}) and maximum power point (*MPP*) all included.

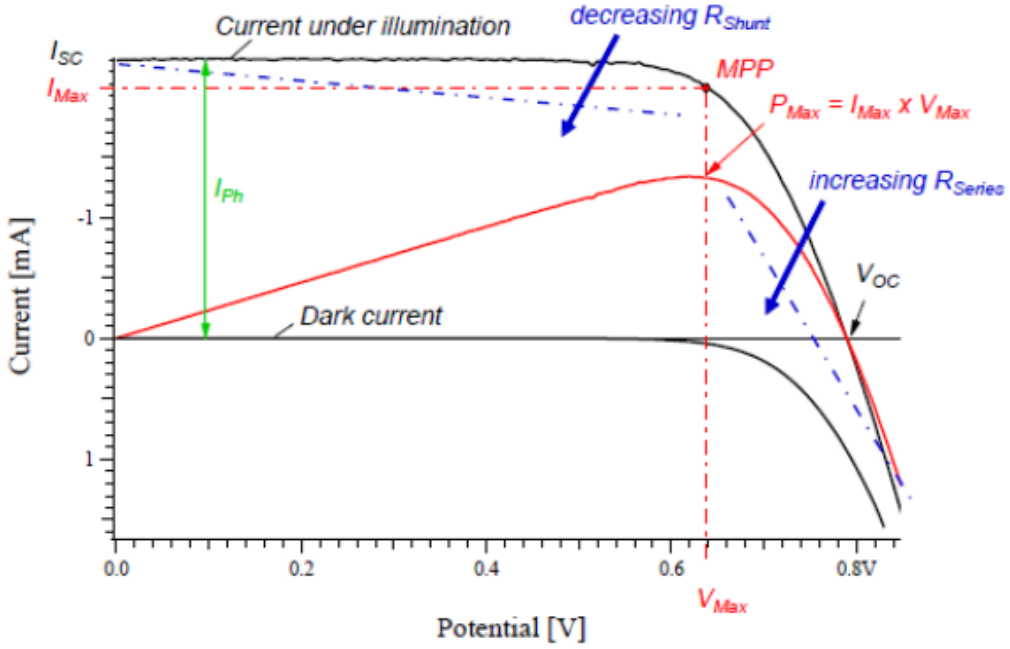

Figure 3. Current-voltage curve of the solar cell with characteristic points labeled.

A useful parameter - Fill Factor - is usually derived to show general quality of the system (effects of recombination, ideality factor and parasitic resistances are hidden there). It is the ratio of the power at maximum power point divided by the product of short circuit current and open circuit voltage.

$$FF = \frac{P_{max}}{V_{oc} I_{sc}}$$

It is then easy to define the efficiency of device as the maximum obtained power divided by the power of incident sunlight.

$$\eta = \frac{P_{max}}{P_{in}} = \frac{V_{oc} I_{sc} FF}{P_{in}}$$

The maximum obtainable V_{oc} comes from the bandgap of the dye with deducted driving force needed for injection and regeneration, as can be seen in Fig. 2. The difference between the bandgap and the obtained voltage is called loss-in potential and is one of the biggest factors limiting the maximum efficiency of the device [3].

The maximum value of the I_{sc}, which is equal to the photocurrent, has several limiting factors. Dividing the obtained current by the elemental charge and incident photon flux one obtains so called Incident Photon to Current Efficiency (IPCE).

$$\frac{I_{sc}}{e\phi_{ph}} = IPCE_{total}$$

It is a product of several factors (some of them wavelength dependent), each limiting total efficiency of the device:

$$IPCE(\lambda) = LHE(\lambda) * \varphi_{ei} * \varphi_{reg} * \eta_{cc}$$

- *LHE* stands for "light harvesting efficiency" and is equal to $1\text{-}10^{-A}$ where *A* is the absorbance of the device.
- φ_{ei} stands for the electron injection efficiency. It describes the percentage of photo-excited electrons that are successfully injected from the excited state of the dye into the oxide network instead of relaxing back to the ground state.
- φ_{reg} describes percentage of dye molecules which successfully injected electron and got a new one from the redox couple instead of recombination with the electrons in oxide network.
- η_{cc} is charge collection efficiency. It is the number of electrons that travelled through the oxide network without recombining with the electrolyte, compared to all successfully injected electrons that didn't recombine with the dye before its regeneration.

3.2 Dyes

Dye is one of the vital elements of dye sensitized solar cell (hence providing its name). In order to perform its job well, there are several conditions that a dye must fulfill:

- Since it is photosensitizing the oxide, it should cover the sun spectrum in its entity if possible.
- The energy level of the excited state of dye molecule should be above the conduction band edge of the oxide.
- The energy level of the oxidized state should be more positive than the redox potential of the electrolyte utilized.
- It should have an appropriate anchoring group (carboxylic, phosphonic etc.).
- Dye should be photo-,thermally- and electrochemically stable.
- In general, dye molecules should not have a tendency to aggregate.

Hundreds of compounds have been already proposed as sensitizers, divided into several distinguishable groups. The first type of compounds that attracted a lot of scientific attention and helped to obtain high efficiencies were the dyes based on metal complexes with organic ligands. Although several metals were tested, Ru complexes proved to be the most successful ones. Two members of the family of these dyes -N3 and N719- became standards in the community, with reference performance values. Another group of photosensitizer are porphyrins and phthalocyanines, which show better near-IR response. While the latter encounter many problems with solubility, the former resulted in efficiencies over 12%, with YD2 molecule being a notable example. Finally, there is a big group of organic sensitizers, which have the advantages of higher extinction coefficient and lower production cost. They are divided into multitude of sub groups. The most widely researched are tri-arylamine based dyes (with D35 being an organic performance standard, and its numerous derivatives obtaining high efficiencies), indoline dyes (with most popular D149 and its derivative D358 being investigated in this thesis), carbazole dyes (high efficiency MK2 dye and its derivative ADEKA-1, also investigated in this work), coumarin dyes and squaraine dyes. Structures of the popular members of these three dye families are presented in Fig. 4.

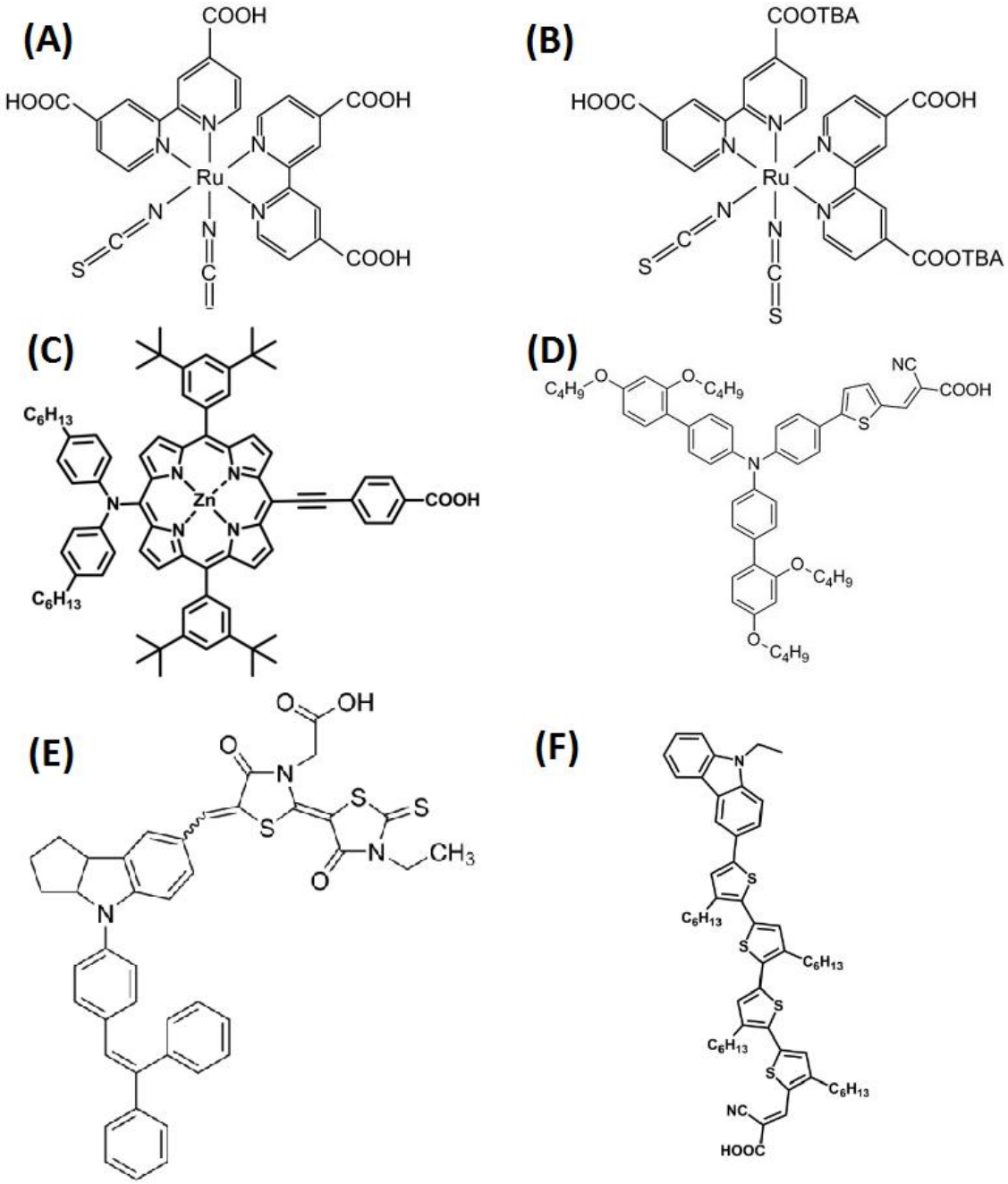

Figure 4. Molecular structures' of the popular dyes belonging to the metal complexes family - N3 (A) and N719 (B), porphyrin family - YD2 (C), tri-arylamine family - D35 (D), indoline family - D149 (E) and carbazole family - MK2 (F).

3.3 Structure of the photoanode

Variation in the photoanode's structure may have two origins - the type of material used and its morphology. When it comes to the semiconductor used, there are several requirements:

- The bandgap must be appropriate (position of the conduction band edge, as described earlier).
- The material should be n-type semiconductor.
- The material should be abundant in nature and affordable.
- Nanoparticles and other structures of the material should be obtainable easily and in inexpensive way.
- Material shouldn't react with the commonly used redox couples.

Out of various candidates, presented in Fig. 5, two members pass all these requirements - titanium dioxide (TiO_2, most commonly used in the anatase form) and zinc oxide (ZnO).

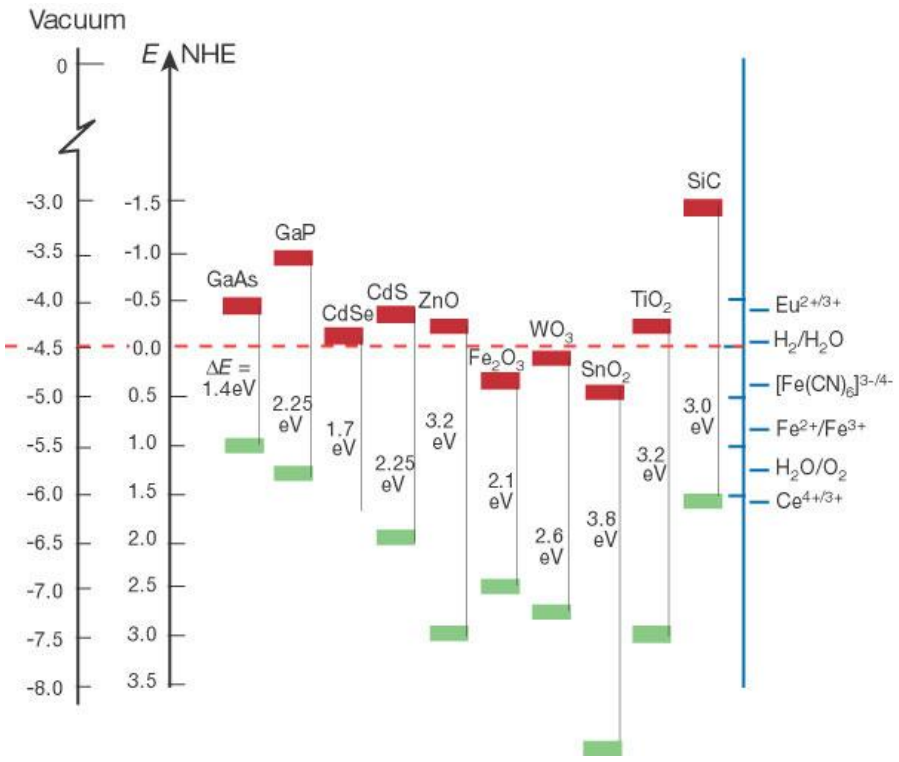

Figure 5. Band positions of various semiconductors relatively to the hydrogen electrode and vacuum level together with redox levels of various electrolyte couples [4].

When it comes to morphology, sintered mesoporous nanoparticle network to date remains the most widespread solution due to its ease of preparation and high surface-to-volume ratio. Nevertheless, other morphologies are being tested as well, mainly with the aim of enhancing the transport properties (nanowires) or improving the process of capturing light (by creation of scattering centers which improve the "optical thickness" of the cell without effect on the real thickness). ZnO is particularly grateful subject for such experiments, thanks to its ability to be easily prepared in variety of morphologies using wet techniques (sol-gel, hydrothermal etc.). The summary of ZnO structures tested so far is presented in Fig. 6, with further details (beyond the scope of this thesis) available in the source article [5]. There were also experiments performed with TiO_2 of different morphologies, albeit to a lesser extent. Solutions based on nanowires [6] or nanotubes [7] are the most common, yet their efficiency fails to reach the one offered by traditional mesoporous designs.

Structure	Photosensitizer	Efficiency	Ref.	Structure	Photosensitizer	Efficiency	Ref.
Nanoparticles	N719	0.44%, 2.1% (0.06 sun), 2.22%	[72,77,115]	Nanotips	N719	0.55%, 0.77%	[126,127]
	N719	5% (0.1 sun)	[73,74]	Nanotubes	N719	1.6%, 2.3%	[124,125]
	N3	0.4%, 0.75%, 2% (0.56 sun), 3.4%	[67,76,80,93]	Nanobelts	N719	2.6%	[95]
	heptamethine cyanine	0.16%, 0.67	[192,193]	Nanosheets	N719	2.61%, 3.3%	[91,94]
	unsymmetrical squaraine	1.5%	[194]		N3	1.55%	[93]
	eosin-Y	1.11%	[66]	Nanotetrapods	N719	1.20%, 3.27%	[96,97]
	acriflavine	0.588%	[200]	Nanoflowers	N719	1.9%	[128]
	mercurochrome	2.5%	[195,196]	Core–shell nanoparticles ($ZnO-TiO_2$)	N719	1.78%	[180]
Nanoporous films	N3	5.08% (0.53 sun)	[85]	Core–shell nanoparticles ($ZnO-SiO_2$)	N719	5.2%	[179]
	N719	3.9%, 4.1%	[88,90]	Core–shell nanoparticles (TiO_2-ZnO)	N3	4.3%, 4.51%, 9.8%	[135,146,147]
	N719	0.23%(hybrid ZnO/N719)	[62]				
	D149	4.27%	[92]		N719	6.55%	[150]
	eosin-Y	2.0%, 2.4%	[198,199]		N3	1.21% (0.2 sun, flexible substrate)	[144]
	eosin-Y	3.31% (0.1 sun)	[198]	Core–shell nanoporous films ($ZnO-TiO_2$)	N719	1.02%	[61]
Nanowires	N3	0.73%, 2.1%, 2.4%, 4.7%	[113,117,171,197]	Core–shell nanowires ($ZnO-TiO_2$)	N719	2.25%	[183]
	N719	0.3%, 0.6%, 0.9%, 1.5%, 1.54%	[110,115,116,118,119]	Core–shell nanowires ($ZnO-Al_2O_3$)	N719	↓	[183]
	QDs (CdSe)	0.4%	[205]	Core–shell nanotubes (TiO_2-ZnO)	N719	0.704%	[181]
Dendritic nanowires	N719	0.5%, 1.1%	[103,129]	Aggregates	N3	3.51%, 4.4%, 5.4%	[168–170,174]
Nanowire/nanoparticle composite films	N719	0.9% ;(flexible substrate)	[122]				
	Mercurochrome	2.2%	[121]				

Figure 6. Summary of DSSCs based on various ZnO nanostructures [5].

3.4 Redox Couples

The redox couple most commonly used in the construction of dye sensitized solar cells is the iodide/triiodide system. It has several advantages - has appropriate redox potential for cell operation, high solubility, absorbs little light on its own and provides rapid dye regeneration. It also has some drawbacks - it works using two electrons during one cycle, it's corrosive for many materials and evaporates easily (lowering the stability of the device). Most importantly, when combined with most dyes, it yields excessive loss-in potential, having redox level more than 0.5 V over the HOMO level of the dye. Therefore, a lot of effort was put in order to find viable alternatives with bromide, Fe or Cu based complexes and organic compounds (like TEMPO) all being tested [8]. However, it was the family of Co complexes that turned out to be the most promising redox alternative, with the efficiency reaching 12.3% [9]. Most popular Co redox couples are presented in Fig. 7 together with their energy levels.

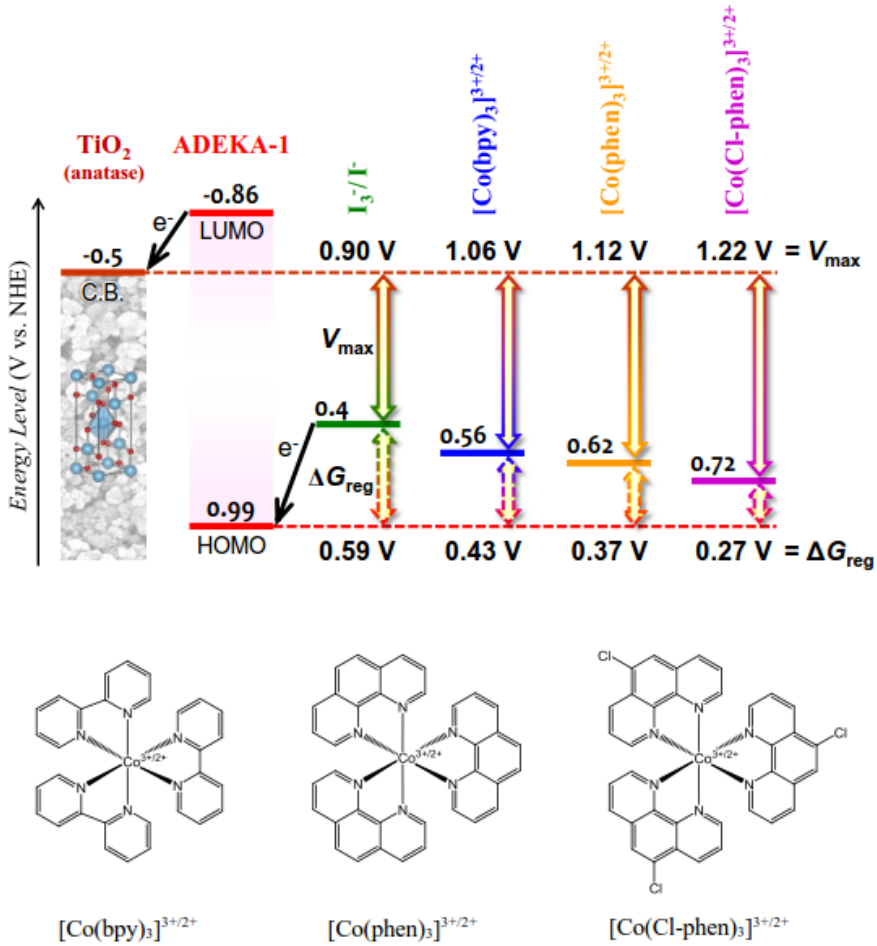

Figure 7. Popular Co based redox couples and their redox levels in comparison to ADEKA-1 dye (MK2- derivative) and conduction band of TiO_2 [10].

Despite their favorable redox levels, Co complexes bear some disadvantages as well, which need to be addressed. Contrary to iodide/triiodide, Co based redox couples have a positive charge, which attracts electrons in travelling through the oxide network, drastically increasing the recombination. Moreover, the size of these complexes has effect on their ability to penetrate the pores of the photoanode, creating diffusion limits for the efficient regeneration process.

3.5 Surface modifications and electrolyte additives

The combination of the dye, oxide and electrolyte usually needs further tuning by shifting energy levels to minimize potential losses and suppress unwanted processes. This tuning is most commonly achieved in two ways – adding the electrolyte additives and surface modification of the oxide framework.

Among the first group, the most popular compound is 4-tert-butylpyridine (TBP). It was found to shift the conduction band of the oxide upwards by deprotonating the surface. As a result, choosing a proper concentration of this compound in the electrolyte allow the maximization of cell voltage, while maintaining the driving force necessary for the injection. Moreover, TBP helps to fight recombination, creating a layer preventing the access of electrolyte to the oxides surface [11]. Lithium salts have adverse effect, by protonating the surface they bring the conduction band down. It was found experimentally that despite their contradictory effect, adding the both compounds is most the beneficial, however the full mechanism of their mutual interaction with oxide and electrolyte is not fully understood yet.

Surface modifications come in the form of either thin layer of additional oxide on the existing framework (deposited from solution, by ALD method or developed during the preparation of the photoanode) [12-14] or the layer of organic molecules attached to the oxide surface - called capping treatment [10]. In both cases the aim is to achieve reduced recombination and improved charge transport. In the former case, huge increase in the voltage and the reduction of recombination come at the expense of successful electron injection. In the latter one, deposition process of additional molecules often leads to dye dissolution and as a result decreased absorbance and photocurrent is observed.

3.6 Tandem devices

Choosing an optimal bandgap for a solar cell always comes with a tradeoff between obtained current and voltage. Smaller bandgap means more photons absorbed, but less energy extracted from each photon and vice versa. These losses together with emission losses, Carnot losses (heat loss to the surroundings) and Boltzmann losses (entropy increase) form the limit of the total efficiency of solar cell, called the Shockley-Queisser limit (around 31%). For crystalline cells it is well represented by Fig. 8A, where the area of the plot represent total incident power, while the power extracted from the device is the blue rectangle (which one wants as big as possible). In DSSCs situation looks similar with the exception that there are more voltage losses (combined by loss-in potential as described before), yet similar optimization of the energy gap can be performed, taking loss-in potential as one of the parameters [3]. The two biggest loss mechanisms (thermalization and loss of photons below E_g) can be minimized by introducing multi-junction device that combines several sub-cells of different bandgaps, as shown of Fig. 8B. First, the more energetic part of the spectrum is captured by the sub-cell of larger bandgap and the increased energy extracted from them lowers the thermalization loss. Then, less energetic photons are absorbed by the second junction, yielding another power contribution. This way the Shockley-Queisser limit can be crossed. The tandem approach is more popular in crystalline cells, where efficiencies up to 45% in four junction devices were reported. There are also attempts, however, of integrating DSSCs in tandems as well [15-16].

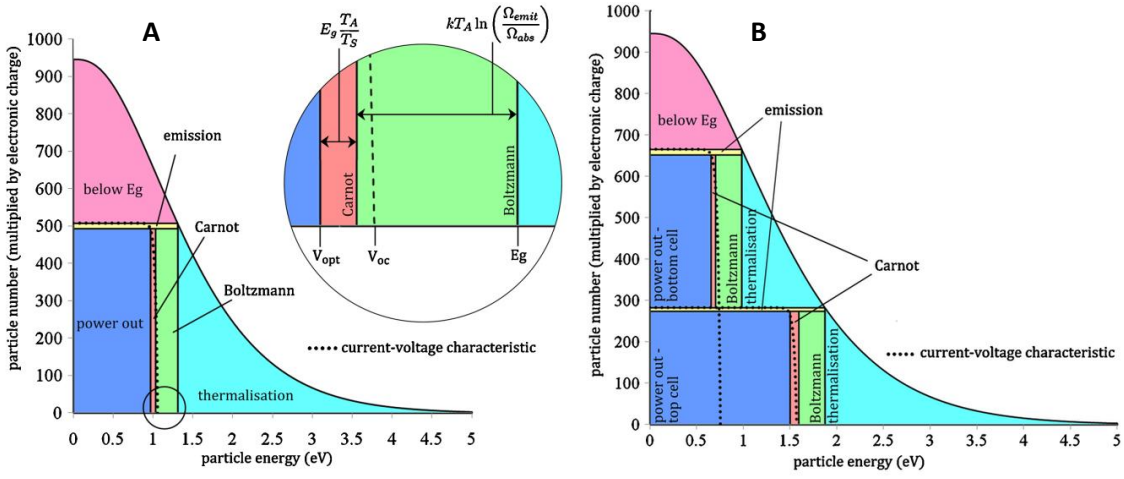

Figure 8. Energy diagram representing losses in single-junction (A) and multi-junction (B) solar cell.

4. Experimental methods

4.1 Doctor blade technique

Doctor blade technique is the easiest method of deposition of the mesoporous oxide layer on the conductive glass substrate in order to create the DSSC's photoanode. The first step of this technique is creating a mask for the deposition using an adhesive tape. Then, in the unmasked area, a blob of paste is left, containing nanoparticles of proper size (usually from 10 to 50 nm) and made of semiconductor of choice. The thickness of the tape should be chosen in accordance with the thickness of the layer one wants to achieve. In our case, most often the tape used had the thickness of 25 µm. Subsequently, "doctor blade" (usually a laboratory glass plate) is swiped on top of the mask in order to remove excess paste, leaving the layer of paste of desired shape and thickness. Adhesive mask is then removed and the glass plate with residual paste is sintered in order to remove the organic binder of the paste, leaving final mesoporous oxide layer formed of the connected nanoparticles. Of course, the loss of organic part of the paste results in the thickness shrink to about 20-30% of the initial paste thickness. The process is shown schematically in Fig. 9. Unless mentioned otherwise, it was used to produce photoanodes, which were utilized in the cells being studied in publications [Sob-A], [Sob-C], [Sob-D] and [Sob-E]. It is the oldest method of preparation of the photoanode, today commonly replaced by screen-printing (used in [Sob-F]).

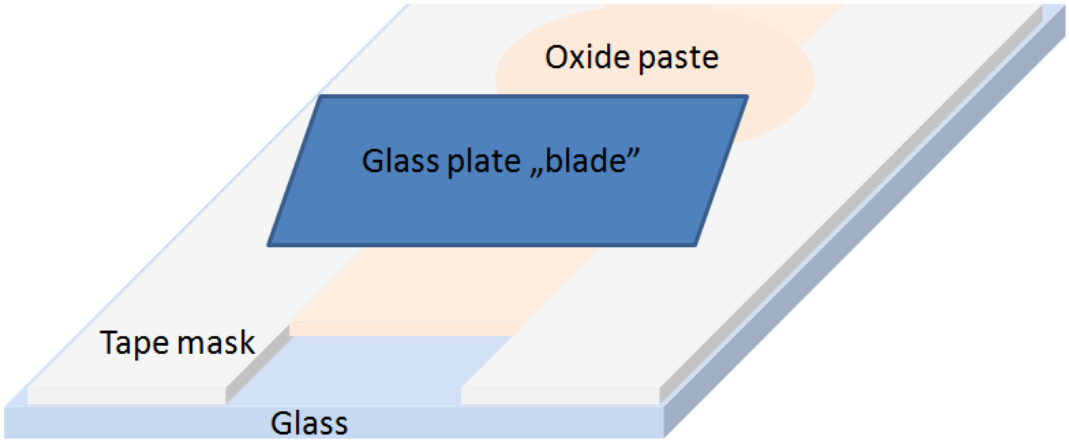

Figure 9. Schematic picture of the formation of the layer, made of oxide nanoparticle containing paste, with the doctor blade method.

4.2 Current-voltage characteristics measurement

General current-voltage characterization and measurements of the total efficiency of the cells were performed using a potentiostat (model M101 with frequency response analyzer FRA32M module, Metrohm Autolab) as a measuring tool and solar simulator equipped with Xe lamp and AM1.5G spectral filter (Instytut Fotonowy), with intensity set to 100 mW/cm^2 using a calibrated silicon cell (RR-74, Rera Systems). The whole setup, a property of Quantum Electronics Laboratory of Adam Mickiewicz University in Poznań, is shown in Fig. 10. It was used for evaluation of the basic parameters of the cells in all experimental papers - [Sob-A], [Sob-C], [Sob-D], [Sob-E] and [Sob-F].

Figure 10. Setup used for general current-voltage measurements and IPCE measurements consisting of the potentiostat (left) and Xe lamp with photoelectric spectrometer (right).

4.3 IPCE measurements

IPCE measurements were performed using the second channel of the setup used for general current-voltage characterization where, instead of using full AM1.5G spectrum, a photoelectric spectrometer was utilized (Instytut Fotonowy). The constant light intensity was obtained through the optical fiber feedback loop. Photocurrent action spectra for zero bias voltage were measured, at the conditions typically used for IPCE measurements. Data was collected using M101 potentiostat triggered by the signal from the spectrophotometer and analyzed using the software provided by Instytut Fotonowy. These measurements were performed for publications [Sob-D] and [Sob-E].

4.4 Electrochemical Impedance Spectroscopy

Electrochemical Impedance Spectroscopy is used to determine processes happening in DSSCs on the timescales ranging from ms to s (charge collection efficiency, magnitude of the transport recombination and any diffusion limitations of the device). It can also help to find relative conduction band shift between the cells, and the parameters such as trap states density, carrier lifetime and ideality factor of the device. Measurements for publications [Sob-A], [Sob-C], [Sob-D] and [Sob-E] were performed by the same setup that was used for the current-voltage and IPCE characteristics. In paper [Sob-F] a different potentiostat was used - SP-300 (BioLogic). Most often the measurement was done for fifty frequency points ranging from 0.1 Hz to 100 kHz distributed in equal distances on the logarithmic scale. Bias voltages used spanned from 0 V up to the value over the open circuit voltage of the device in 50 mV increments. The set of curves obtained was analyzed using the ZView software and equivalent circuit consisting the transport line element [17].

4.5 UV-VIS spectroscopy

UV-VIS spectroscopy was used to analyze the absorption spectra of the dyes in the solution (shape of the spectrum, effects of the co-adsorbent and dye concentration determination) and the spectra of the photoanodes with the deposited dye (in order to determine shifts in the spectra originating from the substrate and calculate the amount of absorbed photons). It is one of the basic, irreplaceable techniques and it was utilized in all the publications except [Sob-B]. Measurements were performed using the UV-VIS-550 (Jasco) in Quantum Electronics Laboratory of Adam Mickiewicz University in Poznań, presented in Fig. 11.

Figure 11. Jasco UV-VIS-550 spectrophotometer used for the measurements of stationary absorption spectra.

4.6 Flash photolysis

Flash photolysis measurements give insight into the processes of the cell taking part on the timescales from nanoseconds to microseconds (mainly connected with dye regeneration) and was utilized in papers [Sob-A], [Sob-D], [Sob-E] and [Sob-F]. The measuring setup used was based on the Q-switched Nd:YAG laser and 150 W Xe arc lamp as the excitation and probing light sources respectively. The pump pulse was 532 nm and the probing wavelength was chosen accordingly to the sample, as described separately in the publications. The whole setup used belongs to the Center for Ultrafast Laser Spectroscopy of Adam Mickiewicz University.

4.7 Transient absorption spectroscopy

Transient absorption spectroscopy measurements provide information about the fastest processes occurring in DSSCs (injection, charge separation and ultrafast recombination) and was an important experimental tool in publications [Sob-A], [Sob-C], [Sob-D], [Sob-E] and [Sob-F]. The setup used for measurements, belonging to the Quantum Electronics Laboratory, Faculty of Physics of Adam Mickiewicz University in Poznań, consists of theHelios spectrometer (Ultrafast Systems) and Spectra Physics laser system. Its broader description is available elsewhere[18].The pump pulses were set at 500 or 600 nm and the IRF (pump-probe cross correlation function) was about 250 fs (FWHM). The typical pump pulse energy of 60 nJ corresponds to energy density of about 100 $\mu J/cm^2$. The transient absorption measurements were usually performed in the spectral ranges of 450-850 nm (VIS) and 800-1550 (NIR) and in the time range window of up to 3 ns. The setup for ultrafast transient absorption in mid-IR spectral range (3-10 µm) is the 2DQuick Transient spectrometer, PhaseTech Spectroscopy. The whole apparatus is presented below in Fig. 12. The global analysis of the transient absorption data was performed using Surface Explorer software (Ultrafast Systems). A multi-exponential function (convoluted with IRF) fitted to the kinetic vectors of a selected number of singular values was used for spectrum decomposition. As a result of the analysis, the characteristic time constants were obtained as well as the wavelength-dependent amplitudes associated with them (also called decay associated difference spectra or pre-exponential factor spectra).

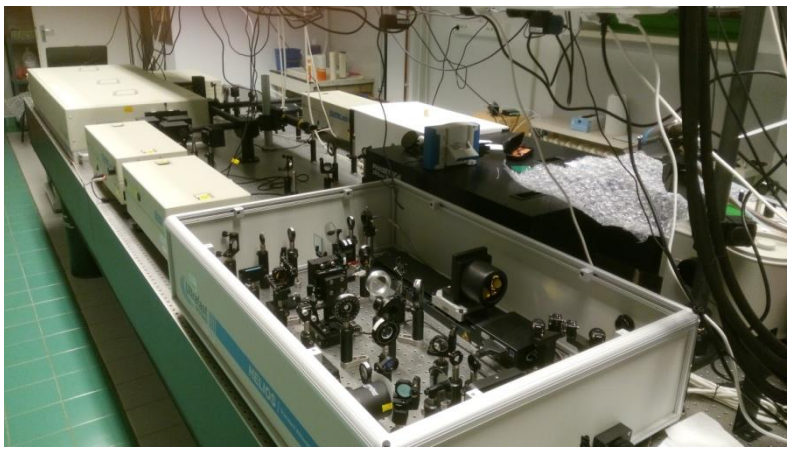

Figure 12. Setup used for transient absorption spectroscopy in VIS, NIR and mid-IR range.

4.8 Scanning Electron Microscopy

Morphology imaging and measurements were done using Scanning Electron Microscopy. In case of surface and nanoparticle size analysis, the photoanode was imaged from the top. In order to measure the thickness of the photoanode and check its homogeneity, the cross section was scanned, prepared by breaking the electrode in half. These measurements were taken for the purposes of publications [Sob-A] and [Sob-C]. All the samples were covered with about 1 nm thick gold layer by evaporation and attached to the holder with a conductive carbon tape to minimize any charge accumulation on the surface. All the imaging work was done in NanoBioMedical Centre in Poznań, using JEOL 7001TTLS microscope presented in Fig. 13. Scans were obtained using Secondary Electron mode (which yields better topographical information) with the accelerating voltage of 15 kV in most cases.

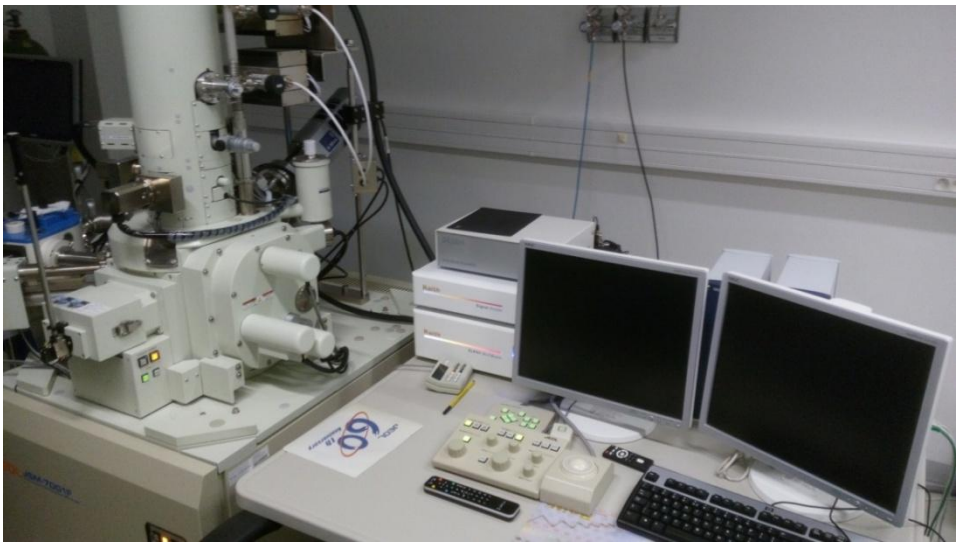

Figure 13. JEOL 7001TTLS microscope used for the scanning electron imaging.

4.9 Transmission Electron Microscopy

In order to check the features of the photoanode, where SEM resolution was insufficient (for example checking the uniformity and thickness of the core-shell structures), Transmission Electron Microscopy was used. Because, unlike SEM, it does not allow samples of any thickness, nanowires were removed from the glass substrate prior to imaging. Obtained nanopowder was dispersed in ethanol and added drop-wise on top of the copper mesh. Imaging was performed in NanoBioMedical Centre in Poznań, using JEOL TEM 1400 microscope with the LaB_6 source and accelerating voltage of 120 kV. It is shown in Fig. 14. This technique was used to check thickness and conformity of the TiO_2 shell on ZnO nanowires in paper [Sob-E].

Figure 14. JEOL TEM 1400 microscope used for the transmission electron imaging.

4.10 Atomic Layer Deposition

Atomic layer deposition was used in papers [Sob-E] and [Sob-F] to prepare the core-shell structures on the photoanode's surface. It was performed in NanoBioMedical Centre in Poznań, using a Picosun R-200 reactor. Titanium tetrachloride, trimethylaluminium and deionized water were used as titanium, aluminium and oxygen sources respectively. Purging gas was nitrogen and reaction temperature was in the range of 200-300°C, depending on the recipe.

5. Realization of the aims of the thesis in the presented publications

It will be shortly presented below, how the main aims of the thesis, listed in section 2, were realized. It is shown how particular goals and problems were studied across the different publications on which the thesis is based ([Sob-A]- [Sob-F]).

i) Optimization of the nanostructure film:

i.i) Effect of different semiconductor material (TiO_2, ZnO, Al_2O_3).

Comparison of cells based on ZnO and TiO_2 was tackled in publications [Sob-A], [Sob-C] and [Sob-E]. In paper [Sob-A] I built cells based on D149 indoline dye with the use of commercial TiO_2 paste and ready ZnO electrodes obtained from the laboratory in Seville. Photocurrents that I measured for ZnO cells turned out to be 3-4 times lower than for TiO_2 (after taking into account thickness and absorption correction). Electrochemical Impedance Spectroscopy has shown that the lifetime of electrons in ZnO cells was longer than in TiO_2 (9 ms vs 0.5 ms at 0.6 V bias voltage), so the transport properties were not responsible for the inferior photocurrent. Prepared cells were then subjected to flash photolysis and femtosecond transient absorption measurements. I took part in analysis of nanosecond results which showed that both materials are characterized by the similar regeneration efficiency; therefore regeneration process is not responsible for lower photocurrent in ZnO as well. As it turned out, the lower performance of ZnO based devices originated from the processes occurring on fs-ns timescale. The work on D149 dye was continued in paper [Sob-C], this time however the oxide pastes used for preparation of the photoanode were manufactured in the comparable conditions in our lab. Impedance measurements that I performed have confirmed the results obtained previously, with electron lifetime about the order of magnitude longer in ZnO cells than TiO_2 ones. The analysis of the results as a function of voltage has enabled me to compare the ideality factor (which was better for ZnO cells, in agreement with higher FF) and the trap density distribution in both materials. More detailed current-voltage characteristics measurements have revealed to me the quicker degradation of ZnO cells (with initial photocurrent only two times smaller than in TiO_2, but dropping significantly over several hours). Possible dye dissolution and reattachment, leading to self-quenching

was proposed as the explanatory process. In case presented measurements required it, I prepared Al_2O_3 reference cells as well. I also analyzed the thickness and morphologies of photoanodes in publication [Sob-A] and [Sob-C] by Scanning Electron Microscopy. This phenomenon of smaller injection yield for ZnO based cells was further analyzed in paper [Sob-E] where D358 dye (very similar to D149) was used. Ultrafast analysis has showed there that the first charge transfer state is formed less than 1 ps after the absorption of the photon. In the next 2-200 ps it has several pathways of evolution - charge separation, self-quenching or creation of the bound excitonic complex. It seems that the parameters previously considered unimportant - dielectric constant and refraction index - decide that the desired, first pathway is less often chosen in ZnO cells, making it ultimately inferior material compared to TiO_2.

i.ii) Effect of different nanostructure morphology.

The effect of the change in morphology of the photoanode was tested in paper [Sob-E] on the example of ZnO nanoparticle and nanowire films. Electrochemical measurements that I have done for these cells have shown that while nanowire structure exhibit better transport properties just as expected (probed by the photocurrent decay time rates, 5 ms for nanowires and 24 ms for nanoparticles at zero bias voltage), they show lower ideality factor (leading to lower fill factor). Moreover, they degrade as fast as other ZnO based cells and do not show notable differences on the ultrafast scale.

i.iii) Effect of various surface treatment ($TiCl_4$, core-shell, capping).

In an attempt to improve the ultrafast properties of ZnO devices, ZnO/TiO_2 core/shell structures have been prepared with the ALD method and studied in paper [Sob-E] (I have also verified thickness and uniformity of obtained shells by Transmission Electron Microscopy imaging). Unfortunately, this shell introduced little to no effect on the sub-ns mechanisms, as they seem to be decided by volumetric properties of the medium and therefore the shell with the thickness in the range of single nanometers has almost no impact on the efficiency. The remaining modifications were tested in conjunction with TiO_2 based devices. In the paper [Sob-D] I tested the benefits from $TiCl_4$ surface treatment on the efficiency of the cells with iodide and cobalt based electrolyte. By the means of Electrochemical Impedance Spectroscopy I found that it

greatly enhances the ideality factor of the devices (from 7.2 to 2.1 for cobalt devices and from 3.0 to 1.9 for their iodide counterparts) and increase the carrier lifetime by about order of magnitude. Moreover, UV-VIS measurements showed that it increases amount of deposited dyes as well, probably due to the increase in the surface roughness factor. All these factors translate into huge increase in the photocurrent (from 3.6 to 10 mA/cm^2 for cobalt devices, reflected also by IPCE measurements I have done)and the total efficiency. Additional ways of surface treatment, capping treatment and creation of alumina shell, were introduced in publication [Sob-F] in conjuncture with ADEKA-1 dye. Their desired purpose was to reduce the transport recombination, which is a big loss mechanism in cobalt based devices. I performed the capping treatment by dipping the photoanodes with deposited dye in the solutions of organic acids with various lengths of the carbon chain prior to the cell assembly. While the single capping treatment (using one solution) was questionably beneficial, multi capping treatment increased both the photocurrent (from 5 to 6.6 mA/cm2) and the photovoltage (from 762 to 867 mV). It was also found by impedance measurements that capping slightly improves the ideality factor of the device and lowers the conductive band edge of titania by about 55 mV. No significant negative impact of the capping treatment was found on the ultrafast scale, for bad cells it slightly increases the injection yield. Thin alumina shell was deposited using ALD method on the photoanodes before dye deposition. It was soon found from the current-voltage characteristics that the effect of such treatment depends on whether a full uniform shell is form or an island growth mode dominates. In the former case I found that alumina shell leads to the big voltage and fill factor increase, but at the expense of the photocurrent (ultrafast measurements have shown that with the increase in thickness of the Al_2O_3 shell dye-oxide charge transfer is impeded, decreasing injection yield and increasing ultrafast recombination). With shorter deposition times, islands of Al_2O_3 are created at the titania surface, acting similarly to the capping molecules. Photocurrent is increased (8.6 vs. 6.3 mA/cm^2), with voltage increased by several mV. The impedance measurements have confirmed that both these treatments lead to significant increase in the carrier lifetime and achievement of charge collection efficiency over 90%.

ii) Optimization of the electrolyte composition:

ii.i) Cobalt and iodide redox couple.

The impact of the type of the redox couple used in electrolyte was analyzed in publication [Sob-D]. I built the cells with iodide and Co-bipyridine based electrolyte using the popular carbazole dye - MK2. Current voltage characteristics revealed expected higher voltage of the cobalt based devices, albeit by a significantly smaller margin than expected from the difference in redox potentials (20 vs. 220 mV). Probably the biggest reason for this discrepancy is the increased transport recombination, which was found by EIS measurements, and that can be suppressed by the surface treatment as described earlier. Flash photolysis have showed no notable differences in the regeneration rates of both electrolytes (around 1 μs), proving that the driving force for this process is still sufficient despite the shift of the redox potential towards HOMO level of the dye. In the ultrafast time scale both redox systems have shown analogous behavior as well. In publication [Sob-F] redox couple enabling even higher voltages, Co-phenantroline, was utilized (which shares most of the properties with Co-bipyridine).I have also compared the effect of iodide- and cobalt-based electrolytes in the numerical paper [Sob-B]. Assuming that the minimum loss-in potential for DSSC with iodide electrolytes is 0.75 V, while that for cobalt electrolytes is 0.60 V, I calculated the maximum achievable efficiency for the both types of solar cells. For example, in single-cell devices the best efficiency is 17.6 % for cobalt-based DSSC, and 14.3 % for iodide based cell. For tandem configurations (with two sub-cells)the best efficiency of DSSC with the cobalt-based electrolyte can be improved to 23.6 %, with respect to the value of 19.8 % for iodide-based cells.

ii.ii) Electrolyte additives (TBP and Li^+).

The effect of electrolyte additives on the charge separation processes was investigated in publication [Sob-D]. Since lithium salts and TBP have inverse effect, constant concentration of the former was used (0.1 mM) and results were derived as a function of TBP content. Current-voltage confirmed the expected voltage increase with addition of TBP attributed to the conduction band shift. Electron Impedance Spectroscopy showed that there are no big changes in the carrier lifetimes, when open circuit

voltage is taken as a reference point. The cells I prepared were used in time-resolved laser spectroscopy studies. Flash photolysis have shown that TBP has a marginally positive effect on the dye regeneration dynamics. More effects appeared in the ultrafast picture. First, the injection is slowed down, which is reasonable since TBP shifted the conduction band closer to the excited level of the dye. More importantly, it was found that adding TBP slows down the ultrafast recombination on the scale of hundreds of ps significantly (characteristic time increased from 160 to 624 ps for iodide cells and from 210 to 760 ps for cobalt based devices). Cells with and without TBP were used in article [Sob-E] as well, to investigate the ultrafast dynamics, with results in agreement with those in article [Sob-D].

iii) Optimization of the dye:

iii.i) Determination of the best dye absorption band.

In publication [Sob-B] I used a general rule set for the construction of tandem cells in series (current is the same on all junctions and is equal to the total current of the device, total voltage of the device is the sum of voltages on all junctions) to derive an algorithm which calculates absorption onsets of multi-junction devices resulting in the best efficiency. Then, I implemented it in C and used obtained program to generate sets of results for up to five junctions and different loss-in potentials. Flexibility of the program allows to generate IPCE spectra needed as the input or open the existing ones, the effect of the real shape of the IPCE spectra and the absorption onset mismatch was checked as well. I managed to obtain two important conclusions from the calculations. The first is that there is possibly a class of dyes having high quantum efficiency, that doesn't have the absorption onset good enough to show high efficiency on their own, but may be perfectly suited for the tandem devices. The best dye absorption bands depend on the number of junctions. For example, for double-cell devices the absorption onsets are at around 720 nm and 1100 nm for both DSSCs with cobalt based electrolytes, while for single-junction device it is at around 890 nm. The second conclusion is that n-p tandem dye sensitized solar cells have very limited efficiency with the limiting factor being loss-in potential on the p side (maximum total losses cannot be higher than 1.7 V).

iii.ii) Different families of all-organic dyes.

In the studies of this thesis I compared two popular families of the dyes indoline and carbazole one. Both dye families - indoline used in publications [Sob-A], [Sob-C] and [Sob-E] and carbazole used in publications [Sob-D] and [Sob-F] have many traits in common. Both staple dyes - D149 and MK2 - are characterized by high molar attenuation coefficient, absorption maximum close to 500 nm and favorable position of energy levels. Therefore, it is no surprise that they exhibit high photovoltaic performance. The only difference that stood out during my laboratory work was that the carbazole based cells are less prone to photocurrent degradation after extended periods of time.

iii.iii) Effect of dye anchoring unit.

Effect of the substitution of the dye anchoring unit from carboxylic to silyl group was tested in publication [Sob-F] on the examples of MK2 dye (with carboxylic anchor unit) and its derivative ADEKA-1 (with silyl anchor unit). Utilization of silyl anchoring group results in the beneficial current-voltage response to the capping treatment, which did not occur when such treatment was applied to MK2 cells. It comes at the expense of more difficult dye synthesis, with affinity for polymerization. Having longer anchoring group, ADEKA-1 is also prone to tilting on the surface and generally was found to have the worse ultrafast performance. Inferior sub-ns behavior is was tried to be alleviated by fine-tuning of the surface treatment and co-adsorbent addition.

iii.iv) Effect of co-adsorbent.

Addition of co-adsorbent was used in paper [Sob-C] in order to increase the distance between the molecule, thus reducing self-quenching losses. Transient absorption measurements (of the cells I prepared and characterized) have shown that indeed increased concentration of chenodeoxycholic acid (CDCA) results in higher injection yields in TiO_2 cells. No such effect was observed in ZnO devices, which agrees with detachment-reattachment mechanism of aggregate formation, leading to self-quenching, proposed before for this material. I used different co-adsorbent – isooctyltrimethoxysilane (OTMS), suitable for silyl-anchor dyes - in publication [Sob-F] in order to minimize the ultrafast spatial recombination by tilting the dye molecules

perpendicularly to the surface of the oxide. Current voltage characteristics have shown decrease in the photocurrent (expected from the decrease in the dye loading of the photoanode and consequently number of absorbed photons) with the slight increase in voltage attributed to delicate conduction band shift of titania (similar effect to TBP, but smaller magnitude - 20 mV) and correction for the smaller photocurrent. Impedance measurements have also given information about slightly higher transport resistance upon addition of OTMS. Nevertheless, in the ultrafast measurements I revealed desired loss in amplitude and extension of the characteristic time of the spatial recombination process, confirming beneficial impact of OTMS. In both cases I used the UV-VIS spectroscopy to check the impact of the co-adsorbent on the stationary spectra and calculate the number of the photons absorbed by the film.

6. Comments on the publications

Below, each of the publications on which the thesis is based is separately commented. Their main findings, based on both my work and that of other co-authors, are summarized.

6.1 Publication Sob-A

Comparison of TiO_2 and ZnO Solar Cells Sensitized with an Indoline Dye: Time-Resolved Laser Spectroscopy Studies of Partial Charge Separation Processes, **Jan Sobuś**, Gotard Burdziński, Jerzy Karolczak, Jesus Idígoras, Juan A. Anta and Marcin Ziółek, Langmuir, **30** (2014) 2505–2512

The main scope of this work was finding the reason inferior performance exhibited by the DSSCs built using ZnO nanoparticles compared to their TiO_2 based counterparts., despite these two materials having similar band gap size and position. The indoline D149 dye was used and all the cell assembly techniques and electrolyte composition were the same in both cases. Reference cell built with Al_2O_3 nanoparticles was used as well, as the band position in this semiconductor is expected to block any electron transfer processes. Initial current-voltage measurements showed that ZnO devices transfer 3-4 times less of absorbed photons into photocurrent, compared to TiO_2 devices, with alumina based devices having negligible current as expected. Voltage of the cells was similar in both cases. Various measurement techniques were used to

probe properties of these devices in the time scales ranging from femtoseconds to seconds. The impedance spectroscopy results showed that the charge collection efficiency is high in both materials. Similarly, flash photolysis experiment showed that the regeneration efficiency in both types of cells is over 95%, so it shouldn't have much impact on the relative performance between materials. Finally, femtosecond transient absorption in visible range was used to study the efficiency of injection mechanism of both devices. As it turned out, 200 ps after the laser pumping pulse there were three times more electrons in the TiO_2 than ZnO (based on the signal of radical cation). Time resolved emission studies supported these findings by showing that the lifetime of excited state of D149 dye is three times shorter on the TiO_2 surface compared to ZnO. Therefore, the ensuing conclusion is that the slower injection process is responsible for the lower performance of ZnO based cells in comparison to TiO_2 based ones

6.2 Publication Sob-B

Optimization of absorption bands of dye-sensitized and perovskite tandem solar cells based on loss-in-potential values, **Jan Sobuś** and Marcin Ziółek, Phys. Chem. Chem. Phys., **16** (2014) 14116-14126

In this work a numeric approach was chosen in order to find out the optimal wavelength cutoffs for photovoltaic tandem devices, based on their loss-in potentials and expected IPCE of each constituting sub-cell. A program was written that simulates up to 10 devices connected in series, so that for n sub-cells:

$$J_{total} = J_1 = J_2 = \cdots = J_n$$

and

$$V_{total} = V_1 + V_2 + \cdots V_n$$

It is capable of both: finding optimal parameters of devices yet to be built and proposing the parameters of add-ons to already existing ones. Using reasonable parameters of IPCE magnitude of 90% and fill factor of 73% (obtainable by champion devices produced today), series of tandem devices were simulated with loss-in potentials varying from 0.75 V (typical for iodide electrolyte), through 0.60 V (typical for Co based electrolytes), to 0.45 V (typical for perovskite cells, which are new type of cells that emerged from DSSCs).Optimal wavelength offsets and corresponding

efficiencies were calculated for devices consisting up to 5 sub-cells. Special paragraph was devoted to analysis of n-p DSSC tandem, which resulted in its limited feasibility due to the large driving force needed for the p part. The importance of this study is enhanced by the fact that dyes working best in single junction solutions are often not the best candidate for tandem devices, as was shown by calculations on the example of experimental tandem realized with N719 and DX2 dyes [19]. Finally, the program developed (with its code attached to this publication) has great flexibility and can be used for modeling tandem devices combining different architectures (with the full freedom of choice when it comes to simulation parameters, together with the ability to load real IPCE spectra for some of the sub-cells), like for example popular lately perovskite-Si or perovskite-DSSC tandems [16][20].

6.3 Publication Sob-C

Transient states and the role of excited state self-quenching of indoline dyes in complete dye-sensitized solar cells, **Jan Sobuś**, Jerzy Karolczak, Dariusz Komar, Juan A. Anta and Marcin Ziółek, Dyes and Pigments, **113** (2015) 692-701

This work is again dedicated to the cells based on ZnO, TiO_2 and Al_2O_3 nanoparticles and D149 dye. This time the effects of addition of the co-adsorbent (chenodeoxycholic acid - CDCA) and light intensity were taken into account. Moreover, self-made oxide pastes were used to create all the electrodes for better comparison between them. As before (in paper [Sob-A]), charge collection efficiency estimated from impedance spectroscopy data is high enough for efficient operation in all cases. In fact, transport resistance and carrier lifetime is slightly better for ZnO based devices. Steady state spectroscopy shows slight blue-shift of absorption spectra depending on CDCA concentration, fluorescence decay slows down as well. New results come in the form of identification of two different excited states in D149 - locally excited state (LE) and charge transfer state (CT), discovered by analysis of transient spectra in visible and near-infrared range. Again, while in TiO_2 device there is clear formation of radical cation form the CT state and rapid injection from the LE state, the ZnO devices present much slower characteristic times of those processes, comparable with those of the reference Al_2O_3 sample. Light intensity dependence measurements showed decrease

in the injection efficiency by 50% upon increasing the energy of the pump pulse ten times. It indicates strong self-quenching process competing with injection (which was confirmed by the same experiment on Al_2O_3 cell). As the quenching rate is the rate of energy transfer between molecules, it should decrease with the increase of distance between them. Addition of CDCA was found to suppress the quenching process in TiO_2 cells. ZnO cells, on the other hand, showed little response to CDCA addition. It was proposed that the poorer performance of ZnO cells (and TiO_2 after extended time) comes from dye molecules detaching from the oxide surface in presence of electrolyte and reattaching near other molecules, forming self-quenching aggregates. This mechanism was supported by the study of the films without electrolyte and confirmed that self-quenching is the mechanism responsible for suboptimal current in indoline based DSSCs.

6.4 Publication Sob-D

Carbazole Dye- Sensitized Solar Cells Studied from Femtoseconds to Seconds —Effect of Additives in Cobalt and Iodide-Based Electrolytes, **Jan Sobuś**, Jacek Kubicki, Gotard Burdziński and Marcin Ziółek, ChemSusChem, **8** (2015) 3118–3128

This paper focused on the analysis of the performance popular carbazole dye - MK2 with different electrolytes, additional surface treatment and/or electrolyte additives. It is especially important in the light of increasing successful use of cobalt electrolytes and recent achievements of MK2 derivative – ADEKA-1 [10] (high sunlight conversion efficiencies of above 12%, this dye is investigated in [Sob-F]). $TiCl_4$ treatment turned out to have a positive effect on the cell in all the cases. Not only did it increase the absorbance, but also improved the ideality factor of the devices and increased the recombination time by at least one order of magnitude, as found by impedance spectroscopy. The effect of tert-butylpyridine (TBP) addition to the electrolyte was discovered to be far more complex. First of all, as expected, it increased the Voc of the cells by moving the conduction band of titania towards higher energies. Regeneration measurements showed negligible effect of TBP addition for both, iodide and cobalt based electrolytes, with the regeneration times around 1 μs in all cases. Transient absorption in the mid-IR region revealed more interesting phenomena. First of all, it showed that the injection times with addition of TBP are slower compared to the cells

without it, which is reasonable concerning the conduction band shift and loss of the available electron acceptor states interacting with the dye. More importantly, these results also showed the fast recombination process (between the injected electrons and oxidized dye molecule) on the timescales of several hundred ps. Addition of TBP slowed down this unwanted process significantly. These findings were supported by the results of transient absorption in visible and near-IR regions, as the shortest components of global fit are representing the injection process and their behavior agrees well with mid-IR results. Two longer components represented the fast recombination process, with the faster one connected to the trapped electrons, while longer one was presumably connected with conduction band carriers. Again, addition of TBP to electrolyte led to suppression of this unwanted mechanism as seen in increase of its characteristic times. Finally, the importance of this study was underlined by the fact that magnitude of such fast recombination directly corresponds to the total photovoltaic performance of the device.

6.5 Publication Sob-E

Effect of different photoanode nanostructures on the initial charge separation and electron injection process in dye sensitized solar cells: a photophysical study with indoline dyes, Jesús Idígoras, **Jan Sobuś**, Mariusz Jancelewicz, Eneko Azaceta, Ramon Tena-Zaera, Juan A. Anta and Marcin Ziółek, Materials Chemistry and Physics, **170** (2016) 218-228

This paper is a further extension of publications [Sob-A] and [Sob-C]. Two main problems are analyzed: effect of different morphologies of the photoanode on the performance of the cells and understanding the processes undergoing in the D358 dye (which is a derivative of previously studied D149 dye with double carboxylic anchor group and longer carbon chain in the structure). Various morphologies of ZnO based DSSCs are analyzed including: nanoparticles, nanowires, electrodeposited mesoporous layer and their core-shell derivatives. Initial efficiency measurements showed that, similarly to D149, the photocurrent of ZnO devices is much lower than for TiO_2 counterparts and degrades faster with cell aging. Regeneration was also found to be slower in ZnO cell, especially in nanowire based cells (order of magnitude difference). Injection efficiency was found to be at most half of that in TiO_2, with the worst

performance in the case of nanowire cells (probably to the enhanced self-quenching of dye molecules). Preparing core-shell nanowires did not help to alleviate the difference. It shows that the interaction of the dye with the core material is crucial to understand the ultrafast picture of the dye-oxide interaction. Detailed femtosecond transient absorption study suggested that lower ZnO performance is a "universal" property of this material and showed several origins of its worse efficiency. Firstly, the contribution of bound radical cations was higher in case of ZnO due to its lower dielectric constant (and consequently higher electrostatic binding energy between injected, but yet to be separated electron and oxidized dye). Secondly, higher energy transfer between dye molecules (leading to self-quenching) was discovered in ZnO cells compared to TiO_2 counterparts. Its origin comes from the lower refraction index of the former material (2.0 vs. 2.6).Different morphologies did not have any significant impact on the ultrafast dye behavior.

6.6 Publication Sob-F

Factors affecting the performance of champion silyl-anchor carbazole dye revealed in the femtosecond to second studies of complete ADEKA-1 sensitized solar cells. **Jan Sobuś,** Błażej Gierczyk, Gotard Burdziński, Mariusz Jancelewicz, Anders Hagfeldt and Marcin Ziółek Paper in preparation: finalized and sent to co-authors for corrections.

The work of last several months (which has the paper being prepared at the moment) revolves around the recently reported modification of MK2 dye - ADEKA1 - which has reportedly reached over 12% efficiency [10]. The dye molecule has the same core as MK2 with the alkoxysilane anchoring group, creating much stronger bond with the oxides surface than carboxylic one. It enables the capping treatment (successive dipping in the solutions of organic acids to form an organic thicket between dye molecules) without extensive dye dissolution during the process. We performed series of experiments in order to investigate the effect of the capping treatment, creation of the thin alumina shell and co-adsorbent addition on the processes occurring on the timescales reaching from fs to s. In this way both the benefits and the drawbacks of these modifications were found. In short, the addition of co-adsorbent lowered the ultrafast recombination between oxide and dye donor part at the expense of

absorbance of the cell and slight decrease in charge collection efficiency. Capping treatment brings even bigger cost in absorbance, yet it increases the charge collection efficiency up to over 90% without significant drawbacks on the ultrafast timescale. Alumina was deposited on the photoanodes using Atomic Layer Deposition. It was found that depending on the process conditions, two completely different effects can be achieved. Short deposition and purge times (insufficient for the creation of uniform shell on the whole surface of mesoporous oxide) lead to the island growth, increasing the photocurrent with no big effect on the voltage or fill factor. Longer deposition greatly enhances the voltage and fill factor, but at the expense of the photocurrent. The suggested mechanism for both results is presented. No notable effect on regeneration process efficiency has been found in any case. Additionally, a new synthesis route for ADEKA-1 dye was developed with the high yield and the low degree of polymerization of the product. Hopefully, these results will pave the way for more successful dye modifications and help breach the glass ceiling in DSSC efficiency.

7. Summary

During the course of this thesis the significant number of dye sensitized solar cells based on popular indoline (D149 and D358) and carbazole (MK2, ADEKA-1) dyes were prepared in order to unravel the effect of modifications to the photoanode's structure (material, morphology, surface treatment) and electrolyte (redox couple type and the effect of its additives)on the fundamental processes ongoing on the timescales from femtoseconds to seconds in the devices. The combination of the wide range of experimental techniques such as stationary and transient spectroscopy, photoelectrochemical measurements (current-voltage characteristics, IPCE, electrochemical impedance spectroscopy) and electron imaging (TEM, SEM) shed new light on these complex mechanisms. In particular, it was found that:

- Titanium dioxide is "universally" better material for construction of DSSCs than zinc oxide, despite similar bandgap.
- No big difference between these two materials is observed when it comes to charge collection efficiency or regeneration efficiency (both over 90%). The difference in total performance comes from the worse injection and initial charge separation in the latter material.
- Differences in the performance on the ultrafast scale comes from the stronger electron-dye cation interaction (as a result of lower dielectric constant in ZnO, 3 vs. 85) and more abundant self-quenching (possible dye agglomeration and easier energy transfer due to the lower effective refraction index in ZnO).
- Different photoanode's morphologies (especially ZnO nanowires vs. ZnO nanoparticles)showed some differences in the charge transport on ms time scale (e.g. faster for nanowires than nanoparticles), but similar performance was observed, when it comes to ultrafast (sub-ns) behavior. The latter was significantly worse with respect to that of TiO_2cell, e.g. the residual signal in NIR range(which is a measure of efficiency of the initial charge separation processes)lies in the range of 10-22% for all ZnO morphologies compared to about 50 % in titania.

- Ultrafast recombination, happening on the timescales of tens and hundreds of picoseconds, was analyzed in the context of electrolyte additives for the first time. It was found to be suppressed by TBP addition (studied for MK2-sensitized cells).
- Cobalt based cells exhibit much higher transport recombination compared to iodide ones, surface treatment helps to reduce it for both electrolytes (e.g. for MK2-sensitized cells it is reflected by efficiency rising from 2.4 to 4.2% for iodide and from 0.7 to 4% for cobalt based cells).
- Both alumina shell and molecular capping treatment help to improve the charge collection efficiency, but former at the expense of the photocurrent, and the latter at the expense of absorption of photons in the solar cell.
- Tunable amount of surface additives (co-adsorbent, capping molecules) not only affects the distance between the dyes but can also reduce the sub-ns recombination of electrons between titania and dyes.

Experimental work was supported by numeric analysis of the optimal parameters of multi-junction devices. A flexible simulation model was derived and provided important results:

- Absorption onsets resulting in the highest efficiency were found for the simulated devices consisting of DSSC-based (iodide or Co) or perovskite-based sub-cells (for example 716 nm and 1019 nm for a two-junction, cobalt based cell, which would yield theoretical efficiency of 23.6%).
- Narrow viability of n-p based tandem DSSCs was shown due to the too high energy losses in the p-part.
- The need of finding appropriate dyes for the planned tandem architecture was underlined, as seldom champion dyes in traditional designs can provide maximum efficiency in the multi-junction cell.

List of references

[1] "A low-cost, high-efficiency solar cell based on dye-sensitized colloidal TiO_2 films", B. O'Regan, M. Grätzel Nature **353** (1991), 737–740

[2] "Conversion of light to electricity by cis-X2bis(2,2'-bipyridyl-4,4'-dicarboxylate)ruthenium(II) charge-transfer sensitizers (X = Cl-, Br-, I-, CN-, and SCN-) on nanocrystalline titanium dioxide electrodes", M. K. Nazeeruddin, A. Kay, I. Rodicio, R. Humphry-Baker, E. Mueller, P. Liska, N. Vlachopoulos, M. Graetzel, J. Am. Chem. Soc., **115** (1993), 6382–6390

[3] "Estimating the Maximum Attainable Efficiency in Dye-Sensitized Solar Cells", H. J . Snaith, Advanced Functional Materials, **20** (2010), 13–19

[4] "Photoelectrochemical cells", M. Grätzel, Nature **414**, 338-344

[5] "ZnO Nanostructures for Dye-Sensitized Solar Cells ", Q. Zhang, C.S. Dandeneau, X. Zhou, and G. Cao,. Adv. Mater., **21** (2009), 4087–4108.

[6] "Ultra-long anatase TiO_2 nanowire arrays with multi-layered configuration on FTO glass for high-efficiency dye-sensitized solar cells", W. Wu-Qiang, X. Yang-Fan, S. Cheng-Yong and K. Dai-Bin, Energy Environ. Sci.,**7** (2014), 644-649

[7] **"**TiO2 nanotubes and their application in dye-sensitized solar cells**"**, R. Poulomi, K. Doohun, L. Kiyoung, E. Spiecker and P. Schmuki, Nanoscale,**2** (2010), 45-59

[8] "Iodine/iodide-free redox shuttles for liquid electrolyte-based dye-sensitized solar cells", J. Cong, X. Yang, L. Kloo and L. Sun, Energy Environ. Sci.,**5** (2011), 9180-9194

[9] "Porphyrin-Sensitized Solar Cells with Cobalt (II/III)–Based Redox Electrolyte Exceed 12 Percent Efficiency", A. Yella et al., Science, **334** (2011), 629-634

[10] **"**An achievement of over 12 percent efficiency in an organic dye-sensitized solar cell**",** K. Kakiage, Y. Aoyama, T. Yano, T. Otsuka, T. Kyomen, M. Unno and M. Hanaya, Chem. Commun., **50** (2014), 6379-6381

[11] **"**Quantification of the Effect of 4-tert-Butylpyridine Addition to I-/I3- Redox Electrolytes in Dye-Sensitized Nanostructured TiO2 Solar Cells", G. Boschloo, L. Häggman and A. Hagfeldt, The Journal of Physical Chemistry B, **110** (2006), 13144-13150

[12] "Avoiding Diffusion Limitations in Cobalt(III/II)-Tris(2,2'-Bipyridine)-Based Dye-Sensitized Solar Cells by Tuning the Mesoporous TiO_2 Film Properties", H.N. Tsao, P. Comte, C. Yi and M. Grätzel, ChemPhysChem, **13** (2012), 2976–2981

[13] "Control of Charge Recombination Dynamics in Dye Sensitized Solar Cells by the Use of Conformally Deposited Metal Oxide Blocking Layers", E. Palomares,

J. N. Clifford, S. A. Haque, T. Lutz, and J. R. Durrant, J. AM. CHEM. SOC. **125** (2003), 475-482

[14] "ZnO-Al2O3 and ZnO-TiO2 Core-Shell Nanowire Dye-Sensitized Solar Cells", M. Law, L. E. Greene, A. Radenovic, T Kuykendall, J. Liphardt, and P. Yang, J. Phys. Chem. B, **110** (2006), 22652-22663

[15]**"**Monolithic DSSC/CIGS tandem solar cell fabricated by a solution process**",** S. H. Moon, S. J. Park, S. H. Kim, M. W. Lee, J. Han, J. Y. Kim, H. Kim, Y. J. Hwang, D. K. Lee & B. Koun Min, Scientific Reports **5** (2015), 8970

[16]"Spectral splitting photovoltaics using perovskite and wideband dye-sensitized solar cells", T. Kinoshita, K. Nonomura, N. J. Jeon, F. Giordano, A Abate, S. Uchida, T. Kubo, S. I. Seok, M. K. Nazeeruddin, A. Hagfeldt, M. Grätzel & H. Segawa, Nature Communications **6** (2015), 8834

[17] "Theory of the Impedance of Electron Diffusion and Recombination in a Thin Layer", Juan Bisquert, The Journal of Physical Chemistry B, **106** (2002), 325-333

[18] "The Impact of the Electrical Nature of the Metal-Oxide on the Performance in Dye-Sensitized Solar Cells: New Look at Old Paradigms", J. Idígoras, G. Burdziński, J. Karolczak, J. Kubicki, G. Oskam, J. Anta, M. Ziółek. Journal of Physical Chemistry C, **119** (2015), 3931-3944

[19] "Wideband dye-sensitized solar cells employing a phosphine-coordinated ruthenium sensitizer", T. Kinoshita, J. T. Dy, S. Uchida, T. Kubo, H. Segawa, Nature Photonics, **7** (2013), 535-539

[20] **"**Monolithic perovskite/silicon-heterojunction tandem solar cells processed at low temperature**",** S. Albrecht, M. Saliba, J. P. Correa Baena, F. Lang, L. Kegelmann, M. Mews, L. Steier, A. Abate, J. Rappich, L. Korte, R. Schlatmann, M. K. Nazeeruddin, A. Hagfeldt, M. Grätzel and B. Rech, Energy Environ. Sci., **9** (2016), 81-88

Other publications

Other research papers:

- *"Ogniwa perowskitowe - szansa na przełamanie impasu w rozwoju ogniw słonecznych III generacji",*
  Jan Sobuś, Dokonania Młodych Naukowców, ISSN: 2300-4436 (2014)
- *"Sposoby zwiększenia wydajności w ogniwach barwnikowych",*
  Jan Sobuś, Dokonania Młodych Naukowców, ISSN: 2300-4436 (2014)
- *"Ogniwa słoneczne III generacji – rozwiązania i możliwości, podejście teoretyczne i praktyczne",*
  Jan Sobuś, Wpływ młodych naukowców na osiągnięcia polskiej nauki,
  ISBN: 978-83-63058-39-5 (2014)
- *"Alcothermal synthesis of template-free mesoporous titania for dye-sensitized cells applications",*
  Maciej Zalas, Agata Wawrzyńczak, Paulina Półrolniczak, **Jan Sobuś**, Grzegorz, Schroeder, Stefan Jurga and Elena Selli, Paper under review in Materials Chemistry and Physics.

Important conferences attended:

- 7th International Conference on Hybrid and Organic Photovoltaics, 10-13.05.2015, Rome, Italy
  Poster: *"Cobalt vs. iodide based electrolyte in DSSC: additives effect on charge separation processes studied from femtoseconds to seconds in fully working cells."*
- 6th International Conference on Hybrid and Organic Photovoltaics, 11-14.05.2014, Lausanne, Switzerland
  Poster: "*Optimization of absorption bands of dye-sensitized and perovskite multi-junction solar cells based on loss-in-potential values and IPCE spectra.*"
- NanoPT 2014, Portugal 12-14.02.2014
  Poster: *"Comparison of dye-sensitized solar cells built with TiO_2 and ZnO nanoparticles layer."*

Full text of publications constituting the thesis

Langmuir

Article

pubs.acs.org/Langmuir

Comparison of TiO_2 and ZnO Solar Cells Sensitized with an Indoline Dye: Time-Resolved Laser Spectroscopy Studies of Partial Charge Separation Processes

Jan Sobuś,[†,‡] Gotard Burdziński,[‡] Jerzy Karolczak,[‡,§] Jesús Idígoras,[∥] Juan A. Anta,[∥] and Marcin Ziółek*[,‡]

[†]NanoBioMedical Centre, Adam Mickiewicz University, Umultowska 85, 61-614 Poznan, Poland

[‡]Quantum Electronics Laboratory, Faculty of Physics, Adam Mickiewicz University, Umultowska 85, 61-614 Poznan, Poland

[§]Center for Ultrafast Laser Spectroscopy, Adam Mickiewicz University, Umultowska 85, 61-614, Poznan, Poland

[∥]Departamento de Sistemas Físicos, Químicos y Naturales, Área de Química Física, Universidad Pablo de Olavide, Ctra. Utrera, km 1, E-41013 Sevilla, Spain

Supporting Information

ABSTRACT: Time-resolved laser spectroscopy techniques in the time range from femtoseconds to seconds were applied to investigate the charge separation processes in complete dye-sensitized solar cells (DSC) made with iodide/iodine liquid electrolyte and indoline dye D149 interacting with TiO_2 or ZnO nanoparticles. The aim of the studies was to explain the differences in the photocurrents of the cells (3−4 times higher for TiO_2 than for ZnO ones). Electrochemical impedance spectroscopy and nanosecond flash photolysis studies revealed that the better performance of TiO_2 samples is not due to the charge collection and dye regeneration processes. Femtosecond transient absorption results indicated that after first 100 ps the number of photoinduced electrons in the semiconductor is 3 times higher for TiO_2 than for ZnO solar cells. Picosecond emission studies showed that the lifetime of the D149 excited state is about 3 times longer for ZnO than for TiO_2 samples. Therefore, the results indicate that lower performance of ZnO solar cells is likely due to slower electron injection. The studies show how to correlate the laser spectroscopy methodology with global parameters of the solar cells and should help in better understanding of the behavior of alternative materials for porous electrodes for DSC and related devices.

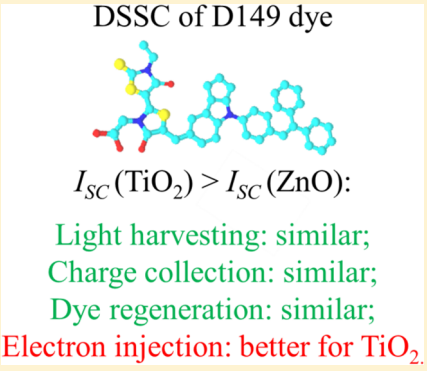

1. INTRODUCTION

In recent years a few novel photovoltaic solutions have emerged using the latest advances in nanotechnology. It is the dye-sensitized solar cell (DSC) which has been up to date one of the most promising.[1−4] The main advantages of DSCs over the silicon and thin films solar cells are much lower production cost and better performance in conditions of intermediate or low sunshine.

The working principle of DSC is the interaction between dyes and semiconductor metal oxide nanoparticles (most often TiO_2), to which the dyes are attached.[2,3,5] The nanoparticles covering one of the photocell's electrodes (photoanode) form a mesoporous structure of a very large effective surface area. After photoexcitation of the dye, electron injection from the dye to the conduction band of titania nanoparticle takes place. This electron is transported via the nanoparticle network to the electrodes. After the electron injection, the oxidized dye (radical cation) has to be regenerated from the redox pair in the electrolyte (most often iodide/triiodide couple, I^-/I_3^-). Finally, the redox couple is oxidized in the reaction at the other electrode (cathode), which closes up the electron cycle and enables the current to flow through the solar cell circuit. The unwanted processes that can compete with correct charge separation are internal conversion in the excited dye and electron recombination from the conduction band to the oxidized dye or to the redox couple in electrolyte.

The photocurrent, which determines the overall efficiency of the solar cell, depends on the quantum yield of electron generation by the incoming solar photons. This is called the incident photon to current efficiency (IPCE):[3]

$$J_{sc} = \int \mathrm{IPCE}(\lambda) e \Phi_{ph}(\lambda)\, d\lambda \quad (1)$$

where $\Phi_{ph}(\lambda)$ is the photon flux. IPCE is usually expressed as a function of the wavelength λ of the incoming light in the following way:

$$\mathrm{IPCE}(\lambda) = \mathrm{LHE}(\lambda)\phi_{ei}(\lambda)\phi_{reg}(\lambda)\eta_{cc} \quad (2)$$

where LHE (light-harvesting efficiency) is the fraction of the incident light that is absorbed (LHE = $1 - 10^{-A}$, where A is the total absorbance of the dyes attached to the titania nanoparticles surface). The other factors in eq 2 are the quantum

Received: December 16, 2013
Revised: February 12, 2014

   dx.doi.org/10.1021/la404782s | Langmuir XXXX, XXX, XXX−XXX

yields of elementary charge separation processes, which occur in the time scale from tens of femtoseconds to single seconds. The fastest processes (10 fs−1 ns) determine the quantum yield of electron injection (φ_{ei}) from the excited state of the dye to the conduction band of the nanoparticle. The intermediate ones (1 ns−100 μs) govern the quantum yield of dye regeneration (φ_{reg}) by the electrolyte. Finally, the slowest processes (100 μs−10 s) are connected with the charge collection efficiency (η_{cc}) from the nanoparticle layer.

The quantum yield of dye regeneration is determined by the competition with back electron transfer to the oxidized dye (electron recombination) and for steady state conditions can be calculated as

$$\phi_{reg} = \frac{k_{reg}[I^-]}{k_{reg}[I^-] + k_{recom}n_{el}} \quad (3)$$

where k_{reg} and k_{recom} are second-order rate constants for regeneration and recombination, respectively, while $[I^-]$ and n_{el} are the concentration of iodide ions and electrons in the semiconductor, respectively.

The standard techniques used for temporal characterization of DSC (like electrochemical impedance spectroscopy, photovoltage decay studies, or intensity modulated spectroscopy) only provide information about the slowest charge collection processes (milliseconds). Fast and ultrafast laser spectroscopy tools are needed to gain access to the partial charge separation processes occurring on a shorter time scale.

Despite numerous studies of DSCs in recent years, not many of them describe the rate constants and quantum yields of these fast individual processes leading to final charge separation, especially in DSC with organic dyes. Moreover, for many years the electron injection was considered to occur on subpicoseconds time scale for all efficient devices, based on the studies of the isolated systems. In the first work in 2005, it was shown that electron injection can be quite different in a complete DSC.[6] Since then, a few contributions reported the studies of electron injection in real DSC.[7−18] Most of them showed that electron injection is slowed down, mainly due to the effect of additives in electrolyte that shift the semiconductor conduction band edge. However, opposite findings have been also reported.[15,19] It is thus important to study the complete DSC filled with functioning electrolyte in order to get the real rates and quantum yields of charge separation processes.

Therefore, we have chosen a system composed of liquid electrolyte with the iodine/iodide redox couple and the indoline-based D149 dye (Figure S1 in the Supporting Information) interacting with TiO_2 or ZnO nanoparticles. This system is thoroughly studied by time-resolved laser spectroscopy techniques in the time range from femtoseconds to seconds. D149 dye is one of the most studied organic dyes in the DSC field.[20−29] Recently, it has also been studied by ultrafast time-resolved laser spectroscopy: in solution,[30,31] in the isolated ZnO and TiO_2 films,[27,32] and in complete TiO_2 cells probed in the mid-IR range.[11] We have also studied the complete D149/TiO_2 solar cells by the flash photolysis technique.[33]

ZnO is an alternative material to TiO_2 to be used in DSC. It has a similar bandgap as TiO_2 but shows better transport properties in the bulk and allows for easy fabrication of different nanostructures.[34] However, the reported efficiencies of ZnO-based solar cells are still far below their TiO_2 counterparts, and it is yet to be clear which processes are responsible for the worse performance of ZnO-based devices.[34,35] It should be also noted that ZnO material has a potential application in photocatalysis and nanomedicine[36] as well as electron-selective contact in the new concept of perovskite-based solar cells.[37,38]

The aim of this study is to compare the performance of solar cells made with TiO_2 and ZnO in order to identify the partial charge separation process that is responsible for the observed differences in the global sunlight conversion efficiencies of these materials. The studies will show how to correlate the laser spectroscopy methodology with global parameters of the solar cells and should provide a better understanding of the behavior of alternative materials for porous electrodes in DSC.

2. EXPERIMENTAL SECTION

The TiO_2 films were prepared from highly transparent titania nanoparticle paste (Ti-Nanoxide HT, Solaronix SA), containing anatase nanocrystalline particles of about 10 nm diameter. A layer of paste was coated onto the FTO electrode using the "doctor blade" technique between two parallel adhesive Scotch tapes. The film was then annealed at 450 °C to fabricate the mesoporous TiO_2 layer.

The ZnO films were prepared from commercial (Evonik) dispersion of hydrophilic nanoparticles of ZnO in water (VP AdNano@Zn20, 35 wt %) with approximate nanoparticle size of 20 nm. The films were deposited by spin-coating and heated to 420 °C for 30 min.

For the Al_2O_3 films, the paste was obtained by mixing 1 g of Al_2O_3 nanoparticles (diameter <50 nm, Sigma-Aldrich) dispersed in a solution containing: 100 mL of ethanol, 1 mL of distilled water, and 1 mL of acetic acid. Then, 1.6 g of ethyl cellulose and 10 mL of α-terpineol were added into the solution. The films were deposited by the "doctor blade" technique and annealed at 450 °C.

The films were immersed in a 3×10^{-5} M solution of D149 dye (Sigma-Aldrich) in dichloromethane (DCM, spectroscopic grade >99.5%, Aldrich) and kept at room temperature for about 1 h. The platinized counter electrode was obtained by spreading a Pt-based solution (Platisol T, Solaronix SA) on FTO glass and annealing at 450 °C. To make a complete solar cell, the counter electrode was assembled with thermal adhesive film (25 μm Surlyn, Meltronix, Solaronix SA) that acts as separator and sealing element. The functioning solar cells were filled with a commercial liquid electrolyte (Iodolyte AN-50, Solaronix SA) containing the I^-/I_3^- redox couple ($[I_2]$ = 50 mM), ionic liquid, lithium salt, and pyridine derivative in acetonitrile (ACN) solution. The reference samples for flash photolysis experiments were filled with ACN (spectroscopic grade >99.5%, Aldrich).

The nanosecond flash photolysis setup was based on Q-switched Nd:YAG laser and a 150 W xenon arc lamp as the excitation and the probing light sources, respectively. The experimental parameters were the same as previously described.[33] For the femtosecond−picosecond transient absorption measurements the Ti:sapphire laser system[39] and NOPA (noncollinear optical parametric amplifier) were used. The pump pulses were at 520−550 nm, and the IRF (pump−probe cross-correlation function) was 150−200 fs (fwhm). The pump pulse energy was 270 nJ, corresponding to energy density of about 1 mJ/cm^2. The probe beam was the white light continuum generated in a 1 cm cell of water. All the spectra analyzed were corrected for chirp of white light continuum. The transient absorption measurements were performed in the spectral range of 420−720 nm and the time range of 0−500 ps. The data were analyzed using the multiexponential global fit program.[40]

The time-resolved emission measurements in the picosecond time window were performed using a time-correlated single photon counting technique (TCSPC).[41] The measurements were carried out at the magic angle with the pump wavelength of 425 nm. The samples (solar cells) were irradiated from the working electrodes side, and the angle between cells surface and direction of the excitation beam was tuned to get the best temporal resolution (at 80°). In the best configuration the IRF of the setup was about 60 ps (fwhm), about

dx.doi.org/10.1021/la404782s | Langmuir XXXX, XXX, XXX−XXX

twice as the one obtained during the studies in solution with the same setup.[41]

The steady-state UV−vis absorption spectra were measured with a UV-VIS-550 (Jasco) spectrophotometer. A M101 potentiostat with FRA32 M module (Autolab) was used to measure electrochemical impedance spectra (10 mV perturbation in the 10^{-1}−10^{6} Hz range), and the data were analyzed with Nova 1.9 (Autolab) software.

The morphology of the nanoparticle films was analyzed using a scanning electron microscope (JEOL 7001 TTLS). Samples were sputtered with 5 nm 80:20 Au/Pd layer to obtain a conductive surface. Then, SE mode with acceleration voltage of 15 kV was used to collect images.

3. RESULTS AND DISCUSSION

3.1. Global Characterization of Solar Cells. Table 1 contains the comparison of the global parameters of the studied cells: short circuit current density (J_{SC}), open circuit voltage (V_{OC}), and the amplitude of the maximum of the D149 absorption band at 520 nm (A). The fill factor for all cells was around 0.50. The setup configurations require relatively large active surface of the cell (~1 cm^2), which leads to a large series resistance, hence deteriorating the fill factor (about 40 Ω, as revealed from the impedance spectra). After correcting for series resistance, the fill factor raises to about 0.60 for TiO_2 cells and 0.52 for ZnO cells. It is also important to mention that the photocurrents and photoconversion efficiencies are generally low due to the need of keeping the cells transparent enough for transmission laser spectroscopy (see Figure S1 for absorption and emission spectra of D149 solar cell). However, as shown below, the electron collection efficiencies approach 100% in the studied devices, which guarantee that the conclusions obtained for these cells of low light-harvesting features can still be considered general enough to be extrapolated to more efficient devices where the better performance is mainly due to a greater active layer absorbance.

Table 1. Parameters of the Studied Cells: Amplitude of Maximum of the D149 Absorption Band at 520 nm (A_{max}), Open Circuit Voltage (V_{OC}), and Short Circuit Current Density (J_{SC}) for 1 sun Conditions, Number of Absorbed Photons (N_{ph}) Calculated from Eq 4, and J_{SC}/N_{ph} Ratio

sample	TiO_2	TiO_2 "diluted"	ZnO	Al_2O_3
A_{max}	1.2	0.45	0.35	1.1
V_{OC}, mV	560	500	540	250
J_{SC}, mA/cm^2	3.0	1.6	0.4	0.1
$N_p \times 10^{16}$, s^{-1} cm^{-2}	4.53	2.55	2.12	4.35
J_{SC}/N_{ph}, mA s	0.66	0.63	0.19	0.02

Under the same soaking conditions, the maximum absorbance of the sensitized ZnO film (A = 0.35) was significantly smaller than that of the TiO_2 sample (A = 1.2). This was due to differences in the film preparation, leading to different film thickness. As revealed in SEM pictures (Figure S2), the average thickness of the TiO_2 material was 4.5 μm, while that of ZnO was 1 μm. Therefore, in order to compare the photocurrents of TiO_2 and ZnO, the ratio of (J_{SC}) and number of absorbed photons (N_{ph}) was calculated (Table 1), where

$$N_{ph} = \int (1 - 10^{-A(\lambda)})\Phi_{ph}(\lambda)\, d\lambda \quad (4)$$

and the photon flux $\Phi_{ph}(\lambda)$ was taken from the AM1.5 standard.

As it can be seen, the ratio is 3.5 times higher for TiO_2 (J_{SC}/N_{ph} = 0.66) than ZnO (J_{SC}/N_{ph} = 0.19) solar cells. In order to be sure that the observed effect is not connected with the total absorbance of the sample, another TiO_2 cell was prepared (denoted as "diluted" in Table 1) with an absorbance (A = 0.45) comparable to that of ZnO by using more diluted paste (after adding ethanol of about 50% volume, giving effective thickness 3 μm) and shorter soaking time in the dye solution. In this case J_{SC}/N_{ph} = 0.63, which is similar to that of the TiO_2 sample with higher absorbance.

For the reference D149/Al_2O_3 cell no electron transfer process should occur due to large bandgap of Al_2O_3 semiconductor. Thus, as expected, the photocurrent for this system is negligible (J_{SC}/N_{ph} = 0.02, Table 1).

Combining eqs 1, 2, and 4, it can be seen that J_{SC}/N_{ph} is proportional to the product of electron injection, dye regeneration, and charge collection (φ_{ei}, φ_{reg}, η_{cc}). Therefore, these processes will be separately explored to gain knowledge about which one is responsible for the lower performance of the ZnO solar cell.

The electrochemical impedance spectroscopy results (Figure S3 and Table S1) allow to extract transport and recombination resistances in the photoanode. The shape of the spectra and the obtained values for these quantities (much larger recombination resistance than transport resistance) indicate that the collection efficiencies for both types of cell (TiO_2 and ZnO) are high. Therefore, the dynamics in the millisecond−second time regime are not responsible for lowering the global performance of the ZnO solar cells. This observation is in line with previous, more detailed studies of electron transport properties in ZnO.[24,34]

3.2. Nanosecond to Microsecond Studies. Flash photolysis results for D149/TiO_2 solar cells had been investigated by us in detail previously.[33] We had observed a contribution of dynamic Stark shift effect to the transient spectra, and we had found that the signal of D149 radical cation at 680 nm is the best probe wavelength of the regeneration dynamics because it is close to the band maximum and the influence of Stark shift signal is minimized.[33] Therefore, we have chosen a probing wavelength at 680 nm for the present studies. In samples with electrolyte both dye regeneration and electron recombination take place, while the reference inert cells (filled with pure ACN instead of electrolyte) were used to observe only the electron recombination process.

Figure 1A presents a comparison of electron recombination dynamics measured for reference cells filled with an inert solvent (ACN). The signals for ZnO sample are lower and thus more noisy than those of TiO_2 due to lower photocurrent of the solar cells. As can be seen, the dynamics are similar for both systems and they spread over many time scales, which is commonly observed in DSCs.[42−44] Therefore, data were fitted with a stretched exponential function:

$$A(t) = A_0 e^{-(t/\tau)\beta} \quad (5)$$

This function contains two parameters: the characteristic time τ and the dispersion parameter β ($0 < \beta < 1$, lower β values mean more stretched decay, extending the decay time scale). The average rate constant k of the process described by function 5 was calculated as[45]

$$k = \left(\frac{\tau}{\beta}\Gamma\left(\frac{1}{\beta}\right)\right)^{-1} \quad (6)$$

dx.doi.org/10.1021/la404782s | Langmuir XXXX, XXX, XXX−XXX

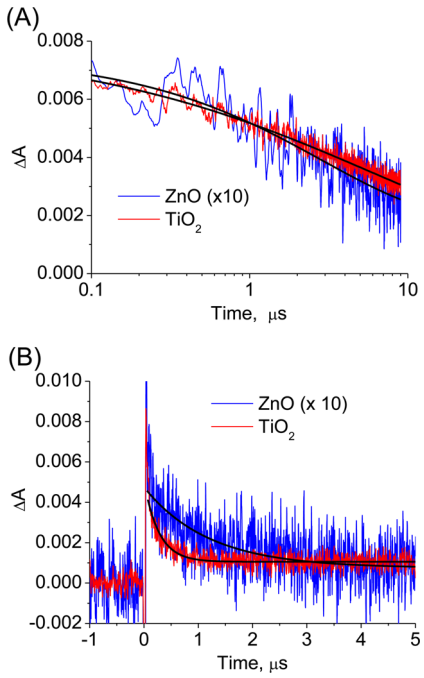

Figure 1. Transient absorption kinetics from nanosecond flash photolysis experiment for D149/TiO_2 and D149/ZnO cells filled with (A) ACN and (B) iodide electrolyte, measured at 680 nm under a pump pulse of 300 μJ/cm^2 at 532 nm. The solid black lines show the best fits of (A) stretched exponential function given by eq 6 with the parameters τ = 2.9 μs and β = 0.62 for ZnO and τ = 5.8 μs and β = 0.40 for TiO_2, yielding average rate constants (from eq 6) of $k = 13 \times 10^4$ s^{-1} for ZnO and $k = 9 \times 10^4$ s^{-1} for TiO_2, and (B) single-exponential function giving the rate constants $k = 1.0 \times 10^6$ s^{-1} for ZnO and $k = 5.0 \times 10^6$ s^{-1} for TiO_2.

The average rates calculated from eqs 5 and 6 are $k_{inert} = 13 \times 10^4$ s^{-1} for ZnO and $k_{inert} = 9 \times 10^4$ s^{-1} for TiO_2 (subscript "inert" corresponds to ACN). The transient absorption kinetics for the cells with electrolyte are presented in Figure 1B. The one-exponential fits give the rates $k_{electrol} = 1.0 \times 10^6$ s^{-1} for ZnO and $k_{electrol} = 5.0 \times 10^6$ s^{-1} for TiO_2.

A commonly used procedure is to directly take the rates obtained in the cells with electrolyte ($k_{electrol}$) and with inert solvent (k_{inert}) and, assuming the pseudo-first-order rates for both regeneration and recombination process, calculate the regeneration as ($k_{electrol} - k_{inert}$) and its efficiency as

$$\varphi_{reg} = \frac{k_{electrol} - k_{inert}}{k_{electrol}} \quad (7)$$

In this way the quantum yields of dye regeneration can be estimated as 0.87 for ZnO and 1.00 for TiO_2 cells.

However, comparing with eq 3, which is formulated at steady state, this approach is equivalent with the assumption that concentrations of the species reacting with the oxidized dye molecules are in large excess. The concentration of $[I^-]$ is constant if the light intensity is not too high, so the regeneration process can usually be considered as a first-order reaction. In contrast, the concentrations of free and trapped electrons (n_{el} in eq 3) change with time as the Fermi level falls after the pulse excitation in flash photolysis experiment. This is the reason for the stretched exponential behavior of the decay. Therefore, eq 7 can only be used if the excitation pulse intensity is small compared to the bias light. In our case we used 300 μJ/cm^2 pulse intensity, and the bias light originating from probing pulsed light from Xe lamp is about 4 suns. These relative intensities do not guarantee that the small perturbation approximation holds in the experiment.

Thus, and in order to provide further assurance of the validity of the obtained results, we have fitted a one-exponential function to the initial 15% decay of the inert and active samples, when n_{el} does not change significantly and can be considered as constant. Following this alternative procedure, the obtained rates were $k_{inert} = 0.3 \times 10^6$ s^{-1} for both ZnO and TiO_2, $k_{electrol} = 6.0 \times 10^6$ s^{-1} for ZnO, and $k_{electrol} = 14.0 \times 10^6$ s^{-1} for TiO_2. So, the initial regeneration efficiency after pulse excitation, calculated from eq 3, were equal to 0.95 for ZnO and 0.98 for TiO_2 cells.

In both cases, the slightly lower regeneration efficiency of ZnO cell is due to slower regeneration. However, this difference in the regeneration yield observed in nanosecond−microsecond time scale cannot account for 3−4 times lower relative photocurrent of (Table 1). Therefore, investigation on a shorter time scale, presented in the next section, is necessary.

It should be noted that recent contributions[45,46] reported a detailed and more exhaustive approach for the proper calculation of dye regeneration of complete DSC under working conditions (1 sun, open circuit or maximum power point). Such careful consideration is beyond the scope of our work in which we focus on the comparison between two systems at the same conditions. Hence, it can be reasonably assumed that the observed differences in regeneration yield will not change significantly under working conditions of the solar cell.

3.3. Femtosecond to Picosecond Studies. Femtosecond transient absorption spectra were studied in the visible range (420−720 nm) under excitation at 520 or 550 nm and the data was analyzed with a global multiexponential fit.

The spectra for selected delays between pump and probe pulses measured for the reference system of D149 dye in DCM solution (after excitation near stationary absorption maximum at 550 nm) are presented in Figure S4A. Figure S4B shows wavelength-dependent amplitudes of the indicated time constants from the global fit. Positive signals below 500 nm and between 520 and 630 nm are due to the absorption from the excited S_1 state, while negative bands are due to ground state depopulation (around 550 nm) and stimulated emission (maximum shifts from 620 to 670 nm over few picoseconds). The fastest evolution is connected with a stimulated emission band that undergoes a characteristic red-shift (Figure S4A) due to the solvation dynamics. As Figure S4B presents, this process can be modeled by a single-exponential component in global analysis with the time constant τ_1 = 1 ps and negative amplitude in 550−650 nm range (decrease of stimulated emission signal) and positive above 650 nm (increase of stimulated emission). The further evolution is connected with a decay of the relaxed S_1 state that takes place with much longer, 700 ps time constant[31] (Figure S4B). This results are in line with previous transient absorption studies and emission studies where solvation dynamics on time scales characteristic for each solvent were observed and S_1 lifetime changed with solvent polarity and hydrogen bonding ability.[30,31]

A much more complicated picture is obtained for the D149/TiO_2 solar cell. Figure 2A shows transient absorption spectra for different time delays between pump and probe for this sample. In Figure 2B the calculated wavelength-dependent amplitudes of the three components obtained from multi-exponential global analysis (τ_1 = 0.5 ps, τ_2 = 20 ps, and τ_3 = 1

dx.doi.org/10.1021/la404782s | Langmuir XXXX, XXX, XXX−XXX

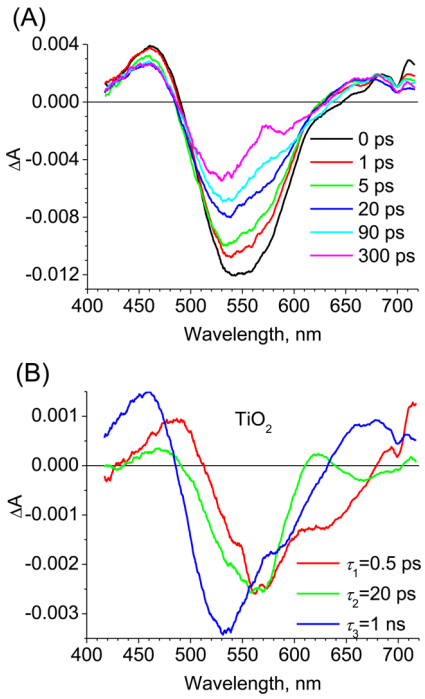

Figure 2. (A) Transient absorption spectra of D149/TiO_2 solar cell for selected, indicated time delays between the pump (at 550 nm) and probe pulses. (B) Wavelength-dependent amplitudes of the components with time constants given in the inset obtained by multiexponential global fit for D149/TiO_2 solar cell.

ns) are given. According to our knowledge, this is the first report of femtosecond transient absorption experiment of a complete D149 solar cell in the visible range. The spectrum of longest 1 ns component (that can be treated as constant in the time window of the experiment) is similar to that observed in flash photolysis experiment, and it can be assigned to the D149 radical cation.[33] Two faster components are partially connected with electron injection dynamics. It should be noted that the transient absorption of complete D149/TiO_2 cells measured in mid-IR range revealed electron injection dynamics with similar time constants: 400 fs (50% contribution) and 30 ps (50% contribution).[11] The negative amplitudes of τ_1 and τ_2 components for wavelength longer than 620 nm indicate the decrease of stimulated emission from excited S_1 state and buildup of the positive radical cation spectrum (Figure 2B) associated with the electron injection process. However, the spectrum of the τ_1 component is influenced by the solvation dynamics (occurring faster in ACN-based electrolyte than in DCM), while that of τ_2 component by transient Stark shift buildup. The latter process was recently observed for isolated D149/ZnO film, and its dynamics (20 ps) was slower than that of electron injection (below 250 fs).[32] The Stark shift signal in D149 solar cells was observed over the nanosecond time scale as negative transient absorption band below 520 nm and a positive band above 520 nm.[33] Therefore, the buildup of such signals should be manifested in time component amplitudes with similar spectral regions but with opposite signs. This is partially observed when the spectra of τ_1 (without Stark shift buildup) and τ_2 (with Stark shift buildup) components are compared (Figure 2B). Moreover, negative amplitudes near the ground state absorption maximum (520 nm) for τ_1 and τ_2 components might indicate partial ground state dye recovery without injection of electrons into TiO_2.

Therefore, it is not possible to quantitatively evaluate the contribution of electron injection in the spectra of both τ_1 and τ_2 components for D149/TiO_2 solar cell. The situation looks even worse when D149/ZnO solar cell is considered, for which the global analysis is presented in Figure 3A. The fitted fast

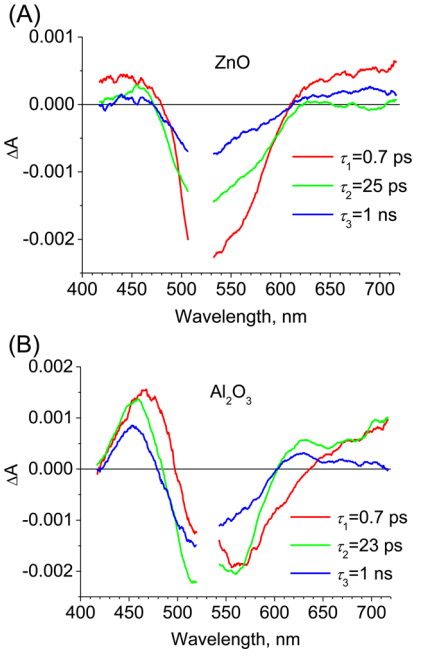

Figure 3. Wavelength-dependent amplitudes of the components with time constants given in the inset obtained by multiexponential global fit for (A) D149/ZnO and (B) D149/Al_2O_3 solar cells.

components are similar to those of TiO_2 sample (τ_1 = 0.7 ps, τ_2 = 25 ps), but the contribution of electron injection is probably smaller (no negative amplitudes >620 nm). However, in this case the transient absorption signal is lower and the smaller signal-to-noise ratio makes the analysis too speculative. On the other hand, one thing that can be clearly resolved for ZnO sample is a much smaller contribution of the longest τ_3 component, assigned to oxidized D149 dye. On the basis of the strongest signal at negative ground state depopulation band, we estimated (from Figures 2B and 3A) that the radical cation contribution for TiO_2 is 49% with respect to that of initial signal (around 530 nm), while it is only 16% for ZnO sample (see also Figure S5). This means that after first 200 ps there is much less oxidized dyes in ZnO solar cell and, therefore, much less injected electrons.

In principle, there are two possible reasons for the observed difference in femtosecond transient absorption spectra, supported by some experimental findings. The first possibility is slower electron injection into ZnO material than TiO_2 due to a smaller effective electron mass in ZnO and, thus, lower density of acceptor states in this material.[35,47,48] If the electron injection rate is slow enough to permit effective competition of internal deactivation of the excited dye, then the electron injection quantum yield might decrease. Another explanation is that bound charge-transfer pairs are formed between electrons injected into in ZnO conduction band and the positively charged oxidized dye.[49,50] This process could be much more efficient in ZnO due to its lower dielectric constant compared to TiO_2. Such charge-transfer pairs might suffer from fast recombination before full charge separation occurs, and thus

dx.doi.org/10.1021/la404782s | Langmuir XXXX, XXX, XXX−XXX

the number of injected electrons in the conduction band decreases.

Our transient absorption results cannot definitively exclude any of these explanations. Therefore, we devised time-resolved emission studies with TCSPC setup for the aforementioned samples. Such emission studies only probe the excited state of the dye, not charge-transfer pairs, so faster electron injection should increase emission decay rate. The excitation wavelength was set at 425 nm and emission wavelength at 660 nm, close to the maximum of emission band (Figure S1). We have checked that the contribution of the signal from electrolyte (which is partially excited at 425 nm) gives negligible contribution to the emission transients above 600 nm. The kinetic traces for TiO_2 and ZnO samples are shown in Figure 4 and exhibit clearly a

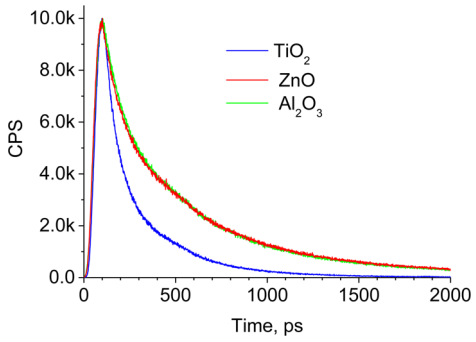

Figure 4. Fluorescence decays obtained in TCSPC experiment at 660 nm after 425 nm excitation.

nonsingle exponential behavior. The fit of the slower part was performed with stretched exponential function given by eq 5, yielding the following parameters: τ = 280 ps, β = 0.67 for ZnO and τ = 100 ps, β = 0.63 for TiO_2 samples. The average decay time constant—reciprocal of rate given by eq 6—is 370 ps for ZnO sample and 140 ps for TiO_2 sample. As can be seen, the fluorescence decay is almost 3 times slower for ZnO than TiO_2 solar cell. It means that, most probably, the slower electron injection is the most important factor that explains the lower photocurrent and performance of D149-sensitized ZnO solar cells with respect to the TiO_2 ones.

The decays presented in Figure 4 also contain a faster part of time constant below 10 ps (with 47% and 52% amplitude contribution for ZnO and TiO_2, respectively) which is unresolved in TCSPC experiment (fwhm of IRF around 60 ps). Therefore, we made a control experiment of the same cells with the up-conversion setup of better time resolution. The results, although more noisy (Figure S6), clearly show that the differences in the kinetics observed in TCSPC experiment are also maintained on the shorter time scale.

Finally, we have also performed the ultrafast studies for a reference D149/Al_2O_3 cell in order to get the yields of electron injection for TiO_2 and ZnO materials. As presented above (Table 1), the photocurrent of large bandgap Al_2O_3 cell is very small, so electron injection is expected to be absent and the observed dynamics should only reproduce the internal deactivation of D149 dye attached to nanoparticles. Figure S7 shows transient absorption spectra for different time delays between pump and probe while wavelength-dependent amplitudes of the three components obtained from multi-exponential global analysis are presented in Figure 3B. The fluorescence decay profiles are shown in Figure 4 and Figure S6. The averaged decay time is 350 ps for Al_2O_3 in TCSPC experiment, giving 60% electron injection efficiency in TiO_2, while in shorter time scale in up-conversion experiment (Figure S6) it is about 80%. Surprisingly, the characteristic time constants for absorption and emission data and the level of residual transient absorption signal are almost the same for ZnO and Al_2O_3 samples. This would suggest that electron injection yield for ZnO is practically zero, which is in obvious contradiction to the 10 times higher photocurrent for ZnO than Al_2O_3 cells (Table 1). We can propose three different explanations for this finding: (i) electron injection yields below 10−20% are hard to be observed in our time-resolved setups due to limited signal/noise ratio; (ii) the internal deactivation of D149 interacting with Al_2O_3 nanoparticles is slightly faster than that with ZnO, which means that Al_2O_3 is not a good reference material for ZnO samples; (iii) there is (relatively slow) electron injection from D149 into the deep trap states of Al_2O_3 material, which makes the dynamics very similar to the poorly injecting D149/ZnO samples in first 200 ps; however, the injected localized electrons in Al_2O_3 cannot move away from the oxidized dye (through the conduction band) and quickly recombine, giving almost no photocurrent. All of the above explanations confirm that electron injection has a low yield for D149/ZnO, although its exact value is hard to extract in our experiment.

The latter possibility can be supported by the recent studies of D149 in films in air. In the transient absorption studies including ZrO_2 layer[32] (which is used as another reference material for which conduction band has too high energy for injection to occur), the electron injection into ZrO_2 trap states was found to be as fast as that for ZnO. The up-conversion experiments performed for D149-sensitized films showed the fluorescence decay half-lifetimes of about 1 ps for TiO_2 and 4 ps for Al_2O_3.[27] The ratio is similar to the fluorescence half-lifetimes in our cells (Figure S6: 3 ps for TiO_2 and 12 ps for ZnO). The prolongation of lifetimes in complete cells can be explained by the electrolyte effect, as discussed in the Introduction.

4. CONCLUSION

DSCs made with iodine/iodide liquid electrolyte and D149 dye sensitizing TiO_2 or ZnO nanoparticles were prepared, and 3−4 times higher photocurrent was observed for TiO_2 cells than for ZnO ones. Time-resolved laser spectroscopy techniques in the time range from femtoseconds to seconds were applied for complete DSCs to reveal processes responsible for lower performance of ZnO samples.

The electrochemical impedance spectroscopy results indicate that the collection efficiencies for both types of cells are high. Similarly, nanosecond flash photolysis brought information about regeneration and recombination processes. Although the regeneration rate is higher for TiO_2 than ZnO sample, the estimated regeneration yield are similar for both samples and cannot explain the observed differences in solar cells photocurrent.

Femtosecond transient absorption results indicated that after first 200 ps the number of radical cations (thus photoinduced electrons in the semiconductor) is 3 times higher for TiO_2 than ZnO solar cells. Picosecond emission studies showed that the lifetime of the D149 excited state is about 3 times longer for ZnO then for TiO_2 samples. The reference Al_2O_3 sample exhibits a very similar ultrafast behavior to that of ZnO one. Therefore, the results indicate that lower performance of ZnO solar cells is due to much slower electron injection.

dx.doi.org/10.1021/la404782s | Langmuir XXXX, XXX, XXX−XXX

The study presented here shows that it is possible to correlate laser spectroscopy performed on complete solar cells with global parameters and should help in better understanding of the behavior of alternative materials for porous electrodes in DSCs.

■ ASSOCIATED CONTENT

Supporting Information

Figures S1−S7 and Table S1. This material is available free of charge via the Internet at http://pubs.acs.org.

■ AUTHOR INFORMATION

Corresponding Author

*E-mail: marziol@amu.edu.pl (M.Z.).

Notes

The authors declare no competing financial interest.

■ ACKNOWLEDGMENTS

This work was supported by NCN (National Science Centre, Poland) under project 2012/05/B/ST3/03284 and partially from National Centre for Research and Development in Poland project PBS1/A9/13/2012. Transient absorption and TCSPC studies were made at the Center for Ultrafast Laser Spectroscopy at the A. Mickiewicz University in Poznan, Poland. We thank Prof. Abderrazzak Douhal for the possibility of making the control femtosecond up-conversion measurements in his laboratory at Universidad de Castilla-La Mancha in Toledo, Spain. J.S. is a holder of a scholarship funded within Human Capital Operational Programme, European Social Fund. J.A.A. and J.I. thank Abengoa Research for support under collaboration agreement.

■ REFERENCES

(1) O'Regan, B.; Grätzel, M. A Low-Cost, High-Efficiency Solar Cell Based on Dye-Sensitized Colloidal TiO_2 Films. *Nature* **1991**, *353*, 737−740.

(2) Grätzel, M. Photoelectrochemical Cells. *Nature* **2001**, *414*, 338−344.

(3) Hagfeldt, A.; Boschloo, G.; Sun, L.; Kloo, L.; Pettersson, H. Dye-Sensitized Solar Cells. *Chem. Rev.* **2010**, *110*, 6595−6663.

(4) Kamat, P. V. Meeting the Clean Energy Demand: Nanostructure Architectures for Solar Energy Conversion. *J. Phys. Chem. C* **2007**, *111*, 2834−2860.

(5) Moser, J. E. Dynamics of interfacial and surface electron transfer processes. In *Dye-Sensitized Solar Cells*, 2010 ed.; Kalyanasundaram, K., Ed.; EPFL Press: Lausanne, 2010; pp 403−456.

(6) Haque, S. A.; Palomares, E.; Cho, B. M.; Green, A. N. M.; Hirata, N.; Klug, D. R.; Durrant, J. R. Charge Separation versus Recombination in Dye-Sensitized Nanocrystalline Solar Cells: the Minimization of Kinetic Redundancy. *J. Am. Chem. Soc.* **2005**, *127*, 3456−3462.

(7) Koops, S. E.; O'Regan, B. C.; Barnes, P. R. F.; Durrant, J. R. Parameters Influencing the Efficiency of Electron Injection in Dye-Sensitized Solar Cells. *J. Am. Chem. Soc.* **2009**, *131*, 4808−4818.

(8) Pijpers, J. J. H.; Ulbricht, R.; Derossi, S.; Reek, J. N. H.; Bonn, M. Picosecond Electron Injection Dynamics in Dye-Sensitized Oxides in the Presence of Electrolyte. *J. Phys. Chem. C* **2011**, *115*, 2578−2584.

(9) Giannouli, M.; Fakis, M. Interfacial Electron Transfer Dynamics and Photovoltaic Performance of TiO_2 and ZnO Solar Cells Sensitized with Coumarin 343. *J. Photochem. Photobiol. A: Chem.* **2011**, *226* (1), 42−50.

(10) Wang, L.; Wang, H. Y.; Fang, H. H.; H, W.; Yang, Z. Y.; Gao, B. R.; Chen, Q. D.; Han, W.; Sun, H. B. Universal Electron Injection Dynamics at Nanointerfaces in Dye-Sensitized solar Cells. *Adv. Funct. Mater.* **2012**, *22*, 2783−2791.

(11) Juozapavicius, M.; Kaucikas, M.; van Thor, J. J.; O'Regan, B. C. Observation of Multiexponential Pico- to Subnanosecond Electron Injection in Optimized Dye-Sensitized Solar Cells with Visible-Pump Mid-Infrared-Probe Transient Absorption Spectroscopy. *J. Phys. Chem. C* **2013**, *117*, 116−123.

(12) Ziółek, M.; Martín, C.; Cohen, B.; Garcia, H.; Douhal, A. Virtues and Vices of an Organic Dye and Ti-Doped MCM-41 Based Dye-Sensitized Solar Cells. *J. Phys. Chem. C* **2011**, *115*, 23642−23650.

(13) Ziółek, M.; Martín, C.; Sun, L.; Douhal, A. Effect of Electrolyte Composition on Electron Injection and Dye Regeneration Dynamics in Complete Organic Dye Sensitized Solar Cells Probed by Time-Resolved Laser Spectroscopy. *J. Phys. Chem. C* **2012**, *116*, 26227−26238.

(14) de Miguel, G.; Marchena, M.; Cohen, B.; Pandey, S. S.; Hayase, S.; Douhal, A. Relating the Photodynamics of Squaraine-Based DSSCs to the Molecular Structure of the Sensitizers and to the Presence of Additives. *J. Phys. Chem. C* **2012**, *116*, 22157−22168.

(15) Teuscher, J.; Décoppet, J.-D.; Punzi, A.; Zakeeruddin, S. M.; Moser, J.-E.; Grätzel, M. Photoinduced Interfacial Electron Injection Dynamics in Dye-Sensitized Solar Cells under Photovoltaic Operating Conditions. *J. Phys. Chem. Lett.* **2012**, *3*, 3786−3790.

(16) Juozapavicius, M.; Kaucikas, M.; Dimitrov, S. D.; Barnes, P. R. F.; van Thor, J. J.; O'Regan, B. C. Evidence for "Slow" Electron Injection in Commercially Relevant Dye-Sensitized Solar Cells by vis−NIR and IR Pump−Probe Spectroscopy. *J. Phys. Chem. C* **2013**, *117*, 25317−25324.

(17) Marchena, M. J.; de Miguel, G.; Cohen, B.; Organero, J. A.; Pandey, S.; Hayase, S.; Douhal, A. Real-Time Photodynamics of Squaraine-Based Dye-Sensitized Solar Cells with Iodide and Cobalt Electrolytes. *J. Phys. Chem. C* **2013**, *117*, 11906−11919.

(18) Ziółek, M.; Karolczak, J.; Zalas, M.; Hao, Y.; Tian, H.; Douhal, A. Aggregation and Electrolyte Composition Effects on the Efficiency of Dye-Sensitized Solar Cells. A Case of a Near-Infrared Absorbing Dye for Tandem Cells. *J. Phys. Chem. C* **2014**, *118*, 194−205.

(19) Kuang, D.; Ito, S.; Wenger, B.; Klein, C.; Moser, J. E.; Humphry-Baker, R.; Zakeeruddin, S. M.; Grätzel, M. High Molar Extinction Coefficient Heteroleptic Ruthenium Complexes for Thin Film Dye-Sensitized Solar Cells. *Adv. Funct. Mater.* **2006**, *128*, 4146−4154.

(20) Horiuchi, T.; Miura, H.; Sumioka, K.; Uchida, S. High Efficiency of Dye-Sensitized Solar Cells Based on Metal-Free Indoline Dyes. *J. Am. Chem. Soc.* **2004**, *126*, 12218−12219.

(21) Ito, S.; Zakeeruddin, S. M.; Humphry-Baker, R.; Liska, P.; Charvet, R.; Comte, P.; Nazeeruddin, M. K.; Péchy, P.; Takata, M.; Miura, H.; Uchida, S.; Grätzel, M. High-Efficiency Organic-Dye-Sensitized Solar Cells Controlled by Nanocrystalline-TiO_2 Electrode Thickness. *Adv. Mater.* **2006**, *18*, 1202−1205.

(22) Howie, W. H.; Claeyssens, F.; Miura, H.; Peter, L. M. Characterization of Solid-State Dye-Sensitized Solar Cells Utilizing High Absorption Coefficient Metal-Free Organic Dyes. *J. Am. Chem. Soc.* **2008**, *130*, 1367−1375.

(23) Snaith, H. J.; Petrozza, A.; Ito, S.; Miura, H.; Grätzel, M. Charge Generation and Photovoltaic Operation of Solid-State Dye-Sensitized Solar Cells Incorporating a High Extinction Coefficient Indolene-Based Sensitizer. *Adv. Funct. Mater.* **2009**, *19*, 1810−1818.

(24) Guillén, E.; Peter, L.; Anta, J. A. Electron Transport and Recombination in ZnO-Based Dye-Sensitized Solar Cells. *J. Phys. Chem. C* **2011**, *115*, 22622−22632.

(25) Guillén, E.; Eneko Azaceta, E.; Peter, L. M.; Zukal, A.; Tena-Zaera, R.; Anta, J. A. ZnO Solar Cells with an Indoline Sensitizer: a Comparison between Nanoparticulate Films and Electrodeposited Nanowire Arrays. *Energy Environ. Sci.* **2011**, *4*, 3400−3407.

(26) Cheng, H. M.; Hsieh, W. F. Electron Transfer Properties of Organic Dye-Sensitized Solar Cells Based on Indoline Sensitizers with ZnO Nanoparticles. *Nanotechnology* **2010**, *21*, 485202.

(27) Fakis, M.; Stathatos, E.; Tsigaridas, G.; Giannetas, V.; Persephonis, P. Femtosecond Decay and Electron Transfer Dynamics of the Organic Sensitizer D149 and Photovoltaic Performance in Quasi-Solid-State Dye-Sensitized Solar Cells. *J. Phys. Chem. C* **2011**, *115*, 13429−13437.

(28) Cappel, U. B.; Feldt, S. M.; Schöneboom, J.; Hagfeldt, A.; Boschloo, G. The Influence of Local Electric Fields on Photoinduced Absorption in Dye-Sensitized Solar Cells. *J. Am. Chem. Soc.* **2010**, *132*, 9096−9101.
(29) Fattori, A.; Peter, L. M.; Wang, H.; Miura, H.; Marken, F. Fast Hole Surface Conduction Observed for Indoline Sensitizer Dyes Immobilized at Fluorine-Doped Tin Oxide-TiO_2 Surfaces. *J. Phys. Chem. C* **2010**, *114*, 11822−11828.
(30) Lohse, P. W.; Kuhnt, J.; Druzhinin, S. I.; Scholz, M.; Ekimova, M.; Oekermann, T.; Lenzer, T.; Oum, K. Ultrafast Photoinduced Relaxation Dynamics of the Indoline Dye D149 in Organic Solvents. *Phys. Chem. Chem. Phys.* **2011**, *13*, 19632−19640.
(31) Fakis, M.; Hrobárik, P.; Stathatos, E.; Giannetas, V.; Persephonis, P. A Time Resolved Fluorescence and Quantum Chemical Study of the Solar Cell Sensitizer D149. *Dyes Pigm.* **2013**, *96*, 304−312.
(32) Oum, K.; Lohse, P. W.; Flender, O.; Klein, J. R.; Scholz, M.; Lenzer, T.; Duc, J.; Oekermannz, T. Ultrafast Dynamics of the Indoline Dye D149 on Electrodeposited ZnO and sintered ZrO_2 and TiO_2 Thin Films. *Phys. Chem. Chem. Phys.* **2012**, *14*, 15429−15437.
(33) Burdziński, G.; Karolczak, J.; Ziółek, M. Dynamics of Local Stark Effect Observed for a Complete D149 Dye-Sensitized Solar Cell. *Phys. Chem. Chem. Phys.* **2013**, *15*, 3889−3896.
(34) Anta, J. A.; Guillén, E.; Tena-Zaera, R. ZnO-Based Dye-Sensitized Solar Cells. *J. Phys. Chem. C* **2012**, *116*, 11413−11425.
(35) Tiwana, P.; Docampo, P.; Johnston, M. B.; Snaith, H. J.; Herz, L. M. Electron Mobility and Injection Dynamics in Mesoporous ZnO, SnO_2, and TiO_2 Films Used in Dye-Sensitized Solar Cells. *ACS Nano* **2013**, *5*, 5158−5166.
(36) Vaseem, M.; Umar, A.; Hahn, Y.-B. ZnO Nanoparticles: Growth, Properties, and Applications. In *Metal Oxide Nanostructures and Their Applications*; Umar, A., Hahn, Y.-B., Eds.; American Scientific Publishers: New York, 2010; Vol. *5*, pp 1−36.
(37) Burschka, J.; Pellet, N.; Moon, S.-J.; Humphry-Baker, R.; Gao, P.; Nazeeruddin, M. K.; Grätzel, M. Sequential Deposition as a Route to High-Performance Perovskite-Sensitized Solar Cells. *Nature* **2013**, *499*, 316−319.
(38) Bi, D.; Boschloo, G.; Schwarzmüller, S.; Yang, L.; Johansson, E. M. J.; Hagfeldt, A. Efficient and Stable $CH_3NH_3PbI_3$-Sensitized ZnO Nanorod Array Solid-State Solar Cells. *Nanoscale* **2013**, *5*, 11686−11691.
(39) Maciejewski, A.; Naskręcki, R.; Lorenc, M.; Ziółek, M.; Karolczak, J.; Kubicki, J.; Matysiak, M.; Szymański, M. Transient Absorption Experimental Set-up with Femtosecond Time Resolution. Femto- and Picosecond Study of DCM Molecule in Cyclohexane and Methanol Solution. *J. Mol. Struct.* **2000**, *555*, 1−13.
(40) Katilius, E.; Hindorff, J.; Woodbury, N. ASUFIT program available at www.public.asu.edu/~laserweb/asufit/asufit.html.
(41) Wróżowa, T.; Ciesielska, B.; Komar, D.; Karolczak, J.; Maciejewski, A.; Kubicki, J. Measurements of Picosecond Lifetimes by Time Correlated Single Photon Counting Method: The Effect of the Refraction Index of the Solvent on the Instrument Response Function. *Rev. Sci. Instrum.* **2004**, *75* (10), 3107−3121.
(42) Nelson, J.; Haque, S. A.; Klug, D. R.; Durrant, J. R. Trap-Limited Recombination in Dye-Sensitized Nanocrystalline Metal Oxide Electrodes. *Phys. Rev. B* **2001**, *63*, 205321.
(43) Barzykin, A. V.; Tachiya, M. Mechanism of Charge Recombination in Dye-Sensitized Nanocrystalline Semiconductors: Random Flight Model. *J. Phys. Chem. A* **2002**, *106*, 4356−4363.
(44) Haque, S. A.; Tachibana, Y.; Willis, R. L.; Moser, J. E.; Grätzel, M.; Klug, D. R.; Durrant, J. R. Parameters Influencing Charge Recombination Kinetics in Dye-Sensitized Nanocrystalline Titanium Dioxide Films. *J. Phys. Chem. B* **2000**, *104*, 538−547.
(45) Anderson, A. Y.; Barnes, P. R. F.; Durrant, J. R.; O'Regan, B. C. Quantifying Regeneration in Dye-Sensitized Solar Cells. *J. Phys. Chem. C* **2011**, *115*, 2439−2447.
(46) Li, F.; Jennings, J. R.; Wang, Q. Determination of Sensitizer Regeneration Efficiency in Dye-Sensitized Solar Cells. *ACS Nano* **2013**, *7*, 8233−8242.
(47) Anderson, N. A.; Lian, T. Ultrafast Electron Transfer at the Molecule-Semiconductor Nanoparticle Interface. *Annu. Rev. Phys. Chem.* **2005**, *56*, 491−519.
(48) Martín, C.; Ziółek, M.; Marchena, M.; Douhal, A. Interfacial Electron Transfer Dynamics in a Solar Cell Organic Dye Anchored to Semiconductor Particle and Aluminum-Doped Mesoporous Materials. *J. Phys. Chem. C* **2011**, *115*, 23183−23191.
(49) Stockwell, D.; Yang, Y.; Huang, J.; Anfuso, C.; Huang, Z.; Lian, T. Comparison of Electron-Transfer Dynamics from Coumarin 343 to TiO_2, SnO_2, and ZnO Nanocrystalline Thin Films: Role of Interface-Bound Charge-Separated Pairs. *J. Phys. Chem. C* **2010**, *114*, 6560−6566.
(50) Furube, A.; Katoh, R.; Yoshihara, T.; Hara, K.; Murata, S.; Arakawa, H.; Tachiya, M. Ultrafast Direct and Indirect Electron-Injection Processes in a Photoexcited Dye-Sensitized Nanocrystalline Zinc Oxide Film: The Importance of Exciplex Intermediates at the Surface. *J. Phys. Chem. B* **2004**, *108*, 12583−12592.

Supporting information

for

Comparison of TiO_2 and ZnO solar cells sensitized with an indoline dye: time-resolved laser spectroscopy studies of partial charge separation processes.

Jan Sobuś [1,2], Gotard Burdziński [2], Jerzy Karolczak [2,3], Jesús Idígoras [4], Juan A. Anta [4] and Marcin Ziółek [2]*

[1] *NanoBioMedical Centre, Adam Mickiewicz University, Umultowska 85, 61-614 Poznan, Poland.*

[2] *Quantum Electronics Laboratory, Faculty of Physics, Adam Mickiewicz University, Umultowska 85, 61-614 Poznan, Poland.*

[3] *Center for Ultrafast Laser Spectroscopy, Adam Mickiewicz University, Umultowska 85, 61-614, Poznan, Poland.*

[4] *Departamento de Sistemas Físicos, Químicos y Naturales, Área de Química Física, Universidad Pablo de Olavide, Ctra. Utrera, km 1,E-41013 Sevilla, Spain*

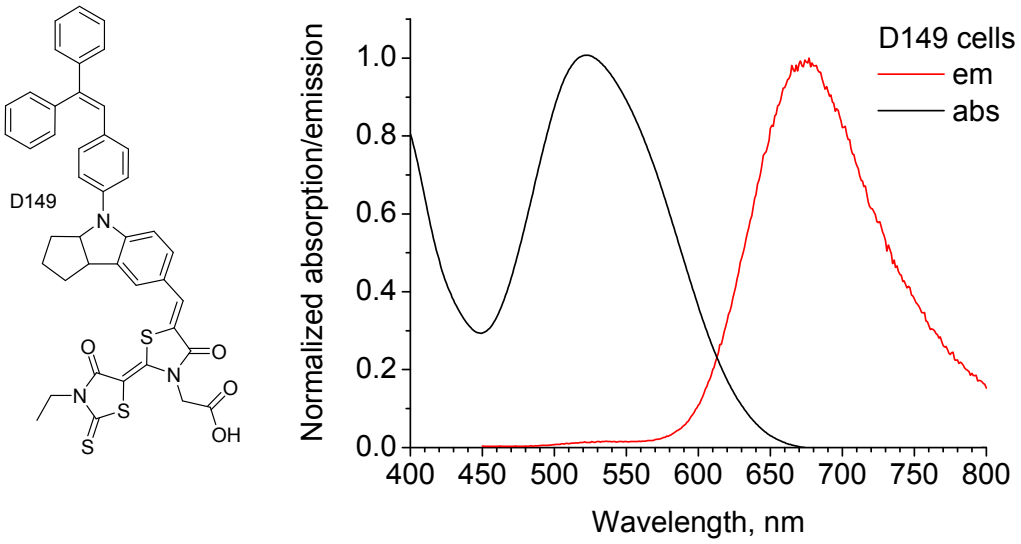

Figure S1. Structure of D149 dye (left) and selected stationary absorption and emission (after excitation at 425 nm) spectra (right) of complete DSC devices made with D149 dye.

(A)

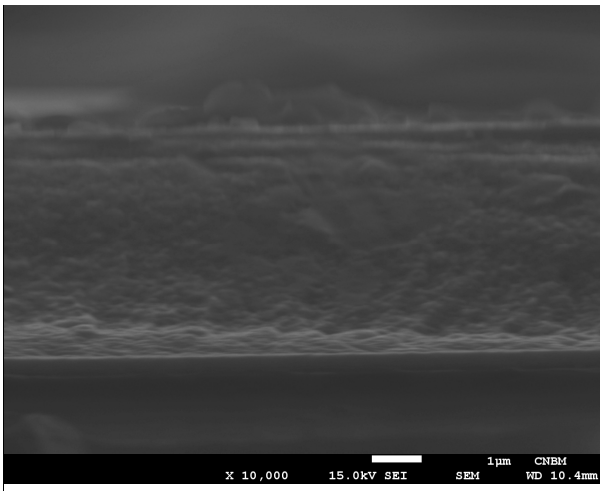

(B)

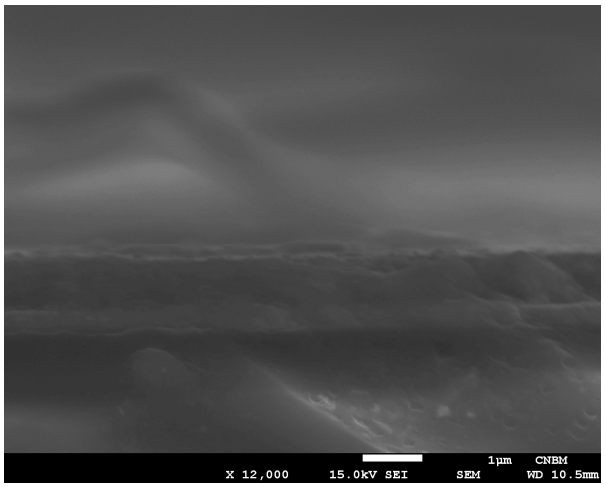

(C)

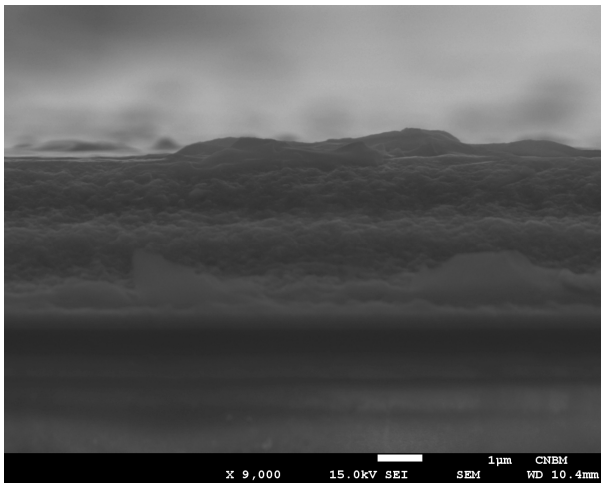

Figure S2. SEM pictures of cross-sections of working electrodes of: (A) TiO_2 cell, (B) ZnO cell, (C) TiO_2 "diluted" cell.

Results of electrochemical impedance spectroscopy studies

The fits to the typical equivalent circuit used for DSC studies for selected polarizations from 0 V to 0.6 V (presented in Figure S3) yielded the transport resistance (R_t), charge transfer resistance (R_{ct}) and chemical capacitance (C_μ) in the oxide-electrolyte interface. These parameters are collected in Table S1. The electron recombination lifetime (calculated as $R_{ct}C_\mu$) is longer for the ZnO solar cell than for the TiO_2 one. This might be due to lack of a blocking layer between working electrode and electrolyte, which usually contributes to the recombination at low V_{OC} [S1]. The relative transport diffusion length (calculated as $(R_{ct}/R_t)^{1/2}$ in units of film thickness) is always longer for ZnO sample (for example 20 vs. 12 at 0.5 V and 7.5 vs. 1.5 at 0.6 V). However, for both samples and all voltages applied, the relatively diffusion length is much larger than one, which is an evidence of good collection efficiencies in the photoanodes.

Equivalent circuit of DSC used to fit electrochemical impedance data:

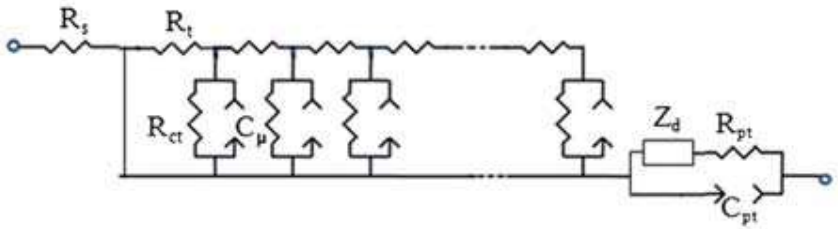

Voltage, V	ZnO	TiO_2
0	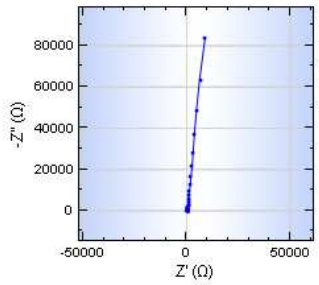	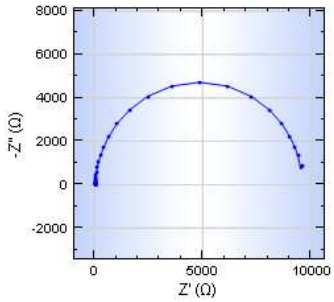
0.2	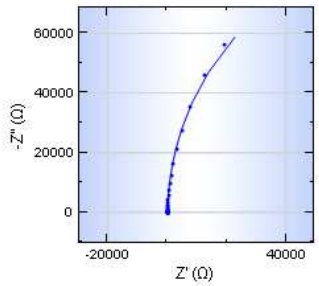	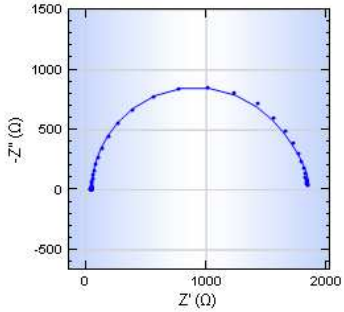
0.4	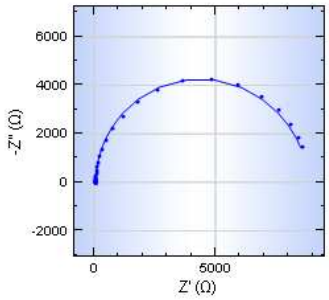	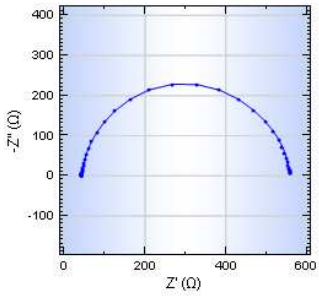
0.5	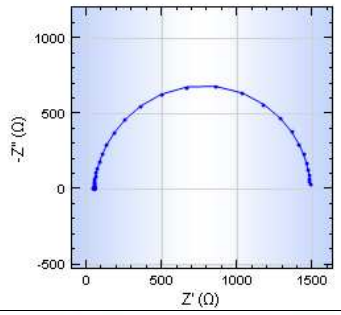	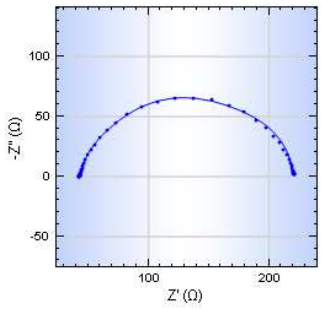
0.6	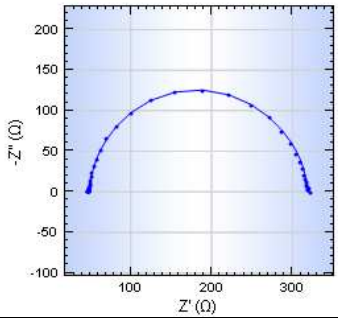	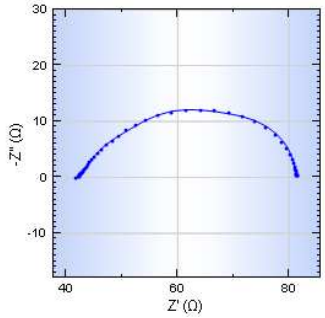

Figure S3. Fits to complex plain impedance plots with parameters given in Table S1.

Table S1. Parameters of the fits of the equivalent circuit (presented above) and potentials applied from 0 V to 0.6 V for (A) ZnO and (B) TiO_2 solar cell: transport resistance (R_t), charge transfer resistance (R_{ct}) and chemical capacitance (C_μ) in the oxide-electrolyte interface. The fits are shown in Figure S3.

(A) ZnO

Voltage, V	R_t, Ω	R_{ct}, Ω	C_μ, μF	$R_{ct}\,C_\mu$, ms	$(R_{ct}/R_t)^{1/2}$
0	--	1.15×10^6	18.9	21 700	--
0.2	20.5	1.75×10^5	24.1	4 200	92
0.4	1.35	8 300	30	249	78
0.5	3.21	1 300	36.5	47	20
0.6	4.1	231	39.9	9.2	7.5

(B) TiO_2

Voltage, V	R_t, Ω	R_{ct}, Ω	C_μ, μF	$R_{ct}\,C_\mu$, ms	$(R_{ct}/R_t)^{1/2}$
0	--	9300	13.5	126	--
0.2	--	1650	15.9	26	--
0.4	--	408	27.2	11	--
0.5	0.7	95	58.2	5.5	11.6
0.6	2.15	5.1	104	0.53	1.5

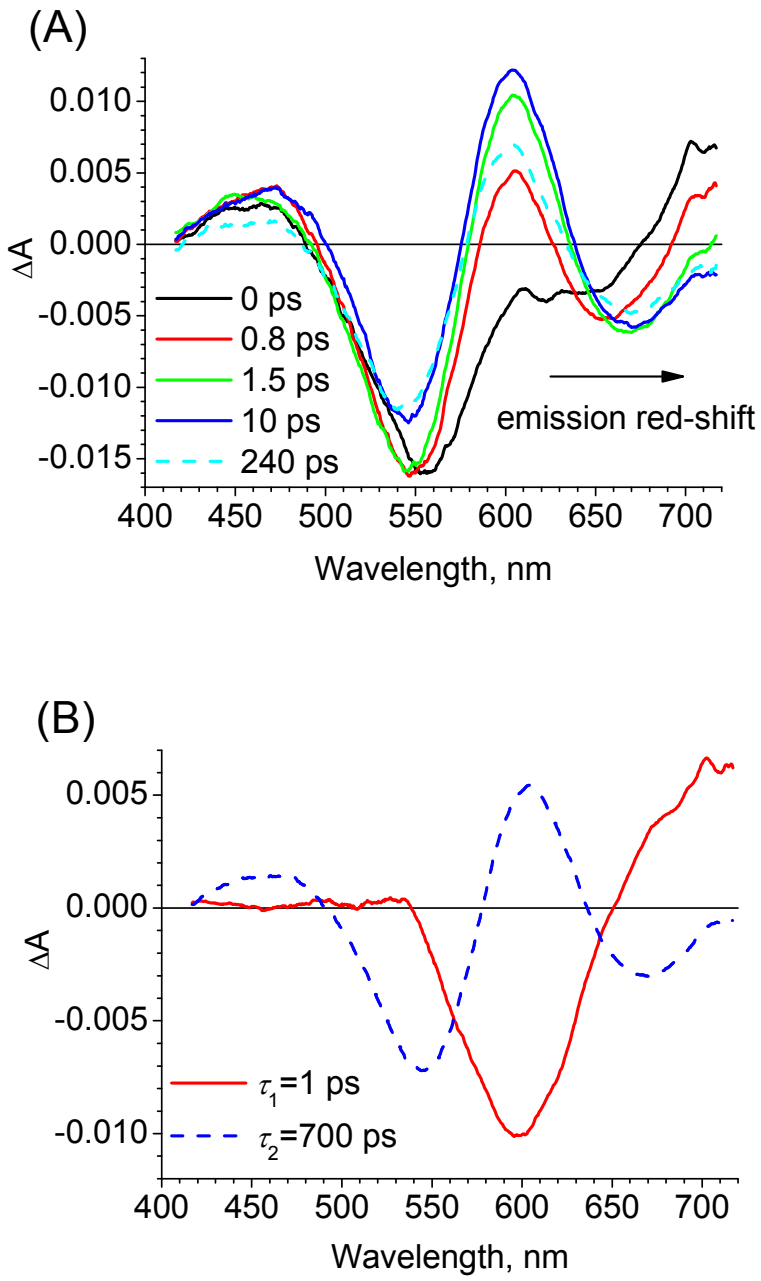

Figure S4. (A) Transient absorption spectra of D149 in DCM for selected, indicated time delays between the pump (at 550 nm) and probe pulses. The arrow shows the direction of the temporal changes. (B) The wavelength-dependent amplitudes of the components, having time constants given in the inset obtained by a multi-exponential global fit for D149 in DCM.

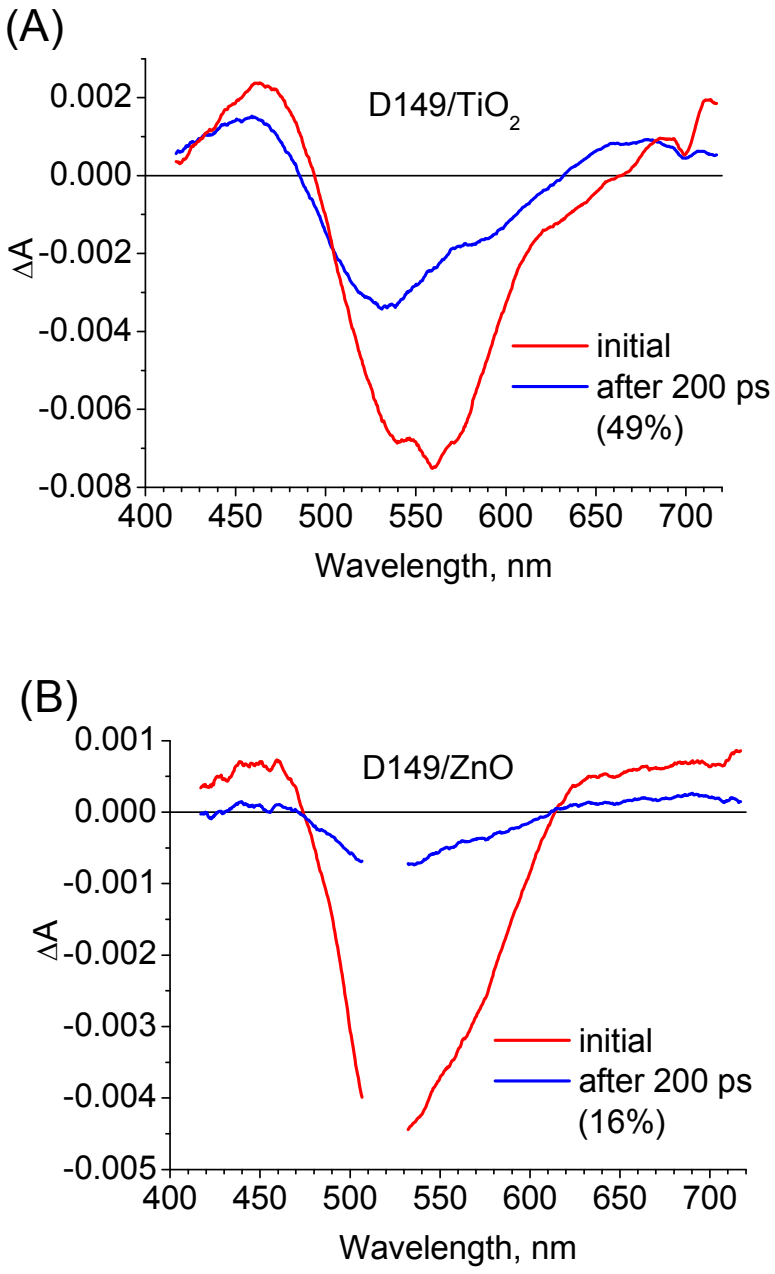

Figure S5. Comparison of transient absorption spectra of (A) D149/TiO_2 and (B) D149/ZnO solar cell for 0 ps (initial) and 200 ps delay time between the pump (at 550 nm) and probe pulses.

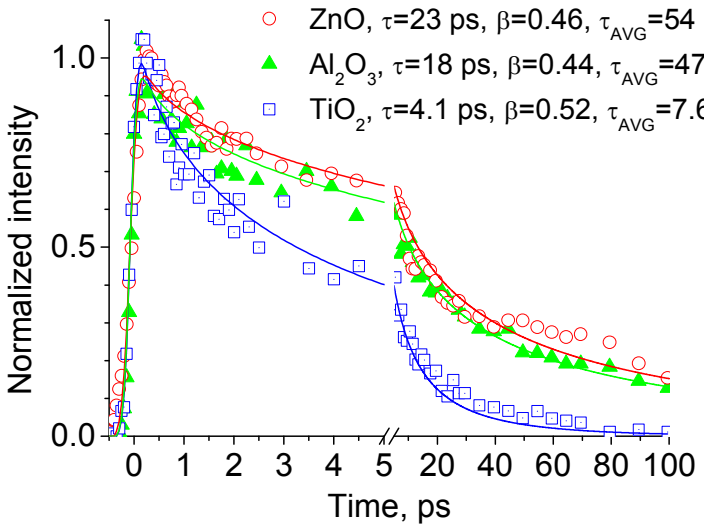

Figure S6. Femtosecond emission transients measured with up-conversion setup of IRF=300 fs (FWHM). The emission was observed at 660 nm, and upon excitation with 500 nJ/cm^2 pulses at 580 nm. The solid lines are from the best fit using the convolution of IRF of the setup with a stretched exponential function given by eq. (6) and (7) and the parameters given in the inset.

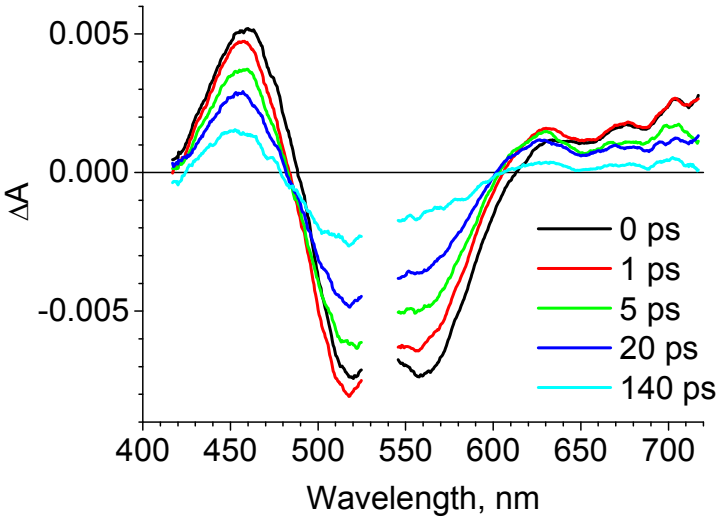

Figure S7. Transient absorption spectra of D149/Al_2O_3 for selected, indicated time delays between the pump (at 530 nm) and probe pulses.

PCCP

PAPER

View Article Online
View Journal | View Issue

Cite this: *Phys. Chem. Chem. Phys.*, 2014, **16**, 14116

Optimization of absorption bands of dye-sensitized and perovskite tandem solar cells based on loss-in-potential values†

Jan Sobuś[ab] and Marcin Ziółek*[b]

Received 5th May 2014,
Accepted 22nd May 2014

DOI: 10.1039/c4cp01937g

www.rsc.org/pccp

A numerical study of optimal bandgaps of light absorbers in tandem solar cell configurations is presented with the main focus on dye-sensitized solar cells (DSSCs) and perovskite solar cells (PSCs). The limits in efficiency and the expected improvements of tandem structures are investigated as a function of total loss-in-potential (V_L), incident photon to current efficiency (IPCE) and fill factor (FF) of individual components. It is shown that the optimal absorption onsets are significantly smaller than those derived for multi-junction devices. For example, for double-cell devices the onsets are at around 660 nm and 930 nm for DSSCs with iodide based electrolytes and at around 720 nm and 1100 nm for both DSSCs with cobalt based electrolytes and PSCs. Such configurations can increase the total sunlight conversion efficiency by about 35% in comparison to single-cell devices of the same V_L, IPCE and FF. The relevance of such studies for tandem n–p DSSCs and for a proposed new configuration for PSCs is discussed. In particular, it is shown that maximum total losses of 1.7 V for DSSCs and 1.4 V for tandem PSCs are necessary to give any efficiency improvement with respect to the single bandgap device. This means, for example, a tandem n–p DSSC with TiO_2 and NiO porous electrodes will hardly work better than the champion single DSSC. A source code of the program used for calculations is also provided.

1. Introduction

So far, the commercial photovoltaic market is dominated by crystalline Si and thin film solar cells. However, the cost of both technologies is still too high for the widespread use of photovoltaics. In recent years a few novel, photovoltaic solutions have emerged using the latest advances in nanotechnology, like organic photovoltaics (OPVs), dye-sensitized solar cells (DSSCs), quantum dot solar cells (QDSCs) and perovskite solar cells (PSCs). They are expected to become low-cost alternatives to the crystalline inorganic semiconductor technologies. Within emerging photovoltaics the current laboratory record efficiencies (under standard sunlight conditions AM1.5) are: 15% for PSCs,[1–3] 12.3% for DSSCs,[4] 10.6% for OPVs[5] and 7.0% for QDSCs.[6] Despite huge progress in recent years, these efficiencies are still not high enough to compete with crystalline inorganic semiconductor technologies.[7]

Still, despite their inferior absolute efficiency, they have clear advantages when economical and environmental issues are taken into account. Due to the solution based processing technologies without need for elevated temperatures, energy input needed for production of 1 m^2 of modules of the DSSC, PSC or OPV is lower by at least one order of magnitude, compared to the crystalline inorganic semiconductor technologies. This leads to energy payback time (EPBT) shortened from the 6 month period for thin film PV to 1 month for OPV, with predicted EPBT for solution processed PSCs in the range of days. Moreover, there is also a great reduction of greenhouse gases emission, compared to the first and second generation cells (not to mention the classical fossil fuels). With the lack of scarce and environmentally hazardous materials (lead in PSCs being the only notable exception) and the predicted cost of around 0.2$/W, significantly lower than 0.5–1$/W offered by the best contemporary thin-film technologies – the OPV, DSSC and PSC offer a viable way to challenge the ever-growing energy demand of the future.[8,9]

On the one hand, in order to improve the global efficiency of the cell, absorption onset of the photoactive material should be extended into the red part of the spectrum to increase the photocurrent (J_{sc}). On the other hand, an increase in absorption onset also results in decreased open circuit voltage (V_{oc}), and, accordingly, decreased global efficiency. Therefore, there is a

[a] *NanoBioMedical Centre, Adam Mickiewicz University, Umultowska 85, 61-614 Poznan, Poland*
[b] *Quantum Electronics Laboratory, Faculty of Physics, Adam Mickiewicz University, Umultowska 85, 61-614 Poznan, Poland. E-mail: marziol@amu.edu.pl*

† Electronic supplementary information (ESI) available: The code (in C) of the program for predicting sunlight conversion efficiency (*code.c*). The sunlight spectrum (*AM15ext.txt*) and an exemplary IPCE file for rectangle-like shape (*ipce1.txt*). Description of the program for optimizing bandgaps and Fig. S1 (*pdf* file). See DOI: 10.1039/c4cp01937g

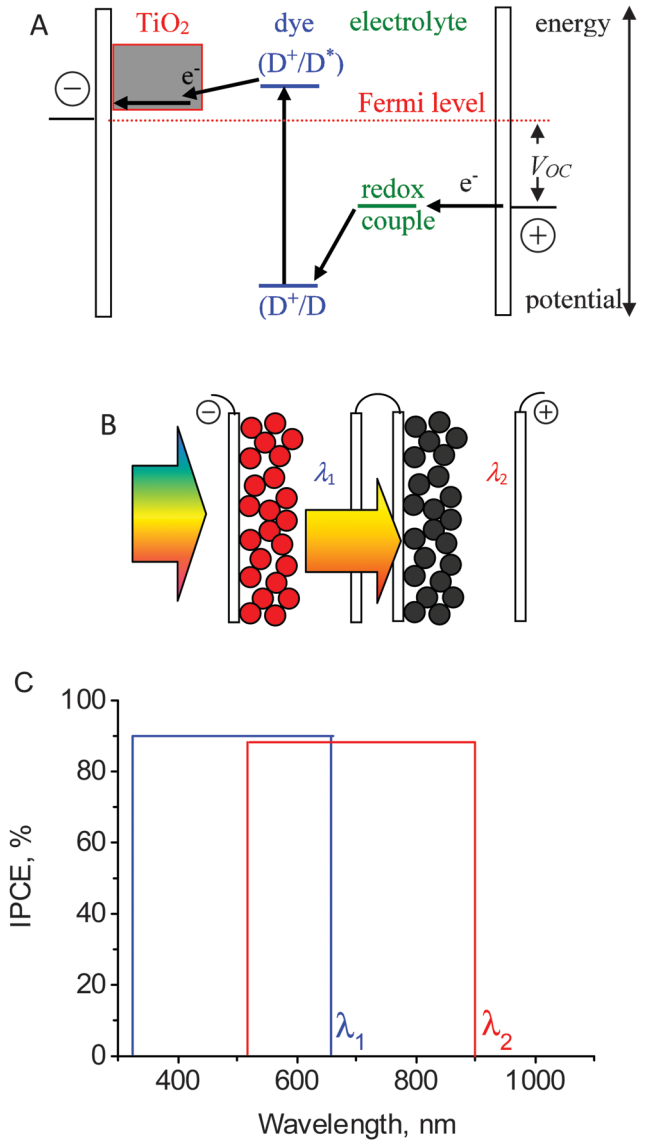

Fig. 1 Schemes of DSSC energetics (A), the simplest tandem cell connected in series (B) and the idealized IPCE spectra for a double bandgap tandem cell (C).

certain optimum wavelength for absorption onset at which the efficiency reaches a maximum. In the crystalline inorganic semiconductor photovoltaics this is the main reason for the well-known Shockley–Queisser limit of sunlight conversion efficiency of the single-bandgap device, which is 31% for a bandgap of 1.31 eV (absorption onset at 950 nm).[10] Other numerical calculations give a limit of 33% for a bandgap of 1.34 eV (925 nm) for the unfocused standard Sun spectrum at the Earth surface (AM1.5).[11,12]

As was recently nicely shown by Snaith, this optimum onset is not valid for DSSCs which possess a large loss-in-voltage.[13] Certain driving forces are required to efficiently inject electrons, transport them through the nanoparticle network, and regenerate the dye by the electrolyte (Fig. 1A), so V_{oc} is always significantly lower than the difference in potentials of the ground and excited states of the dye (absorption bandgap). For an iodide-based electrolyte the typical losses are about 0.75 V and the absorption onset was reported to be at 840 nm giving the maximum possible global efficiency of 13.4% (with a fill factor of 0.73 and the incident photon to current efficiency 90%).[13] Interestingly, this is very close to the best reported laboratory efficiencies obtained for a ruthenium-complex DSSC and an iodide-based electrolyte (11.2% for N719[14] and 11.7% for C106 dye,[15] both with absorption onset at 800 nm). This example emphasises that for the champion cells with the iodide electrolyte the quantum yields of charge transfer processes are almost optimised and, without changing the electrolyte, not much of further improvement can be achieved.

The idea of tandem structures was successfully used in crystalline silicon and GaAs photovoltaic devices in the so-called third generation solar cells based on multi-junction systems.[16,17] It is based on separating the absorption of the polychromatic solar spectrum into materials with different bandgaps. High energy photons are absorbed by the high bandgap junction and lower energy photons are absorbed at the lower bandgap, which allow a large portion of the solar spectrum to be absorbed while decreasing thermalization losses from carriers relaxing to the conduction band minimum. With this concept, the Shockley–Queisser limit of the efficiency of single-bandgap devices can be overcome. Indeed, the current record sunlight conversion efficiency is 44% for a three-junction solar cell.[7]

Among the emerging photovoltaics, in the organic solar cell technology the tandem structure has recently resulted in the improvements of record efficiency (10.6%[5]) with respect to that of a single device (9.2%[18]). In OPVs a strong limitation is the maximum width of the absorption bandgap in polymers, so the better efficiency in the tandem structure is mainly due to extension of the absorption range. In DSSCs and QDSCs the best tandem structures still have lower sunlight conversion efficiencies than their single-cell counterparts.

We think that one of the main factors that limit the successful use of a tandem concept in emerging photovoltaics progress is the lack of proper adjustment of absorption onsets of the building absorber components. Due to certain differences with respect to the classical crystalline inorganic semiconductor cells, mainly much larger loss-in-potential, the results obtained for multi-junction devices cannot be directly applied for OPVs, DSSCs and QDSCs. Therefore, new calculations for these devices are necessary, which are the subject of this contribution. As shown above and discussed in recent papers, loss-in-potential is a simple but very useful parameter to estimate the possible global performance of photovoltaic devices.[13,19,20] In this work we extend this model towards tandem structures of a solar cell. We mainly focus on the discussion of the DSSC and PSC, but the studies are also relevant for the improvement of other photovoltaic devices, like the OPV and QDSC.

2. Methods

The global efficiency (η) of a solar cell is calculated as:

$$\eta = \frac{J_{sc} V_{oc} FF}{P_{in}}, \quad (1)$$

where FF is the fill factor of the cell and P_{in} is the irradiance of the light, which under standard AM1.5 conditions (at Earth's surface)

equals 100 mW cm^{-2}. J_{sc} is related to the incident photon to current efficiency (IPCE) which describes the probability of conversion of one incident photon at a given wavelength to one electron, in the following way:

$$J_{sc} = \int_{\lambda_0}^{\lambda_{onset}} \mathrm{IPCE}(\lambda) e \varphi_{ph}(\lambda) \mathrm{d}\lambda, \quad (2)$$

where e is the elementary charge, φ_{ph} is the photon flux (under AM1.5 conditions), λ_{onset} is the absorption onset (the long-wavelength limit of the active material or the dye absorption band), and λ_0 is the starting wavelength for the sunlight spectrum (λ_0 = 300 nm, below this value the amount of photons is negligible from a photovoltaic point of view). The AM1.5 spectrum was taken from the ASTM G173-03 reference spectra (hemispherical tilted 37 degrees).[21] V_{oc} is the difference between the maximum possible potential due to the energy bandgap and the internal loss-in-potential V_L:

$$V_{oc} = \frac{1240}{\lambda_{onset}[\mathrm{nm}]} - V_L(\text{in volts}). \quad (3)$$

For example, for DSSCs, V_{oc} is the difference (Fig. 1A) between the Fermi level in the semiconductor nanoparticles (close to the bottom edge of their conduction band) and the redox potential of the redox pair in the electrolyte. Therefore, in our calculations for a single device, the λ_{onset} parameter varied for the given V_{loss}, FF and IPCE values, the efficiencies are calculated from eqn (1) to (3), and the best one is found. It is similar to the procedure used previously.[13]

Absorption onset λ_{onset} is the parameter that can be experimentally measured in the IPCE spectra. In most cases it can be directly related to the active material bandgap: E_g [eV] = 1240/λ_{onset} [nm]. However, in some configurations of DSSCs the electron injection from a hot excited state of the dye can be more efficient than that from the relaxed state (when the latter lies below the TiO_2 conduction band). In that case the absorption onset from the IPCE spectra corresponds to higher energy than the dye absorption bandgap.

For tandem structures a series connection of the building sub-cells is assumed since it is usually easier for technical implementation (Fig. 1B). Therefore, the current-matching conditions should be fulfilled for the optimized configuration:

$$J_{sc} = \int_{\lambda_0}^{\lambda_1} \mathrm{IPCE}_1(\lambda) e \varphi_{ph}(\lambda) \mathrm{d}\lambda = \int_{\lambda_0}^{\lambda_2} \mathrm{IPCE}_2(\lambda) e \varphi_{ph}(\lambda) \mathrm{d}\lambda = \ldots = \int_{\lambda_0}^{\lambda_n} \mathrm{IPCE}_n(\lambda) e \varphi_{ph}(\lambda) \mathrm{d}\lambda, \quad (4)$$

where $\lambda_1, \lambda_2, \ldots, \lambda_n$ are the absorption onsets of the materials in each parts ($\lambda_1 < \lambda_2 < \ldots < \lambda_n$). If the currents are not matched, then the smallest photocurrent of those achieved in each of particular n sub-cells is the one that occurs in the whole tandem device. The total V_{oc} of the device is the sum of open circuit voltages in each parts:

$$V_{oc} = \left(\frac{1240}{\lambda_1[\mathrm{nm}]} - V_{L1}\right) + \left(\frac{1240}{\lambda_2[\mathrm{nm}]} - V_{L2}\right) + \ldots + \left(\frac{1240}{\lambda_n[\mathrm{nm}]} - V_{Ln}\right), \quad (5)$$

where $V_{L1}, \ldots, V_{Ln}$ are loss-in-voltages in each part of the tandem device. Therefore, searching for an optimized configuration is realized by scanning absorption onsets and calculating efficiencies from eqn (1), (4) and (5). In the first approximation, the idealized rectangular shapes of the IPCE spectra are considered (Fig. 1C). Then, more realistic shapes without steep onsets are taken into account. All the calculations were performed using the program, which code (in C) can be downloaded as ESI.† The ESI† also contains more detailed description of how the program works.

3. Results and discussion

3.1. Initial considerations

Unless stated otherwise, all the results below will be presented for a fixed value of FF = 0.73 for the whole tandem cell and the maximum value of the IPCE spectrum equals 90% in all parts of the tandem cell, for consistency with the previous studies on single cells.[13] These values are target parameters for good solar cells. If both the FF and IPCE are different from these values (but the same in all parts) it will only proportionally affect the global efficiency of the device, not the optimized absorption onsets.

At the beginning, we assume that the IPCE spectra have steep onsets (Fig. 1C). For a constant relationship between IPCE in each sub-cell there is a constant relationship between absorption onsets of each part: $\lambda_1, \lambda_2, \ldots, \lambda_n$. It is a direct consequence of current matching conditions (eqn (4)). Fig. 2 presents this relationship for up to n = 5 tandem cells as a function of the most short-wavelength onset of the first part of the tandem cell, λ_1. These calculations are performed assuming that IPCE amplitudes of each part are the same and none of the incident photons from one part of the cell matching its IPCE spectrum is transferred to the proceeding part. Thus, if λ_1 is

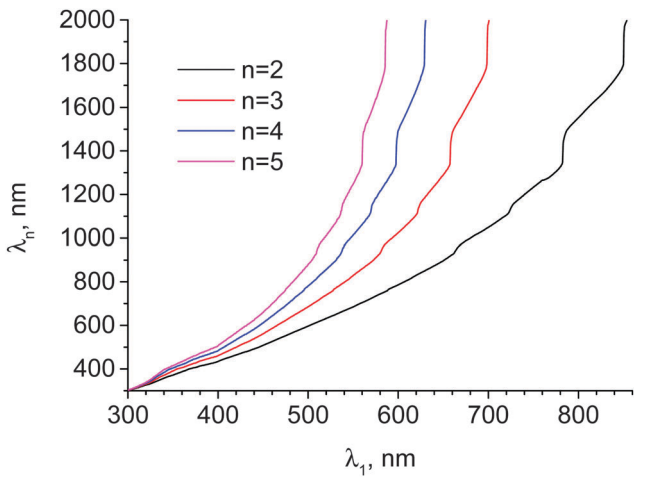

Fig. 2 The dependence of the sub-cell absorption onsets on the onset of the first compartment for n = 2, n = 3, n = 4 or n = 5 tandem cells for perfect current matching conditions. The calculations are done assuming that IPCE amplitudes of each part are the same and none of the incident photons from one part of the cell matching its IPCE spectrum is transferred to the proceeding part.

given for certain loss-in-potential, the rest of absorption onsets are automatically determined (and can be taken from Fig. 2).

Next, as comes from eqn (5), only the total loss-in-potential of all parts can be considered as the varying parameter: $V_{LT} = V_{L1} + V_{L2} + \ldots + V_{Ln}$. This means that for tandem solar cell performance, it is not important if losses are higher in one part and smaller in another, as long as their sum remains constant. It has a significant practical implementation – a tandem system can consist of the parts in which different driving forces (and thus losses in the available voltage) are necessary for effective charge separation. Therefore the energy levels can be tuned in one of the "weak" sub-cells to keep IPCE values high enough to maintain current-matching conditions.

We will present and discuss the cases of 3 different representative values of loss-in-potential, V_L. The efficiencies in the corresponding tandem cells consisting of n parts, where the total loss-in-potential is assumed to be $V_{LT} = nV_L$, are shown. The first, highest value is $V_L = 0.75$ V which corresponds to a DSSC with an iodide/iodine electrolyte.[13] In this system the major contribution to the loss-in-potential is the large difference between the redox potentials of the dye and the I_3^-/I^- redox couple, necessary for efficient dye regeneration. Nevertheless, the systems with ruthenium dyes and iodide-based electrolytes still keep the best certified DSSC efficiencies. A similar loss-in-potential of 0.75–0.80 V is given by the best OPV devices.[18,20] Next, $V_L = 0.60$ V is considered, which corresponds to the Co-complex based electrolyte. It is one-electron redox shuttle which requires less reduction/oxidation steps in the regeneration process and has a redox potential shifted positively by about 0.2 V with respect to iodide/triiodide.[4,22] Therefore, a gain of at least 0.15 V can be expected. Although the best DSSC laboratory efficiency is reported just for the cobalt-based electrolyte,[4] it suffers from fast recombination and, so far, has only worked well with specially designed dyes that block the access of the redox couple to the titania surface. Finally, the best and the lowest loss-in-potential values of 0.45 V correspond to organometal halide perovskite solar cells.[20] It is very recent and rapidly developing kind of solar cells with the active material exhibiting remarkable absorption and charge transport properties.[1,2,20,23,24] As it has been shown recently, the low loss-in-potential of PSCs is approaching the best values of GaAs (below 0.3 V) and crystalline Si or CIGS solar cells (around 0.4 V).[20] The calculations for other loss-in-potentials can be easily obtained with the help of the attached program.

Finally, it should be noted that our simulations are not relevant for the systems when more than one absorbing material interacts with the same electrode. For example, in DSSCs this is the case for co-sensitized dyes on nanoparticles, additional dyes interacting through Fourier resonance energy transfer or making stacking nanoparticle layers sensitized with different dyes.[25–28] In many cases such structures have yielded better overall efficiencies of the solar cell (including the current champion DSSC with porphyrin dyes[4]) due to the extension of the overall absorption range and are also often called tandem structures. However, they yield one photovoltage determined by the smallest bandgap absorber and cannot take full advantage of the multi-bandgap concept (decreasing thermalisation losses). The optimization of absorption bandgaps of all contributors of such a system should be done by matching the total absorbance to the best absorption range of a single device with the loss-in-potential of the smallest bandgap absorber.

3.2. Calculations for an idealized model

The calculated best efficiencies for a single cell are $\eta = 14.3\%$ for $V_L = 0.75$ V (with $\lambda_{onset} = 812$ nm), $\eta = 17.6\%$ for $V_L = 0.60$ V (with $\lambda_{onset} = 892$ nm) and $\eta = 20.6\%$ for $V_L = 0.45$ V (with $\lambda_{onset} = 896$ nm). They can be used as reference for tandem devices. It can be noted that our optimum absorption onset and efficiency for $V_L = 0.75$ V (812 nm, 14.3%) are slightly different from that reported previously ($\eta = 13.4\%$ and $\lambda_{onset} = 840$ nm).[13] The possible reason is that in the previous calculations an increase in IPCE to occur over 50 nm from the absorption onset was considered and the integration of photons from the sunlight spectrum started from 400 nm, while in our case we start from 300 nm, see eqn (2).

An interesting feature is that the optimum onsets for $V_L = 0.60$ V and $V_L = 0.45$ V are almost the same (892 and 896 nm). This is because in the AM1.5 spectrum there is a huge gap from 890 to 990 nm due to the absorption of water vapors in the atmosphere. Therefore, the current gain due to the absorption red-shift is very small, and losses smaller than 0.25 V are necessary to "skip" this gap for the compensation of V_{oc} decrease. Indeed, when we made a control optimization with the assumed unreal photon flux spectrum without the gap (Fig. S1, ESI†), then the absorption onsets were at 890 nm for $V_L = 0.60$ V and 990 nm for $V_L = 0.45$ V. This feature of the sunlight spectrum at the Earth surface has quite important practical implications. For example, it indicates that one does not need materials with absorption onset within the discussed gap because either λ_{onset} up to 900 nm and or λ_{onset} above 990 nm are optimal, depending on V_L.

This and other gaps in the sunlight spectrum also have implications in the optimized wavelengths of the tandem devices. Fig. 3 presents the comparison of efficiencies of tandem devices with $V_L = 0.75$ V, $V_L = 0.60$ V and $V_L = 0.45$ V with respect to the absorption onset of the first sub-cell, λ_1. Double-cell devices are shown in part A, while Fig. 3B and C show the results for $n = 3$ and $n = 4$, respectively. Several "saw-like" features in the curves are due to the above-mentioned gaps. The corresponding absorption onsets for the rest of compartments, λ_i (i = 2,3,4) can be found from Fig. 2. The best efficiencies and the corresponding optimized absorption onsets are also collected in Table 1. For example, for the simplest $n = 2$ tandem device the best efficiencies are: $\eta = 19.8\%$ for $V_L = 0.75$ V (with $\lambda_1 = 661$ nm and $\lambda_2 = 929$ nm), $\eta = 23.6\%$ for $V_L = 0.60$ V (with $\lambda_1 = 716$ nm and $\lambda_2 = 1095$ nm), and $\eta = 27.9\%$ for $V_L = 0.45$ V (with $\lambda_1 = 718$ nm and $\lambda_2 = 1110$ nm). Again, there is hardly any difference in the optimized onsets for $V_L = 0.60$ V and $V_L = 0.45$ V due to the water-vapor absorption gap in the sunlight spectrum. The best efficiencies are better by a factor of about 1.36 with respect to those of single devices. Further increase of the number of sub-cells does not provide such

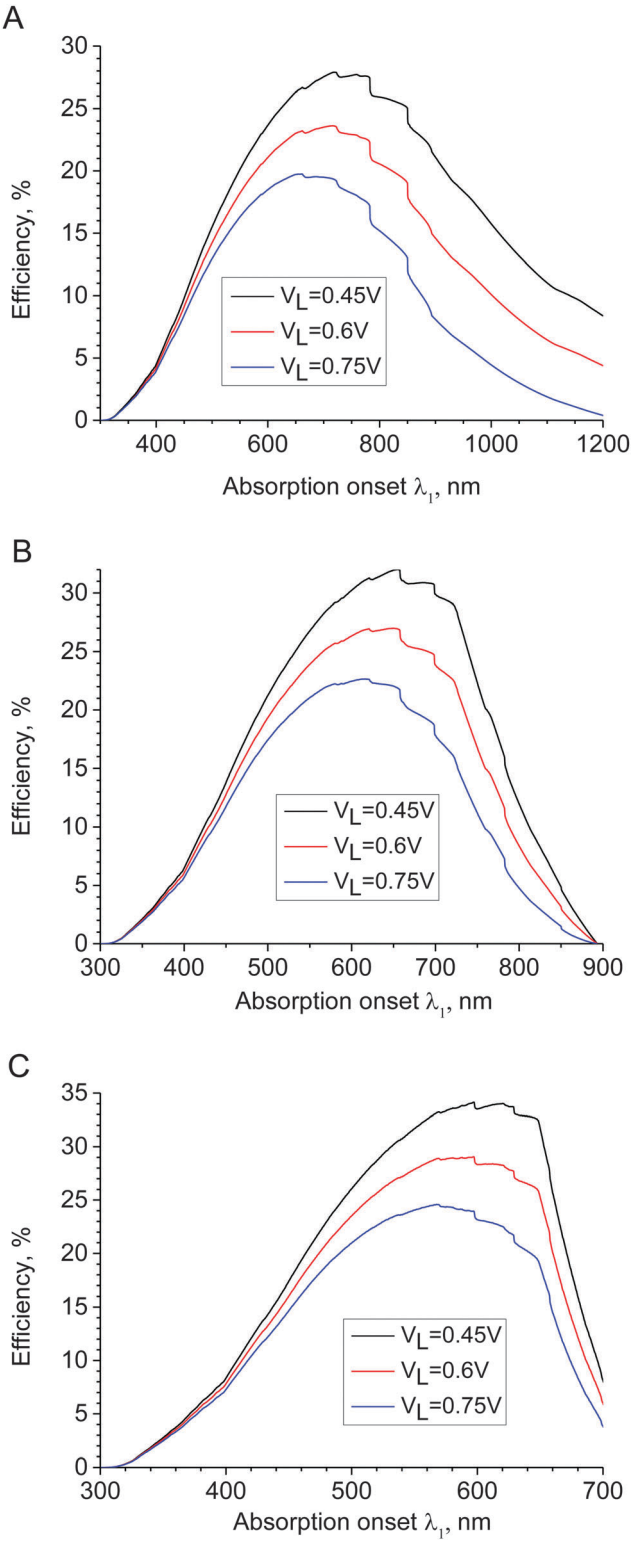

Fig. 3 Comparison of efficiencies of tandem devices with different loss-in-potentials as a function of the absorption onset of the first sub-cell for n = 2 (A), n = 3 (B) and n = 4 (C).

significant improvements: it is only an additional factor of 1.15 for n = 3 and an extra factor of 1.07 for n = 4 (see Table 1). As expected, the trend in absorption onsets is similar to that

Table 1 The best efficiencies (η) and the corresponding optimized absorption onsets (λ_i) for the indicated number of sub-cells (n) and loss-in-potential (V_L) in a single sub-cell. The total loss-in-potential is assumed to be $V_{LT} = nV_L$

	V_L = 0.75 V	V_L = 0.60 V	V_L = 0.45 V
n = 1	η = 14.3% λ_1 = 812 nm	η = 17.6% λ_1 = 892 nm	η = 20.6% λ_1 = 896 nm
n = 2	η = 19.8% λ_1 = 661 nm λ_2 = 929 nm	η = 23.6% λ_1 = 716 nm λ_2 = 1095 nm	η = 27.9% λ_1 = 718 nm λ_2 = 1100 nm
n = 3	η = 22.7% λ_1 = 616 nm λ_2 = 820 nm λ_3 = 1088 nm	η = 27.0% λ_1 = 650 nm λ_2 = 895 nm λ_3 = 1287 nm	η = 32.0% λ_1 = 655 nm λ_2 = 911 nm λ_3 = 1319 nm
n = 4	η = 24.6% λ_1 = 568 nm λ_2 = 720 nm λ_3 = 885 nm λ_4 = 1105 nm	η = 29.1% λ_1 = 597 nm λ_2 = 780 nm λ_3 = 1013 nm λ_4 = 1330 nm	η = 34.1% λ_1 = 597 nm λ_2 = 780 nm λ_3 = 1013 nm λ_4 = 1330 nm

reported already for single solar cells – the wavelengths are shorter with increasing loss-in-potential.[13]

The values collected in Table 1 can be compared with those for multi-junction solar cells. The studies of maximum possible efficiencies are well established and have been calculated with different thermodynamic approaches or detailed balance theory.[29] The corresponding bandgaps for such devices have been calculated using either analytical or numerical sunlight spectrum.[11,12,29] For the updated AM1.5 non-concentrated spectrum and series connection they are: 1.60 eV (λ_1 = 775 nm) and 0.94 eV (λ_2 = 1320 nm) for 2-junction solar cells (giving a maximum efficiency of 46%), and 1.90 eV (λ_1 = 653 nm), 1.37 eV (λ_1 = 905 nm) and 0.94 eV (λ_3 = 1320 nm) for 3-junction solar cells (giving a maximum efficiency of 52%).[11] However, the optimized absorption onsets are the target values only for GaAs and Si devices, which possess low internal voltage losses. As shown in our calculations, these values are not relevant for realistic tandem cells of novel photovoltaic systems (like DSSC, OPV, QDSC, PSC), for which the absorption onsets are shifted towards shorter wavelengths.

Recently, it has also been shown that for the multi-junction inorganic semiconductor solar cells the optimum bandgaps depend on the quality and the luminescence efficiency of the material.[30,31] With increasing nonradiative recombination in the material (and, thus, decreasing luminescence quantum yield) the bandgaps should be lowered, the trend similar to the one obtained in our calculations. The luminescence efficiency was related to the open circuit voltage of the solar cell.[32] However, in the case of DSSCs and PSCs the luminescence properties of the absorbing material have a lower impact on the maximum photovoltage. It is because charge transport is realized in other components than those absorbing the light. Therefore, the main contribution to loss-in-voltage comes from the driving forces necessary for both efficient electron and hole separations at interfaces, for example, electron injection and dye regeneration for DSSC.

Several tandem DSSC structures using two separate cells were investigated with the cell of shorter absorption onset facing the Sun.[33–38] It seems that in many previous attempts to build efficient tandem cells the optimized conditions were not fully realized. Quite often a "good" dye was taken for the first cell (having significant efficiency and absorbing up to 800 nm) and then another dye, absorbing more to the red, was added to the second unit, left with insufficient sunlight to achieve similar photocurrent. It also does not make sense to look for dyes for DSSCs absorbing further in NIR than up to 930 nm for iodide based electrolytes. For cobalt-based electrolytes (or perovskites) the materials do not need to have absorption beyond 1100 nm for double-band tandem cells. For the first compartment of the tandem DSSC, dyes with absorption onsets at around 660 nm are best suited for iodide based electrolytes. This means that a lot of "forgotten" dyes that did not give high efficiencies in single devices (but had a high maximum of IPCE spectra) can be reinvestigated for tandem applications. On the other hand, if a dye for a second compartment does not absorb sufficiently far in the red, than it is better to optimize the absorption onset of the first dye towards even shorter wavelengths (close to 600 nm) to fulfill the matching current conditions. The same situation applies if a second sub-cell has an IPCE spectrum of much lower values than those of the first sub-cell. We will come back to these issues in Sections 3.4 and 3.5 below.

3.3. Combined n–p type tandem configurations

A significant challenge in tandem configurations is the way of making the efficient optical and electrical connection between the sub-cells. Completely separate units (like the ones schematically presented in Fig. 1B) are rather expensive, for example, due to the additional costs of electrodes. In multi-junction solar cells the connection between different compartments is realized through tunnel junctions, however this approach is both expensive and not possible for fabrication with novel solar cells discussed here. In tandem QDSCs and OPVs recombination layers are used.[39,40] For DSSCs, other approaches like the floating electrode for the bottom cell[41] or integrated tandem cells[42] have also been proposed.

However, tandem configuration of double DSSCs can be realized in intuitively elegant and potentially cheap combined n–p DSSCs.[43] Its scheme is shown in Fig. 4A. The n-type part is the photoanode used in the classical DSSC, built of a nanoparticle network of a n-doped semiconductor (usually TiO_2) that collects and transports injected electrons. The p-type part is in many ways the reverse concept to the n-type one.[44] A porous material is placed on the counter electrode to collect and transport the injected holes. The holes (instead of electrons) are injected to the valence band (instead of the conduction band) of a semiconductor (usually NiO) from the dyes attached with the electron withdrawing group to the nanoparticles' surfaces. The dyes are regenerated by the hole transfer from the redox pair in the electrolyte, the latter process being the equivalent of the redox pair oxidation on the counter electrode in classical DSSCs. In the combined n- and p-type device, the same electrolyte is used to regenerate the dyes on the n-type side.

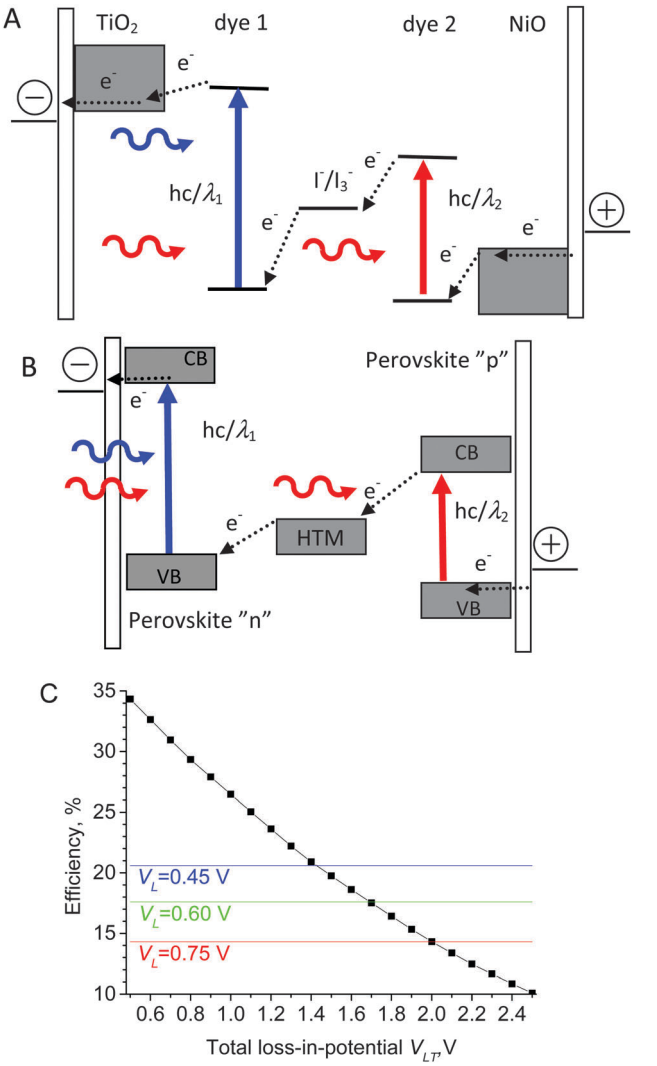

Fig. 4 Scheme of a n- and p-type tandem DSSC (A) and a proposed new structure of a tandem perovskite solar cell (B). The best efficiency as a function of total loss-in-potential for a tandem cell with 2 sub-cells, $n = 2$ (C). The horizontal lines indicate the best efficiencies of single devices for indicated V_L corresponding to a PSC (V_L = 0.45 V), a cobalt-based DSSC (V_L = 0.60 V) and an iodide-based DSSC (V_L = 0.75 V).

The best efficiencies of p-type DSSC devices are still very low, up to 1.3%,[45] so n–p tandems also suffer from poor performance. The problem with the p-type part is that significant driving forces are necessary (and, thus, large loss-in-potential) for obtaining reasonable IPCE values. For example, the systems with high IPCE require the blue-absorbing dye on the p-part.[46] Therefore, it is reasonable to ask what is the limit of total loss-in-potential (V_{LT}) at which the maximum efficiency of the tandem device drops below the maximum efficiency of a single device. Our calculations indicate (Fig. 4C) that it is maintained for $V_{LT} < 2.0$ V for iodide-based electrolytes and $V_{LT} < 1.7$ V for cobalt-based electrolytes. Taking the optimized absorption onsets for such limiting systems we can calculate from eqn (5) that the minimum total V_{oc} of such systems has to be 1.4 V for iodide DSSCs and 1.6 V for cobalt DSSCs. It should be noted that we

refer to iodide- or cobalt-based electrolytes only on the context of target best efficiency of a single device. In the n–p DSSC device the type of redox couple used does not influence the total V_{oc} – it can only modify the IPCE spectra of both n- and p-components.

Note that the differences between the potential of the conduction band edge of TiO_2 (about −0.5 V *vs.* NHE) and the valence band edge of NiO (about 0.6 V *vs.* NHE) is the maximum V_{oc} available from such a tandem device (Fig. 4A) and it is only about 1.1 V. This means that a tandem n–p DSSC made with TiO_2 and NiO will hardly give the expected better efficiency than a champion single DSSC device. Our calculations indicate that in order to maintain V_{oc} as small as 1.1 V and have the best efficiency above 19% (to beat a single cobalt-based DSSC with best η = 17.6%, see Table 1) one needs a very unrealistic total loss-in-potential of $V_{LT} = V_{L1} + V_{L2}$ = 1.3 V and an absorption onset of the second dye as far as λ_2 = 1500 nm. We think that it is quite an important conclusion which suggests that it is better to work on the photocathodes with semiconductors of much more positive potential of the valence bandgap than NiO. $CuAlO_2$ and $CuGaO_2$ have potentials by about 0.2 V more positive with respect to NiO, which puts them on the similar best possible efficiency as single DSSCs. Better improvement can be reached with $CuGaO_2$ whose valance band energy is further 0.2 eV lower.[47] In such conditions both V_{LT} can be higher and λ_2 can be smaller to maintain the best efficiency above 19%.

According to our knowledge, tandem structures of perovskite solar cells have not been reported so far. Therefore, we would like to propose a possible compact configuration of such a tandem device based on the n–p concept of a DSSC (Fig. 4B). It should be noted that it uses perovskite materials for both sub-cells. The proposed configuration takes the advantage of the perovskite material that is a very good electron and hole transporter.[24] Indeed, it has been reported for efficient PSCs that the electron transporting TiO_2 material can be substituted with Al_2O_3 and electrons are efficiently transported through the perovskite material itself.[48] Similarly, quite efficient PSCs without any additional hole transporting material was built.[49] Therefore, two perovskite mesoporous layers with optimized absorption onsets can substitute both sensitizing dye and charge transporting mesoporous semiconductor layers, and it can work on the photoanode (perovskite "n") as well as on the photocathode (perovskite "p"). Hole transporting materials (HTM, for example spiro-OMeTAD) can act as analogues to the redox couple in n–p DSSCs. The maximum possible V_{oc} would be the difference between the potential of the conduction band edge of perovskite "n" and the valence band edge of perovskite "p".

Due to the lower loss-in-potential of PSCs the conditions for tandem n–p perovskite configuration are even more rigorous than for DSSCs. According to our calculations, the total loss in potential has to be $V_{LT} < 1.4$ V for such tandem configuration to give better efficiency than a single device with V_L = 0.45 V (Fig. 4C). This means that a potential of the valence band of perovskite "p" has to lie significantly below the HOMO level of HTM. Such modification can be quite challenging within organometal halide perovskites used so far. All the reported modifications that result in lowering the valence band led to a simultaneous increase in conduction band energy when atoms of higher electronegativity are used. For example, the valence band edge of $CH_3NH_3PbBr_3$ is 0.14 eV below that of $CH_3NH_3PbI_3$, but at the same time the bandgap increases from 1.5 to 2.2 eV.[50] In this way, the loss-in-potential for electron transfer to HTM would be too high. Therefore, probably new types of perovskites are necessary for such tandem devices.

3.4. Optimization limits

We would like to discuss the limits in which the absorption onset can be changed without significant alteration of the global efficiency (up to 10% relative change). The example will be discussed for n = 2 and iodide-based DSSCs. The crucial role of the current matching conditions should be emphasised, which is even more important than the long enough absorption onset of the dyes. For example, if the long-wavelength onset is shifted by 100 nm (from λ_2 = 929 to λ_2 = 829 nm) and the short-wavelength one is shifted accordingly to keep the optimum matching (from λ_1 = 661 nm down to λ_1 = 620 nm) then the tandem maximum efficiency does not drop so much: from 19.8% to 19.1% (with $V_{L1} = V_{L2}$ = 0.75 V), which is only 4% relative change. However, if λ_1 stays fixed at 661 nm and we move only λ_2, much bigger losses occur (gathered in Fig. 5). It is visible immediately that too short λ_2 is more harmful (reaching 10% relative efficiency loss with absorption shift of around $\Delta\lambda_2 = -40$ nm), while for too long λ_2 the loss is significantly lower ($\Delta\lambda_2$ of around 140 nm needed for 10% relative efficiency loss).

These results, presented in Fig. 5, can be explained by the balance between I_{sc} and V_{oc} in eqn (1). Below optimal cutoff, the voltage of the second junction is higher, but its current is lower than the one of the first junction and it effectively becomes I_{sc}, lowering the efficiency of the entire device. Thus, for example, if we cannot get sufficiently red-absorbing material for a second sub-cell of tandem DSSCs, it is better to shift the absorption of the first sub-cell towards shorter wavelengths to maintain current matching conditions. In the too long regime, however,

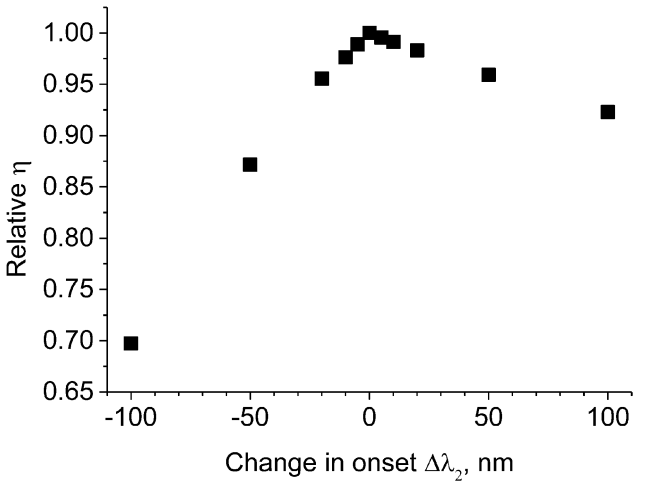

Fig. 5 Relative loss in global efficiency of the tandem cell with fixed λ_1 and λ_2 shifted by $\Delta\lambda_2$ from the optimized position.

the I_{sc} stays constant (being the lower current on the first junction, which remains unchanged). The only part that gets lowered is the voltage of the second sub-cell which decays as $1/\lambda_2$ (resulting $V_{oc} = 0.37 + 1240/\lambda_2$). This means that the global efficiency loss of 10% will be met when V_{oc} will drop to 90% of the initial value, which happens at $\lambda_2 = 1070$ nm. In fact, as long as $1240/\lambda_2$ is higher than 0.75 V, the V_{L1} of the second junction, the tandem cell will be more efficient than a single one with a given offset λ_1. It holds true for λ_2 up to 1650 nm.

When we fix λ_2 at an optimum 929 nm and change λ_1, the situation is reversed. Moving λ_1 towards shorter wavelengths results in λ_2 too far in the red and a slow decrease in performance, while moving λ_1 towards longer wavelengths makes λ_2 too short for optimal matching resulting in more rapid loss. Therefore, moving λ_1 can be explained in terms of the previous example. One can take new optimal λ_2 for the moved λ_1 from Fig. 2, and then again treat λ_1 as a fixed parameter, with $\Delta\lambda_2$ equal to the difference between fixed λ_2 and optimal λ_2 from Fig. 2 (with the base efficiency for given λ_1 taken form Fig. 3). In both cases, losses from the onsets lying too close to each other are 3–4 times higher than in the situation when they are lying too far, for the same mismatch amplitude concerned.

3.5. Gradually increasing IPCE spectra

Finally, we would like to discuss the influence of more realistic shapes of the IPCE spectra and simulate the results for a couple of already reported tandem configurations.

The first thing that is taken into account in this chapter is the fact that the real IPCE spectra do not end instantly, but decay (usually in a gauss fashion) with some half-width. We checked the effect of this blur for single and double cells with the initial cutoff lengths optimized and $V_L = 0.75$ V ($\lambda_1 = 812$ nm for $n = 1$, and $\lambda_1 = 661$ nm and $\lambda_2 = 929$ nm for $n = 2$). The IPCE spectra were fixed, so that the half of maximum amplitude lies always at the wavelengths mentioned before. Gaussian decay was generated using expression (6) with λ_d tweaked so that half of the amplitude is fixed at one wavelength and A being the maximum amplitude of IPCE.

$$\mathrm{IPCE}(\lambda) = A\exp\left(-\frac{(\lambda-\lambda_d)^2}{2\sigma^2}\right) \quad (6)$$

Starting with $\sigma = 0$ nm (square) up to $\sigma = 200$ nm the IPCE curves are presented as insets in Fig. 6A and B for $n = 1$ and $n = 2$ respectively. When calculating the efficiency two situations were considered, taking absorption onset at the half amplitude (keeping it constant independent of σ) and taking absorption onset at a wavelength with 10% of the initial amplitude. The first case (constant absorption onset λ_{onset} at a half amplitude of IPCE) corresponds to the situation when for $\lambda > \lambda_{onset}$ smaller absorption gap ($1240/\lambda$) is compensated by loss-in-potential smaller then optimum, keeping the ($1240/\lambda - V_L$) value constant. Therefore, the increase of IPCE is due to the insufficient driving force and the quantum yields of primary charge separation process (for example electron injection in DSSCs). In contrast, the case of maintaining absorption onset at

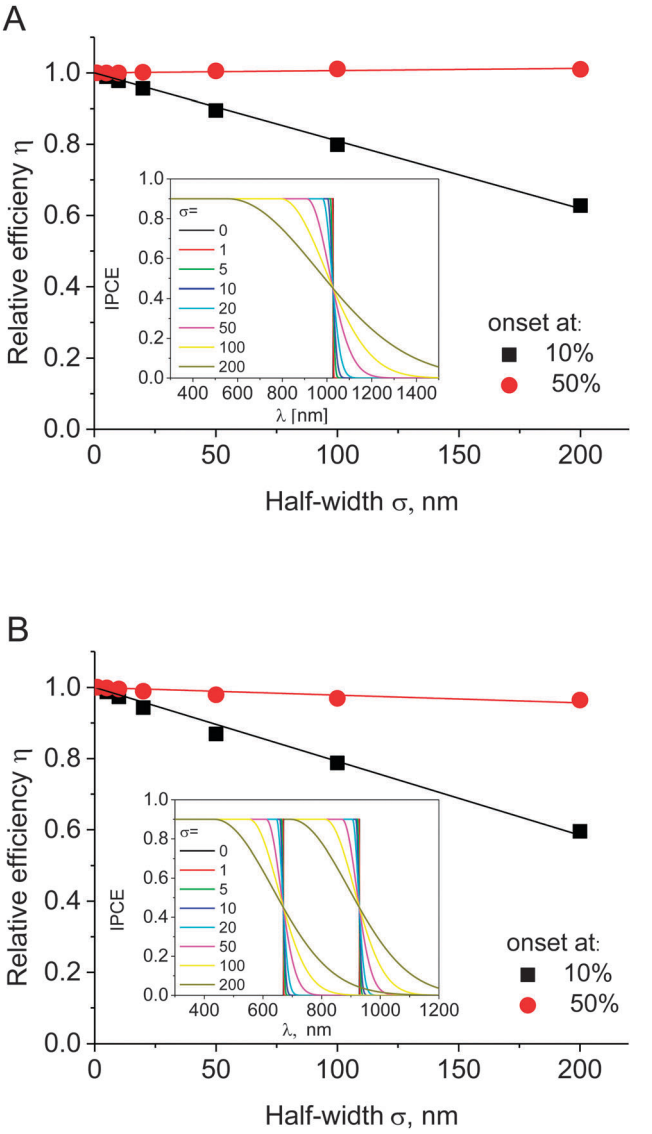

Fig. 6 Relative loss in global efficiency of the tandem cell with fixed λ_1 and λ_2 with the changing half-width σ for a single cell (A) and a tandem cell (B). The absorption onset is set either to 50% or to 10% of the IPCE curve. The insets show IPCE curves for given σ.

10% of increasing IPCE corresponds to the situation when a finite rise in IPCE is due to the insufficient absorption of light, for example, due to too thin absorption layer.

The obtained relative efficiencies (compared to $\sigma = 0$) can be seen in Fig. 6A and B for $n = 1$ and $n = 2$ respectively. It can be clearly observed that for both cells the blur has hardly any effect on the efficiency when the absorption onset is kept at a constant value (only a change in I_{sc} would contribute here, but the current fluctuation is less than 3% up to $\sigma = 100$ nm). This means that all our previous considerations based on the ideal rectangle-like IPCE spectra (Fig. 1C) are also valid in this case.

With the moving onsets resulting in diminishing V_{oc}, one can see the corresponding efficiency loss. Surprisingly, the loss scales fairly linearly in this region with about 10% loss in the relative performance at $\sigma = 50$ nm for a single cell and $\sigma = 45$ nm

for a tandem cell. This convenient fact yields a nice method of estimation of maximum efficiencies of single and tandem devices, with the knowledge of the IPCE spectra.

So far we assumed that maxima of IPCE spectra of all tandem components have the same value (90%). Our procedure and the provided program also enable the calculation in the cases when IPCE maxima are different, *i.e.* due to lower charge separation yields in some compartments. As expected, in these cases the optimized absorption onset might be different to those shown above. For example, for n = 2 and iodide DSSCs (V_L = 0.75 V) we checked a rather extreme case of $IPCE_1$ = 90% and $IPCE_2$ = 50% of rectangular shape. The obtained best efficiency was equal to 16.2% with absorption onsets at λ_1 = 632 nm and λ_2 = 1096 nm. Therefore, compared to the case of the same intensity of IPCE (Table 1), the onset of the first compartment is shifted to shorter wavelengths, while that of the second compartment to longer wavelengths. When the values of IPCE intensity were exchanged ($IPCE_1$ = 50%, $IPCE_2$ = 90% and assuming that no light within the IPCE spectrum of the first sub-cell passes to the second one), the situation is reversed: the optimized onsets are at λ_1 = 715 nm (red shifted) and λ_2 = 896 nm (blue shifted). However, in this case the efficiency is only 12.7%, which is smaller than that of single devices (14.3%, Table 1).

Finally, we would like to present the example of using our procedure to check the performance and suggest the way of improving a real tandem DSSC cell. We have chosen a recently reported tandem configuration with one of the best efficiencies reported so far (11.4%) utilizing novel DX1 dye and a traditional sensitizer N719.[38] The IPCE spectra provided in this contribution were digitized and used as inputs in the program. Calculations yielded data that corresponded well with values reported by the authors: I_{sc} = 11.3 mA cm^{-2}, V_{oc} = 1.46 V and η = 11% when absorption onsets were taken at wavelengths corresponding to 10% of the maximum IPCE amplitude (712 nm and 940 nm for the top and bottom cells respectively). Simulation shows a little mismatch of the current (11.3 mA cm^{-2} for the top cell and 13.3 mA cm^{-2} for the bottom cell), but generally the results are representing experimental data, with less than 10% error. Looking at Table 1 one can see that the λ_2 of DX1 dye lies close to the optimal theoretical wavelength for the tandem system with the iodide electrolyte – 929 nm. The λ_1, however, is lying too far to the red, lowering the total efficiency. Hence, we performed more simulations leaving the bottom cell IPCE spectrum and the FF intact, while taking the IPCE of the top cell as a rectangle of height 0.7 spanning from 300 nm to the varying λ_1. It turned out that the maximum efficiency of 13.5% is achieved when λ_1 is taken at 650 nm with I_{sc} = 11.7 mA cm^{-2} and V_{oc} = 1.72 V. When we consider that there are dyes with IPCE ending within the region of 600–650 nm which can achieve a uniform IPCE of 0.9 amplitude, the global efficiency can be pushed even higher. When the height of the top cell rectangular spectrum is set to 0.9 the simulated efficiency can reach 16.1% with λ_1 = 623 nm, I_{sc} = 13.2 mA cm^{-2} and V_{oc} = 1.81 V.

Therefore, as alternatives to N719 some triphenylamine dyes with more blue shifted absorption onset can be proposed for the tandem configuration with DX1 dye. For example, TPC1[51] and TH305[52] dyes have high IPCE values and the time-resolved studies with our contribution confirmed high electron injection and dye regeneration quantum yields of these systems.[53,54] A DSSC with TPC1 dye has a flat IPCE spectrum of 80–90% extending up to 530 nm with gradual decay up to 630 nm, while that with TH305 has an IPCE spectrum shifted further to red by 70 nm. Another alternative that has been introduced very recently is RK1 dye, having similar IPCE onsets to that of TH305 but yielding even better efficiencies.[55]

4. Conclusions

Loss-in-potential, V_L, of the solar cell (being the difference in the energy bandgap of the active material and the open circuit voltage of the cell) is a simple parameter that can help simulating the behavior of different photovoltaic devices. In this contribution we use this parameter to calculate the optimal absorption onsets of tandem DSSCs and perovskite solar cells. Based on the proposed procedure and the provided program, a number of results relevant for better optimization of such devices are shown and discussed.

For an ideal case of the rectangle IPCE spectra (with steep onset) the following optimal onsets and sunlight conversion efficiencies are obtained for tandem configurations with two sub-cells (assuming the maximum IPCE value of 90% and FF = 0.73): λ_1 = 661 nm, λ_2 = 929 nm and η = 19.8% for iodide-based DSSCs (V_L = 0.75 V), λ_1 = 716 nm, λ_2 = 1095 nm and η = 23.6% for cobalt-based DSSCs (V_L = 0.60 V), and λ_1 = 718 nm, λ_2 = 1110 nm and η = 27.9% for perovskite solar cells (V_L = 0.45 V). Such configurations can increase the total sunlight conversion efficiency by about 35% in comparison to the single-cell devices. It is shown that if the materials with optimized wavelengths are not available, it is better to vary the absorption onsets of all compartments to fulfill the current matching conditions than keeping one onset at a fixed optimized position and vary other onsets. For more realistic IPCE curves (with Gaussian rise) the results do not depend on the width of the spectral increase if absorption onsets are kept the same. If absorption onsets change according to the width of IPCE increase, then the sunlight conversion efficiency decreases linearly with a relative drop of about 20% of the initial value per 100 nm width increase.

A novel configuration for a tandem perovskite solar cell is proposed based on a tandem n–p DSSC device. The conditions at which both of such tandem devices can be superior with respect to single solar cells are investigated. It is revealed that the sum of both loss-in-potentials in a n–p DSSC cannot exceed 1.7 V. Due to large potential losses of a typical n–p DSSC with TiO_2 and NiO mesoporous films, such configurations will hardly provide better sunlight conversion efficiency than a single DSSC, therefore alternatives to NiO material with more positive potential of the valence band should be explored. For tandem perovskite cells the conditions are even more rigorous and the total loss in potential has to be smaller than 1.4 V. This implies the need of new types of perovskites with a more positive valence band potential.

Finally, the example of the real IPCE spectra of a functioning DSSC tandem device was used for calculation and discussion of the best absorption onsets. The provided procedure and program enable calculation of optimal absorption bandgaps and efficiencies for any given configuration of tandem solar cells and the assumed loss-in-potential.

Acknowledgements

This work was supported by NCN (National Science Centre, Poland) under the project 2012/05/B/ST3/03284. J. S. is a holder of a scholarship funded within Human Capital Operational Programme, European Social Fund.

References

1 J. Burschka, N. Pellet, S.-J. Moon, R. Humphry-Baker, P. Gao, M. K. Nazeeruddin and M. Grätzel, *Nature*, 2013, **499**, 316–319.
2 M. Liu, M. B. Johnston and H. J. Snaith, *Nature*, 2013, **501**, 395–398.
3 H.-S. Kim, S. H. Im and N.-G. Park, *J. Phys. Chem. C*, 2014, **118**, 5615–5625.
4 A. Yella, H.-W. Lee, H. N. Tsao, C. Yi, A. K. Chandiran, M. K. Nazeeruddin, E. W.-G. Diau, C.-Y. Yeh, S. M. Zakeeruddin and M. Grätzel, *Science*, 2011, **334**, 629–634.
5 J. You, L. Dou, K. Yoshimura, T. Kato, K. Ohya, T. Moriarty, K. Emery, C.-C. Chen, J. Gao, G. Li and Y. Yang, *Nat. Commun.*, 2013, **4**, 1446.
6 A. H. Ip, S. M. Thon, S. Hoogland, O. Voznyy, D. Zhitomirsky, R. Debnath, L. Levina, L. R. Rollny, G. H. Carey, A. Fischer, K. W. Kemp, I. J. Kramer, Z. Ning, A. J. Labelle, K. W. Chou, A. Amassian and E. H. Sargent, *Nat. Nanotechnol.*, 2012, **7**, 577–582.
7 www.nrel.gov/ncpv, National Renewable Energy Laboratory (NREL).
8 D. Yue, P. Khatav, F. You and S. B. Darling, *Energy Environ. Sci.*, 2012, **5**, 9163–9172.
9 S. B. Darling and F. You, *RSC Adv.*, 2013, **3**, 17633–17648.
10 W. Shockley and H. J. Queisser, *J. Appl. Phys.*, 1961, **32**, 510–519.
11 S. P. Bremner, M. Y. Levy and C. B. Honsberg, *Prog. Photovoltaics*, 2008, **16**, 225–233.
12 A. S. Brown and M. A. Green, *Physica E*, 2002, **14**, 96–100.
13 H. J. Snaith, *Adv. Funct. Mater.*, 2010, **20**, 13–19.
14 M. K. Nazeeruddin, F. De Angelis, S. Fantacci, A. Selloni, G. Viscardi, P. Liska, S. Ito, B. Takeru and M. Grätzel, *J. Am. Chem. Soc.*, 2005, **127**, 16835–16847.
15 Q. Yu, Y. Wang, Z. Yi, N. Zu, J. Zhang, M. Zhang and P. Wang, *ACS Nano*, 2010, **4**, 6032–6038.
16 G. Conibeer, *Mater. Today*, 2007, **10**, 42–50.
17 L. C. Hirst and N. J. Ekins-Daukes, *Prog. Photovoltaics*, 2011, **19**, 286–293.
18 Z. He, C. Zhong, S. Su, M. Xu, H. Wu and Y. Cao, *Nat. Photonics*, 2012, **6**, 591–595.
19 B. E. Hardin, H. J. Snaith and M. D. McGehee, *Nat. Photonics*, 2012, **6**, 162–169.
20 H. J. Snaith, *J. Phys. Chem. Lett.*, 2013, **4**, 3623–3630.
21 http://rredc.nrel.gov/solar/spectra/am1.5/ASTMG173/ASTMG173.html.
22 S. M. Feldt, E. A. Gibson, E. Gabrielsson, L. Sun, G. Boschloo and A. Hagfeldt, *J. Am. Chem. Soc.*, 2010, **132**, 16714–16724.
23 N. G. Park, *J. Phys. Chem. Lett.*, 2013, **4**, 2423–2429.
24 S. D. Stranks, G. E. Eperon, G. Grancini, C. Menelaou, M. J. P. Alcocer, T. Leijtens, L. M. Herz, A. Petrozza and H. J. Snaith, *Science*, 2013, **342**, 341–344.
25 B. E. Hardin, E. T. Hoke, P. B. Armstrong, J. H. Yum, P. Comte, T. Torres, J. M. J. Fréchet, M. K. Nazeeruddin, M. Grätzel and M. D. McGehee, *Nat. Photonics*, 2009, **3**, 406–411.
26 S. K. Balasingam, M. Lee, M. G. Kang and Y. Jun, *Chem. Commun.*, 2013, **49**, 1471–1487.
27 Y. Ogomi, S. S. Pandey, S. Kimura and S. Hayase, *Thin Solid Films*, 2010, **519**, 1087–1092.
28 M. Cheng, X. Yang, J. Li, F. Zhang and L. Sun, *ChemSusChem*, 2013, **6**, 70–77.
29 A. Martí and G. L. Araújo, *Sol. Energy Mater. Sol. Cells*, 1996, **43**, 203–222.
30 N. L. A. Chan, N. J. Ekins-Daukes, J. G. J. Adams, M. P. Lumb, M. Gonzalez, P. P. Jenkins, I. Vurgaftman, J. R. Meyer and R. J. Walters, *IEEE J. Photovoltaics*, 2012, **2**, 202–208.
31 T. P. White, N. N. Lal and K. R. Catchpole, *IEEE J. Photovoltaics*, 2014, **4**, 208–214.
32 G. Smestad and H. Ries, *Sol. Energy Mater. Sol. Cells*, 1992, **25**, 51–71.
33 W. Kubo, A. Sakamoto, T. Kitamura, Y. Wada and S. Yanagida, *J. Photochem. Photobiol., A*, 2004, **164**, 33–39.
34 M. Dürr, A. Bamedi, A. Yasuda and G. Nelles, *Appl. Phys. Lett.*, 2004, **84**, 3397–3399.
35 M. Yanagida, N. Onozawa-Komatsuzaki, M. Kurashige, K. Sayama and H. Sugihara, *Sol. Energy Mater. Sol. Cells*, 2010, **94**, 297–302.
36 L. Li, Y. Hao, X. Yang, J. Zhao, H. Tian, C. Teng, A. Hagfeldt and L. Sun, *ChemSusChem*, 2011, **4**, 609–612.
37 D. Xiong and W. Chen, *Front. Optoelectron.*, 2012, **5**, 371–389.
38 T. Kinoshita, J. T. Dy, S. Uchida, T. Kubo and H. Segawa, *Nat. Photonics*, 2013, **7**, 535–539.
39 X. Wang, G. I. Koleilat, J. Tang, H. Liu, I. J. Kramer, R. Debnath, L. Brzozowski, D. A. R. Barkhouse, L. Levina, S. Hoogland and E. H. Sargent, *Nat. Photonics*, 2011, **5**, 480–484.
40 T. Ameri, N. Li and C. J. Brabec, *Energy Environ. Sci.*, 2013, **6**, 2390–2413.
41 K. Uzaki, S. S. Pandey and S. Hayase, *J. Photochem. Photobiol., A*, 2010, **216**, 104–109.
42 R. Tagliaferro, D. Gentilini, S. Mastroianni, A. Zampetti, A. Gagliardi, T. M. Brown, A. Reale and A. Di Carlo, *RSC Adv.*, 2013, **3**, 20273–20280.
43 A. Hagfeldt, G. Boschloo, L. Sun, L. Kloo and H. Pettersson, *Chem. Rev.*, 2010, **110**, 6595–6663.

44 J. He, H. Lindström, A. Hagfeldt and S. E. Lindquist, *J. Phys. Chem. B*, 1999, **103**, 8940–8943.
45 S. Powar, T. Daeneke, M. T. Ma, D. Fu, N. W. Duffy, G. Götz, M. Weidelener, A. Mishra, P. Bäuerle, L. Spiccia and U. Bach, *Angew. Chem.*, 2013, **125**, 630–633.
46 A. Nattestad, A. J. Mozer, M. K. R. Fischer, Y.-B. Cheng, A. Mishra, P. Bäuerle and U. Bach, *Nat. Mater.*, 2009, **9**, 31–35.
47 M. Yu, T. Draskovic and Y. Wu, *Phys. Chem. Chem. Phys.*, 2014, **16**, 5026–5033.
48 M. M. Lee, J. Teuscher, T. Miyasaka, T. N. Murakami and H. J. Snaith, *Science*, 2012, **338**, 643–647.
49 W. A. Laban and L. Etgar, *Energy Environ. Sci.*, 2013, **6**, 3249–3253.
50 J. H. Noh, S. H. Im, J. H. Heo, T. N. Mandal and S. I. Seok, *Nano Lett.*, 2013, **13**, 1764–1769.
51 H. Tian, X. Yang, R. Chen, R. Zhang, A. Hagfeldt and L. Sun, *J. Phys. Chem. C*, 2008, **112**, 11023–11033.
52 H. Tian, X. Yang, J. Cong, R. Chen, J. Liu, Y. Hao, A. Hagfeldt and L. Sun, *Chem. Commun.*, 2009, 6288–6290.
53 M. Ziółek, B. Cohen, X. Yang, L. Sun, M. Paulose, O. K. Varghese, C. A. Grimes and A. Douhal, *Phys. Chem. Chem. Phys.*, 2012, **14**, 2816–2831.
54 M. Ziółek, C. Martín, L. Sun and A. Douhal, *J. Phys. Chem. C*, 2012, **116**, 26227–26238.
55 D. Joly, L. Pelleja, S. Narbey, F. Oswald, J. Chiron, J. N. Clifford, E. Palomares and R. Demadrille, *Sci. Rep.*, 2014, **4**, 4033.

Supporting information

for

Optimization of absorption bands of dye-sensitized and perovskite tandem solar cells based on loss-in-potential values.

Jan Sobuś [1,2] and Marcin Ziółek [2]*

[1] *NanoBioMedical Centre, Adam Mickiewicz University, Umultowska 85, 61-614 Poznan, Poland.*

[2] *Quantum Electronics Laboratory, Faculty of Physics, Adam Mickiewicz University, Umultowska 85, 61-614 Poznan, Poland.*

Program description

The code of the program (in C) is attached as separate file (*code.c*). The code can be compiled to executable file by most compilers under Windows or Linux (for example Dev C++ for Windows which can be downloaded at http://www.bloodshed.net/dev/devcpp.html). Upon launching the user has 4 options:

1. Generate IPCE
2. Optimize cell
3. Simulate cell
4. Exit

1. Generating IPCE

When this option is chosen, the program first asks for the number of spectra to be generated (1-10). They will be saved in separate files from *ipce1.txt* to *ipce10.txt.* After entering the number of spectra, program asks for the shape and parameters of each spectrum. Square shaped spectrum needs 3 parameters: height between 0 and 1, beginning of the interval and its end in nm (between 300 and 2500). They should all be given in one line, separated by spaces. Note that for the absorption onset optimization the end of the interval should be longer than the expected absorption onset (for general cases the interval can be from 300 to 2500 nm, see the exemplary attached file *ipce1.txt*). Gaussian shaped spectrum needs 4 parameters. When 'Cancel' is chosen, the spectrum with the current number is not modified. First 3 of them are the same as in square shape, maximum amplitude and two wavelengths between which the amplitude is preserved. The last parameter is the decay half-width σ, which determines shape of the slopes according to the formula (6). When the desired number of curves is generated, program returns to main menu.

2. Cell optimization

After choosing this mode, program first asks for the number of junctions (sub-cells) that constitute entire simulated device. Then it asks for V_{loss} on each junction of the system, FF is fixed at a reasonable value of 0.73. Finally it asks for the mode of operation, full or decaying currents. In multi-junction devices, when the 'full current' mode is chosen only the sub-cells matching the current of the first sub-cell will contribute to the final efficiency, the rest is dismissed. In 'decaying current' mode all the sub-cells with non-zero currents will contribute to the result and the lowest of these currents will be picked as I_{sc}. For the simulation of single cell 'full current' mode is chosen automatically. IPCE for the n^{th} sub-cell is taken from *ipcen.txt* file. Simulations works as follows. The program is calculating the current of the first

cell by integration according to formula (2) beginning in 300nm and with the step of 0.5nm. After each step, rest of the sub-cells have their currents integrated until the point they reach the current of the sub-cell over them (n^{th} sub-cell tries to match the current of $(n-1)^{th}$ sub-cell) or their currents rises no more. The light absorbed by the cells over the n^{th} is taken into account. Wavelength onsets corresponding to each sub-cell are stored and used to calculate voltage of each part according to formula (3), which leads to calculating Voc as in (5). I_{sc} is picked according to the chosen mode and efficiency is calculated according to formula (1) with P_{in} fixed at 100mWcm^{-2}. Results after each step are written to the file *output.txt*. Its header has number of junctions and V_{loss} of each junction. Underneath there are results of each calculation step: onsets for all the subcells, number of "useful" junctions according to the chosen current mode, I_{sc}, number of the sub-cell with the lowest current, V_{oc} and efficiency. Dismissed sub-cells have their onset wavelength set as 0. When the current of the first sub-cell rises no more, simulation ends and program closes itself (to prevent accidental overwriting *output.txt*).

3. Simulating cell

This part simulates actual (tandem) cell with the given parameters. It asks for the number of sub-cells, V_{loss} for each subcell and FF. It also asks for the cutoff factor CF. It is a parameter with the values between 0 and 1. It gives information where to take the onset for calculating V_{oc} – for each sub-cell it will be taken at the wavelength, where the amplitude is equal to the maximum amplitude multiplied by CF. IPCE curves are taken in the same manner as in optimize cell section. Then the program calculates current for each sub-cell, taking into account the light absorbed by the sub-cells above. The amount of light that goes through the sub-cell at a given wavelength is given by formula (S1).

$$Light(\lambda) = \left(1 - \frac{IPCE(\lambda)}{IPCE_{\max}}\right) \quad \text{(S1)}$$

The cutoff wavelength, current and voltage (including loss) of each sub-cell is written out. Then the lowest current is chosen as I_{sc}, V_{oc} and efficiency are calculated and also written out and the program returns to main menu.

In both optimize cell and simulate cell operation modes user IPCE spectra can be used, provided they maintain the structure:

$IPCE_{max}$

300[Tab]IPCE(300)

300.5[Tab]IPCE(300.5)

…

2500[Tab]IPCE(2500)

User can also provide his own sunlight spectrum by substituting the file *AM15ext.txt*. It has the format in which the first column represents wavelength and the second one – photon flux multiplied by elementary charge. By default, the file attached uses ASTM G173-03 reference spectra.

4. Exit

Self explanatory.

Figure

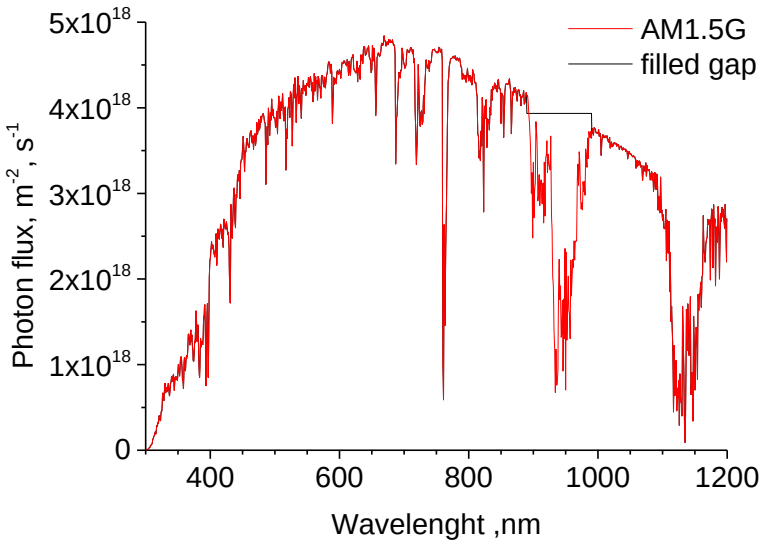

Figure S1. Photon flux for AM1.5G reference sunlight spectrum used in all calculations and the modified spectrum with filled gap in 890-990 nm range due to water vapor absorption for control calculations.

Dyes and Pigments 113 (2015) 692–701

Contents lists available at ScienceDirect

Dyes and Pigments

journal homepage: www.elsevier.com/locate/dyepig

Transient states and the role of excited state self-quenching of indoline dyes in complete dye-sensitized solar cells

Jan Sobuś [a, b], Jerzy Karolczak [b, c], Dariusz Komar [b], Juan A. Anta [d], Marcin Ziółek [b, *]

[a] NanoBioMedical Centre, Adam Mickiewicz University, Umultowska 85, 61-614 Poznan, Poland
[b] Quantum Electronics Laboratory, Faculty of Physics, Adam Mickiewicz University, Umultowska 85, 61-614 Poznan, Poland
[c] Center for Ultrafast Laser Spectroscopy, Adam Mickiewicz University, Umultowska 85, 61-614 Poznan, Poland
[d] Departamento de Sistemas Físicos, Químicos y Naturales, Area de QuímicaFísica, Universidad Pablo de Olavide, Ctra. Utrera, Km 1, E-41013 Sevilla, Spain

ARTICLE INFO

Article history:
Received 28 August 2014
Received in revised form
6 October 2014
Accepted 9 October 2014
Available online 18 October 2014

Keywords:
Indoline dyes
Dye sensitized solar cells
Ultrafast spectroscopy
Dye aggregation
Titanium dioxide nanoparticles
Zinc oxide nanoparticles

ABSTRACT

The photo behaviour of indoline dye D149 on different metal oxide nanoparticles in functioning solar cells is investigated by time-resolved studies in the time range from 100 fs to several ns. The cells are also characterized by standard photovoltaic measurements. The electron injection is found to occur on the time scales from <200 fs to several tens of ps. Locally excited (LE) and charge transfer (CT) excited states of the dye are identified to participate in the electron injection and dye deactivation mechanisms. The dependence of the ultrafast dynamics on the coadsorbent concentration and energy density of the pump pulse indicates the important role of excited state self-quenching. A decrease in the photocurrent of the cells upon aging (very fast for ZnO and slower for TiO_2 nanoparticles) is found to be correlated with the transient absorption kinetics, with a probable explanation suggested as electrolyte-induced dye rearrangement and aggregate formation.

1. Introduction

Indoline dye D149 [1] is a popular metal-free sensitizer used in dye-sensitized solar cells (DSSC) [2,3]. The best sunlight conversion efficiency of DSSC with this dye and iodine-based liquid electrolyte is 9% [4], which can be compared to record efficiencies of best metal-free dyes, 10.2% with iodine-based electrolyte [5], 10.65% with cobalt-based electrolyte [6], ruthenium dyes 11.7% [7], and porphyrin dyes, 13.0% [8]. Besides the high efficiency, D149 showed remarkable promising properties when used with less volatile ionic liquids, solid state electrolytes and alternative metal oxides [4,9–13]. DSSC systems with this dye were also widely studied in the context of the observed transient Stark shift [14–18]. Moreover, the new dyes containing indoline moiety have recently shown very high conversion efficiencies [6,19].

Dynamics and quantum yield of electron injection in DSSC, which can be studied by ultrafast laser spectroscopy techniques [20–28], are important parameters that might determine the sunlight conversion efficiency of the device [29,30]. This issue became even more important in recent years, when it was revealed that in many cases the rate of electron injection from the excited state of the dye to the conduction band of metal oxide is slower in the complete cells than in the isolated systems investigated before [31–35]. Therefore, since the characteristic time scale is often longer than sub-ps, many internal deactivation processes present in the dye might efficiently compete with electron injection and lower the photovoltaic performance of DSSC. In particular, we have recently shown that lower photocurrent of D149 solar cell with ZnO nanoparticles compared to those with TiO_2 ones is directly related to the ultrafast processes occurring in the first 500 ps and that electron injection is slower for ZnO cells than for TiO_2 [36].

D149 dye has been studied in solution by femtosecond transient absorption [37] and femtosecond up-conversion techniques [38]. These studies revealed a formation of charge transfer (CT) state in polar solvent and solvent-dependent decay of CT state. Moreover, picosecond fluorescence studies with time-correlated single photon counting(TCSPC) technique indicated the occurrence of isomerization process [39] and the excited-state proton transfer process [40] as responsible for the enhanced deactivation rate. Femtosecond up-conversion of D149 on TiO_2 films showed a decay of the first singlet excited state with the averaged time constant of about 2 ps [12]. A different conclusion was drown from femtosecond transient absorption studies of D149 (with the coadsorbent) on TiO_2 and ZnO films in the visible range [17]. In that studies the

* Corresponding author. Tel.: +48 61 829 5011.
E-mail address: marziol@amu.edu.pl (M. Ziółek).

http://dx.doi.org/10.1016/j.dyepig.2014.10.008
0143-7208/

ultrafast (<250 fs) dynamics of electron injection was observed, similar for both metal oxides. However, our recent investigation of complete solar cell of D149 without coadsorbent revealed much worse electron injection efficiency in ZnO than TiO_2 cells [36]. Next, for the reference system of D149 on ZrO_2 films fs transient absorption studies showed similar ultrafast (<250 fs) formation of a cation–electron complex (explained by the interaction of the dye with the trap states below ZrO_2conduction band) [17]. On the contrary, TCSPC studies of D149/ZrO_2 films showed excited state deactivation on the time scale of hundreds of ps (fast component) and single ns (slow component), with increasing lifetime for higher coadsorbent (chenodeoxycholic acid, CDCA) content [39]. The mid-infrared measurements in complete D149 solar cells indicated the double exponential <300 fs to 30 ps electron injection kinetics [34]. However, for high intensity of the pulses the kinetics became significantly faster [34].The above results, often in contradiction to each other, clearly show the need of further investigation of the dynamics of fully organic dyes, like D149, in DSSC to understand which processes play a key role in functioning devices.

Therefore, in this contribution we have significantly extended our previous study to better understand the ultrafast processes occurring in D149 molecule attached to metal oxide nanoparticles in complete solar cells. For comparison, we have also measured D149 in solution and on metal oxide films in air. The main novel features of the present studies are the following: (i) the femtosecond transient absorption measurements in the visible spectral range (450–800 nm) were performed with a higher signal-to-noise ratio and longer time window up to 3 ns; (ii) new femtosecond transient absorption studies in near-infrared (NIR, 800–1500 nm) spectral range were used; (iii) studies with different amount of coadsorbent and different pump pulse intensity were performed. All of these enabled us to better explain the differences between the dynamics in TiO_2 and ZnO solar cells, to understand the discrepancy between previous ultrafast results of D149, and to discover new processes and transient states in D149 relevant for efficient electron injection. We believe that our studies enable better understanding the photophysics of indoline dyes interacting with inorganic nanomaterials. Moreover, the mechanisms we found should be relevant for many all-organic dyes with high extinction coefficient used in DSSC and our findings are important for improving solar cell efficiency in general.

2. Materials and methods

Indoline dye D149, chenodeoxycholic acid (CDCA) and Al_2O_3 nanoparticles (diameter <50 nm) were purchased from Sigma–Aldrich. ZnO (VP ZnO20) and TiO_2 (P25) nanoparticles were received from Evonik. The procedure of preparing the paste with oxide nanoparticles was the same for all the materials, with the exception of acetic acid content: it was 0 ml for ZnO, 0.5 ml for TiO_2 and 1 ml for Al_2O_3. Pastes were prepared as follows. First 3 g of nanoparticles powder was mixed with acetic acid, 20 ml of ethanol and left in ultrasonic bath for 3 h. Then another solution of 10 ml α-terpineol, 1.5 g of ethyl cellulose and 13.5 g of ethanol was prepared. Two solutions were mixed together and placed in ultrasonic bath for another hour. Afterwards they were stirred for 16 additional hours. Finally, the ethanol was removed with a rotary evaporator operating at 60 °C and the ready to use paste was obtained.

The films were deposited by doctor-blade technique on fluorine doped tin oxide (FTO) glass plates and heated at 450 °C (TiO_2 and Al_2O_3) or 420 °C (ZnO) for 60 min. Then, the films were immersed in a 0.2 mM solution of D149 with different concentrations of CDCA (0 mM, 0.2 mM and 2 mM) in acetonitrile (ACN): tert-butanol mixture (1:1) and kept at room temperature for about 1 h. The platinised counter electrode was obtained by spreading a Pt-based solution (Platisol T, Solaronix SA) on FTO glass and annealing at 450 °C. The transmission of Pt layered electrode varies from 75% at 450 nm to 90% at 800 nm with respect to pure FTO glass. To make a complete solar cell (the active area of 1.1 cm^2 was prepared), the counter electrode was assembled with thermal adhesive film (25 μm Surlyn, Meltronix, Solaronix SA) that acts as separator and sealing element. The cells were filled (by vacuum backfilling method) with a commercial liquid electrolyte (Iodolyte AN-50, Solaronix SA) containing the I^-/I_3^- redox couple ($[I_2] = 50$ mM) in ACN solution.

For ultrafast transient absorption experiments a commercial femtosecond broadband transient absorption spectrometer (Helios, Ultrafast Systems) was used in a single-beam configuration, with all reflective white light continuum generator and depolarizer in the pump beam to avoid influence of rotational dynamics. The femtosecond pulses were provided by Spectra Physics setup consisting of MaiTai SP oscillator, Spitfire Ace amplifier (pumped by Empower laser) and Topas Prime wavelength convertor (optical parametric amplifier). The pump pulses were at 555 nm and the IRF (pump-probe cross correlation function) was 250–300 fs (FWHM). The typical pump pulse energy was 500 nJ, corresponding to energy density of about 1 mJ/cm^2. In some experiments 200 nJ and 2 μJ pulses were also used. The probe light continuum was generated in sapphire or YAG-type crystal. All the spectra analyzed were corrected for chirp of white light continuum. The transient absorption measurements were performed in the spectral ranges 450–800 nm (VIS) and 800–1500 (NIR) and in the time range of up to 3 ns.

The transient absorption spectra are the combination of positive signals originating from the absorption of transient species, negative signals due to ground state depopulation (corresponding spectrally to steady-state absorption bands), and negative signals due to stimulated emission from the excited state (occurring for the wavelength for which steady-state emission is present). To analyze the transient absorption dynamics in more detail, we used a global approach. The global analysis of the data was done using Surface Explorer program (Ultrafast Systems) which fits multi-exponential function (convoluted with IRF of our setup, FWHM between 250 and 300 fs) to the kinetic vectors of selected number of singular values and reproduces the spectra of the amplitudes associated with the time components. As a result, the characteristic time constants are revealed for the whole spectral range investigated (in our case combined VIS and NIR regions), and the wavelength-dependent amplitudes associated with these time constants are obtained (also called decay associated difference spectra). The positive value of the amplitude at certain wavelength indicates a change towards less positive (or more negative) transient absorption signals at this wavelength, while a negative value of amplitude indicates opposite. In all figures presenting transient absorption spectra the time zero (maximum of IRF) is set at 0 ps, while for all figures showing kinetic traces it is shifted to 1 psin order to present the time axis in logarithmic scale.

Analysis at particular probe wavelength was done by fitting stretched exponential function (convoluted with IRF) to the transient absorption signals. The function is defined as:

$$A\left(t\right) = A_0\, e^{-(t/\tau)^{\beta}}. \tag{1}$$

This function contains two parameters: the characteristic time τ and the dispersion parameter β ($0<\beta<1$, lower β values mean more stretched decay, extending the decay time scale). The average time of the process described by function (1) was calculated as:

$$\tau_{AVG} = \frac{\tau}{\beta}\Gamma\left(\frac{1}{\beta}\right). \tag{2}$$

We should note that sometimes the averaged time constant from stretched exponential fit given by Eq. (2) is not a good parameter to compare when the dispersion parameter differs too much (for example, for one sample $\beta > 0.7$ and another $\beta < 0.4$, in the latter case the averaged lifetime is too long). Therefore, in all tables in which the decay parameters are shown, a half-decay time is also given.

The time-resolved emission measurements in the picosecond time window were performed using a time correlated single photon counting technique (TCSPC) [41]. The measurements were carried out at the magic angle with the pump wavelength of 425 nm. The analysis was done by fitting stretched exponential function (Eqs. (1)–(2)) convoluted with the IRF of the setup (measured by light scattering of the same samples at pump wavelength) to the fluorescence decays at the wavelength around 660 nm (corresponding to the maximum of emission band). The steady-state UV–visible absorption spectra were measured with a UV-VIS-550 (Jasco) spectrophotometer. An M101 potentiostat with FRA32M module (Autolab) was used to measure electrochemical impedance spectra (10 mV perturbation in the 10^{-1}–10^{6} Hz range) in the dark and at open circuit, and the data sets were analyzed with Nova 1.10 (Autolab) software. The potentiostat was also used to measure current–voltage (J–V) curves under the irradiation of white light LED lamp. The distance between the LED lamp source and the solar cell was adjusted to give a photocurrent corresponding to that obtained in the control experiment for the same samples at 1 Sun conditions using a solar simulator (Sun 2000 class A, Abet Technologies, equipped with an AM 1.5 G filter). The morphology of the nanoparticle films was analyzed using a Scanning Electron Microscope (JEOL 7001 TTLS).

3. Results and discussion

3.1. Photovoltaic performance, steady-state spectroscopy and time-resolved emission studies

Table 1 collects the most important parameters of the cells prepared with TiO_2, ZnO and reference Al_2O_3 films (all sensitized with 0.2 mM D149 and 2 mM CDCA). The trend is similar to that reported by us previously for the D149 cells prepared without coadsorbent and with different TiO_2 and ZnO pastes [36]. The relatively low short circuit current of D149/TiO_2 cell ($J_{sc} = 4$ mA/cm^2 under conditions similar to those of AM1.5 (1 Sun) is mainly due to limited absorbance of the sensitized metal oxide layer (absorbance of about 1 at the maximum of D149 band) required in our time-resolved studies. D149/TiO_2 cells prepared without CDCA showed about 50% higher absorption and 20% higher J_{SC}.

Table 1
Photovoltaic parameters of the samples using 2 mM CDCA: amplitude (A_{max}) and wavelength (λ_{max}) corresponding to the maximum of the D149 absorption band, thickness of the mesoporous layer (d), open circuit voltage (V_{OC}), short circuit current density (J_{SC}) for 1 Sun conditions, fill factor (FF), number of absorbed photons (N_{ph}) calculated as previously [36], and J_{SC}/N_{ph} ratio.

Sample:	TiO_2	ZnO	Al_2O_3
A_{max}	1.0	0.3	1.2
λ_{max}, nm[a]	516	505	507
d, μm	3	1	3.5
V_{OC}, mV	630	600	200
J_{SC}, mA/cm^2	4.0	0.80 → 0.15[b]	0.05
FF	0.45[c]	0.60	–
N_{ph}, x10^{16}, s^{-1}cm^{-2}	6.06	3.18	6.86
J_{SC}/N_{ph}, x 10^{-16}, mA/s	0.66	0.25 → 0.05[b]	0.01

[a] Films in air.
[b] Decrease after 1 day.
[c] $FF = 0.55$ after series resistance correction.

The absorbance of the dye in ZnO cells is smaller than that of TiO_2. The initial photocurrent per number of absorbed photons (J_{sc}/N_p in Table 1) of D149/ZnO cells is 2–3 times lower than that of D149/TiO_2 cells. However, the photocurrent drops rapidly. 2 h after preparation it is only 30–40% of its initial value, and after 1 day it is only 20%. On the contrary, for D149/TiO_2 cells we observed a drop of the photocurrent of the same magnitude that in D149/ZnO after 2 weeks instead of 2 h. Due to the measurements duration, all time-resolved studies of complete D149/ZnO cells presented in next sections correspond to the conditions at which the relative photocurrent (per absorbed photons) is about 10 times smaller than that of TiO_2 samples. We have checked that D149 dye molecules can be dissolved from ZnO film as indicated before [42]. As shown in Fig. S1A (in the supporting information, SI), the absorption of D149/ZnO film decreases by about 40% after 20 h immersion in neat acetonitrile (similar for the films sensitized with and without CDCA addition). This might be the reason for quick lowering of the photocurrent in D149/ZnO cells. However, as will be revealed in next sections, the explanation is probably more complex.

Finally, the reference D149/Al_2O_3 cells show some small, but nonzero photocurrent (Table 1, about 1% to that of D149/TiO_2 cells), in similar fashion as found by us previously [36]. The origin of this photocurrent might be either due to the presence of very deep trap states below conduction band in alumina or due to the presence of trace impurities in commercial Al_2O_3 nanopowder. We have checked that the Al_2O_3 cells without D149 dye give no photocurrent at all, so it is certainly due to the electrons transferred from the excited dyes.

Exemplary SEM pictures of the surface of metal oxide layers and their cross-sections are presented in Fig. S2. They show that the thickness of the TiO_2 layer (3 μm) is about 3 times larger than that of ZnO (1 μm). We also used electrochemical impedance spectroscopy to characterize the cells and metal oxide layers. The results are shown in supporting information (Table S1 and Fig. S3–S5). The charge recombination in ZnO layer is slightly slower than that of TiO_2 for the corresponding bias voltages, but for both materials the relative diffusion length (the ratio of the diffusion length over the nanoparticle layer thickness) is always larger than 3, indicating good collection efficiency.

The effect of adding coadsorbent to the sensitizing solution on the steady-state absorption spectra is shown in Fig. 1A and Fig. S1B. The absorption band of D149 is shifted slightly to the blue when more CDCA is added, in accordance to the previous report [43]. For D149/TiO_2 film the maximum changes from 523 nm (no CDCA) to 516 nm (2 mM CDCA), while for D149/Al_2O_3 the corresponding change is from 521 nm to 507 nm. The small absorption changes lie in contrast with our recent studies of NIR absorbing dye HY103 [44]. In that case, even upon small addition of CDCA (0.2 mM), a drastic change in steady-state absorption spectra was observed due to the diminish of H-aggregates band (on the short-wavelength side of monomer's band). However, as will be shown in next sections, the impact of CDCA addition on the transient kinetics of D149 is much higher than it could be expected from the steady-state spectra.

We performed TCSPC experiments to check the effect of coadsorbent for D149/TiO_2 cells (Fig. 1B). As can be seen, upon the addition of CDCA the fluorescence decay becomes longer with the average decay times equal to 50 ps for the samples without CDCA, 90 ps for 0.2 mM CDCA and 170 ps for 2 mM CDCA. It indicates the possible competing quenching process which will be further explored in next sections. We also compared the fluorescence decays for cells with different metal oxides for moderate CDCA concentration (0.2 mM CDCA, Fig. S6). The trend is similar to that reported by us previously for the cells without CDCA [36]. The

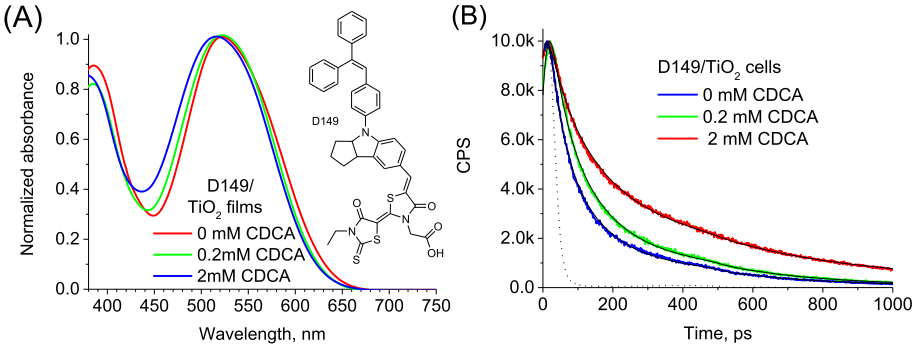

Fig. 1. (A) Steady-state absorption spectra of D149/TiO_2 films for different concentrations of coadsorbent (CDCA) in the sensitizing solution. The inset shows the structure of D149 molecule. (B) Fluorescence decays obtained in TCSPC experiment at 660 nm after 425 nm excitation for D149/TiO_2 cells with different concentration of coadsorbent. The black line shows the best fit using stretched exponential function with parameters given in Table S2A.

averaged decay time is 200 ps for D149/Al_2O_3, 170 ps for D149/ZnO and 90 ps for D149/TiO_2 cells. The electron injection yield calculated on the basis of such values is equal to 55% for D149/TiO_2 cells and much smaller (15%) for D149/ZnO cells.

3.2. Transient absorption studies

3.2.1. D149 in solution and D149/Al_2O_3 cells

Transient absorption studies of D149 in solution are presented in the supporting information (text and Fig. S7). The spectra of all fitted components in global analysis are presented in Fig. 2A. The most important information for further studies of DSSC are the following. Two excited states of D149 with different spectral characteristics are identified. The decay of the first one, LE state, with time constant 0.4 ps is accompanied by the positive amplitudes with maximum around 720 nm in the VIS range and positive amplitudes for wavelength <1100 nm and >1450 nm in NIR range. The decay of subsequent and relaxed CT state is connected with the positive amplitudes with maxima around 600 nm and 1370 nm, and is clearly mono-exponential (time constant 420 ps). The absorption from both states has a significant contribution in the NIR range (in fact their extinction coefficients in NIR are comparable to those in VIS range). In studies of some DSSC it is assumed that only radical cations and electrons in metal oxide conduction band give contributions to the signals in NIR and, thus, the rise of such signals can be directly related to the electron injection dynamics. Our transient absorption results in NIR clearly show that it is not in the case of D149 dye, and probably in the whole family of indoline dyes, because the strong transient absorption signals from the excited states are also present in this range.

For D149/Al_2O_3 reference cells (with 0.2 mM CDCA) we do not expect significant contribution of electron injection, although the nonzero photocurrent mentioned above indicates the possible small contribution of a charge separation process. The global analysis (Fig. 2B) brings three time components of $\tau_1 = 0.2$ ps, $\tau_2 = 3.0$ ps and $\tau_3 = 65$ ps as well as the fourth component ($\tau_4 > 1$ ns) which represents the residual signal, constant in the time window of our setup. Interestingly, the complex wavelength-dependent spectra indicate that the decay of the dye attached to alumina cannot be simply explained by the decay of one excited state, even if the vibrational relaxation and cooling are taken into account. On the contrary, the amplitude spectra of all three components are positive in the region above 600 nm, up to 1500 nm, and we can observe two distinguished spectral features which relative contribution changes for different time constants. For short time constants ($\tau_1 = 0.2$ ps and $\tau_2 = 3.0$ ps) a dominant feature is one with a maximum around 720 nm, while for the longer component ($\tau_3 = 65$ ps) the main band is that with a maximum around 600 nm. The spectral similarity in VIS region to those observed in solution (and discussed above) suggests that we also observe LE and CT states for D149/Al_2O_3 cells. It should be noted that the decays of LE and subsequent CT states are not mono-exponential and they both contribute to the amplitude spectra of more than one component from the global fit. In particular, the band at 720 nm (LE) is present not only in τ_1 spectra, but also in those of τ_2 and τ_3 components (but with decreasing contribution). Similarly, the CT band at 600 nm is observed not only in τ_3 spectra, but also in shorter τ_2 spectra.

A decay of LE in NIR is manifested as positive amplitudes of $\tau_1 = 0.2$ ps component for wavelengths<1100 nm and >1300 nm, similar to those of D149 in solution. As for CT state, which is abundant in amplitude spectra of longer components (τ_2 and τ_3), its band in NIR is significantly spectrally broader than that observed in solution. The possible explanation is that the nature of CT state is slightly different when the molecules are chemically bonded to semiconductor surface. Probably, the LUMO orbital extends more towards the metal oxide structure (in this case Al atoms) and the absorption spectra in NIR are especially sensitive to such changes [45]. The CT state might be therefore more like exciplex nature, rather than bound radical cation–electron complex, maintaining its electronically excited state character with respect to the dye. The residual component (τ_4) with positive maxima at around 630 nm and 1100 nm (and negative ground state depopulation maximizing at around 500 nm, Fig. 2B) clearly shows that some portion of the excited dyes do not relax to the ground state but, most probably, inject electrons to deep trap states in alumina, possibly due to the presence of impurities or surface defects. Therefore, we might assign the residual spectra to the bounded complex between dye and trapped electrons. Eventually, in some portion of these complexes, further charge separation might occur giving rise to the small photocurrent observed in D149/Al_2O_3 cells (as found in the previous section).

3.2.2. D149/TiO_2 and D149/ZnO cells

For D149/TiO_2 cells with 0.2 mM CDCA (Fig. 2A and S8A-B) the time constants of globally fitted components ($\tau_1 = 0.2$ ps, $\tau_2 = 3.5$ ps, $\tau_3 = 70$ ps and $\tau_4 > 1$ns) do not differ too much from those obtained for D149/Al_2O_3 cells, which is consistent with our previous report for the cells without CDCA [36]. However, more detailed investigation shows that it is rather the coincidence due to spreading of the dynamics over many time scales in both systems, while the main difference lies in the relative amplitudes between the components of both cells. Indeed, the final, residual signal (amplitude of τ_4 component) is much higher than that found in

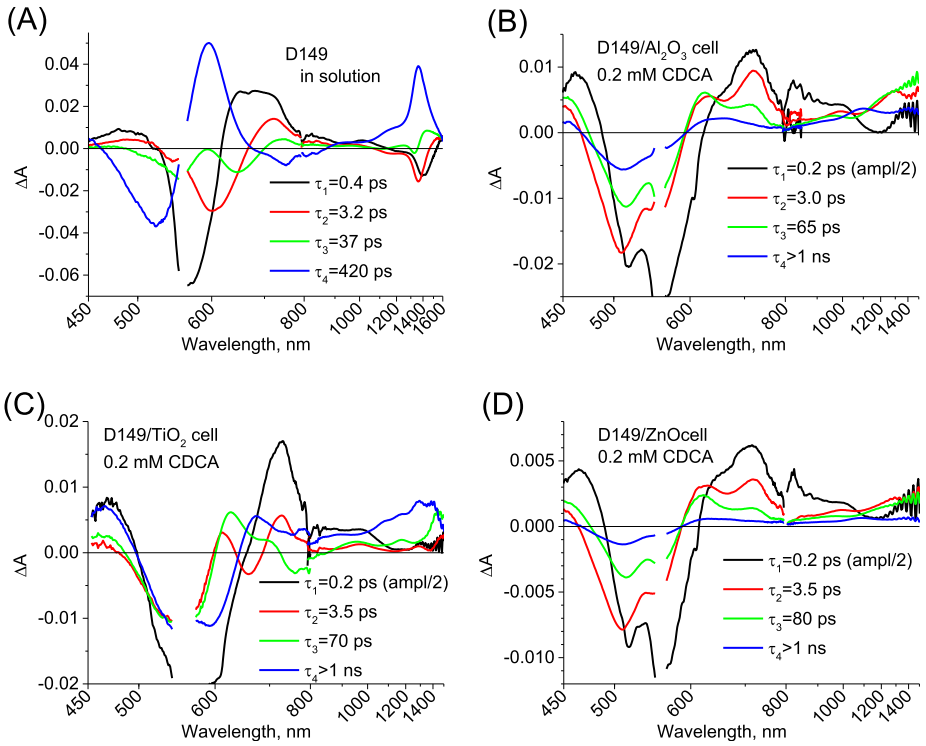

Fig. 2. The wavelength-dependent amplitudes of the components with time constants given in the inset obtained by multi-exponential global fit for (A) D149 in ACN:tert-butanol (1:1) solution (B) D149/Al_2O_3, (C) D149/TiO_2, and (D) D149/ZnO cells. In (B)–(D) cases the concentration of CDCA was 0.2 mM and the amplitude of the fastest component ($\tau_1 = 0.2$ ps) is decreased by 2 because the fitting procedure makes it larger due to the convolution with comparable IRF (FWHM = 0.25–0.3 ps).

D149/Al_2O_3 cells (see also Fig. 2B). Moreover, the spectrum of this component is also different: the negative signal extends further into long-wavelength range (up to 630 nm, while for D149/Al_2O_3 it was up to 580 nm), the maximum in the visible range is shifted to 670 nm, and the signal in NIR contains dominant features for wavelengths around 1300 nm. All of these differences can be explained by the fact that for D149/TiO_2 cells with efficient electron injection a large concentration of D149 radical cation is present, the electrons in titania conduction band contribute to the signal (especially in NIR range), and there is a transient Stark shift signal originating from the electric field created by the electrons in the semiconductor. The latter is responsible for the transient features having the shape of first derivative of steady-state absorption band, which results in the apparent shift of the negative transient absorption band towards the red [18]. The differences in the VIS range are similar to those previously reported in transient absorption studies of D149 in films [17]. In these studies the transient Stark shift was observed for D149/TiO_2 and D149/ZnO samples, while it was absent for D149/ZrO_2 samples.

The efficient creation of D149 radical cation is also revealed in the shape of the amplitudes of $\tau_2 = 3.5$ ps and $\tau_3 = 70$ ps components. Unlike their analogues in D149/Al_2O_3 cells, they contain negative regions for $\lambda > 600$ nm, which indicate a rise of the signal due to higher extinction coefficient of the D149 radical cation than that of CT state for these wavelengths. For the $\tau_2 = 3.5$ ps component a rise occurs in the range 630–680 nm, while for $\tau_3 = 70$ ps a rise is present in the range 720–850 nm. In the latter case the rise might be also due to the changes in the radical cation spectrum due to the hole transfer within its structure [46].

Besides the clear formation of radical cation from CT state, our present data also indicates partial, faster electron injection from LE state. This state decays much faster in D149/TiO_2 cell than in the reference D149/Al_2O_3 cell. Although the time components from global analysis are similar, the feature at 730 nm (characteristic for LE state) contributes mainly to the spectra of$\tau_1 = 0.2$ ps and, a little bit, to $\tau_2 = 3.5$ ps components for D149/TiO_2 sample (Fig. 2C), while for D149/Al_2O_3 sample the contribution is comparable for $\tau_1 = 0.2$ ps and $\tau_2 = 3.0$ ps spectra, and it is also present in $\tau_3 = 65$ ps spectra (Fig. 2B). This difference can also be directly visualized when the transient kinetics at 730 nm are compared. This is presented in Fig. 3A together with the stretched exponential fit, whose results are shown in Table 2A. The average decay time is about 10 times faster for D149/TiO_2 samples (0.7 ps) than for D149/Al_2O_3 ones (8.0 ps).

Next, we present the global fit results of D149/ZnO cells with 0.2 mM CDCA (Fig. 2D and S8C-D). Also in line with our previous report [36], the spectra and time constants are similar to those found for reference D149/Al_2O_3 cells, consistent with the poor photocurrent in D149/ZnO cells. The decay of LE state in D149/ZnO cell is only slightly faster than that in D149/Al_2O_3 and much longer than for D149/TiO_2 cells (kinetics at 730 nm, Fig. 3A), indicating a significantly slower injection for ZnO cells. There is no indication of transient Stark signal, and the residual signal in both VIS and NIR ranges is very small ($\tau_4 > 1$ ns component), with the spectral shape more similar to that of D149/Al_2O_3 (possible bounded complex between dye and trapped electrons) than D149/TiO_2 cells (separated radical cations and electrons in conduction band).

One of the explanations for poor performance of D149/ZnO cells might be the before-mentioned detachment of dyes from ZnO surface in the presence of solvent. However, we do not observe any indication of free dyes in electrolyte, whose presence should appear as mono-exponential long decay. On the contrary, the decay of transient absorption signal in D149/ZnO cells for wavelengths corresponding to the CT state is even faster than in two other cells with high dispersion parameter (see, for example, kinetics at 630 nm presented in Fig. 3B), pointing out the enhanced excited

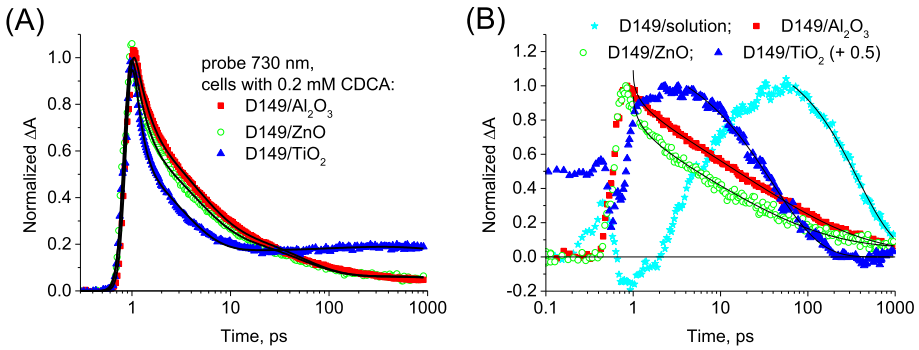

Fig. 3. Kinetic traces of transient absorption measured for the indicated samples (D149 in solution and different cells with 0.2 mM CDCA) at (A) 730 nm and (B) 630 nm. The pump pulse was 0.5 μJ at 555 nm. The black line shows best fit with parameters given in Table 2. In (B) the fit was without convolution with IRF and the kinetics for D149/TiO_2 were shifted upwards by 0.5 to better show the differences in the time scale of the decay. The time zero is shifted to 1 ps in order to present the time axis in logarithmic scale.

state self-quenching in D149/ZnO cells. We will come back to these interesting features below.

3.2.3. *Light intensity and coadsorbent concentration dependence*

Now we will present the effect of different excitation pulse energy and CDCA concentration for the complete cells. Fig. 4A presents transient absorption kinetics probed at 1300 nm with different intensities of pump pulse for D149/TiO_2 cells without CDCA. As shown before, both excited LE and CT states of D149 probably contribute to the transient absorption signal at this wavelength. The parameters of the fitted decay are collected in Table 3. As can be seen, a strong dependence on excitation intensity is observed for both the decay time and the residual signal (3 ns after excitation). The latter signal corresponds to the combined absorption of D149 radical cations and electrons in the semiconductor, so its relative amplitude (with respect to the initial signal) is proportional to the efficiency of electron injection (assuming that the initial signal does not contain significant contribution from electron injection products, which means that electron injection from LE state in times below 100 fs can be neglected). Increasing the energy of the pump pulse 10 times (from 0.2 μJ to 2 μJ, corresponding to the change in excitation fluence from 0.4 mJ/cm^2 to 4 mJ/cm^2) results in about a 10-fold decrease in characteristic time of stretched exponential decay and decrease of its dispersion parameter (from 0.6 to 0.3, making the decay more stretched). Moreover, the electron injection efficiency drops 2 times (residual signal decreases from 52% to 27%). The most likely explanation is that a significant contribution of excited state self-quenching occurs, with singlet–singlet annihilation mechanism being the most probably explanation. Indeed, this process, competing with electron injection, was proposed to be responsible for deactivation of dyes in DSSC systems before [47–49]. Since it is a second order process with respect to the concentration of excited species, its rate is proportional to the excitation intensity, which is being observed by us in the current studies (Fig. S9B). To confirm this hypothesis we repeated the same experiments for reference D149/Al_2O_3 cells without CDCA. Indeed, the results presented in Fig. 4B and Table 3B indicate a similar behavior in a system where dye molecules are densely packed on nanoparticles and there is no significant injection (as mentioned above).

Table 2
Values of the parameters of the best stretched exponential function given by Eqs. (1)–(2) fitted to the transient absorption signals of different cells with 0.2 mM CDCA. The pump pulse energy was 0.5 μJ and probe wavelength was 730 nm (A) and 630 nm (B). Last column presents half-decays of the kinetics.

Sample:	τ/ps	β	τ_{AVG}/ps	$\tau_{1/2}$/ps
(A)				
D149/TiO_2 cell	0.32	0.47	0.72	0.4
D149/ZnO cell	0.83	0.32	5.8	1.5
D149/Al_2O_3 cell	1.29	0.33	8.0	2.2
(B)				
D149/ACN + t-but solution	400	1.00	400	300
D149/TiO_2 cell	40	0.78	46	30
D149/ZnO cell	10	0.33	62	5
D149/Al_2O_3 cell	25	0.34	139	17

Furthermore, the rate of excited state self-quenching of dye molecules is the rate of the energy transfer from one singlet to another singlet state, so it should depend on the average distance between the molecules too. This is exactly confirmed in our experiments with D149/TiO_2 cells with different CDCA concentration. Representative kinetics at 1300 nm are presented in Fig. 5A together with the fitted function of parameters collected in Table 4A. The trend with increasing CDCA concentration (thus increasing the averaged distance between D149 dyes) is the same as that of decreasing pump pulse intensity: longer decay and higher electron injection yield. For the reference D149/Al_2O_3 cells with 2 mM CDCA the transient absorption measurements with different excitation energies were also made (Fig. S9A and Table S3). The decay is longer than that for the samples without CDCA for the corresponding energies (compare Figs. S9A and 5B). The dependence on the energy is smaller, but it is still present, which means that even for relatively high CDCA concentration the self-quenching is still present to some extent. The interaction of closely packed D149 molecules forming some type of aggregates is probably reflected in steady-state absorption spectra as slight red-shift of absorption band with smaller CDCA concentration (Fig. 1A and S1B).

On the contrary, the transient absorption kinetics for D149/ZnO cells exhibit a small dependence on the CDCA concentration (Fig. 5B and Table 4B). The residual signal is small (about 5% of that of the initial amplitude at 1300 nm) in line with the poor photocurrent of the ZnO cells. The characteristic decay time constants are shorter and the dispersion parameters are smaller than those for D149/TiO_2 and D149/Al_2O_3 cells. This is in line with faster quenching shown in Fig. 3B (kinetics at 630 nm) as discussed in the previous section. Again, we do not observe any contribution of the free dyes in solution (that have longer lifetimes). Our explanation is that D149 molecules are easily detached from ZnO surface in the presence of liquid electrolyte in complete cells (see also Fig. S1A). However, they do not stay free in the electrolyte but they attach again to the places close to other D149 molecules forming a type of aggregations, probably enhanced by ionic shells around other dyes. In such conditions they suffer from huge self-quenching and do not inject electrons efficiently. Therefore, irrespectively of the initial

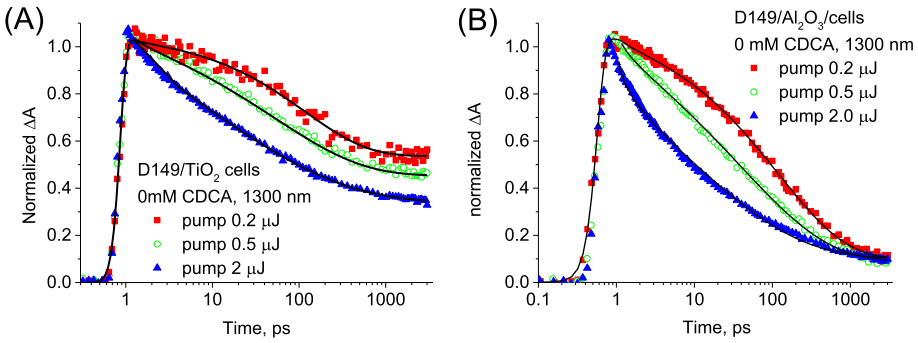

Fig. 4. Kinetic traces of transient absorption measured at 1300 nm for (A) D149/TiO_2 and (B) D149/Al_2O_3 cells at the indicated pump pulse energies (at 555 nm). The cells were without coadsorbent. The black line shows best fit with parameters given in Table 3. The time zero is shifted to 1 ps in order to present the time axis in logarithmic scale.

distribution of D149 molecules and coadsorbent presence, after immersion in electrolyte a new distribution is being formed, and quickly appearing D149 aggregates are responsible for the fast drop of photocurrent in D149/ZnO cells. We think that this is a second reason for the bad performance of DSSC made of ZnO semiconductor and D149 dye, apart from the slower electron injection reported by us before [36].

Finally, we measured NIR transient absorption for old D149/TiO_2 cells (with 2 mM CDCA). Two weeks after preparation J_{SC} of such cells drop from 4.0 mA/cm^2 to 1.7 mA/cm^2. As can be seen in Fig. 5A and Table 4, the residual signal at 1300 nm is about 3.5 times smaller (in accordance with the decrease of the photocurrent) and the decay is faster than that of the fresh sample. It is also supported by the global analysis in NIR range shown in Fig. S10: for the fresh cell the fastest time component ($\tau_1 = 0.6$ ps) has positive amplitudes for $\lambda < 1100$ nm and $\lambda > 1400$ nm while for the old cell the amplitudes are also positive between 1100 and 1400 nm (indicating self-quenching of LE and/or CT state). Similarly, the contribution of the decay of the second fastest component ($\tau_2 = 14$ ps) is larger for older sample than for the fresh one. So, most probably, the decreased photovoltaic performance of aging D149/TiO_2 cells is connected with the same mechanism as for ZnO cells: electrolyte assisted formation of dye aggregates and enhanced excited state self-quenching. However, in the case of TiO_2 such process occurs much slower than for ZnO (weeks instead of hours), due to the stronger chemical interaction of the D149 dye with TiO_2 surface.

3.2.4. D149 in films

In this section, we would like to present control transient absorption experiments conducted on fresh TiO_2, ZnO and Al_2O_3 films sensitized with D149 dye. All samples were studied in air within 1 h after preparation, so the effect of water absorption was minimized.

Table 3
Values of the parameters of the best stretched exponential function given by Eqs. (1)–(2) fitted to the transient absorption signals of (A) D149/TiO_2 cells and (B) D149/Al_2O_3 cells (both without CDCA and for varying pump pulse energies). The probe wavelength was at 1300 nm. Last two columns present half-decays of the kinetics and ratio of residual signal amplitude to the initial amplitude.

Pump energy/μJ	τ/ps	β	τ_{AVG}/ps	$\tau_{1/2}$/ps	Residual signal/%
(A)					
0.2	121	0.61	179	59	52
0.5	56	0.43	152	44	41
2	14	0.29	140	11	27
(B)					
0.2	124	0.51	243	68	9.5
0.5	45	0.39	156	22	8.0
2	11.6	0.32	83	5	9.3

The global analysis results in combined VIS-NIR range for D149/TiO_2 film (0.2 mM CDCA) are presented in Fig. 6A. The differences from the complete D149/TiO_2 solar cell (analogous spectra in Fig. 2C) are probably due to significantly faster electron injection in films (see the discussion in the supporting information).

A very interesting feature can be observed in NIR transient absorption of D149 on different metal oxides (samples with 2 mM of CDCA). The representative kinetics shown in Fig. 6B (for the probing wavelength 1300 nm) indicates that the amplitude of residual signal is very similar for D149/TiO_2 and D149/ZnO films, and much higher than that of D149/Al_2O_3 films. Moreover, the global analysis in NIR range (Fig. S11B-D) for these samples confirms the similarity of the spectra of residual component for TiO_2 and ZnO films, both in the relative amplitude and in the shape (with the increasing contribution of free electrons in the conduction band with increasing wavelength). It is unlike the results in complete cells for which the spectra of D149/ZnO cells with poor photocurrent were rather similar to those of reference D149/Al_2O_3 cells. This interesting feature further supports our explanation that the fast decrease in J_{SC} in D149/ZnO cells is due to the detachment of dyes and the formation of aggregates under the presence of electrolyte. Indeed, in ZnO films (where electrolyte is not present) the electron injection yield is much higher.

3.2.5. Relation to DSSC working conditions

There is a huge difference in the excitation intensity in the time-resolved setups used in our experiments: the pump pulse fluence is only about 30 μJ/cm^2 in TCSPC, while it is about 1 mJ/cm^2 in transient absorption, greatly enhancing singlet–singlet annihilation process in the latter case. This might explain why in the transient absorption experiments the CT state of D149/ZnO cells decays faster than that of D149/TiO_2 (e.g. Figs. 3B and 5) while in TCSPC experiment it is the opposite (Fig. S6). Faster decay of D149 excited state under higher pump pulse intensity implies similarly faster apparent electron injection. This might be the reason why the rise of absorption conduction band electrons probed in mid-IR range (studies in complete cells but on sapphire substrate) was observed to be faster for sufficiently high excitation fluence [34]. Moreover, the excited self-quenching process might also explain the differences between previous results of D149 obtained by TCSPC and pump-probe techniques described in the introduction.

It is always an important question how the conditions in laser spectroscopy studies with pulsed excitation correlate with those under continuous sunlight irradiation. In our transient absorption experiment the excitation with 0.5 μJ pump (1 mJ/cm^2) corresponds to the injection of about 20 electrons per nanoparticle. It is similar to the typical value of 10 electrons per nanoparticle under normal working conditions of DSSC [3]. So, from the point of view

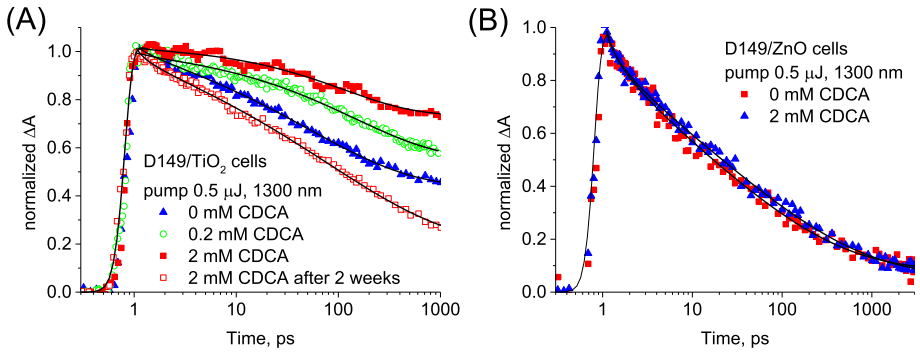

Fig. 5. Kinetic traces of transient absorption measured at 1300 nm for (A) D149/TiO_2 and (B) D149/ZnO cells with the indicated concentration of coadsorbent. The pump pulse was 0.5 μJ at 555 nm. The black line shows best fit with parameters given in Table 4. The time zero is shifted to 1 ps in order to present the time axis in logarithmic scale.

Table 4
Values of the parameters of the best stretched exponential function given by Eqs. (1)–(2) fitted to the transient absorption signals of (A) D149/TiO_2 cells, (B) D149/ZnO cells (both for different CDCA content) and (C) D149 films on different metal oxides (with 2 mM CDCA). The pump pulse energy was 0.5 μJ and probe wavelength was at 1300 nm. Last two columns presents half-decays of the kinetics and ratio of residual signal amplitude to the initial amplitude.

Cell:	τ/ps	β	τ_{AVG}/ps	$\tau_{1/2}$/ps	Residual signal/%
(A)					
no CDCA	56	0.43	152	58	41
0.2 mM CDCA	147	0.53	270	66	56
2 mM CDCA	117	0.63	164	72	72
2 mM CDCA[a]	87	0.37	370	46	19
(B)					
no CDCA	14	0.27	200	8	7
2 mM CDCA	21	0.27	350	11	5
(C)					
D149/TiO_2 film	26.5	0.41	82	12	34
D149/ZnO film	9.4	0.29	102	5.5	30
D149/Al_2O_3 film	85	0.37	355	38	3

[a] After 2 weeks, J_{SC} decreased from 4.0 to 1.7 mA/cm^2.

of number of electrons per particle, the photo behaviour observed in transient absorption is probably more relevant than that found in TCSPC experiments. However, under photostationary conditions the concentration of the transient species is proportional to its lifetime [50], so the concentration of excited dyes per particle is several orders of magnitude smaller than concentration of electrons. Therefore, from the point of view of excited state self-quenching, the conditions of TCSPC experiments are more relevant to 1 Sun.

Assuming average 20 nm diameter of TiO_2 nanoparticles and 50% porosity of the layer, the calculated dye coverage of D149/TiO_2 cells with 2 mM CDCA is 8×10^{13} cm^{-2}, which corresponds to the average distance between the dyes equal to 1.1 nm. When 20 photons are absorbed per nanoparticle in transient absorption experiment (with 0.5 μJ), the average distance between the excited molecules is 4.0 nm, which lies in the limit of efficient resonant energy transfer (<10 nm).

On the other hand, we would like to stress out a direct correlation between the relative amplitude of the residual transient absorption signal (high for fresh D149/TiO_2 cells and low for D149/ZnO and old D149/TiO_2 cells) and the photocurrent measured in exactly the same solar cells. This indicates that this process is still responsible for the real performance of solar cell made with indoline dyes, although the rates of self-quenching under operating conditions of DSSC might be smaller than those observed in transient absorption experiments.

4. Conclusions

Complete DSSC made of popular indoline dye D149, TiO_2 or ZnO substrates and commercial iodide-based liquid electrolyte were investigated by time-resolved laser spectroscopy techniques as well as steady-state absorption, scanning electron microscopy, current–voltage and electrochemical impedance measurements. Combining better sensitivity of transient absorption setup and an extended spectral range towards NIR we were able to reveal significant details about the ultrafast dynamics not reported before. We have identified locally excited and charge transfer states of the dye participating in electron injection process, and found a

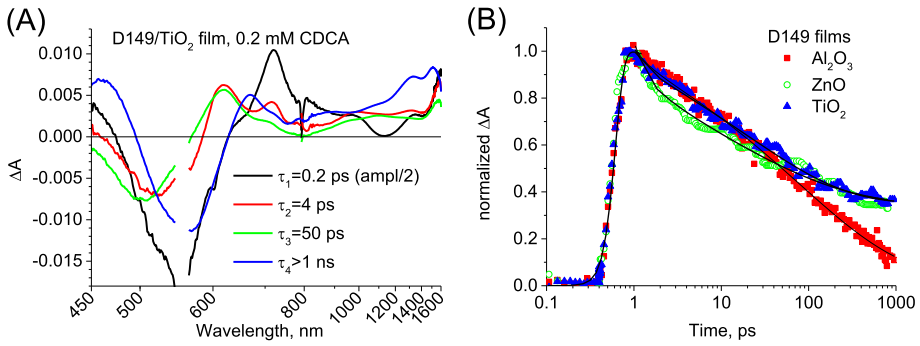

Fig. 6. (A) The wavelength-dependent amplitudes of the components with time constants given in the inset obtained by multi-exponential global fit for D149/TiO_2 with 0.2 mM of CDCA. (B) Kinetic traces of transient absorption measured at 1300 nm for D149 (with 2 mM of CDCA) films on the indicated concentration metal oxides. The pump pulse was 0.5 μJ at 555 nm. The black line shows best fit with parameters given in Table 4C. The time zero is shifted to 1 ps in order to present the time axis in logarithmic scale.

dependence on the observed dynamics on the coadsorbent concentration and excitation energy density. We proposed the explanation for the lower performance with sample aging by electrolyte-induced dye rearrangement and aggregate formation.

We would like to point out that it is commonly assumed that faster decay of the excited state of the dye attached to metal oxide particles in DSSC means faster electron injection and thus better quantum yield of the injection process. However, the situation can be more complex and even opposite. Our studies show that faster decays observed for ZnO cell in comparison to TiO_2 cells are due to enhanced self-quenching of the dyes and in fact the electron injection efficiency is lower in the former than in the latter.

Acknowledgements

This work was supported by NCN (National Science Centre, Poland) under project 2012/05/B/ST3/03284. J. S. is a holder of a scholarship funded within Human Capital Operational Programme, European Social Fund. Dr Maciej Zalas (Faculty of Chemistry, Adam Mickiewicz University in Poznan) is kindly acknowledged for the help in preparation of metal oxide pastes and making the control measurements with solar simulator. We also thank Joanna Bludzinska (Evonik Degussa International AG) for providing us the VP ZnO 20 and P25 nanoparticles. TCSPC studies were made at the Center for Ultrafast Laser Spectroscopy at the A. Mickiewicz University in Poznan, Poland. JAA thanks Abengoa Research for support under collaboration agreement and Junta de Andalucía for funding under grant FQM1851.

Appendix A. Supplementary data

Supplementary data related to this article can be found at http://dx.doi.org/10.1016/j.dyepig.2014.10.008.

References

[1] Horiuchi T, Miura H, Sumioka K, Uchida S. High efficiency of dye-sensitized solar cells based on metal-free indoline dyes. J Am Chem Soc 2004;126:12218–9.
[2] O'Regan B, Grätzel M. A low-cost, high-efficiency solar cell based on dye-sensitized colloidal TiO2 films. Nature 1991;353:737–40.
[3] Hagfeldt A, Boschloo G, Sun L, Kloo L, Pettersson H. Dye-sensitized solar cells. Chem Rev 2010;110:6595–663.
[4] Ito S, Zakeeruddin SM, Humphry-Baker R, Liska P, Charvet R, Comte P, et al. High-efficiency organic-dye-sensitized solar cells controlled by nanocrystalline-TiO_2 electrode thickness. Adv Mater 2006;18:1202–5.
[5] Joly D, Pelleja L, Narbey S, Oswald F, Chiron J, Clifford JN, et al. A robust organic dye for dye sensitized solar cells based on Iodine/Iodide electrolytes combining high efficiency and outstanding stability. Sci Rep 2014;4:4033.
[6] Yang J, Ganesan P, Teuscher J, Moehl T, Kim YJ, Yi C, et al. Influence of the donor size in D–pi–A organic dyes for dye-sensitized solar cells. J Am Chem Soc 2014;136:5722–30.
[7] Yu Q, Wang Y, Yi Z, Zu N, Zhang J, Zhang M, et al. High-efficiency dye-sensitized solar cells: the influence of lithium ions on exciton dissociation, charge recombination, and surface states. ACS Nano 2010;4(10):6032–8.
[8] Mathew S, Yella A, Gao P, Humphry-Baker R, Curchod BFE, Ashari-Astani N, et al. Dye-sensitized solar cells with 13% efficiency achieved through the molecular engineering of porphyrin sensitizers. Nat Chem 2014;6:242–7.
[9] Howie WH, Claeyssens F, Miura H, Peter LM. Characterization of solid-state dye-sensitized solar cells utilizing high absorption coefficient metal-free organic dyes. J Am Chem Soc 2008;130:1367–75.
[10] Snaith HJ, Petrozza A, Ito S, Miura H, Grätzel M. Charge generation and photovoltaic operation of solid-state dye-sensitized solar cells incorporating a high extinction coefficient indolene-based sensitizer. Adv Func Mater 2009;19:1810–8.
[11] Guillén E, Eneko Azaceta E, Peter LM, Zukal A, Tena-Zaera R, Anta JA. ZnO solar cells with an indoline sensitizer: a comparison between nanoparticulate films and electrodeposited nanowire arrays. Energy Environ Sci 2011;4:3400–7.
[12] Fakis M, Stathatos E, Tsigaridas G, Giannetas V, Persephonis P. Femtosecond decay and electron Transfer dynamics of the organic sensitizer D149 and photovoltaic performance in quasi-solid-state dye-sensitized solar cells. J Phys Chem C 2011;115:13429–37.
[13] Guillén E, Peter L, Anta JA. Electron transport and recombination in ZnO-based dye-sensitized solar cells. J Phys Chem C 2011;115:22622–32.
[14] Cappel UB, Feldt SM, Schöneboom J, Hagfeldt A, Boschloo G. The influence of local electric Fields on photoinduced absorption in dye-sensitized solar cells. J Am Chem Soc 2010;132:9096–101.
[15] Fattori A, Peter LM, Wang H, Miura H, Marken F. Fast hole surface conduction observed for indoline sensitizer dyes immobilized at fluorine-doped tin oxide-TiO_2 surfaces. J Phys Chem C 2010;114:11822–8.
[16] Pastore M, De Angelis F. Computational modeling of stark effects in organic dye-sensitized TiO2 heterointerfaces. J Phys Chem Lett 2011;2:1261–7.
[17] Oum K, Lohse PW, Flender O, Klein JR, Scholz M, Lenzer T, et al. Ultrafast dynamics of the indoline dye D149 on electrodeposited ZnO and sintered ZrO2 and TiO2 thin films. Phys Chem Chem Phys 2012;14:15429–37.
[18] Burdziński G, Karolczak J, Ziółek M. Dynamics of local stark effect observed for a complete D149 dye-sensitized solar cell. Phys Chem Chem Phys 2013;15:3889–96.
[19] Wu Y, Marszalek M, Zakeeruddin SM, Zhang Q, Tian H, Grätzel M, et al. High-conversion-efficiency organic dye-sensitized solar cells: molecular engineering on D–A–pi-A featured organic indoline dyes. Energy Environ Sci 2012;5:8261–72.
[20] Anderson NA, Lian T. Ultrafast electron transfer at the molecule-semiconductor nanoparticle interface. Ann Rev Phys Chem 2005;56:491–519.
[21] Wenger B, Grätzel M, Moser JE. Rationale for kinetic heterogeneity of ultrafast light-induced electron Transfer from Ru(II) complex sensitizers to nanocrystalline TiO2. J Am Chem Soc 2005;127:12150–1.
[22] Katoh R, Furube F, Barzykin AV, Arakawa H, Tachiya M. Kinetics and mechanism of electron injection and charge recombination in dye-sensitized nanocrystalline semiconductors. Coord Chem Rev 2004;248:1195–213.
[23] Tachibana Y, Haque SA, Mercer IP, Moser JE, Klug DR, Durrant JR. Modulation of the rate of electron injection in dye-sensitized nanocrystalline TiO2 films by externally applied bias. J Phys Chem B 2001;105:7424–31.
[24] Asbury J, Hao E, Wang Y, Ghosh HN, Lian T. Ultrafast electron Transfer dynamics from molecular adsorbates to semiconductor nanocrystalline thin films. J Phys Chem B 2001;105:4545–57.
[25] Katoh R, Furube A. Electron injection efficiency in dye-sensitized solar cells. J Photochem Photobiol C Photochem Rev 2014;20:1–16.
[26] Benkö G, Kallioinen J, Korppi-Tommola JEI, Yartsev AP, Sundström V. Photoinduced ultrafast dye-to-semiconductor electron injection from nonthermalized and thermalized donor states. J Am Chem Soc 2002;124:489–93.
[27] Ramakrishna G, Singh AK, Ghosh HN, Palit DK. Dynamics of interfacial electron transfer from photoexcited quinizarin (Qz) into the conduction band of TiO2 and surface states of ZrO2 nanoparticles. J Phys Chem B 2004;108:4775–83.
[28] Ye S, Kathiravan A, Hayashi H, Tong Y, Infahsaeng Y, Chabera P, et al. Role of adsorption structures of Zn-porphyrin on TiO2 in dye-sensitized solar cells studied by sum frequency generation vibrational spectroscopy and ultrafast spectroscopy. J Phys Chem C 2013;117:6066–80.
[29] Moser JE. Dynamics of interfacial and surface electron transfer processes. In: Kalyanasundaram K, editor. Dye-sensitized solar cells. 2010 ed. Lausanne: EPFL Press; 2010. p. 403–56.
[30] Thorsmølle VK, Wenger B, Teuscher J, Bauer C, Moser JE. Dynamics of photoinduced interfacial electron transfer and charge transport in dye-sensitized mesoscopic semiconductors. Chimia 2007;61:631–4.
[31] Koops SE, O'Regan BC, Barnes PRF, Durrant JR. Parameters influencing the efficiency of electron injection in dye-sensitized solar cells. J Am Chem Soc 2009;131:4808–18.
[32] Ziółek M, Martín C, Cohen B, Garcia H, Douhal A. Virtues and vices of an organic dye and Ti-doped MCM-41 based dye-sensitized solar cells. J Phys Chem C 2011;115:23642–50.
[33] Giannouli M, Fakis M. Interfacial electron transfer dynamics and photovoltaic performance of TiO2 and ZnO solar cells sensitized with Coumarin 343. J Photochem Photobiol A: Chem 2011;226(1):42–50.
[34] Juozapavicius M, Kaucikas M, van Thor JJ, O'Regan BC. Observation of multi-exponential Pico- to subnanosecond electron injection in optimized dye-sensitized solar cells with visible-pump mid-infrared-probe transient absorption spectroscopy. J Phys Chem C 2013;117:116–23.
[35] Juozapavicius M, Kaucikas M, Dimitrov SD, Barnes PRF, van Thor JJ, O'Regan BC. Evidence for "Slow" electron injection in commercially relevant dye-sensitized solar cells by vis–NIR and IR Pump–Probe spectroscopy. J Phys Chem C 2013;117:25317–24.
[36] Sobuś J, Burdziński G, Karolczak J, Idígoras J, Anta JA, Ziołek M. Comparison of TiO2 and ZnO solar cells sensitized with an indoline dye: time-resolved laser spectroscopy studies of partial charge separation processes. Langmuir 2014;30:2505–12.
[37] Lohse PW, Kuhnt J, Druzhinin SI, Scholz M, Ekimova M, Oekermann T, et al. Ultrafast photoinduced relaxation dynamics of the indoline dye D149 in organic solvents. Phys Chem Chem Phys 2011;13:19632–40.
[38] Fakis M, Hrobárik P, Stathatos E, Giannetas V, Persephonis P. A time resolved fluorescence and quantum chemical study of the solar cell sensitizer D149. Dyes Pigments 2013;96:304–12.
[39] El-Zohry A, Orthaber A, Zietz B. Isomerization and aggregation of the solar cell dye D149. J Phys Chem C 2012;116:26144–53.
[40] El-Zohry A, Zietz B. Concentration and solvent effects on the excited state dynamics of the solar cell dye D149: the special role of protons. J Phys Chem C 2013;117:6544–53.

[41] Wróżowa T, Ciesielska B, Komar D, Karolczak J, Maciejewski A, Kubicki J. Measurements of picosecond lifetimes by time correlated single photon counting method: the effect of the refraction index of the solvent on the instrument response function. Rev Sci Instrum 2004;75(10):3107–21.
[42] Guillén E, Idígoras J, Berger T, Anta JA, Fernández-Lorenzo C, Alcántara R, et al. ZnO-based dye solar cell with pure ionic-liquid electrolyte and organic sensitizer: the relevance of the dye–oxide interaction in an ionic-liquid medium. Phys Chem Chem Phys 2011;13:207–13.
[43] Sakuragi Y, Wang XF, Miura H, Matsui M, Yoshida T. Aggregation of indoline dyes as sensitizers for ZnO solar cells. J Photochem Photobiol A Chem 2010;216:1–7.
[44] Zioł ek M, Karolczak J, Zalas M, Hao Y, Tian H, Douhal A. Aggregation and electrolyte composition effects on the efficiency of dye-sensitized solar cells. A case of a near-infrared absorbing dye for Tandem cells. J Phys Chem C 2014;118:194–205.
[45] Furube A, Katoh R, Yoshihara T, Hara K, Murata S, Arakawa H, et al. Ultrafast direct and indirect electron-injection processes in a photoexcited dye-sensitized nanocrystalline zinc oxide film: the importance of exciplex intermediates at the surface. J Phys Chem B 2004;108:12583–92.
[46] Oum K, Flender O, Lohse PW, Scholz M, Hagfeldt A, Boschloo G, et al. Electron and hole transfer dynamics of a triarylamine-based dye with peripheral hole acceptors on TiO2 in the absence and presence of solvent. Phys Chem Chem Phys 2014;16:8019–29.
[47] de Miguel G, Zioł ek M, Zitnan M, Organero JA, Pandey SS, Hayase S, et al. Photophysics of H- and j-aggregates of indole-based squaraines in solid state. J Phys Chem C 2012;116:9379–89.
[48] de Miguel G, Marchena M, Zioł ek M, Pandey SS, Hayase S, Douhal A. Femto- to millisecond photophysical characterization of indole-based squaraines adsorbed on TiO2 nanoparticle thin films. J Phys Chem C 2012;116:12137–48.
[49] de Miguel G, Marchena M, Cohen B, Pandey SS, Hayase S, Douhal A. Relating the photodynamics of squaraine-Based DSSCs to the molecular structure of the sensitizers and to the presence of Additives. J Phys Chem C 2012;116:22157–68.
[50] Zioł ek M, Burdziński G, Douhal A. Long-living structures of photochromic salicylaldehyde azine: polarity and viscosity effects from nanoseconds to hours. Photochem Photobiol Sci 2012;11:1389–400.

Supporting Information

for

Transient states and the role of excited state self-quenching of indoline dyes in complete dye-sensitized solar cells.

Jan Sobuś [1,2], Jerzy Karolczak [2,3], Dariusz Komar [2], Juan A. Anta [4] and Marcin Ziółek [2]*

[1]*NanoBioMedical Centre,Adam Mickiewicz University, Umultowska 85, 61-614 Poznan, Poland.*

[2]*Quantum Electronics Laboratory, Faculty of Physics,Adam Mickiewicz University, Umultowska 85, 61-614 Poznan, Poland.*

[3]*Center for Ultrafast Laser Spectroscopy, Adam Mickiewicz University, Umultowska 85, 61-614, Poznan, Poland.*

[4]*Departamento de SistemasFísicos , Químicos y Naturales , Área de QuímicaFísica , Universidad Pablo de Olavide, Ctra. Utrera, km 1,E-41013 Sevilla, Spain*

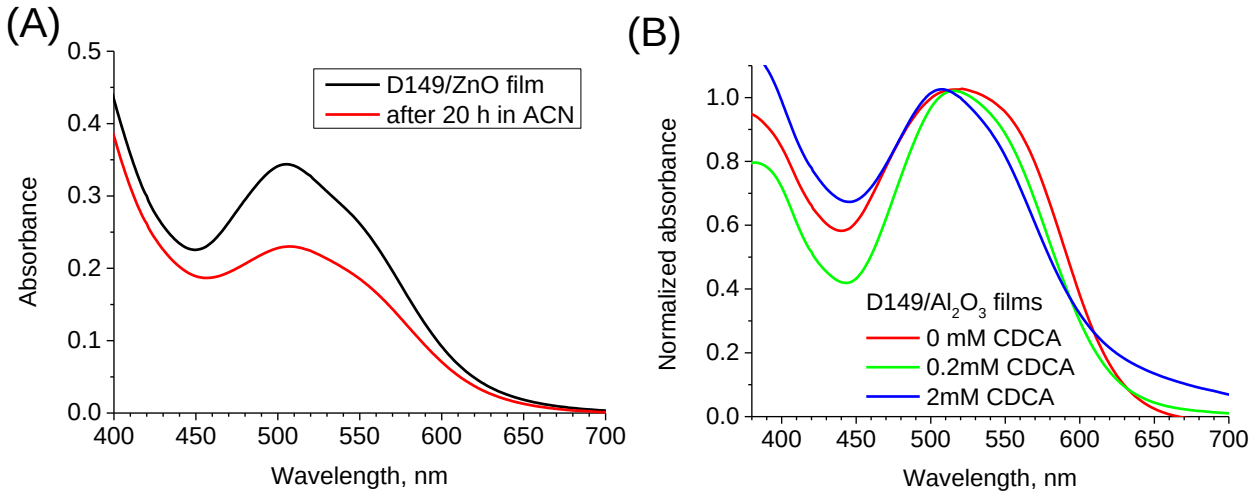

Figure S1. (A) Steady-state absorption spectra of D149/ZnO film measured just after sensitization and after 20 hours immersion in pure ACN. (B) Steady-state absorption spectra of$D149/Al_2O_3$ films for different concentrations of coadsorbent (CDCA) in the sensitizing solution.

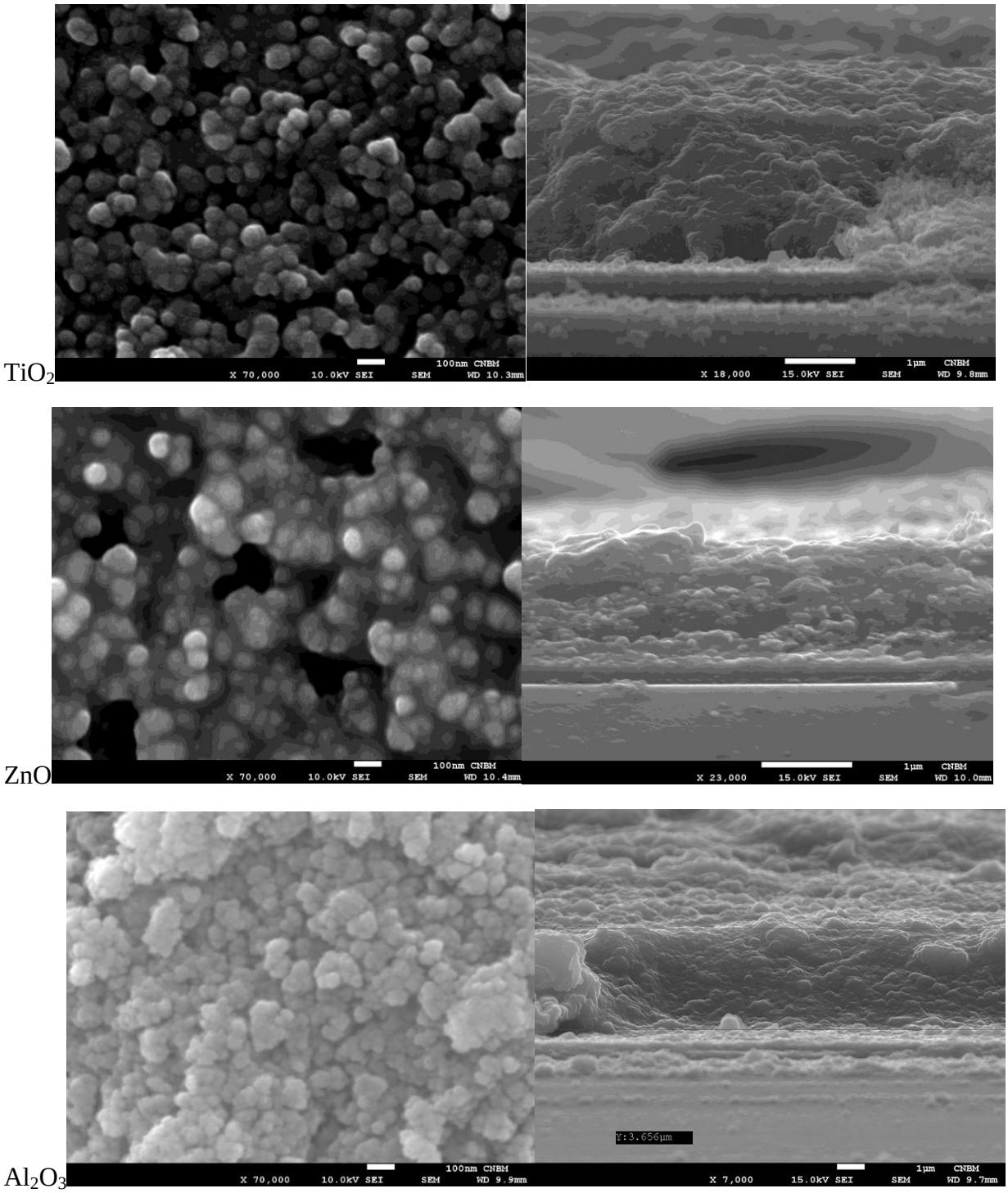

Figure S2. Top view (right) and cross-section (left) pictures obtained by SEM for the mesoporous layers of TiO_2, ZnO and Al_2O_3. The scale bars are indicated on each picture.

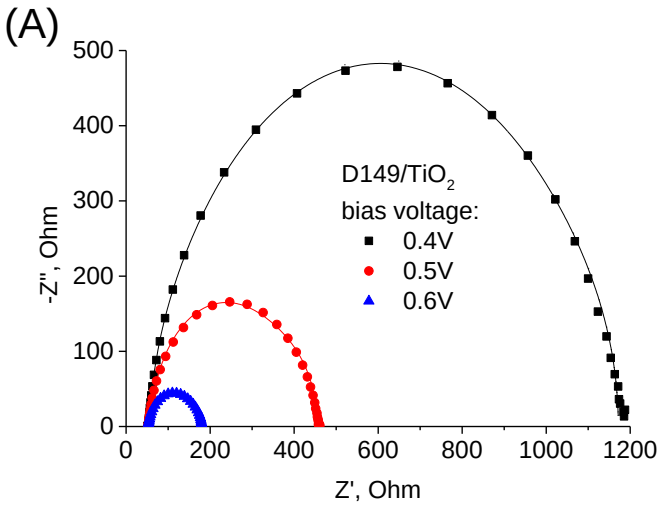

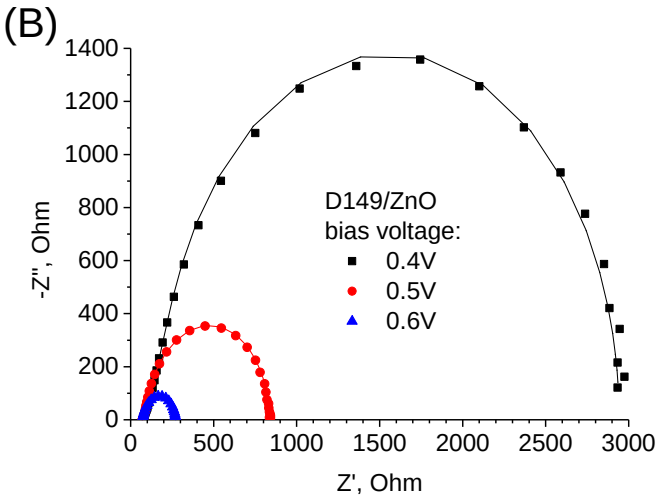

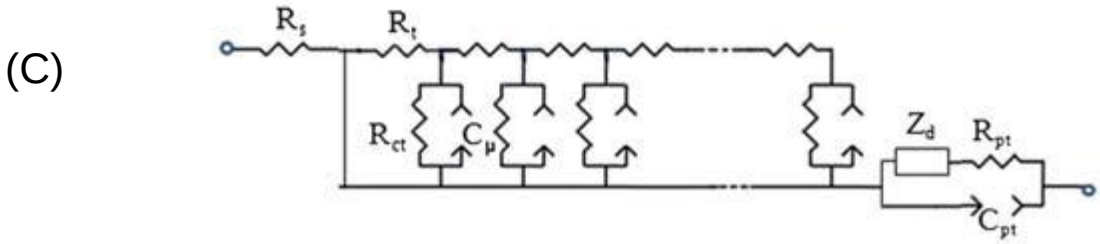

Figure S3. Nyquist plots of (A) D149/TiO_2 and (B) D149/ZnO cells obtained from electrochemical impedance measurements in the dark at the indicated bias voltages. The solid line shows the best fit obtained for the equivalent circuit for DSSC presented in figure (C) with the parameters given Table S1.

Table S1. Parameters of the fits of the equivalent circuit (presented in Figure S3C) and potentials applied from 0 V to 0.6 V for (A) D149/TiO_2 and (B) D149/ZnO solar cells: transport resistance (R_t), charge transfer resistance (R_{ct}) and chemical capacitance (C_μ) in the oxide-electrolyte interface. The table also presents calculated electron recombination lifetime ($R_{ct}\ C_\mu$) and relative electron diffusion length ($(R_{ct}/R_t)^{1/2}$). The exemplary fits are shown in Figure S3A-B.

(A) TiO_2

Voltage, V	R_t, Ω	R_{ct}, Ω	C_μ, μF	$R_{ct}\ C_\mu$, ms	$(R_{ct}/R_t)^{1/2}$
0	--	34 000	13.4	455	--
0.1	--	21 600	12.9	280	--
0.2	--	9 100	13.4	122	--
0.3	--	3 100	14.5	45	--
0.35	--	1 400	15.3	22	--
0.4	--	700	15.1	11	--
0.425	--	510	15.3	7.8	--
0.45	3.3	390	14.4	5.6	10.9
0.475	1.3	260	16.0	4.2	13.9
0.5	10.0	180	15.0	2.8	4.3
0.525	4.8	120	15.6	1.9	5.1
0.55	3.4	82	19.9	1.6	4.9
0.575	2.6	55	25.8	1.4	4.6
0.6	2.3	33	29.7	1.0	3.8

(B) ZnO

Voltage, V	R_t, Ω	R_{ct}, Ω	C_μ, μF	$R_{ct}\ C_\mu$, ms	$(R_{ct}/R_t)^{1/2}$
0	--	285 000	8	2 210	--
0.1	--	88 300	9	810	--
0.2	--	30 000	17	510	--
0.3	--	18 200	25	450	--
0.35	--	8 400	28	240	--
0.4	22	2 360	31	74	10.4
0.425	4.5	1 600	33	53	18.9
0.45	2.5	980	35	34	19.8
0.475	7.5	780	35	27	10.2
0.5	21	590	36	21	5.3
0.525	9.5	375	38	14	6.3
0.55	9.3	246	40	9.8	5.1
0.575	10.3	207	39	8.0	4.5
0.6	12	145	39	5.7	3.5

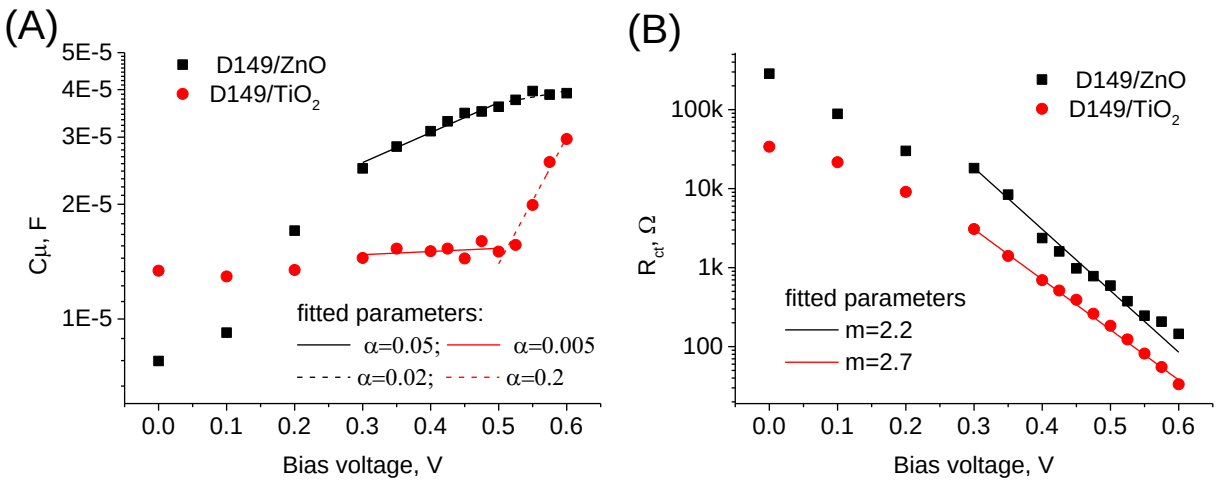

Figure S4. Plots of (A) chemical capacitance and (B) charge transfer resistance as a function of applied bias voltage obtained from electrochemical impedance measurements by fitting equivalent circuit for DSSC (Figure S3C). The lines show the fit of the following functions with the indicated fitted parameters: (A) $C_\mu = C_0 \exp(\alpha\, Ve/kT)$, where α represents trap energy distribution below the conduction band; solid line shows the fit in 0.3-0.5 V, while dashed lines the fit in 0.5-0.6 V range; (B) $R_{ct} = R_0 \exp(-Ve/mkT)$, where m represents the empirical estimation of thereaction order in sublinear recombination kinetics; the fit is in the range 0.3-0.6 V.

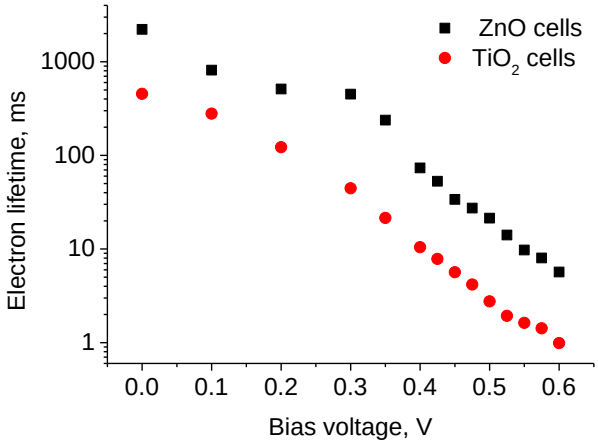

Figure S5. Calculated electron recombination lifetime (product $R_{ct}\ C_\mu$, see Table S1) obtained from electrochemical impedance measurements for D149/TiO_2 and D149/ZnO cells.

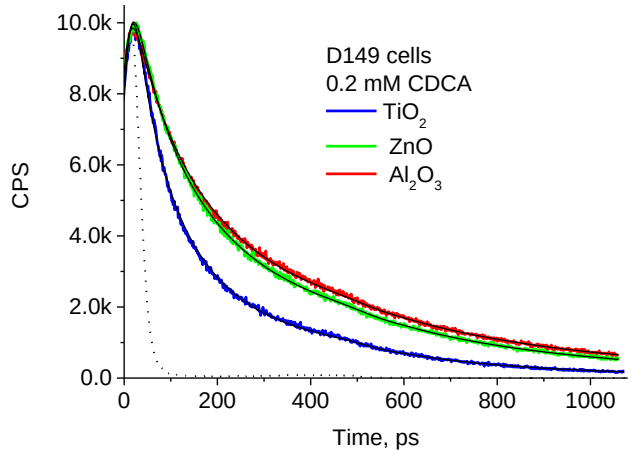

Figure S6.(A) Fluorescence decays obtained in TCSPC experiment at 660 nm after 425 nm excitation for D149 cells with different metal oxides. The concentration of coadsorbent was 0.2 mM. The black line shows the best fit using stretched exponential function with parameters given in Table S2B.

Table S2. Parameters of the best fit (χ^2<1.5) of stretched exponential function (eq. 1, convoluted with IRF) fitted to fluorescence kinetics obtained TCSPC experiment for D149 cells for pump wavelength 425nm, and emission wavelength 660 nm. τ_{AVG}represents the averaged lifetime given by eq. 2. (A) D149/TiO_2 cells for different CDCA concentration; (B) cells of D149 with different metal oxides for 0.2 mM CDCA.

(A)

D149/TiO_2 cell:	τ / ps	β	τ_{AVG} / ps
no CDCA	17	0.42	50
0.2mM CDCA	48	0.52	90
2mM CDCA	88	0.51	170

(B)

Metal oxide:	τ / ps	β	τ_{AVG} / ps
TiO_2	48	0.52	90
ZnO	106	0.57	171
Al_2O_3	127	0.58	200

Transient absorption studies of D149 in solution

Fs-ps transient absorption results of D149 measured in solution (ACN:t-butanol mixture used for sensitization) are shown in Figures 2A and S7A-B. Figure S7A presents the transient spectra in 450-800 nm range (VIS) for the selected time delays between pump and probe pulses, while figure S7B shows the analogous results in 800-1600 nm domain (NIR). Such studies in different solvent have been analyzed in detail before [1]. In addition, recently we showed the results of D149 in dichloromethane (DCM) solution [2], all in VIS range. The new contribution in our present study is using the NIR range, which, according to our knowledge, has not been reported before. Therefore, we will shortly discuss the main findings about how to associate the NIR results with those in VIS range.

Just after excitation, we observe the main positive band with maximum around 720 nm and another band in NIR range, with the maximum between 1400 and 1500 nm (Figure S7B). We assign them to the initially, locally excited (LE) state of the dye. The negative features in the shorter wavelength range are related to ground state depopulation (maximum around 540 nm) and stimulated emission (maximum around 640). Then, an evolution of the transient spectra occurs on the sub-ps and single ps time scale, which is accompanied by the red shift of the stimulated emission and by the changes in the shape of positive signals, both in VIS and NIR domains. In line with previous reports on D149, we assign this dynamic to the solvation process of the molecule with large dipole moment change upon excitation in polar environment[1, 3]. As a result of this evolution, a relaxed excited state stabilized by solvent molecules occurs, with the transient absorption maxima at around 600 nm and 1370 nm. We will refer to this state as relaxed charge transfer (CT) state, in accordance to the nomenclature used in solvation dynamic studies[4, 5]. The CT state finally decays to the ground state on hundreds of ps time scale, accompanied by the simultaneous decrease of its positive band and decay of the ground state depopulation and stimulated emission negative bands. As it was investigated for D149 before, the lifetime changes with solvent polarity and hydrogen bonding ability, and is probably accelerated due to the twisting structural changes[1, 3, 6].

Four components are sufficient to obtain a good fit of our present data, which is one more than we used in the previously reported results of D149 in DCM with worse S/N ratio[2]. The spectra of all fitted components are presented in Figure 2A. Three faster time components (0.4 ps, 3.2 ps and 37 ps) should be assigned to the decay of LE state and the solvation process. The longest time constant of 420 ps represents the lifetime of relaxed CT state.

Transient absorption studies of D149/TiO_2 film

Figure S11A shows the transient spectra in VIS range for the selected time delays between pump and probe pulses for D149/TiO_2 film sensitized with 0.2 mM of coadsorbent. The corresponding global analysis results in combined VIS-NIR range are presented in Figure 6A, which can be compared with the analogous spectra in Figure 2C for the complete D149/TiO_2 solar cell. Similarly to those results, we assign the amplitude maximum of τ_1=0.2 ps component at 715 nm to LE state decay, the maximum of τ_2=4 ps and τ_3=50 ps components at 620 nm to CT state decay and the τ_4>1 ns component to D149 radical cation spectrum (with maximum at 670 nm). Both LE and CT states are probably present despite of lack of polar solvent (electrolyte). We have recently observed and discussed the possibility of occurrence of LE and CT states in solids for the case of triphenylamine dyes deactivation on titania and alumina films[7].

The main difference between the results in films and in complete cell is that in the case of films the negative amplitudes for τ_2 component (in the range 630-680 nm) and τ_3 component (in the range 720-850 nm) are not present. We assigned these negative features observed in the complete cells to the rise of transient absorption band of D149 radical cation (see previous sections). We think that the probable explanation is that in the case of TiO_2 films the effective electron injection is faster and a greater population of radical cation is already created from LE state. A supporting finding comes from TCSPC experiments for D149 on TiO_2 films, in which we observed a fluorescence decaying roughly within the IRF of the setup (results not shown), significantly faster than in complete cells shown for example in Figure 1B.

Our studies should be compared to those reported recently by another group for the same dye measured on electrodeposited ZnO and sintered TiO_2 films in air by transient absorption in VIS range[8]. Their results are similar to our results in a film, but they explained the observed ultrafast dynamics as electron injection with time constants below 250 fs and delayed build-up of Stark shift (with 20 ps time constant), probably caused by the presence of a radical-electron bound pair as an intermediate. In our opinion, in the view of our additional results in NIR range (where no Stark shift signal is present) and of complete cells (with clear signal rises in certain spectral regions), the intermediate state should be rather assigned to CT state, and the slower part of electron injection occurs also from this state.

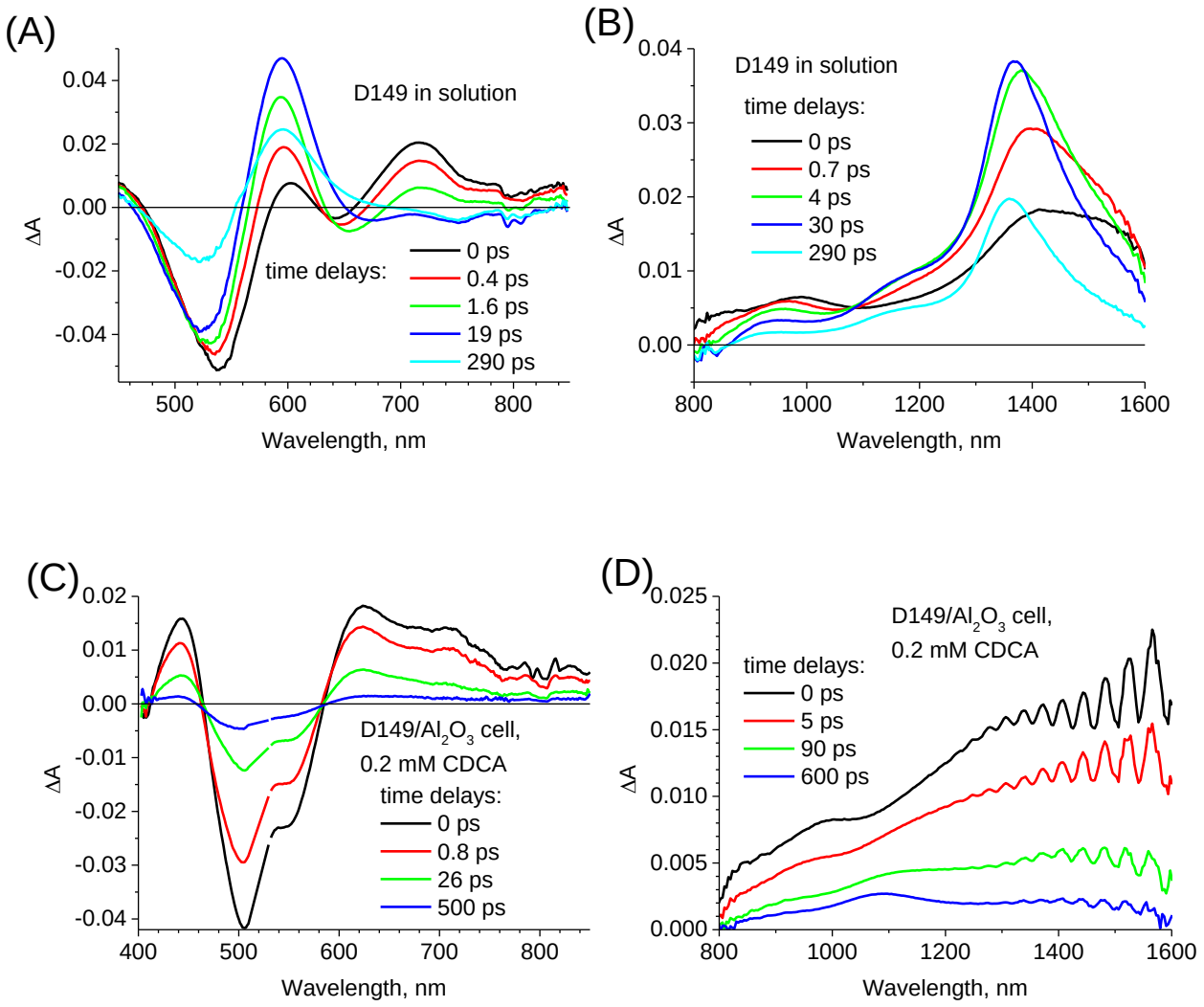

Figure S7. Transient absorption spectra of (A, B) D149 in ACN:tert-butanol (1:1) solution, and (C, D) D149/Al_2O_3 cell (with 0.2mM CDCA) for selected, indicated time delays between the pump (at 555 nm, 0.5 μJ) and probe pulses.

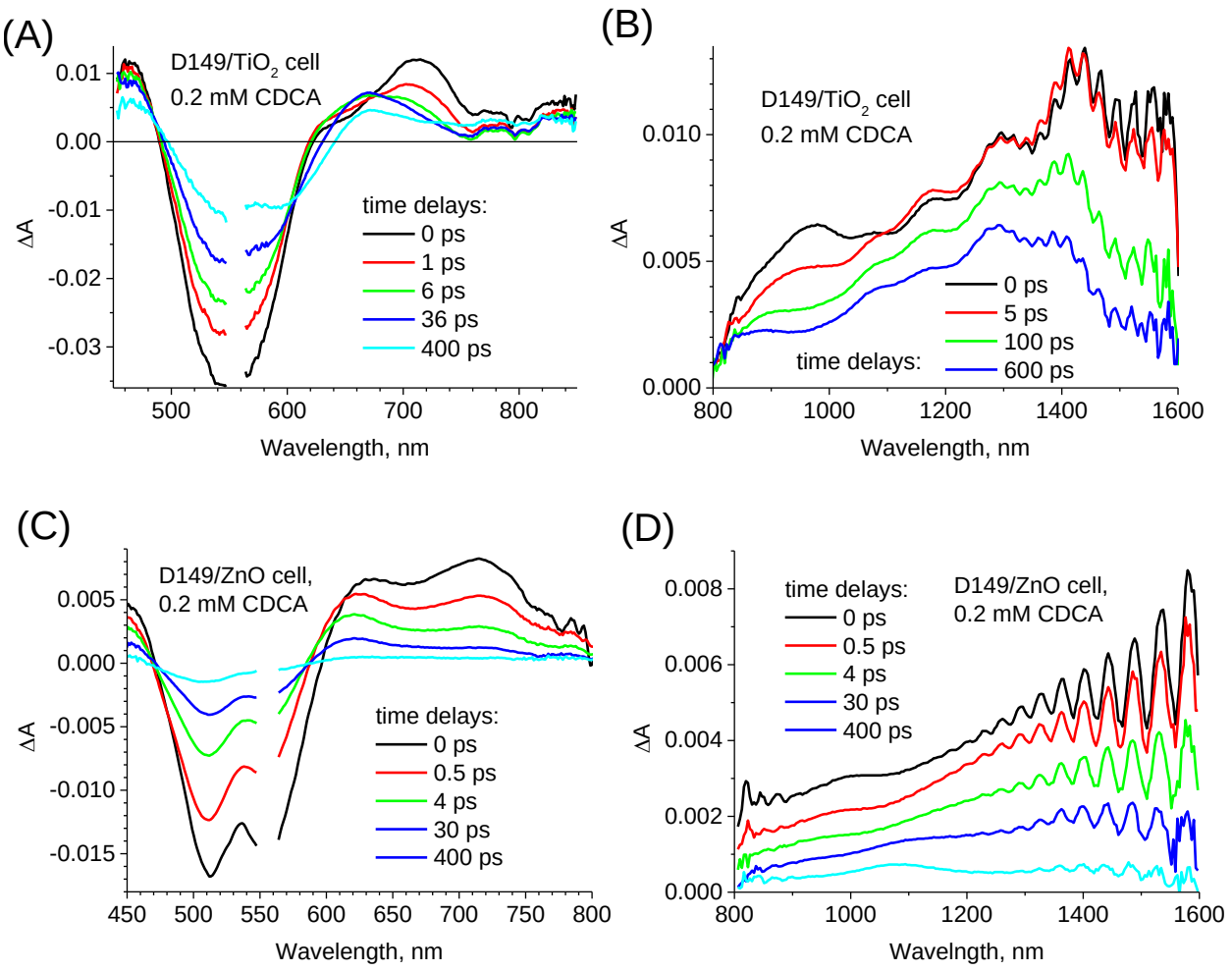

Figure S8. Transient absorption spectra of (A, B) D149/TiO_2, and (C, D) D149/ZnO cells(both with 0.2mM CDCA) for selected, indicated time delays between the pump (at 555 nm, 0.5 μJ) and probe pulses.

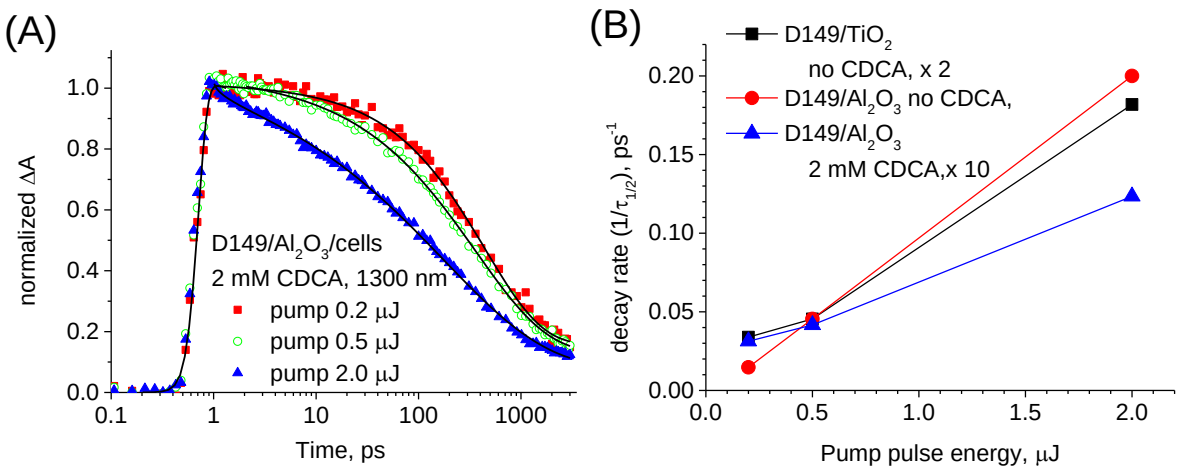

Figure S9. (A) Kinetic traces of transient absorption measured at 1300 nm for D149/Al_2O_3 cell with 2mM of CDCA. for the indicated pump pulse energies (at 555 nm). The black line shows best fit with parameters given in Table S3.The time zero is shifted to 1 ps in order to present the time axis in logarithmic scale.(B) The reciprocal of half-decays measured at 1300 nm for different cells as a function of pump pulse energy (from Tables 3A, 3B and S3)

Table S3. Values of the parameters of the best stretched exponential function given by eq. (1)-(2) fitted to the transient absorption signals of D149/Al_2O_3cells with 2mM CDCA for different pump pulse energy. The pump pulse wavelength was 555 nm and probe wavelength was 1300 nm. Last two columns presents half-decays of the kinetics and ratio of residual signal amplitude to the initial amplitude.

Pump energy / μJ	τ / ps	β	τ_{AVG} / ps	$\tau_{1/2}$ / ps	residual signal / %
0.2	448	0.78	517	320	16
0.5	366	0.62	524	240	13
2	182	0.43	493	81	8

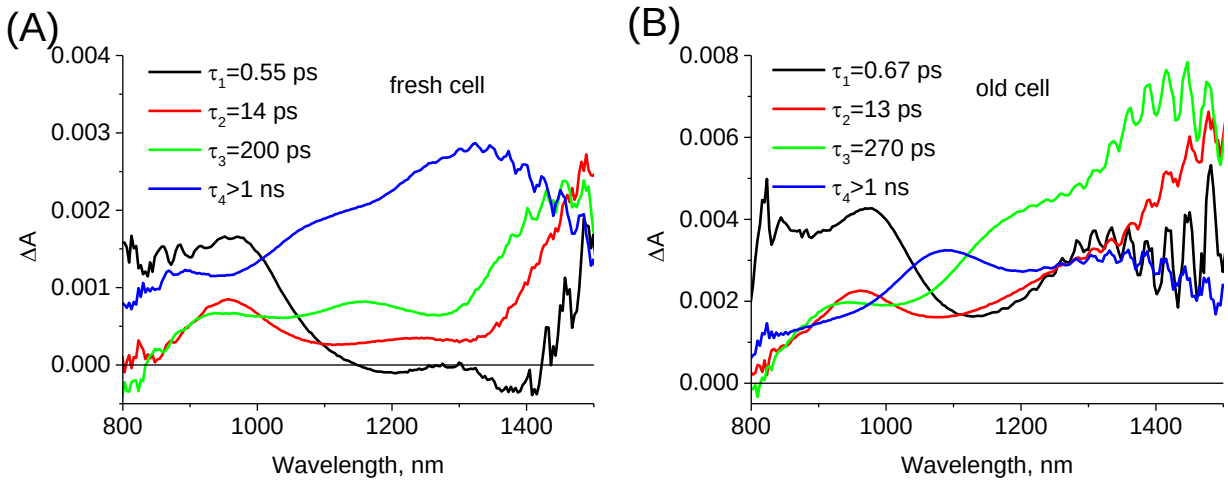

Figure S10. The wavelength-dependent amplitudes of the components with time constants given in the inset obtained by multi-exponential global fit for (A)fresh and (B)old D149/TiO_2 cell. The concentration of CDCA was 2 mM. The old cell is 2 weeks after preparation, J_{SC} decreased from 4.0 to 1.7 mA/cm^2.

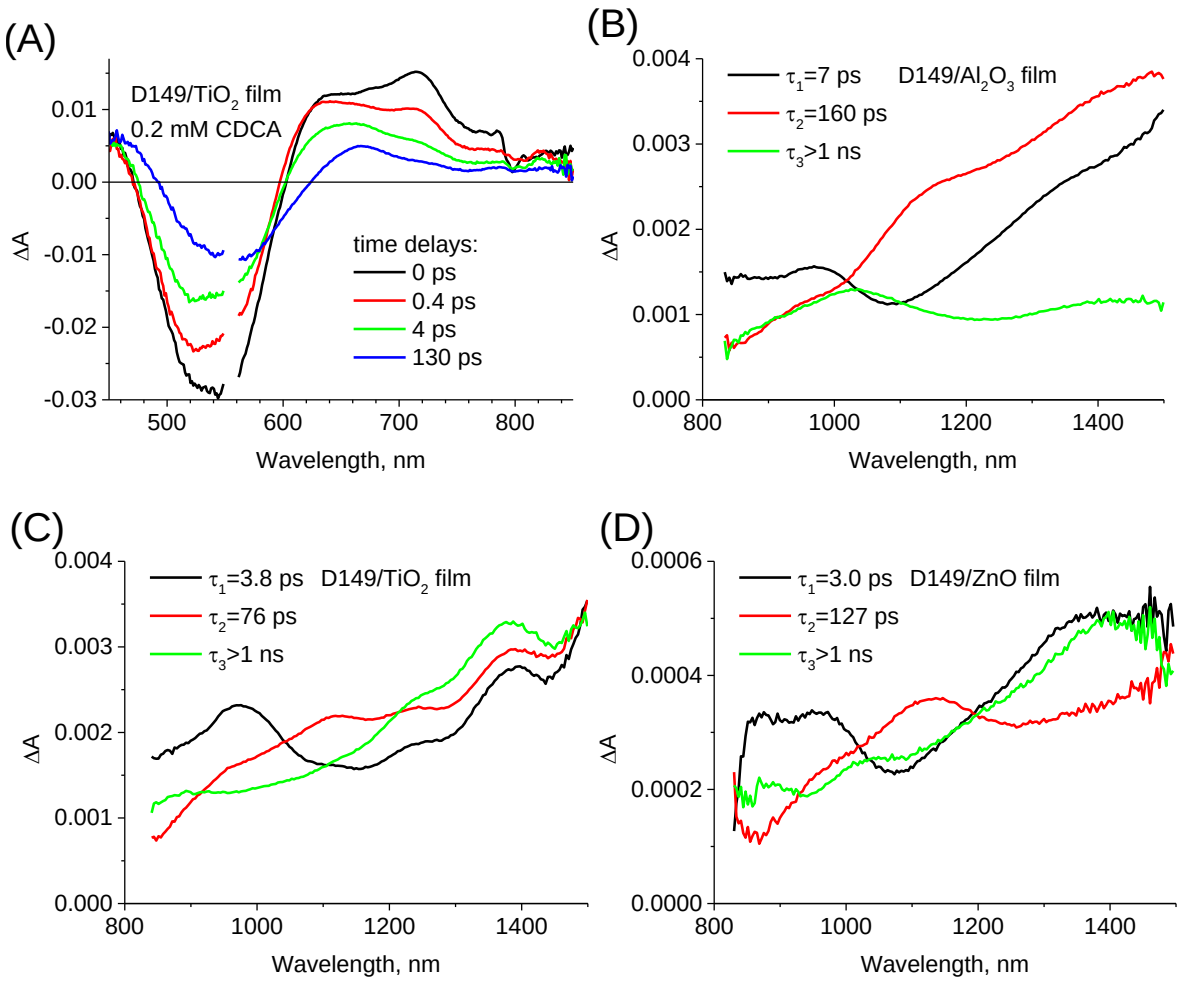

Figure S11. (A) Transient absorption spectra of D149/TiO_2 filmfor selected, indicated time delays between the pump (at 555 nm, 0.5 μJ) and probe pulses. (B-D) The wavelength-dependent amplitudes of the components with time constants given in the inset obtained by multi-exponential global fit for the films of (A) D149/Al_2O_3, (B) D149/TiO_2 and (C) D149/ZnO. The concentration of CDCA was 0.2 mM in (A) and 2 mM in (B-D).

References for SI:

[1] Lohse PW, Kuhnt J, Druzhinin SI, Scholz M, Ekimova M, Oekermann T, et al. Ultrafast photoinduced relaxation dynamics of the indoline dye D149 in organic solvents. Phys Chem Chem Phys. 2011;13:19632-40.

[2] Sobuś J, Burdziński G, Karolczak J, Idígoras J, Anta JA, Ziółek M. Comparison of TiO2 and ZnO Solar Cells Sensitized with an Indoline Dye: Time-Resolved Laser Spectroscopy Studies of Partial Charge Separation Processes. Langmuir. 2014;30:2505-12.

[3] Fakis M, Hrobárik P, Stathatos E, Giannetas V, Persephonis P. A time resolved fluorescence and quantum chemical study of the solar cell sensitizer D149. Dyes and Pigments. 2013;96:304-12.

[4] Glasbeek M, Zhang H. Femtosecond Studies of Solvation and Intramolecular Configurational Dynamics of Fluorophores in Liquid Solution. Chem Rev. 2004;104(4):1929-54.

[5] Ziółek M, Yang X, Sun L, Douhal A. Interrogating the Ultrafast Dynamics of an Efficient Dye for Sunlight Conversion Phys Chem Chem Phys. 2010;12:8098-107.

[6] El-Zohry A, Orthaber A, Zietz B. Isomerization and Aggregation of the Solar Cell Dye D149. J Phys Chem C. 2012;116:26144-53.

[7] Ziółek M, Cohen B, Yang X, Sun L, Paulose M, Varghese OK, et al. Femtosecond to millisecond studies of electron transfer processes in a donor–(pi-spacer)–acceptor series of organic dyes for solar cells interacting with titania nanoparticles and ordered nanotube array films. Phys Chem Chem Phys. 2012;14:2816-31.

[8] Oum K, Lohse PW, Flender O, Klein JR, Scholz M, Lenzer T, et al. Ultrafast dynamics of the indoline dye D149 on electrodeposited ZnO and sintered ZrO2 and TiO2 thin films. Phys Chem Chem Phys. 2012;14:15429-37.

CHEMISTRY & SUSTAINABILITY

CHEMSUSCHEM

ENERGY & MATERIALS

Table of Contents

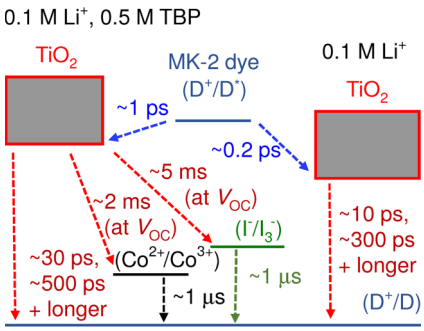

A matter of time: Solar cells sensitized with one of the most promising and efficient carbazole dyes are studied using a number of complex techniques (from ultrafast and fast laser spectroscopy to electrochemical impedance measurements) to provide information about partial charge separation processes occurring from femtoseconds to seconds in complete devices. The observed features have a direct impact on the performance of the solar cells, and therefore are crucial for the construction of more efficient devices.

WILEY-VCH

ChemPubSoc Europe

DOI: 10.1002/cssc.201500628

CHEMSUSCHEM Full Papers

Carbazole Dye-Sensitized Solar Cells Studied from Femtoseconds to Seconds—Effect of Additives in Cobalt- and Iodide-Based Electrolytes

Jan Sobuś,[a, b] Jacek Kubicki,[b] Gotard Burdziński,[b] and Marcin Ziółek*[b]

Comprehensive studies of all charge-separation processes in efficient carbazole dye-sensitized solar cells are correlated with their photovoltaic parameters. An important role of partial, fast electron recombination from the semiconductor nanoparticles to the oxidized dye is revealed; this takes place on the picosecond and sub-nanosecond timescales. The charge-transfer dynamics in cobalt tris(bipyridyl) based electrolytes and iodide-based electrolyte is observed to depend on potential-determining additives in a similar way. Upon addition of 0.5 M 4-*tert*-butylpiridine to both types of electrolytes, the stability of the cells is greatly improved; the cell photovoltage increases by 150–200 mV, the electron injection rate decreases about five times (from 5 to 1 ps^{-1}), and fast recombination slows down about two to three times. Dye regeneration proceeds at a rate of about 1 μs^{-1} in all electrolytes. Electron recombination from titania to cobalt electrolytes is much faster than that to iodide ones.

Introduction

With the ever-growing global energy demand and shrinking deposits of fossil fuels, a multitude of green, clean energy sources have been developed, of which solar energy is the most promising candidate for satisfying the energy hunger worldwide. Among various solar cell designs established over the last 70 years, dye-sensitized solar cells (DSSCs), developed by Graetzel and O'Regan in the early 90s,[1] stand out as a cost-efficient, eco-friendly solution that is viable for use under any lighting conditions.

In these cells, current is generated by photons absorbed by dye molecules attached to the mesoporous titania layer that, upon photoexcitation, inject electrons straight into the semiconductor itself.[2] The choice of dye molecule is of crucial importance. Its LUMO level should lie over the conduction band edge of TiO_2 to provide enough driving force for the process, and its energy gap (S_0–S_1 energy transition) should be appropriate to absorb the optimized part of the solar spectrum (thus maximizing the power output). It should also possess as high an extinction coefficient as possible to decrease the thickness of the titania layer and suppress carrier transport difficulties. The choice of the proper redox couple to regenerate the dye after injection is of no less importance. Not only does the redox level define the voltage obtainable by the cell (with relation to the TiO_2 conduction band edge), but it also should be able to swiftly regenerate the photoexcited dye; thus preventing or at least minimizing the occurrence of unwanted recombination processes. There are several differences between traditional iodide-based electrolytes and novel cobalt-based redox couples. Cobalt complexes have the advantage of being a one-electron system with the redox level lying closer to the HOMO level of most dyes; thus significantly increasing the cell voltage. As a result, the current best laboratory efficiencies of DSSCs (up to 13%) are those that utilize cobalt as the redox pair.[3]

On the other hand, the positive charge makes unwanted recombination a much more probable process. The large molecular size also slows diffusion into titania pores. To finely tune the energy levels of this complicated multielement system, different electrolyte additives are utilized, which protonate or deprotonate the titania surface and shift the energy levels accordingly.

Herein, a high-efficiency carbazole dye (MK-2) was investigated. It is the most promising member of the dye family first proposed in 2006 by Koumura et al.[4] Henceforth, it has been investigated for different reasons, including the manufacture of high-efficiency cells with novel cobalt complexes,[5] application in solid-state devices,[6] and for long-term stability.[7] Various derivatives of this successful dye have also been studied to improve stability in a humid environment,[8] and understand the effect of varying alkyl chains on the recombination process.[9] Recently, a derivative of MK-2, ADEKA1, reached an impressive value of over 12% efficiency.[10] In our studies, it was coupled with various electrolytes, both iodide- and cobalt-based, with the addition of compounds such as 4-*tert*-butylpyridine (TBP) or appropriate lithium salts (depending on the type of electrolyte used). Resulting cells were subjected to an array

[a] J. Sobuś
NanoBioMedical Centre, Adam Mickiewicz University
Umultowska 85, 61-614 Poznan (Poland)

[b] J. Sobuś, Dr. J. Kubicki, Dr. G. Burdziński, Dr. M. Ziółek
Quantum Electronics Laboratory, Faculty of Physics
Adam Mickiewicz University, Umultowska 85
61-614 Poznan (Poland)
E-mail: marziol@amu.edu.pl

Supporting Information for this article is available on the WWW under http://dx.doi.org/10.1002/cssc.201500628.

of measuring techniques to determine kinetics and time constants of various processes occurring over the timescales from femtoseconds to seconds, including impedance spectroscopy and transient absorption measurements in the visible, near-infrared (NIR), and mid-IR regions. To the best of our knowledge, combining the last three detection ranges in one study has not been realized so far for any complete DSSC. However, only in this way can the dynamics of excited dyes, oxidized dyes, trapped electrons, and free electrons be probed simultaneously. Therefore, the general picture of the solar cell's photodynamics was revealed, which led to a better understanding of the basic processes that constitute the operation of DSSCs.

So far, only a few contributions have reported studies on complete DSSCs with cobalt-based electrolytes on the ultrafast timescale.[11] In none of them have the effects of TBP and Li^+ additives and $TiCl_4$ treatment been addressed; this is of crucial importance in solar cell optimization. On one hand, the proper concentration of additives constitutes a balance between a high open-circuit voltage and efficient electron injection in the solar cells. On the other hand, our contribution shows, for the first time (to the best of our knowledge, for any DSSC), how TBP and Li^+ additives influence initial fast recombination dynamics. Such unwanted process occurring between electrons in titania and oxidized dyes on the sub-nanosecond timescale have been recently observed for many efficient DSSCs sensitized with organic dyes.[8–9,11c,12] This means that there is still room for further improvement of DSSC systems based on such dyes, if fast recombination can be minimized or suppressed. Therefore, our studies should have a direct impact on the performance of the solar cells, and are vital for the construction of more efficient devices in the future.

Results and Discussion

Solar cell performances and impedance spectroscopy

Table 1 presents the basic photovoltaic parameters for the MK-2 cells and Figure 1 A shows the incident-photon to current efficiency (IPCE) spectra. The abbreviations used for different cells contain the redox pair name and additives in the electrolyte, and are explained in detail in the Experimental Section. The presented results are averaged for two to four prepared cells. The sunlight conversion efficiencies of the best cells (about 4%) are about two times smaller than the reported best values for MK-2 dye; however, our photoanodes were prepared with a relatively thin mesoporous titania layer (3 μm) and without a scattering layer containing large particles to make the cell transparent enough for time-resolved laser spectroscopy measurements.

Table 1. Photovoltaic parameters of different MK-2 cells one day after preparation: open-circuit voltage (V_{OC}), short-circuit current (J_{SC}), fill factor (FF), and total sunlight conversion efficiency under irradiation of one sun.

Cell	V_{OC} [mV]	J_{SC} [mA cm^{-2}]	FF	Efficiency [%]
ILiTBP no $TiCl_4$	720	6.8	0.49	2.4
ILiTBP	680	10.8	0.57	4.2
ILi	525	10.5	0.54	3.0
CoLiTBP no $TiCl_4$	460	3.6	0.42	0.7
CoLiTBP	700	10.0	0.57	4.0
CoLi	510	9.0	0.44	2.0

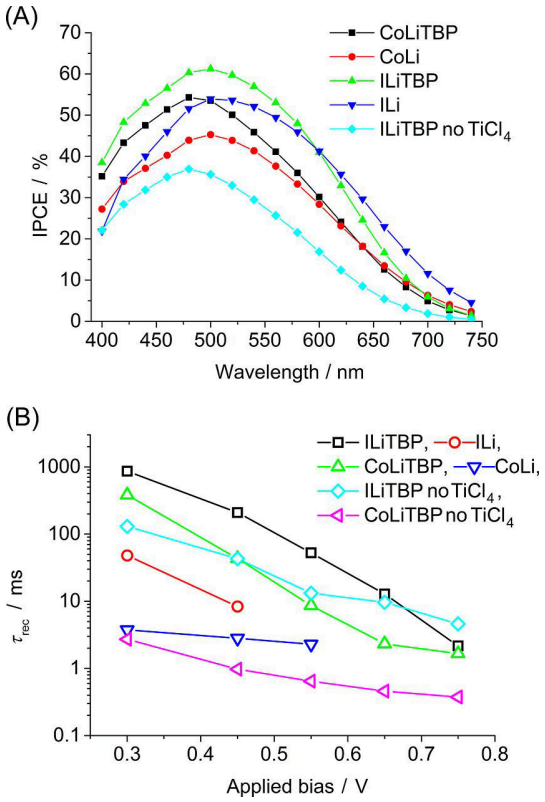

Figure 1. (A) IPCE spectra of the indicated cells. (B) Electron recombination lifetimes obtained from electrochemical impedance measurements for the indicated cells.

First, the addition of TBP in both cobalt and iodide electrolytes improves the photovoltage significantly, which is commonly attributed to the shift of conduction band edge of titania towards more negative potentials.[13] The V_{OC} increases from 525 (ILi sample) to 680 mV (ILiTBP) and from 510 (CoLi) to 700 mV (CoLiTBP). Although the redox potentials of the electrolytes are different by about 0.2 V, the V_{OC} values of the cells with cobalt electrolyte are not much higher than those of the iodide electrolyte. This can probably be attributed to higher electron recombination between titania and electrolyte in the former cells, as confirmed below. The J_{SC} values are similar for cells with and without TBP (between 9 and ≈11 mA cm^{-2}). This is probably because the redox potential of the MK-2 excited state, S^*/S^+, is sufficiently more negative than the conduction band edge potential; thus shifting of the latter upon the addition of 0.5 M TBP does not change the electron injection yield significantly. Fast electron injection dynamics are also confirmed in the next sections. Small variations in the photocurrent generally agree with the maxima of the IPCE spectra (Figure 1 A). However, a drastic change in the solar cell performance occurs for control cells without the $TiCl_4$ protective

treatment, with a more profound impact on the photocurrent and FF values than the photovoltage (Table 1). The sensitized films with $TiCl_4$ treatment have higher absorbance (about $A=1.5$ at the maximum with respect to about $A=1.0$ without $TiCl_4$ treatment; see Figure S1 A in the Supporting Information), which is in agreement with other reports,[14] and blocking of electron recombination is another important factor,[14b,15] as evidenced below from impedance measurements.

The cell performance was checked after (1 h) cell preparation and again a longer period after preparation. For cells with TBP, a small increase in the photocurrent for both iodide- and cobalt-based cells is observed one day after cell construction, along with a small increase in V_{OC} (by 10–20 mV). The cells with TBP are remarkably stable and the photocurrent maintains 85% of the initial value after 4 months of storage in the dark. On the contrary, cells without TBP in the electrolyte were much less stable, with significantly increasing V_{OC} and decreasing J_{SC} over time. For example, the cell parameters 1 h after preparation were as follows: for I_2: $V_{OC}=465$ mV and $J_{SC}=11.5$ mA cm^{-2} for the ILi cell, and $V_{OC}=465$ mV and $J_{SC}=11.1$ mA cm^{-2} for the CoLi cell (cf. Table 1 after one day). Herein, the initial photocurrents are highest for the electrolyte without TBP, yet they diminish rapidly, much faster than for cells with TBP (80% of its initial value after 4 to 6 days).

Electrochemical impedance measurements were performed mainly to study the effect of recombination between electrons in titania and electrolyte, which occurs on the millisecond timescale. Data was fitted with the equivalent circuit for DSSCs to give the charge-transfer resistance (R_{ct}) and chemical capacitance (C_μ) in the oxide–electrolyte interface. For cells with TBP, these two parameters exhibit exponential behavior for applied bias voltages from 300 to 650 mV. The fits of the exponential function to R_{ct} and C_μ dependence on the applied voltage [Eqs. (1) and (2)] give the recombination reaction order (or ideality factor, parameter m) and trap energy distribution below the conduction band (parameter α), respectively.

$$C_\mu = C_0 \exp(\alpha Ve/kT) \quad (1)$$

$$R_{ct} = R_0 \exp(-Ve/mkT) \quad (2)$$

These data are collected in Table 2. As evidenced from these results, the additional protective layer (in $TiCl_4$-treated films) brings the m parameter closer to the ideal value of one; a stronger effect is visible for the cobalt-based cells. The increase in m values correlates well with lowering of the FF values of the cells (Table 1).[16] Another thing to note is that $TiCl_4$ treatment slightly increases the density of trap states (parameter α) as well.

Table 2. The parameters α (trap energy distribution below the conduction band) and m (reaction order in recombination kinetics) obtained from the fit of Equations (1) and (2) for the indicated cells. Charge-transfer resistance (R_{ct}) and chemical capacitance (C_μ) values in the oxide–electrolyte interface were obtained from the electrochemical impedance data measured at different bias voltages (V) in the dark.

Cell	m	α
CoLiTBP	2.1	0.11
CoLiTBP no $TiCl_4$	7.2	0.04
ILiTBP	1.9	0.21
ILiTBP no $TiCl_4$	3.0	0.14

Calculation of the recombination time constant ($\tau_{rec}=R_{ct}C_\mu$) supports these observations. Although, in general, τ_{rec} is higher for the iodide cells than the cobalt-based ones, the lack of a $TiCl_4$ layer decreases the τ_{rec} value in both cases by at least an order of magnitude (Figure 1 B). The recombination process is accelerated with increasing applied voltage. For electrolytes without TBP, the τ_{rec} values are similar to those for electrolytes containing TBP, but at about 250–300 mV smaller bias (in line with the lower V_{OC}).

In summary, the combined addition of TBP and $TiCl_4$ treatment result in a massive increase in the cell performance and stability, especially for the cobalt electrolyte. However, for CoLiTBP cells with the $TiCl_4$ treatment, we observed a relatively larger spread of photovoltaic parameters than those for the ILiTBP cells (despite the same preparation procedure). Among different CoLiTBP cells, the V_{OC} value increased (up to 725 mV) at the expense of the decreased J_{SC} value. Interestingly, an increase in V_{OC} is also accompanied by spectral narrowing in the red side of the IPCE spectra (Figure S1 B in the Supporting Information). The highest narrowing of the IPCE spectrum is observed for cells without the $TiCl_4$ treatment, and indeed the V_{OC} value of ILiTBP is higher for cells without the $TiCl_4$ treatment than for those with treatment (see Table 1; however, for CoLiTBP cells without $TiCl_4$ the V_{OC} is lower due to too much recombination). One possible interpretation of these results is that upon $TiCl_4$ treatment the penetration of TBP towards the nanoparticle surface is more difficult and, due to the inaccuracy in the $TiCl_4$ protection procedure, a variation in cell parameters occurs. Worse penetration results in lower photovoltage and red-side spectral broadening of the IPCE. This is also nicely confirmed by a comparison of the spectra of the cells with and without TBP (Figure 1 A, ILi versus ILiTBP and CoLi versus CoLiTBP). Upon the addition of 0.5 M of TBP, both IPCE (Figure 1 A) and stationary absorption of the cells (Figure S1 A in the Supporting Information) are narrowed by about 25–30 nm. It is interesting that cells without TBP, although generally less efficient, show higher IPCE values in the long-wavelength part of the spectrum (better light harvesting with respect to the sunlight spectrum). One explanation for spectral narrowing with higher TBP penetration (observed in both IPCE and steady-state spectra) might be as follows: intermolecular interactions between MK-2 molecules adsorbed on titania probably lead to additional absorption features on the red side of the spectrum (similar to J-aggregate formation). Better access of TBP to MK-2 molecules disturbs dye self-interactions and decreases the long-wavelength broadening.

Nanosecond transient absorption

Nanosecond transient absorption measurements were used to study dye regeneration dynamics for fully assembled MK-2-sensitized cells. First, the kinetics were probed in the spectral

range from $\lambda = 560$ to 800 nm for the ILiTBP cell. The kinetics were analyzed by global fitting with a two-exponential function (without any offset), and the resultant time constants and wavelength-dependent amplitudes associated with them are shown in Figure 2A. As can be seen, two time constants should be assigned to different species. The first one, decaying with a shorter time constant of about 1 μs, represents the oxidized dye (MK-2 radical cation). Its transient spectrum contains the positive part (dominating for wavelengths longer than $\lambda = 650$ nm with a signal intensity rising up to 800 nm), which is due to the absorption of the oxidized dye, and a negative signal (dominating below $\lambda = 650$ nm), which is present in the range of stationary absorption of the neutral form of MK-2 and occurs due to ground-state depopulation (bleaching signals). The amplitude spectrum related to the longer decaying time constant ($\tau_1 = 50$ μs) is different, with a mainly positive part above $\lambda = 600$ nm (Figure 2A), and is assigned to the spectrum of electrons in titania. Indeed, the presence of such bands assigned to the absorption from deep trap states in TiO_2 was reported in this range;[17] the lifetime of electrons should be much longer than that of the oxidized dye when its regeneration by electrolyte is efficient, as observed in this case. Moreover, the lifetime of the longer component depends on both the pump and probe light intensity (see Figure S2 in the Supporting Information), which is characteristic for electron recombination processes.[18]

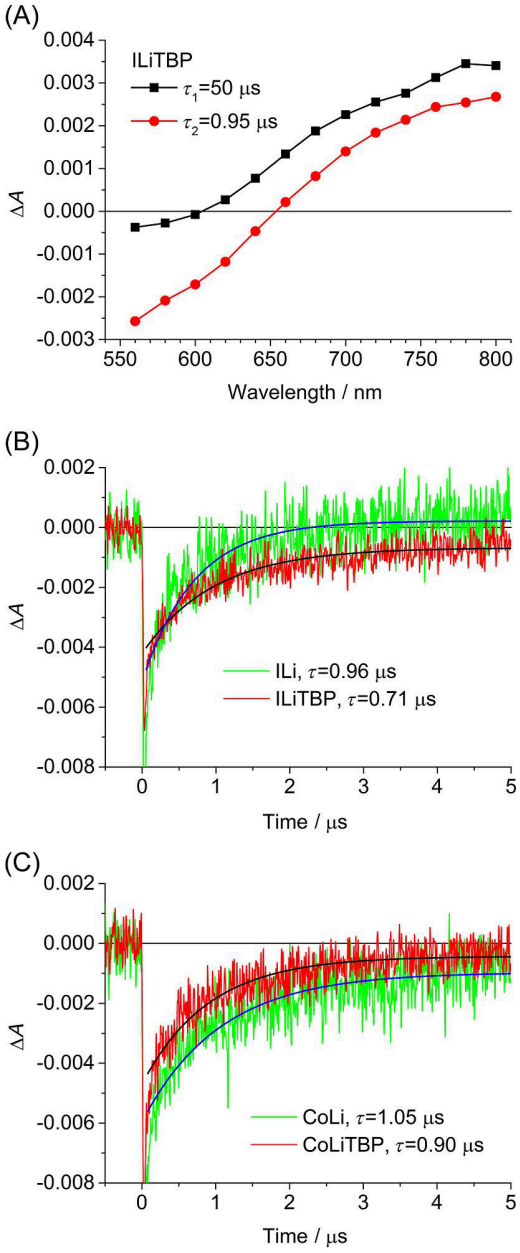

Figure 2. (A) Wavelength-dependent amplitudes of the two-exponential components (with the indicated time constants) obtained from the global fit to the flash photolysis results of the ILiTBP cell. Kinetics at $\lambda = 580$ nm obtained in flash photolysis experiments for the indicated (B) iodide and (C) cobalt cells. The best one-exponential (and constant offset) fits and obtained time constants are also indicated. The pump pulse energy was 0.1 mJ and the excitation wavelength was $\lambda = 535$ nm. The residual negative signal might be due to the Stark shift effect.[27]

Therefore, to be free from the contribution of electrons and to probe exclusively the dynamics of dye regeneration, we chose a probe wavelength of $\lambda = 580$ nm, at which the bleach signal has a significant amplitude (proportional to population of the oxidized dye) and the contribution of electrons is minimized (Figure 2A). The kinetics at $\lambda = 580$ nm for the investigated cells are shown in Figure 2B and C. Interestingly, dye regeneration dynamics are found similar for both types of electrolytes (cobalt and iodide), and do not depend on either the presence or absence of TBP. In all cases, dye regeneration proceeds with a time constant of about 1 μs. As for the comparison between iodide and cobalt redox shuttles, this result reveals that, despite having a smaller driving force for dye regeneration, the process is quite fast for the cobalt electrolyte. Therefore, this confirms sufficient regeneration efficiency by the cobalt complexes used in this study. The standard redox potential of $[Co(bpy)_3]^{2+/3+}$ (bpy = 2,2′-bipyridine) is 0.57 V versus a normal hydrogen electrode (NHE), whereas for the I_3^-/I^- redox couple it is 0.35 V versus NHE, which directly shows the expected improvement in V_{OC} for the cobalt electrolyte.[2,19] However, in the iodide electrolyte, the regeneration reaction is a two-electron process with the possible participation of I_2, and the redox potential for I_2^-/I^- is much more positive: 0.55 V versus NHE. Therefore, the effective driving force for regeneration might be similar in both electrolytes, which is in agreement with the observed dynamics.

The independence of the dye regeneration dynamics on the addition of TBP should be discussed in view of our previous results for other dyes, for which we observed the significant effect of potential-determining ions on the dye regeneration time constant for similar concentrations of Li^+ and TBP.[20] Dye regeneration was faster when no TBP was present in the electrolyte. Those results were obtained for dyes for which the coordinated shift of molecular levels has been recently reported (or can be assumed due to the presence of additional COOH groups in the dye structure).[21] If the S^+/S potential of the dye changes upon adding Li^+ or TBP to the electrolyte, then the regeneration time constant can be affected due to changes in the driving force for this process. For the MK-2 dye (without

any additional COOH groups), the lack of a coordinated shift was reported,[21] and, accordingly, we observed no effect upon the addition of TBP. Therefore, this confirms the key role of the coordinated shift on dye regeneration in DSSCs.

Femtosecond transient absorption in the mid-IR region

The mid-IR range of detection is used to probe the absorption of electrons present in the conduction band or shallow trap states in titania.[9b,22] The absorption of such electrons forms a very broad spectrum (with the amplitudes increasing with wavelength, for example, λ^n, $n \approx 2$),[17,23] so selecting a probing wavelength without any contribution of narrow vibration bands of the dye enables direct examination of the electron injection dynamics. The MK-2 samples used in this range were analogous to complete cells measured by other techniques, except that fluorine-doped tin oxide (FTO) glass plates were substituted by CaF_2 plates because the former material is not transparent enough in the mid-IR range. CaF_2 plates are not conducting; thus the direct measurement of the photovoltaic parameters of the samples was not possible.

Figure 3 presents the kinetics measured at $\lambda = 4800$ nm after pumping the samples at $\lambda = 500$ nm with 60 nJ pulses. The kinetics were fitted to the convolution of the instrument response function (IRF) of the setup (full-width at half-maximum (FWHM) = 0.2 ps) with two exponential rises and one exponential decay plus a constant offset. The rise time reflects the appearance of electrons in the conduction band, so it directly represents the characteristic time of electron injection from the MK-2 dye. As can be seen in Figure 3, the injection time is significantly slower for the electrolytes with TBP. The classical explanation for this effect is the shift of the conduction band edge towards higher energies upon the addition of TBP (which causes an increase in the V_{OC} value of the cell, as confirmed in the section on Solar cell performances and impedance spectroscopy); thus reducing the density of acceptor states in titania that interact with the excited state of the sensitizing dye. The fitted rise times are 0.2 ps for ILi and 1 ps for ILiTBP cell (the latter value is the amplitude averaged time constant from the two rise times resolved in the fit shown in Figure 3 A). For cobalt electrolytes, the rise times are slightly slower (both with and without TBP), but the signal to noise ratio is also worse in this case.

The signal in the mid-IR range decays on the timescale of hundreds of picoseconds (component of 30–50% contribution; the rest is the offset constant in the temporal window of the experiment). In principle, such a decay can reflect the electron-trapping process in titania nanoparticles because the trapped electrons absorb in the shorter wavelength range (visible and NIR).[17] However, the fitted decay time constants are shorter for electrolytes with only Li^+ (about 200 ps) compared with those with both Li^+ and TBP (400–700 ps). Such a difference is hard to explain by the trapping mechanism, and may indicate the presence of partial electron recombination (back electron transfer from titania to the oxidized dye) occurring on this timescale. Further confirmation of the validity of this assumption comes from the femtosecond results in the visible range, which are presented in the next section.

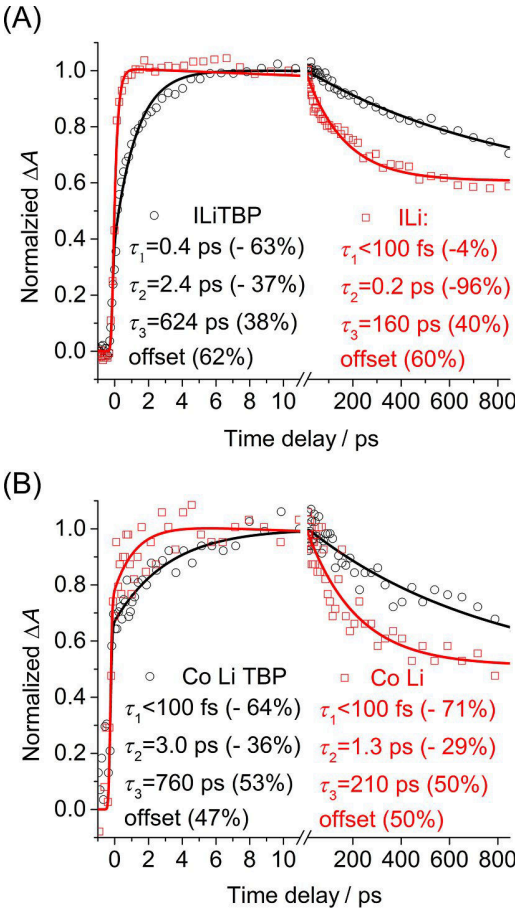

Figure 3. Transient absorption kinetics (points) in the mid-IR range for (A) iodide and (B) cobalt cells. The solid lines shows the best three-exponential (plus constant offset) fits; the time constants and amplitudes (in parentheses) are shown as insets. Negative values of amplitudes indicate rise times. The pump pulse was set at $\lambda = 500$ nm (60 nJ) and the probe wavelength was $\lambda = 4800$ nm.

Femtosecond transient absorption in visible and NIR regions

Femtosecond transient absorption spectra of complete MK-2 cells were measured in the spectral range $\lambda = 500$–850 nm (from $\lambda = 440$ nm in the case of the dye in solution) for visible detection and $\lambda = 800$–1550 nm for NIR detection, both in the temporal range up to 3 ns. The IRF of the setup was about 0.2–0.3 ps (FWHM). In these ranges, different signals of the species participating in primary charge separation occur (positive absorption from the dye in the excited state, from the oxidized dye or trapped electrons, as well as negative signals due to ground-state bleaching and stimulated emission). Therefore, in addition to studies on the cells, the signals of the dye in solution were also measured to identify the spectrum of the MK-2 excited state.

Figure 4 A and B shows the transient absorption spectra of MK-2 in toluene in the visible and NIR regions, respectively, for

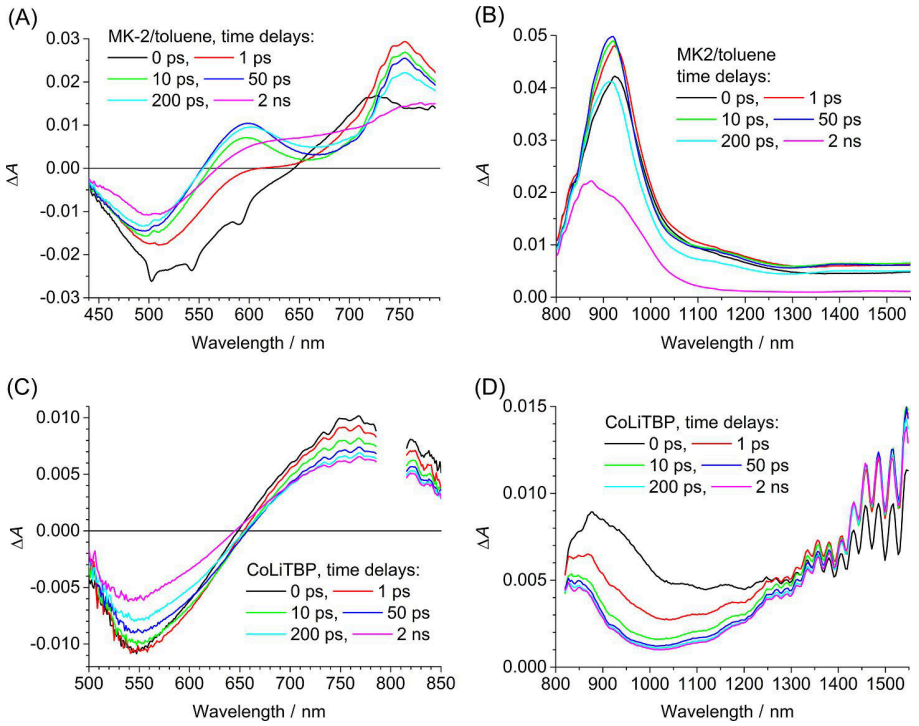

Figure 4. Representative transient absorption spectra for selected time delays between pump and probe pulses for MK-2 in toluene (A, B) and the CoLiTBP solar cell (C, D). The pump pulse (200 nJ for studies in solution and 60 nJ for studies in cells) was set at $\lambda = 500$ nm, and the spectra were probed in the visible (A, C) and NIR (B, D) regions.

selected time delays between pump and probe pulses. As can be seen from these results, the excited state of the dye shows absorption bands with maxima at $\lambda \approx 600$, 750, and 920 nm. The apparent presence of the first two maxima is probably due to the negative stimulated emission band that appears between them (reported maximum of $\lambda \approx 680$ nm[8]). Below $\lambda =$ 550 nm the negative bleaching signal dominates. Multiexponential global analysis was used to extract the time components and wavelength-dependent amplitudes that occurred during deactivation of the dye (Figure S3 in the Supporting Information). The fastest components with durations of 0.2 and 2–7 ps should be assigned to vibrational relaxation and solvation processes in the singlet excited state, respectively, similar to many organic dyes used in DSSCs.[24] The long component with a duration of about 550 ps is due to deactivation of the S_1 state, and its lifetime is long enough to permit a high quantum yield of electron injection when the dye is attached to titania. Finally, the residual signal is present with the positive transient absorption rising from $\lambda = 570$ to 880 nm (Figure 4A and B). The oxygen effect measured in nanosecond transient absorption studies (Figure S4 in the Supporting Information) confirms that it is due to the triplet excited state, which is efficiently populated from the singlet excited state through an intersystem crossing process. Moreover, we have also measured MK-2 in more polar solvents and observed a more complicated picture: a blueshift of the stationary absorption with respect to that in toluene and a strong concentration-dependent maximum of the absorption band (Figure S5 in the Supporting Information), along with additional faster components in the transient absorption decay (Figure S3 in the Supporting Information). This is probably due to the coexistence of neutral and anionic forms of the dye, as observed before for other organic dyes with carboxylic acid groups.[25]

Examples of transient absorption spectra for the complete MK-2 cell are shown in Figure 4C and D. With respect to the results in solution, the negative bleaching signal is shifted towards longer wavelength (up to $\lambda = 650$ nm), which is in agreement with the redshift of the stationary absorption when the dyes are sensitized on titania (for example, compare the IPCE spectra in Figure 1A with the stationary absorption in solution in Figure S5 in the Supporting Information). The positive absorption between $\lambda = 650$ and 1200 nm contains the contribution of the MK-2 excited state (see spectra in solution in Figure 4A and B), the oxidized dye, and deeply trapped electrons (see the spectra from the nanosecond transient absorption experiment in Figure 2A), whereas the positive absorption rising above $\lambda = 1200$ nm is probably due to shallow trapped electrons.

Global analysis is necessary to identify charge separation processes, their dynamics, and participating transients. The results of such multiexponential global fits are presented in Figure 5 for the visible range and in Figure 6 for the NIR range. The fastest components have time constants of 0.1–0.2 ps for the lithium-only electrolytes and are much longer, 0.5–1 ps, for electrolytes with the addition of TBP. For cells with TBP and higher than average V_{OC} values, the time constants are even longer (2–4 ps, results not shown). No systematic differences are observed between iodide- and cobalt-based electrolytes. The amplitudes of these fastest time components have positive bands with maxima at $\lambda \approx 600$ and 750 nm in the visible region, and $\lambda = 920$ nm in the NIR region; these values are very similar to the absorption of the excited singlet state in solution (the spectrum of the 540 ps component in Figure S3 in the Supporting Information or the spectra for time delays of 10–200 ps in Figure 4A and B). Therefore, they can be safely assigned to the decay of the dye excited state due to the electron injection process. Moreover, these components have negative amplitudes for wavelengths longer than $\lambda = 1300$ nm, as caused by the accompanying rise of shallow-trap-state electrons in titania (Figure 6A–C). The time con-

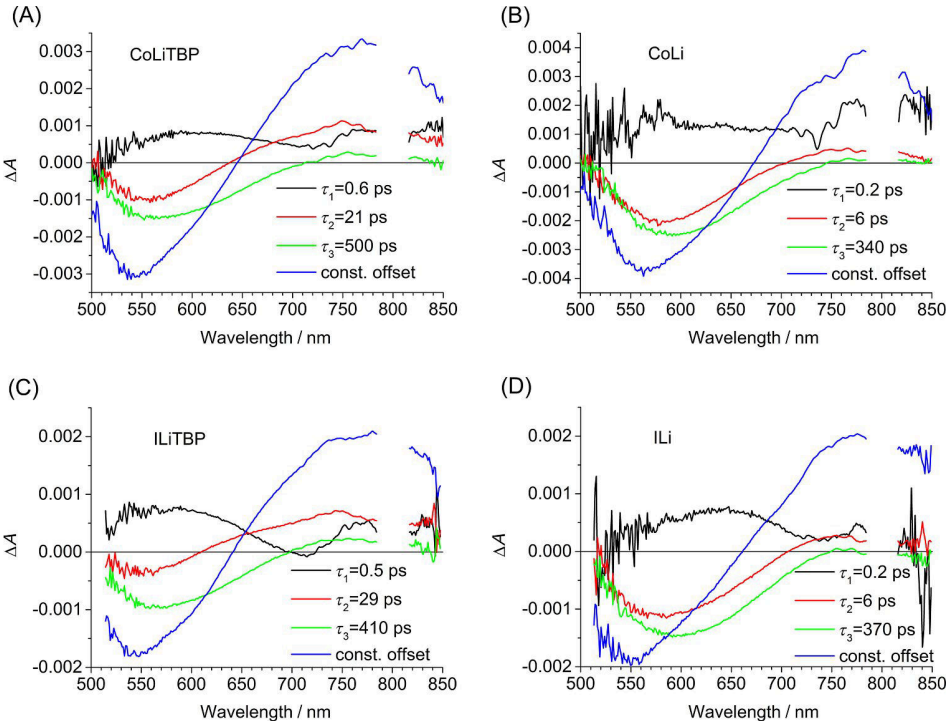

Figure 5. Wavelength-dependent amplitudes of the indicated time constants obtained from global analysis of transient absorption spectra of cobalt (A, B) and iodide (C, D) cells in the visible region. The pump pulse (60 nJ) was set at $\lambda = 500$ nm.

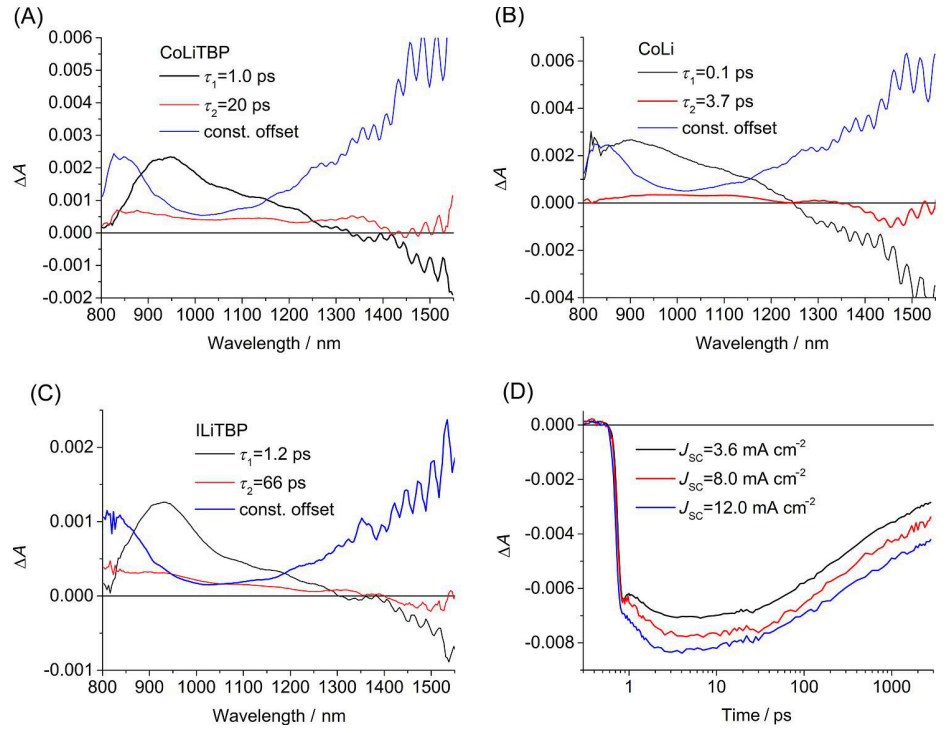

Figure 6. Wavelength-dependent amplitudes of the indicated time constants obtained from global analysis of transient absorption spectra of cobalt (A, B) and iodide (C) cells in the NIR region. (D) Kinetic traces at $\lambda = 600$ nm measured for different CoLiTBP cells, with different indicated J_{SC} parameters (measured under one sun). The time zero is shifted to 1 ps to present the time axis on a logarithmic scale. The pump pulse (60 nJ) was set at $\lambda = 500$ nm in all cases.

stants for electron injection, and the differences between the electrolytes with and without TBP, are fully consistent with the rise times observed in the mid-IR region (Figure 3).

Next, two longer components with time constants of several/several tens of picoseconds and several hundreds of picoseconds are necessary in the global fit. These components are the main contribution to the bleach recovery process (negative amplitudes below $\lambda = 650$ nm that result in a rise of the transient absorption signal; Figure 5). The most probable explanation for this observation is electron recombination between titania and the oxidized dye. For wavelengths longer than those of the bleaching band, the components have positive amplitudes, probably due to decay of the oxidized dyes. The longer time constants are also dependent on the potential-determining additives in the electrolyte. For cells without TBP, they are equal to 6 and around 350 ps in the visible region, whereas for cells with TBP they are 20–30 and 400–500 ps in the same spectral range. In the spectral range of ground-state recovery, both components are present with similar contributions. In the NIR region, only one component is necessary, with a characteristic time closer to the shorter one: several picoseconds without TBP and 20–60 ps with TBP (Figure 6 A–C).

The longer recombination components (hundreds of ps) correspond to decays of the electrons observed in the mid-IR range. Interestingly, the contribution of longer components is negligible in the NIR range and very small in the visible range for wavelengths longer than $\lambda =$ 700 nm. Therefore, faster recombination (tens of ps) is probably more connected with trapped electrons (absorption in the visible and NIR regions), whereas

slower (hundreds of ps) recombination is probably related to conduction band electrons (absorption in the mid-IR range). Nevertheless, the amplitudes of the recombination components in the visible and NIR regions seem to be too small with respect to their contribution in bleach recovery, and the following explanations can be proposed. Faster recombination with the trapped states can be observed due to the formation of some kind of bound complexes (between a dye with an injected electron and the localized, deeply trapped acceptor site in titania) that can suffer from rapid back electron transfer.[26] Such intermediates can have smaller absorptions in the visible range than those of the separated oxidized dye and trapped electron; thus the negative amplitudes (in the bleach bands) are higher than the positive ones (above $\lambda = 650$ nm). For the slower recombination component (hundreds of ps), it can overlap with the electron trapping dynamics: the decay of the signal above $\lambda = 650$ nm due to recombination can be superimposed on its rise due to relaxation of the conduction-band electrons (not absorbing in the visible range) into trapped states. Indeed, when an additional component is added to the global fit, the rise of the trapped electrons appears with a time constant of about 1.3 ns, whereas the positive amplitudes of the recombination component (200 ps) become more prominent (Figure S6 in the Supporting Information). However, the improvement in the fit quality is too small to definitely conclude whether the additional component is really necessary. In summary, the band of ground-state recovery is probably better suited to probe the electron recombination process for DSSCs with carbazole dyes, similarly to dye regeneration described previously.

The final spectra from the global analysis (constant offset in Figures 5 and 6) represent the residual signals from oxidized dyes and electrons in titania that did not suffer from recombination. The negative amplitudes of the spectra associated with constant offset and both recombination components can be used to estimate the part of the initially excited population that did not recombine until 3 ns. This portion is 55–60% for cells with TBP and about 45% for cells without TBP. These numbers correlate with higher J_{SC} and IPCE values (Table 1 and Figure 1 A) for cells with TBP than those without. However, the stationary absorption (and thus bleaching band) in the cells without TBP is redshifted with respect to those with TBP. Therefore, they might overlap differently with the positive absorption bands in both series of cells, and the obtained different contributions of recombination should be treated with caution.

We have also checked the effect of different excitation wavelengths and pump pulse intensities on the results of femtosecond transient absorption. Tuning the pump wavelength from $\lambda = 500$ (maximum of dye absorption) to 600 nm (less vibrational energy excess) does not influence the recombination part observed in the bleach recovery kinetics (Figure S7 C in the Supporting Information). The only difference seen in the global fit (Figure S7 A and B in the Supporting Information) is that there is less contribution of the dye excited state at $\lambda \approx 750$ nm in the fastest electron injection component. This might be explained by the increased contribution of injection to the trap states (which causes a simultaneous decrease in the excited-state signal and an increase in the trap-state signal at $\lambda = 750$ nm) when less energetic photons excite MK-2 dyes. On the contrary, when a higher pump pulse intensity is used (240 nJ per pulse with respect to excitation with 60 nJ per pulse in all other experiments), the contribution of recombination increases and the faster recombination component is accelerated (Figure S8 in the Supporting Information). Therefore, fast recombination is at least partially dependent on light fluence and a direct comparison between ultrafast experiments and one sun steady-state conditions might be difficult.

Finally, we observed a correlation between the level of the bleaching signal at about 3 ns in the transient absorption experiment (due to larger or smaller recombination values) and the measured photocurrent of the same cells. Figure 6 D shows the representative kinetics of bleach-band recovery probed at $\lambda = 600$ nm for three different CoLiTBP cells with different J_{SC} values (two of them are cells with $TiCl_4$ treatment, but different V_{OC} values; the one with the smallest V_{OC} is a cell without $TiCl_4$ treatment). The initial apparent increase in the bleaching signal (up to about 4 ps) is due to electron injection dynamics (the positive contribution of absorption from the excited state at this wavelength diminishes within this time). As seen in Figure 6 D, the residual signal is smallest for the cell with the lowest photocurrent, and highest for the cell with the highest J_{SC}.

Thus, partial recombination occurring on a picosecond timescale has a clear impact on the performance of DSSCs. This observation is in agreement with a few recent reports in which lower or higher recombination in the sub-nanosecond range for different organic dyes was correlated with better or worse performance of the cells prepared with these dyes.[8–9, 12c–e] However, to the best of our knowledge, no detailed investigation of this recombination mechanism has been reported so far. We show that the dynamic of the sub-nanosecond recombination can be modified by the presence of potential-determining additives, and the addition of TBP is beneficial not only to increase the V_{OC} value of the cell, but also as a means of slowing down the recombination dynamics. When the conduction band shifts towards more negative potentials (and the redox positions of the dye (S^+/S, S^+/S^*) are not changed), the driving force for electron injection decreases and electron injection slows down in accordance with the Marcus normal region (strictly speaking, it is due to the density of acceptor states rather than the driving force itself, but the effect is qualitatively the same). At the same time, the driving force for electron recombination (from the titania conduction band to the ground state of the dye) increases, but the recombination process also slows down, similar to electron injection. This is probably because the energy gap for recombination is large and the process lies in the Marcus inverted region.

Conclusions

The effect of TBP additive and $TiCl_4$ treatment was studied for titania photoanodes sensitized with the popular and efficient carbazole dye MK-2 by using both iodide- and cobalt-based

liquid electrolytes. Complete solar cells were measured by using a variety of techniques: femtosecond transient absorption in the visible, NIR, and mid-IR spectral ranges; nanosecond flash photolysis; and electrochemical impedance spectroscopy. Studies on the timescales from femto- to milliseconds revealed the dynamics of electron injection, charge recombination, dye regeneration, and electron transport (see Scheme S2 in the Supporting Information or the Table of Contents graphic). In addition, the photobehavior from femto- to microseconds for the MK-2 dye in solution was also investigated.

The addition of TBP causes the well-known effect of increasing the V_{OC} of the solar cells. An increase in V_{OC} by about 150–200 mV is accompanied by slowing down of the electron injection process from about 0.2 (in electrolytes without TBP) to 1 ps (in electrolyte with 0.5 M TBP) due to a negative shift of the conduction-band potential. Interestingly, the presence of unwanted, partial, fast recombination processes occurring on the timescales of tens and hundreds of picoseconds was revealed, and its contribution correlates with the photocurrent of the cells. Moreover, the dynamics of this recombination process were found to depend on the electrolyte composition: it was slower for electrolytes with TBP (components of 20–30 and 400–500 ps) than electrolytes without TBP (components of 5–10 and 200–300 ps). The kinetics of the recombination of electrons in titania were be different in the visible, NIR, and mid-IR ranges, which indicates the occurrence of the trapping mechanism on a sub-nanosecond timescale and varying contribution of free and shallow- and deep-trapped electrons to recombination.

No difference in electron injection or fast charge recombination dynamics was observed between iodide and cobalt electrolytes for the corresponding amounts of TBP. This indicates a possible more general feature that the effects of potential-determining ions in the electrolyte are the same for cobalt and iodide electrolytes, so the large contemporary knowledge base on these effects from studies of iodide-based solar cells can be directly used in current research on cobalt-based DSSCs.

Dye regeneration was observed to proceed with a time constant of about 1 μs in all electrolytes (iodide and cobalt electrolytes, with and without TBP). On one hand, this confirms sufficient regeneration efficiency by cobalt complexes. On the other hand, no dependence on TBP addition, contrary to some recently investigated dyes with more than one COOH group, proves the important role of the dye ground-state potential on regeneration dynamics in DSSCs.

On the millisecond timescale, the electron lifetime is shorter and the recombination order (parameter *m*) is higher in cobalt-based electrolytes than in iodide-based electrolytes. This indicates the key role of electron recombination between the metal oxide and electrolyte to further improve the performance of DSSCs with one-electron redox shuttles. Moreover, cells made of electrodes without $TiCl_4$ treatment showed significantly worse performance. The decrease in the J_{SC} value could be partially explained by less dye absorption, but lower FF values and shorter electron lifetimes were certainly due to faster recombination; this is especially important for the cobalt electrolyte. The MK-2 solar cell with TBP was remarkably stable (85% of the initial photocurrent after four months). On the contrary, those without TBP, despite initially slightly higher J_{SC} values, suffered from a rapid decrease in the photocurrent, accompanied by an increase the V_{OC} value.

To the best of our knowledge, this is the first comprehensive study of all charge-separation processes in DSSCs with carbazole dyes, including the effect of electrolyte type and composition. The finding of electrolyte-dependent ultrafast charge recombination is novel for studies on DSSCs in general, and provides important implications towards better optimization of these devices. Furthermore, our work contributes to the lack of studies on complete DSSCs with cobalt-based electrolytes, especially for ultrafast and fast partial charge-separation processes. Such systems are the current champions in terms of the best laboratory efficiencies, and are the most promising candidates for further improvements in this kind of photovoltaic devices.

Experimental Section

MK-2 dye (Scheme S1 in the Supporting Information) was purchased from Sigma–Aldrich (95%). TiO_2 (P25) nanoparticles were received from Evonik. Paste with metal oxide nanoparticles was prepared as follows: First nanoparticle powder (3 g) was mixed with acetic acid (0.5 mL) and ethanol (20 mL) and left in an ultrasonic bath for 3 h. Then another solution of α-terpineol (10 mL), ethyl cellulose (1.5 g), and ethanol (13.5 g) was prepared. The two solutions were mixed together and placed in an ultrasonic bath for another hour. Afterwards, the combined solution was stirred for an additional 16 h. Finally, ethanol was removed with a rotary evaporator operating at 60 °C and the ready-to-use paste was obtained.

The films were deposited by the doctor-blade technique on FTO glass plates and heated at 450 °C for 60 min. Unless otherwise indicated, the $TiCl_4$ post-treatment was applied to the electrodes. Sintered electrodes were immersed into a 0.05 M aqueous solution of $TiCl_4$ stored at 70 °C for 30 min. Then the electrodes were washed with distilled water and sintered again at 450 °C for 30 min. Next, the films were immersed in a 0.2 mM solution of MK-2 in toluene and kept at room temperature for about 1 h. The platinized counter electrode was obtained by spreading a platinum-based solution (Platisol T, Solaronix SA) on FTO glass and annealing at 450 °C. To make a complete solar cell (an active area of 0.25 cm^2 was prepared), the counter electrode was assembled with thermal adhesive film (25 μm Surlyn, Meltronix, Solaronix SA) that acted as a separator and sealing element. The cells were filled (by the vacuum backfilling method) with the electrolytes described below.

Iodide- and cobalt-based ($Co^{II/III}$ tris(bpy) tetracyanoborate) electrolytes, both with and without TBP, were prepared in acetonitrile. The content of the individual components was as follows. For the iodide electrolyte without TBP (abbreviated further as ILi): 0.05 M I_2 (99.5%, Fluka), 0.6 M 1,2-dimethyl-3-propylimidazolium iodide (DMPII; 98%, ABCR) and 0.1 M LiI (99%, Aldrich). For the iodide electrolyte with TBP (ILiTBP): 0.05 M I_2, 0.6 M DMPII, 0.1 M LiI, 0.5 M TBP (96%, Aldrich), and 0.1 M guanidine thiocyanate (GuSCN; Aldrich). For the cobalt electrolyte without TBP (CoLi): 0.25 M $[Co(bpy)_3\{B(CN)_4\}_2]$ (Dyenamo), 0.035 M $[Co(bpy)_3\{B(CN)_4\}_3]$ (Dyenamo), and 0.1 M $LiClO_4$ (99.99% Sigma Aldrich). For the cobalt electrolyte with TBP (CoLiTBP): 0.25 M $[Co(bpy)_3\{B(CN)_4\}_2]$, 0.035 M $[Co(bpy)_3\{B(CN)_4\}_3]$, 0.1 M $LiClO_4$, and 0.5 M TBP.

The setup for ultrafast broadband transient absorption has been described previously (Helios spectrometer, Ultrafast Systems, and Spectra Physics laser system).[20] The pump pulses were set at $\lambda =$ 500 or 600 nm and the IRF (pump–probe cross-correlation function) was about 250 fs (FWHM). The pump pulse energy of 60 nJ corresponded to an energy density of about 100 $\mu J\,cm^{-2}$. In some experiments, pulses of four times higher energy (240 nJ) were also used. The transient absorption measurements were performed in the spectral ranges of $\lambda =$ 450–850 (visible) and 800–1550 nm (NIR) and in the time range of up to 3 ns. The setup for ultrafast transient absorption in the mid-IR spectral range (3–10 μm) was a 2DQuick Transient spectrometer, PhaseTech Spectroscopy. The optical parametric amplifier (OPA) with a difference frequency generation (DFG) module generated IR pulses (tunable from 3 to 10 μm). A Ge beam splitter split the IR beam into reference and probe beams, and both were focused onto the sample position, but only the probe beam overlapped with the pump beam in the sample. After passing through the sample, the probe and reference beams were spectrally dispersed in a grating spectrometer (iHR320) and independently imaged on a liquid-nitrogen-cooled HgCdTe detector (2×64 elements) with 7 nm resolution per pixel. The IRF (visible pump–IR probe cross-correlation function) was about 200 fs (FWHM). The nanosecond flash photolysis setup was based on Q-switched Nd:YAG laser and a 150 W xenon arc lamp as the excitation and probing light sources, respectively.[27] The pump pulse wavelength was set at $\lambda =$ 532 nm and the energy was set at 0.1 mJ (energy density of $\approx$250 $\mu J\,cm^{-2}$).

Global analysis of the transient absorption data was performed by using Surface Explorer software (Ultrafast Systems) or the Asufit program.[28] Both programs fit a multiexponential function (convoluted with IRF) to either the kinetic vectors of a selected number of singular values (Surface Explorer) or the kinetic traces for all analyzed wavelengths (Asufit). As a result of the analysis, the characteristic time constants were obtained as well as the wavelength-dependent amplitudes associated with them (also called decay-associated difference spectra or pre-exponential factor spectra).

Current–voltage characterization of the solar cell, total power conversion efficiency, IPCE spectra, photocurrent decays, and electrochemical impedance spectroscopy studies were performed with a potentiostat (model M101 with frequency response analyzer FRA32M module, Autolab) coupled to a photoelectric spectrometer equipped with the option of solar simulator (Instytut Fotonowy (Photon Institute), Poland). The sunlight conditions were simulated by a xenon lamp with an AM 1.5 G spectral filter and intensity adjusted to 100 $mW\,cm^{-2}$ by using a calibrated silicon cell (RR-74, Rera Systems). Electrochemical impedance spectra (10 mV perturbation in the 10^{-1}–10^{6} Hz range) in the dark and at open circuit were analyzed with Zview equivalent circuit modeling software, including the distributed element DX11 (transmission line model).[29] Unless otherwise stated, all stationary and time-resolved measurements were performed one day after preparation of the cells.

Acknowledgements

This work was supported by the NCN (National Science Centre, Poland) under project 2012/05/B/ST3/03284. J.S. is a holder of a scholarship funded within the Human Capital Operational Programme, European Social Fund. Krzysztof Dobek is kindly acknowledged for writing the program used for analysis in the mid-IR region.

Keywords: cobalt · dyes/pigments · iodine · laser spectroscopy · solar cells

[1] B. O'Regan, M. Grätzel, *Nature* **1991**, *353*, 737–740.
[2] A. Hagfeldt, G. Boschloo, L. Sun, L. Kloo, H. Pettersson, *Chem. Rev.* **2010**, *110*, 6595–6663.
[3] a) A. Yella, H.-W. Lee, H. N. Tsao, C. Yi, A. K. Chandiran, M. K. Nazeeruddin, E. W.-G. Diau, C.-Y. Yeh, S. M. Zakeeruddin, M. Grätzel, *Science* **2011**, *334*, 629–634; b) S. Mathew, A. Yella, P. Gao, R. Humphry-Baker, B. F. E. Curchod, N. Ashari-Astani, I. Tavernelli, U. Rothlisberger, M. K. Nazeeruddin, M. Grätzel, *Nat. Chem.* **2014**, *6*, 242–247.
[4] N. Koumura, Z.-S. Wang, S. Mori, M. Miyashita, E. Suzuki, K. Hara, *J. Am. Chem. Soc.* **2006**, *128*, 14256–14257.
[5] a) T. N. Murakami, N. Koumura, T. Uchiyama, Y. Uemura, K. Obuchi, N. Masaki, M. Kimurac, S. Mori, *J. Mater. Chem. A* **2013**, *1*, 792–798; b) M. K. Kashif, J. Axelson, N. W. Duffy, C. M. Forsyth, C. J. Chang, J. R. Long, L. Spiccia, U. Bach, *J. Am. Chem. Soc.* **2012**, *134*, 16646–16653.
[6] A. Abate, M. Planells, D. J. Hollman, S. D. Stranks, A. Petrozza, A. R. S. Kandada, Y. Vaynzof, S. K. Pathak, N. Robertson, H. J. Snaith, *Adv. Energy Mater.* **2014**, *4*, 1400166.
[7] K. Hara, Z.-S. Wang, Y. Cui, A. Furube, N. Koumura, *Energy Environ. Sci.* **2009**, *2*, 1109–1114.
[8] C. Koenigsmann, T. S. Ripolles, B. J. Brennan, C. F. A. Negre, M. Koepf, A. C. Durrell, R. L. Milot, J. A. Torre, R. H. Crabtree, V. S. Batista, G. W. Brudvig, J. Bisquert, C. A. Schmuttenmaer, *Phys. Chem. Chem. Phys.* **2014**, *16*, 16629–16641.
[9] a) X.-H. Zhang, J. Ogawa, K. Sunahara, Y. Cui, Y. Uemura, T. Miyasaka, A. Furube, N. Koumura, K. Hara, S. Mori, *J. Phys. Chem. C* **2013**, *117*, 2024–2031; b) R. Katoh, A. Furube, *J. Photochem. Photobiol. C* **2014**, *20*, 1–16.
[10] K. Kakiage, Y. Aoyama, T. Yano, T. Otsuka, T. Kyomen, M. Unno, M. Hanaya, *Chem. Commun.* **2014**, *50*, 6379–6381.
[11] a) M. J. Marchena, G. de Miguel, B. Cohen, J. A. Organero, S. Pandey, S. Hayase, A. Douhal, *J. Phys. Chem. C* **2013**, *117*, 11906–11919; b) A. Aljarilla, J. N. Clifford, L. Pelleja, A. Moncho, S. Arrechea, P. d. L. Cruz, F. Langa, E. Palomares, *J. Mater. Chem. A* **2013**, *1*, 13640–13647; c) P. Piatkowski, C. Martin, M. R. di Nunzio, B. Cohen, S. Pandey, S. Hayse, A. Douhal, *J. Phys. Chem. C* **2014**, *118*, 29674–29687; d) R. Li, M. Zhang, C. Yan, Z. Yao, J. Zhang, P. Wang, *ChemSusChem* **2015**, *8*, 97–104.
[12] a) J. Wiberg, T. Marinado, D. P. Hagberg, L. Sun, A. Hagfeldt, B. Albinsson, *J. Phys. Chem. C* **2009**, *113*, 3881–3886; b) W.-K. Huang, C.-W. Cheng, S.-M. Chang, Y.-P. Lee, E. W.-G. Diau, *Chem. Commun.* **2010**, *46*, 8992–8994; c) J. Wiberg, T. Marinado, D. P. Hagberg, L. Sun, A. Hagfeldt, B. Albinsson, *J. Phys. Chem. B* **2010**, *114*, 14358–14363; d) M. J. Griffith, K. Sunahara, P. Wagner, K. Wagner, G. G. Wallace, D. L. Officer, A. Furube, R. Katoh, S. Mori, A. J. Mozer, *Chem. Commun.* **2012**, *48*, 4145–4162; e) H.-Y. Hsu, C.-W. Cheng, W.-K. Huang, Y.-P. Lee, E. W.-G. Diau, *J. Phys. Chem. C* **2014**, *118*, 16904–16911.
[13] a) G. Schlichthörl, S. Y. Huang, J. Sprague, A. J. Frank, *J. Phys. Chem. B* **1997**, *101*, 8141–8155; b) G. Boschloo, L. Häggman, A. Hagfeldt, *J. Phys. Chem. B* **2006**, *110*, 13144–13150; c) F. Fabregat-Santiago, J. Bisquert, G. Garcia-Belmonte, G. Boschloo, A. Hagfeldt, *Sol. Energy Mater. Sol. Cells* **2005**, *87*, 117–131; d) B. C. O'Regan, J. R. Durrant, *Acc. Chem. Res.* **2009**, *42*, 1799–1808.
[14] a) P. M. Sommeling, B. C. O'Regan, R. R. Haswell, H. J. P. Smit, N. J. Bakker, J. J. T. Smits, J. M. Kroon, J. A. M. van Roosmalen, *J. Phys. Chem. B* **2006**, *110*, 19191–19197; b) S.-W. Lee, K.-S. Ahn, K. Zhu, N. R. Neale, A. J. Frank, *J. Phys. Chem. C* **2012**, *116*, 21285–21290.
[15] B. C. O'Regan, J. R. Durrant, P. M. Sommeling, N. J. Bakker, *J. Phys. Chem. C* **2007**, *111*, 14001–14010.
[16] a) F. Fabregat-Santiago, G. Garcia-Belmonte, I. Mora-Seró, J. Bisquert, *Phys. Chem. Chem. Phys.* **2011**, *13*, 9083–9118; b) J. A. Anta, E. Guillén, R. Tena-Zaera, *J. Phys. Chem. C* **2012**, *116*, 11413–11425.
[17] a) T. Yoshihara, R. Katoh, A. Furube, Y. Tamaki, M. Murai, K. Hara, S. Murata, H. Arakawa, M. Tachiya, *J. Phys. Chem. B* **2004**, *108*, 3817–3823; b) Y. Tamaki, K. Hara, R. Katoh, M. Tachiya, A. Furube, *J. Phys. Chem. C* **2009**, *113*, 11741–11746.
[18] a) S. A. Haque, Y. Tachibana, R. L. Willis, J. E. Moser, M. Grätzel, D. R. Klug, J. R. Durrant, *J. Phys. Chem. B* **2000**, *104*, 538–547; b) J. Nelson, S. A.

Haque, D. R. Klug, J. R. Durrant, *Phys. Rev. B* **2001**, *63*, 205321; c) A. V. Barzykin, M. Tachiya, *J. Phys. Chem. A* **2002**, *106*, 4356 – 4363.
[19] S. M. Feldt, G. Wang, G. Boschloo, A. Hagfeldt, *J. Phys. Chem. C* **2011**, *115*, 21500 – 21507.
[20] J. Idigoras, G. Burdziński, J. Karolczak, J. Kubicki, G. Oskam, J. A. Anta, M. Ziółek, *J. Phys. Chem. C* **2015**, *119*, 3931 – 3944.
[21] X. Yang, S. Zhang, K. Zhang, J. Liu, C. Qin, H. Chen, A. Islam, L. Han, *Energy Environ. Sci.* **2013**, *6*, 3637 – 3645.
[22] a) N. A. Anderson, T. Lian, *Annu. Rev. Phys. Chem.* **2005**, *56*, 491 – 519; b) M. Juozapavicius, M. Kaucikas, J. J. van Thor, B. C. O'Regan, *J. Phys. Chem. C* **2013**, *117*, 116 – 123.
[23] S. H. Szczepankiewicz, J. A. Moss, M. R. Hoffmann, *J. Phys. Chem. B* **2002**, *106*, 2922 – 2927.
[24] a) M. Ziółek, I. Tacchini, M. T. Martínez, X. Yang, L. Sun, A. Douhal, *Phys. Chem. Chem. Phys.* **2011**, *13*, 4032 – 4044; b) M. Ziółek, B. Cohen, X. Yang, L. Sun, M. Paulose, O. K. Varghese, C. A. Grimes, A. Douhal, *Phys. Chem. Chem. Phys.* **2012**, *14*, 2816 – 2831; c) M. Ziółek, J. Karolczak, M. Zalas, Y. Hao, H. Tian, A. Douhal, *J. Phys. Chem. C* **2014**, *118*, 194 – 205; d) P. W. Lohse, J. Kuhnt, S. I. Druzhinin, M. Scholz, M. Ekimova, T. Oekermann, T. Lenzer, K. Oum, *Phys. Chem. Chem. Phys.* **2011**, *13*, 19632 – 19640; e) M. Fakis, P. Hrobárik, E. Stathatos, V. Giannetas, P. Persephonis, *Dyes Pigm.* **2013**, *96*, 304 – 312; f) J. Sobuś, G. Burdziński, J. Karolczak, J. Idígoras, J. A. Anta, M. Ziółek, *Langmuir* **2014**, *30*, 2505 – 2512.
[25] M. Ziółek, X. Yang, L. Sun, A. Douhal, *Phys. Chem. Chem. Phys.* **2010**, *12*, 8098 – 8107.
[26] a) R. Katoh, A. Furube, A. V. Barzykin, H. Arakawa, M. Tachiya, *Coord. Chem. Rev.* **2004**, *248*, 1195 – 1213; b) H. Němec, J. Rochford, O. Taratula, E. Galoppini, P. Kužel, T. Polívka, A. Yartsev, V. Sundström, *Phys. Rev. Lett.* **2010**, *104*, 197401; c) D. Stockwell, Y. Yang, J. Huang, C. Anfuso, Z. Huang, T. Lian, *J. Phys. Chem. C* **2010**, *114*, 6560 – 6566.
[27] G. Burdziński, J. Karolczak, M. Ziółek, *Phys. Chem. Chem. Phys.* **2013**, *15*, 3889 – 3896.
[28] E. Katilius, J. Hindorff, N. Woodbury, 2.6 ed., program available at http://www.public.asu.edu/~laserweb/asufit/asufit.html.
[29] J. Bisquert, *J. Phys. Chem. B* **2002**, *106*, 325 – 333.

Received: July 13, 2015
Published online on August 3, 2015

CHEMISTRY & SUSTAINABILITY
CHEMSUSCHEM
ENERGY & MATERIALS

Supporting Information

Carbazole Dye-Sensitized Solar Cells Studied from Femtoseconds to Seconds—Effect of Additives in Cobalt- and Iodide-Based Electrolytes

Jan Sobuś,[a, b] Jacek Kubicki,[b] Gotard Burdziński,[b] and Marcin Ziółek*[b]

cssc_201500628_sm_miscellaneous_information.pdf

Scheme S1.

Molecular structure of MK-2 dye.

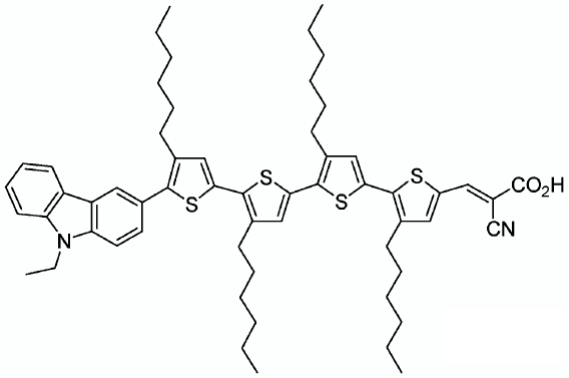

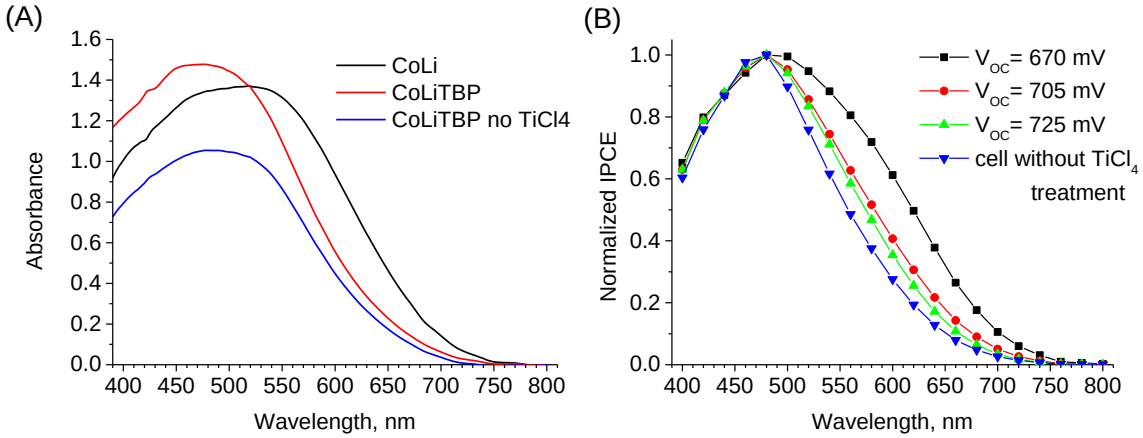

Figure S1. (A) Steady-state absorption spectra of the indicated cells. The absorbance of pure TiO_2 layer was subtracted from all the spectra. (B) Normalized IPCE spectra for different CoLiTBP cells with $TiCl_4$ treatment (giving indicated photovoltage) and without $TiCl_4$ treatment.

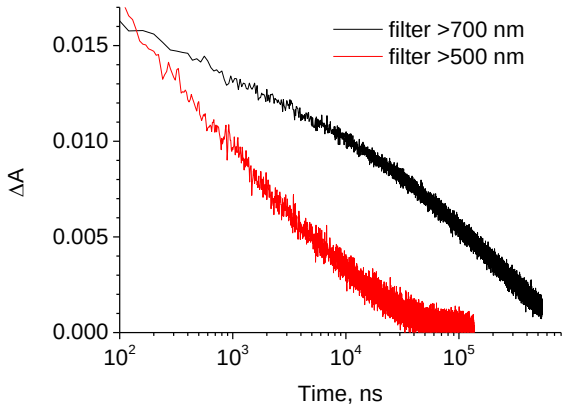

Figure S2. Kinetics measured at 730 nm (with excitation at 535 nm, 0.1 mJ) obtained in flash photolysis experiments of ILiTBP cell with the filters passing the probing light longer than 500 nm and 700 nm, respectively.

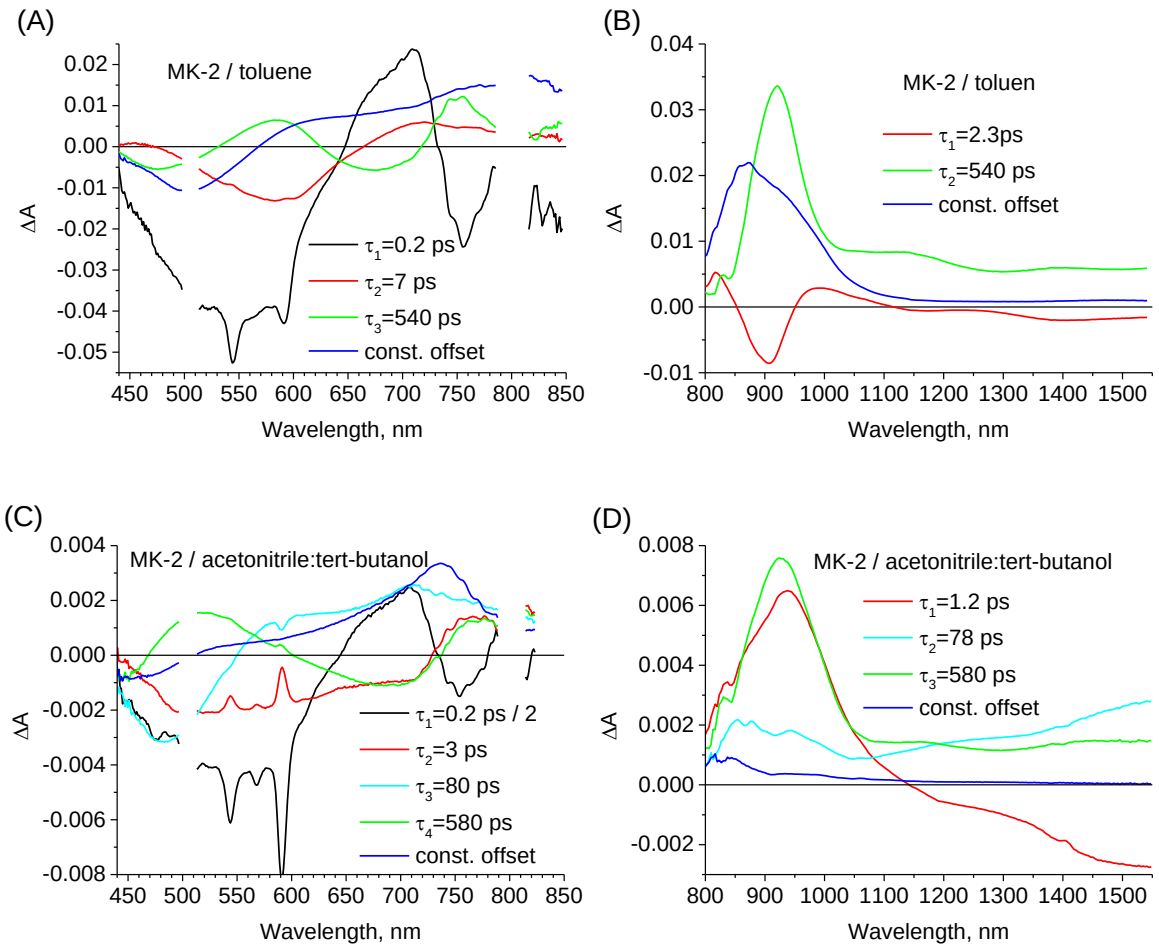

Figure S3. Wavelength dependent amplitudes of the indicated time constants obtained from global analysis of transient absorption spectra of MK-2 in (A, B) toluene and (C, D) acetonitrile-terbutanol mixture. The pump pulse (200 nJ) was at 500 nm, and the spectra were probed in VIS (A, C) and NIR (B, D) ranges.

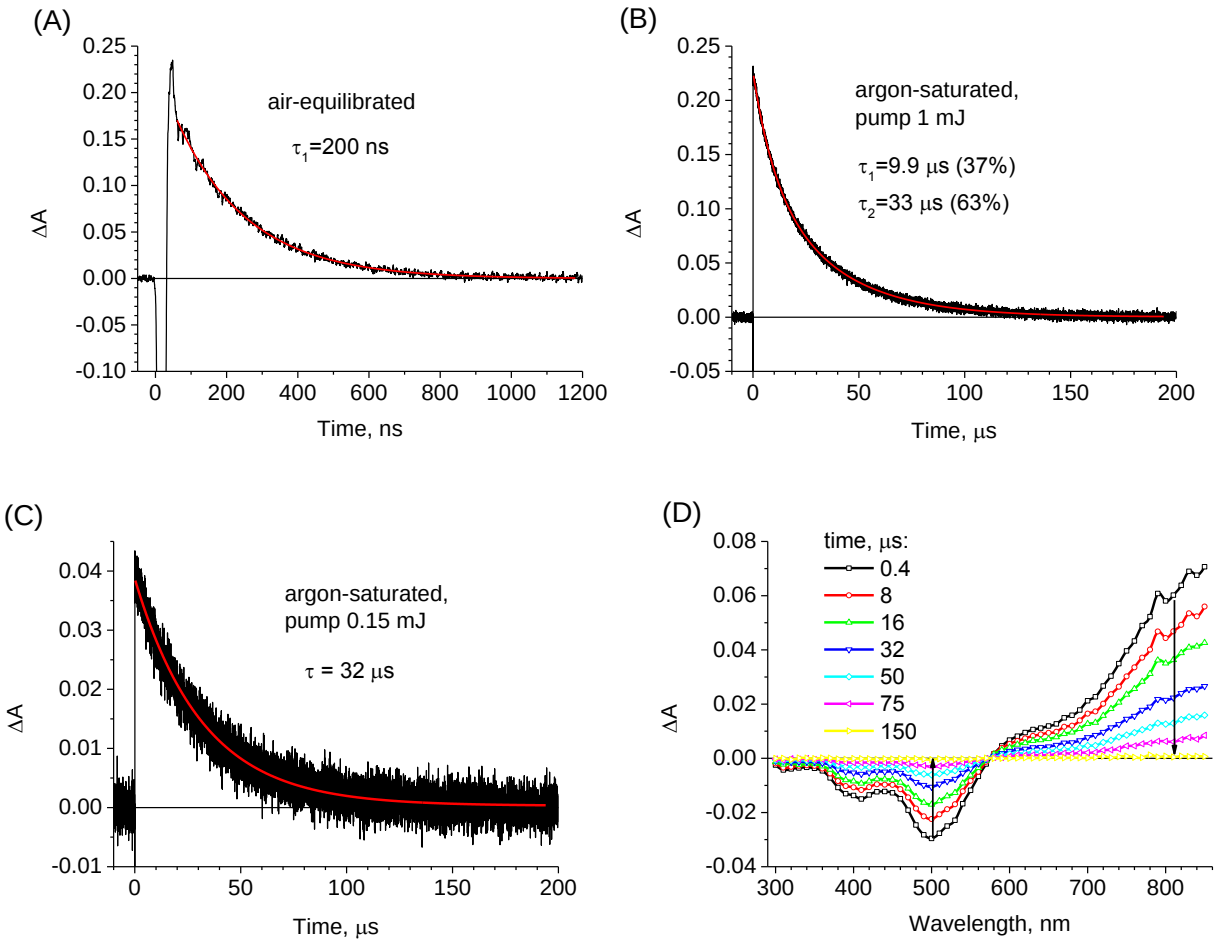

Figure S4. Kinetics measured at 750 nm (with excitation at 535 nm) obtained in flash photolysis experiments of MK-2 in toluene in: (A) air-equilibrated conditions, (B) argon-saturated conditions for pump 1 mJ and (C) argon-saturated conditions for pump 0.15 mJ. The solid red lines shows the best one- or two-exponential fit with the indicated time constants. About two orders of magnitude increase in the time constants of the samples without oxygen (with respect to those in air- equilibrated conditions) indicates the triplet state origin of the observed transient absorption signal. The additional, faster component under higher pump energy (1 mJ vs 0.15 mJ) in argon-saturated sample is probably due to the triplet-triplet annihilation process. (D) Transient absorption spectra for the indicated times after pump pulse (0.15 mJ, 535 nm) for the sample in argon-saturated conditions.

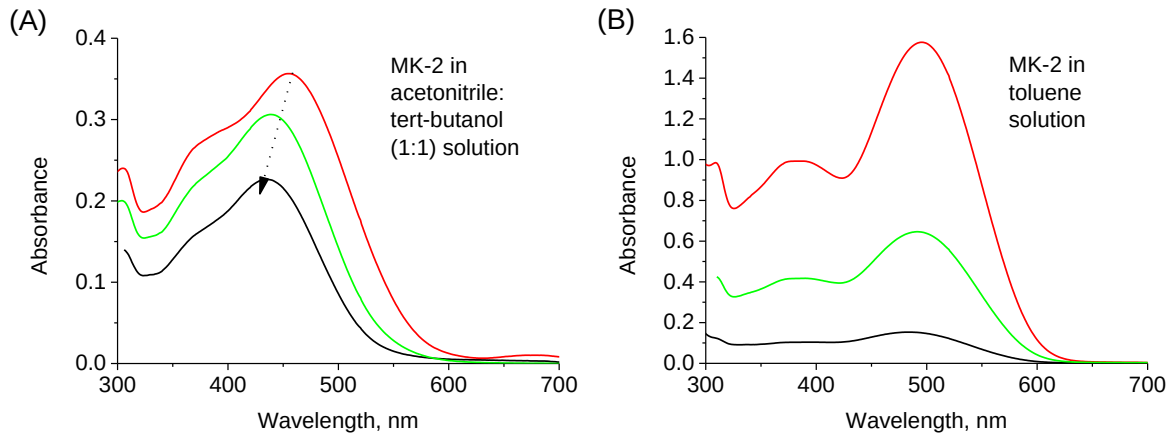

Figure S5. Steady-state absorption spectra of MK-2 in: (A) acetonitrile:tert-butanol (1:1) and (B) toluene solutions. Different MK-2 concentrations and 2 mm cells were used for the measurements.

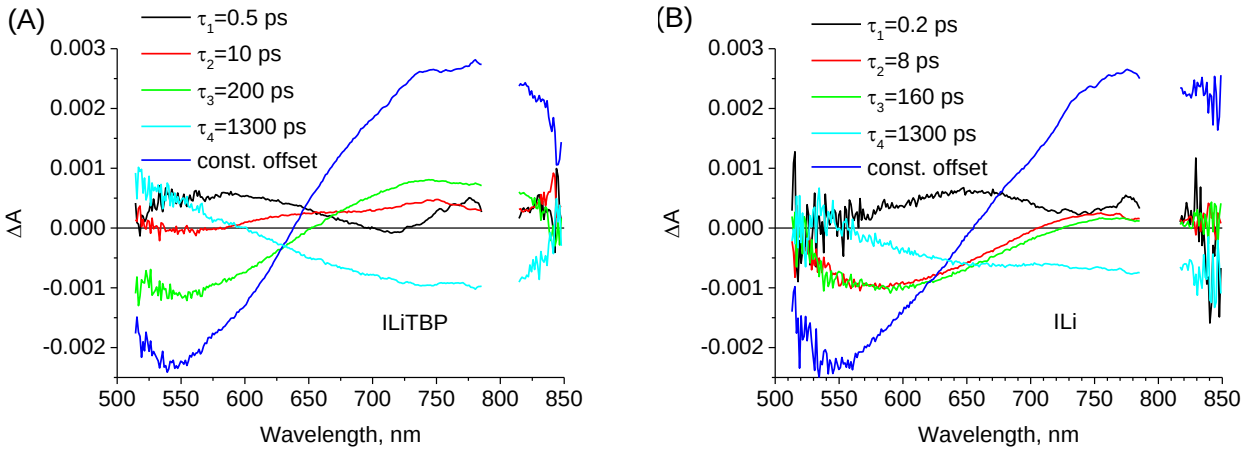

Figure S6. Effect of additional component in global analysis of the transient absorption of the cells. Wavelength dependent amplitudes of the indicated time constants obtained from global analysis of transient absorption spectra of iodide cells in the VIS range (compare with Figure 5C and 5D). The inverse of the spectrum of additional component with 1300 ps time constant (rising amplitude) is similar to the trapped electrons band extracted in flash photolysis (compare with longer component in Figure 2A).

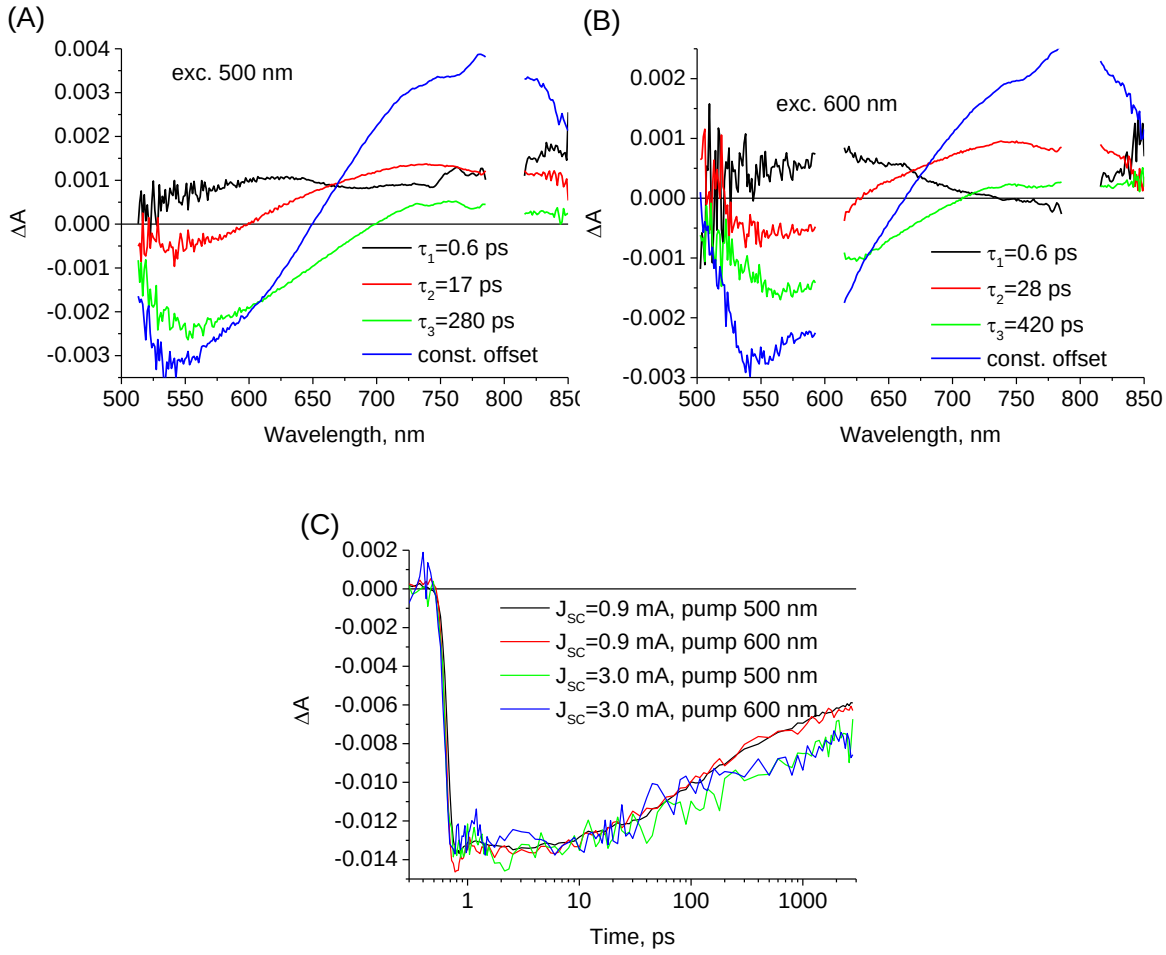

Figure S7. Effect of excitation wavelength on transient absorption spectra. (A, B) wavelength dependent amplitudes of the indicated time constants obtained from global analysis of transient absorption spectra of the same CoLiTBP cell under excitation with 60 nJ pulses centered at (A) 500 nm and (B) 600 nm. (C) Kinetic traces at 500 nm measured for different CoLiTBP cells having different indicated J_{SC} parameters (measured under 1 Sun) and under different indicated excitation wavelength. The time zero is shifted to 1 ps in order to present the time axis in logarithmic scale. Within each cell, the residual amplitude of the signal is the same for 500 nm and 600 nm excitation, while it is smaller for the cells with smaller photocurrent, as explained in more details in Figure 6D.

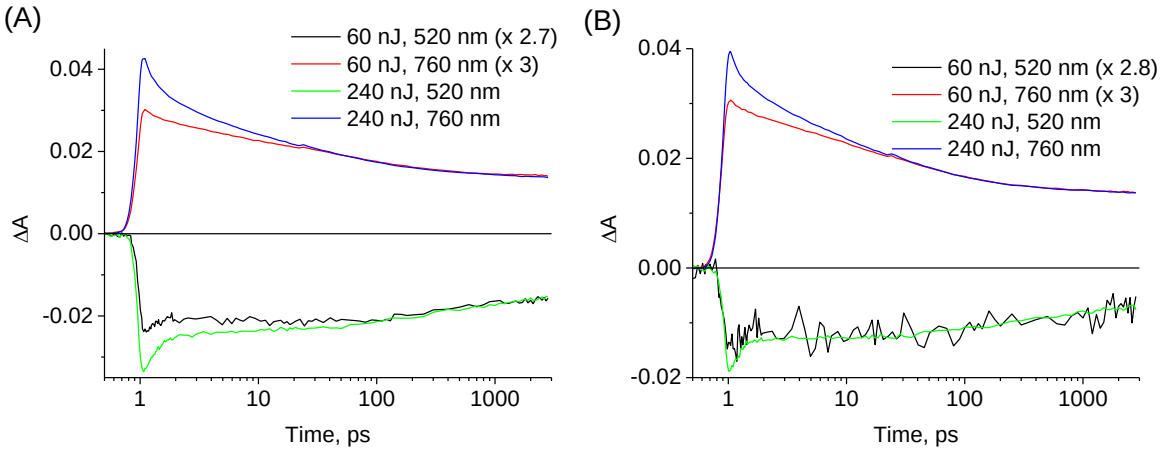

Figure S8. Effect of excitation fluence on transient absorption spectra in (A) ILiTBP and (B) CoLiTBP cells. Kinetic traces at 520 nm and 760 nm measured for different indicated pump fluence (60 nJ or 240 nJ). The normalization factors are also given in insets. The time zero is shifted to 1 ps in order to present the time axis in logarithmic scale.

Scheme S2.

Scheme of energetic levels and electron transfer time constant for MK-2 cell.

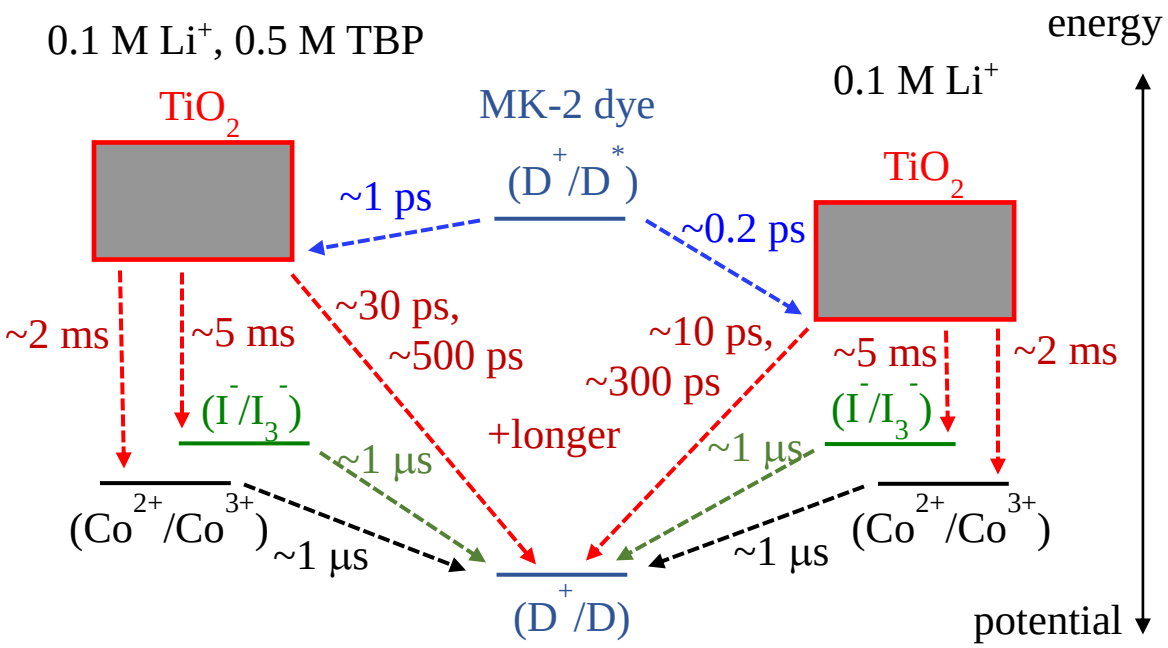

(titania – electrolyte recombination times are at V_{OC})

Materials Chemistry and Physics 170 (2016) 218–228

Contents lists available at ScienceDirect

Materials Chemistry and Physics

journal homepage: www.elsevier.com/locate/matchemphys

Effect of different photoanode nanostructures on the initial charge separation and electron injection process in dye sensitized solar cells: A photophysical study with indoline dyes

Jesús Idígoras [a], Jan Sobuś [b, c], Mariusz Jancelewicz [b], Eneko Azaceta [d], Ramon Tena-Zaera [d], Juan A. Anta [a], Marcin Ziółek [c, *]

[a] Nanostructured Solar Cells Group, Department of Physical, Chemical and Natural Systems, Universidad Pablo de Olavide, Ctra. Utrera, km 1, ES-41013 Seville, Spain
[b] NanoBioMedical Centre, Adam Mickiewicz University, Umultowska 85, 61-614 Poznań, Poland
[c] Quantum Electronics Laboratory, Faculty of Physics, Adam Mickiewicz University in Poznań, Umultowska 85, 61-614 Poznań, Poland
[d] Materials Division, IK4-CIDETEC, Parque Tecnológico de San Sebastián, Paseo Miramón 196, Donostia-San Sebastián, 20009, Spain

HIGHLIGHTS

- Wide variety of morphologies and preparation methods has been checked for ZnO cells.
- All ZnO cells work worse than TiO_2 ones.
- Effective refractive index might be an additional factor in solar cell performance.
- Excited charge transfer state of indoline dyes participates in the charge separation.

GRAPHICAL ABSTRACT

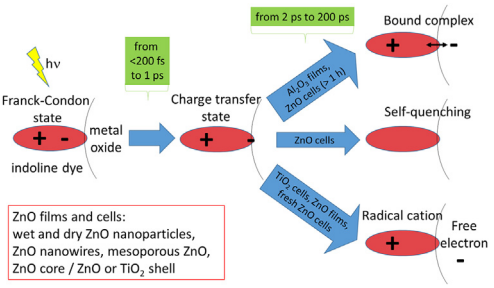

ARTICLE INFO

Article history:
Received 18 March 2015
Received in revised form
26 October 2015
Accepted 19 December 2015
Available online 31 December 2015

Keywords:
Optical properties
Electrical properties
Nanostructures
Interfaces

ABSTRACT

Ultrafast and fast charge separation processes were investigated for complete cells based on several ZnO-based photoanode nanostructures and standard TiO_2 nanoparticle layers sensitized with the indoline dye coded D358. Different ZnO morphologies (nanoparticles, nanowires, mesoporous), synthesis methods (hydrothermal, gas-phase, electrodeposition in aqueous media and ionic liquid media) and coatings (ZnO–ZnO core–shell, ZnO–TiO_2 core–shell) were measured by transient absorption techniques in the time scale from 100 fs to 100 μs and in the visible and near-infrared spectral range. All of ZnO cells show worse electron injection yields with respect to those with standard TiO_2 material. Lower refractive index of ZnO than that of TiO_2 is suggested to be an additional factor, not considered so far, that can decrease the performance of ZnO-based solar cells. Evidence of the participation of the excited charge transfer state of the dye in the charge separation process is provided here. The lifetime of this state in fully working devices extends from several ps to several tens of ps, which is much longer than the typically postulated electron injection times in all-organic dye-sensitized solar cells. The results here provided, comprising a wide variety of morphologies and preparation methods, point to the universality of the poor performance of ZnO as photoanode material with respect to standard TiO_2.

* Corresponding author.
E-mail address: marziol@amu.edu.pl (M. Ziółek).

http://dx.doi.org/10.1016/j.matchemphys.2015.12.042
0254-0584/

1. Introduction

ZnO nanostructures are widely investigated in the group of emerging photovoltaics as promising solutions for pushing the cost-efficiency beyond the reach of contemporary crystalline devices. They are especially explored as photoanodes for dye-sensitized solar cells (DSSC) [1] and n-contacts in both inverted polymer solar cells [2,3] and recently introduced perovskite cells [4,5]. However, in DSSC the predominantly used TiO_2 nanoparticle photoanodes give the record efficiencies of 13% [6], while for the cells based on ZnO the best efficiency is only 7.5% [7]. The difference may seem strange since both oxides share similar energy band properties, with ZnO having much higher carrier mobility (suggesting more favorable transport properties) and an additional useful property of being able to be easily prepared in multitude of morphologies using easy wet methods [1].

Although a large variety of ZnO nanostructures has been proposed to be used as anodes in DSSCs [1], nanoparticles [7,8], nanowire arrays – including more complex variants such multi-branched and hierarchical structures [9–11] – and mesoporous films [12] can be highlighted as those which have attracted most attention. Special interest on the core–shell nanostructures should also be noted [7,13].

In a recent contribution some of us analyzed the performance of ZnO-based DSSC, especially from the point of view of charge separation efficiency within the photoanode on the millisecond time scale [8]. One of the conclusions was that these properties can be at least as good as those of TiO_2 materials. Thus ZnO interaction with dyes and electrolyte is probably the main limiting factor lowering the initial charge injection yield in ZnO-based cells [1,14]. However, the detailed knowledge about such initial charge separation processes in DSSC is still incomplete, especially for the conditions of fully working devices and for a variety of nanostructures. One of the reasons is that the ultrafast dynamics of the interaction of dyes (especially all-organic) with metal oxide nanomaterials, explored by time-resolved laser techniques, is not understood well enough, even for standard TiO_2 nanoparticles.

In this article, the electron injection and dye regeneration dynamics in the most representative architectures of ZnO-based DSSC photoanodes of different morphology (nanoparticles, nanowires, mesoporous, core–shell structures), prepared by different synthesis methods (hydrothermal, gas-phase, electrodeposition in aqueous media and ionic liquid media) [15–17], and sensitized by a fully organic, very absorptive dye are studied. The dynamics and efficiency of these processes is compared to standard TiO_2 nanoparticles with the same dye, i.e. the indoline dye coded D358. Furthermore, as a second objective, an extended analysis of the fundamental processes ongoing during electron injection from the D358 dye and the fingerprints of these processes in transient absorption results, a tool necessary for investigation on ultrashort time scales, is reported. Indoline dyes are a very promising family of all-organic dyes with high extinction coefficient, with best sunlight conversion efficiencies of around 10% [18–20]. The most popular member of this family is D149, which has been recently studied in complete cells by some of us with time-resolved laser spectroscopy techniques [21–23]. In this contribution, its newer modification, D358 dye [24,25], is used. The difference between them is that D358 has two anchoring carboxylic groups and a longer hydrocarbon chain preventing formation of aggregates by steric repulsion. Therefore, both the geometry of the dye attached to the metal oxide surface and the average distance between the dyes might be different for D149 and D358, which can influence e.g. the self-quenching process and electron injection dynamics.

2. Material and methods

The ZnO anodes with different morphologies were prepared by a variety of wet-chemistry techniques, among the most frequently reported to obtain each ZnO nanostructure in particular. Briefly, the ZnO nanoparticles (ZnO NPH) were synthesized by a forced hydrothermal method from reaction of zinc acetate and NaOH in ethanol [26]. The ZnO nanowire arrays (ZnO NW) were electrodeposited from aqueous electrolytes as explained elsewhere [16,27]. The mesoporous ZnO films (ZnO MP) were electrodeposited from ionic liquid-based electrolytes, further details can be found elsewhere [17]. Fig. 1 shows the cross-section FESEM micrographs of the different anodes investigated here.

Some ZnO NW anodes were coated with a thin ZnO or TiO_2 film in order to obtain core–shell nanowires. For ZnO/ZnO core–shell nanowires, the ZnO shell was deposited by the protocol previously reported [16], but varying the number of cycles (i.e. 10 – ZnO NW CS10 and 25 – ZnO NW CS25). For ZnO/TiO_2 core shell photoanodes, the ZnO NW array or ZnO NPH samples were placed in the ALD reactor (Picosun). The TiO_2 thin films were deposited onto the ZnO photoanodes using $TiCl_4$ (titanium tetrachloride) and DI water as ALD precursors. Nitrogen (N_2) flow was used as a carrier and a purging gas. $TiCl_4$ precursor and DI water were evaporated at 20 °C. In this study, the standard cycle consisted of 0.1 s $TiCl_4$ exposure, 3 s N_2 purge, 0.1 s exposure to water and 4 s N_2 purge. The total flow rate of the N_2 was 150 sccm. TiO_2 thin films were grown at 300 °C.

For the comparison, ZnO nanoparticles prepared by gas-phase method (ZnO NPG) were also used, as for the photoanodes in our previous studies for D149 dye [22,23]. Such ZnO films were prepared from a commercial (Evonik) dispersion of hydrophilic nanoparticles of ZnO in water (VP AdNano@Zn20, 35 wt.%) with approximate nanoparticle size of 20 nm. Except the ZnO/ZnO core–shell nanowire arrays, all ZnO anodes were annealed at 420 °C in air before sensitization. TiO_2 solar cell devices were fabricated using films consisting of a layer of 20 nm TiO_2 nanoparticles (Dyesol© paste). Films were deposited onto the conducting glass substrates with the screen printing method, and gradually heated under airflow until 500 °C. After sintering the films, an immersion step in a solution of $TiCl_4$ (40 mM) at 70 °C for 30 min was carried out.

The mean thickness values of the different anodes are the following: 1 μm for ZnO NPG, 2 μm for both ZnO NW and ZnO MP, 3.5 μm for ZnO NPH, and 6 μm for TiO_2. The different film thickness resulted in different absorption of the dye on different photoanodes. Therefore, as will be presented in the next section, the relative photocurrent (divided by the number of absorbed photons estimated from the stationary absorption) was used to compare the performance of the different cells. In transient absorption studies the film thickness was not important because the initial signal is proportional to the number of photoexcited dye molecules, and only the normalized kinetics of different photoanodes were compared.

The photoanodes were prepared by sensitization with the D358 indoline dye (Mitsubishi Paper Mills Limited). The anodes were immersed in a 5×10^{-4} M dye and 7×10^{-4} M chenodeoxycholic acid in acetonitrile/tert-butanol (1:1) solution. The samples remained immersed for 55 min and were subsequently rinsed with the same solvent.

The cells were filled with two electrolytes, both in acetonitrile solvent. The first one (EL1) contains: 0.05 M I_2 (99.5%, Fluka), 0.6 M DMPII (1,2-Dimethyl-3-propylimidazolium iodide, >98%, Iolitec), 0.1 M LiI (99%, Aldrich), 0.5 M TBP (4-tert-butylpiridine, 96%, Aldrich) and 0.1 M GuSCN (guanidine thiocyanate, Aldrich). The second electrolyte (EL2) does not contain TBP and was used for several samples to check the effect of shifting metal oxide conduction band towards more positive potentials. It contains: 0.05 M

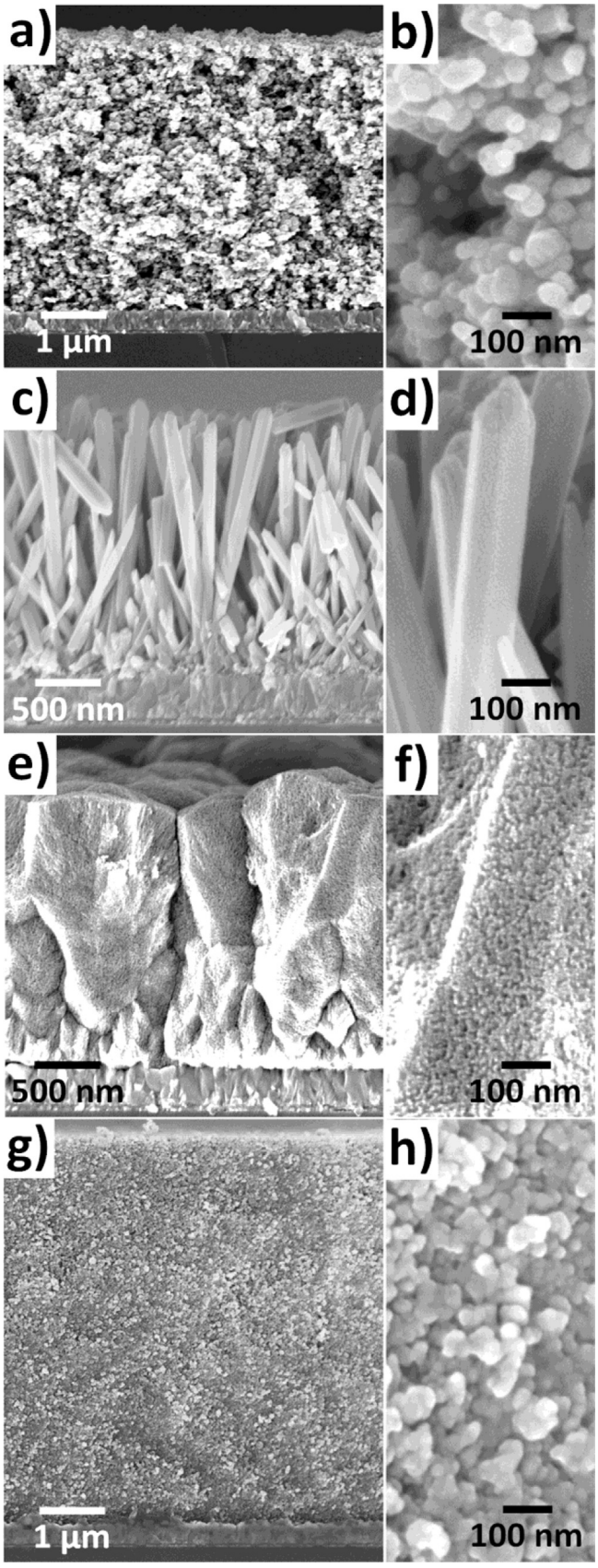

Fig. 1. FESEM micrographs of the cross section of the different architecture anodes. a,b) ZnO nanoparticle-based (ZnO NPH), c,d) ZnO nanowire arrays (ZnO NW), e,f) mesoporous ZnO film (ZnO MP) and g,h) TiO_2 nanoparticle-based.

I_2, 0.6 M BMPII (1-butyl-3-methylimidalozlium iodide, 99%, Aldrich) and 0.1 M LiI.

The setup for ultrafast broadband transient absorption has been described before (Helios spectrometer, Ultrafast Systems, and Spectra Physics laser system) [23]. The pump pulses were at 555 or 520 nm and the IRF (pump-probe cross correlation function) was 250–300 fs (FWHM). The pump pulse energy of 500 nJ corresponds to energy density of about 1 mJ/cm^2. In some experiments the pulses of higher or lower energy were also used. The transient absorption measurements were performed in the spectral ranges 450–800 nm (VIS) and 800–1500 (NIR) and in the time range of up to 3 ns. The nanosecond flash photolysis setup was based on Q-switched Nd:YAG laser and a 150 W xenon arc lamp as the excitation and the probing light sources, respectively [21]. The pump pulse wavelength was 532 nm and probe wavelength was 670 nm.

The steady-state UV–visible absorption spectra were measured with a UV-VIS-550 (Jasco) spectrophotometer. A current–voltage characterization of the solar cell, total power conversion efficiency, incident photon to current efficiency (IPCE) spectra, photocurrent decays and electrochemical impedance spectroscopy studies were performed with a potentiostat (model M101 with frequency response analyzer FRA32M module, Autolab) coupled to photoelectric spectrometer with the option of solar simulator (Instytut Fotonowy – Photon Institute, Poland). The sunlight conditions were simulated either by a white light LED lamp or by a Xe lamp with AM 1.5 G spectral filter and intensity adjusted to 100 mW/cm^2 using a calibrated silicon cell (RR-74, Rera Systems). Electrochemical impedance spectra (10 mV perturbation in the 10^{-1}–10^6 Hz range) in the dark and at open circuit were analyzed with Zview equivalent circuit modeling software, including the distributed element DX11 (transmission line model) [28]. The morphology of the nanostructure films were analyzed using a ULTRA plus ZEISS field emission scanning electron microscope (FESEM).

3. Results and discussion

3.1. Photovoltaic parameters and regeneration rates

Fig. 2A presents representative steady-state absorption of D358 on ZnO NPH and ZnO NW films in air. The maximum of the absorption band lies between 520 and 530 nm in all samples investigated, which is about 10–20 nm red shifted with respect to that of D149 dye [22,23].

Table S1 collects the photovoltaic parameters (short circuit current, J_{SC}, and open circuit voltage, V_{OC}) of the cells made with different TiO_2 and ZnO films. All ZnO cells were filled with EL1, while TiO_2 cells were made with both electrolytes (EL1 and EL2). The parameters obtained are generally consistent with the previous reports [15–17]. However, some differences are observed, especially for the V_{OC}, although a different electrolyte is used here (EL1 electrolyte contains TBP). It should also be noted that photovoltaic characterization has been done here for “fresh” cells, in contrast to the previous reports, and degradation of the dye, as noted below, may significantly influence the reported values of *Jsc* for indoline-sensitized ZnO electrodes. The absorbance of all ZnO samples is smaller than that of TiO_2 ones because of smaller thickness of the nanoporous film and/or smaller surface area (ZnO nanoparticle size is generally larger). Within ZnO samples, the absorbance is smaller for ZnO NW than for ZnO NPH because the layer thickness of the former was smaller than for the latter (Fig. 1) and active surface area of nanowires can be smaller than that of nanoparticles. The relative photocurrent (J_{SC}/N_{ph}, Table S1A) of all ZnO cells is about 2 times smaller than that of TiO_2 cells (with electrolyte EL1). We also checked that the relative photocurrent is comparable for ZnO

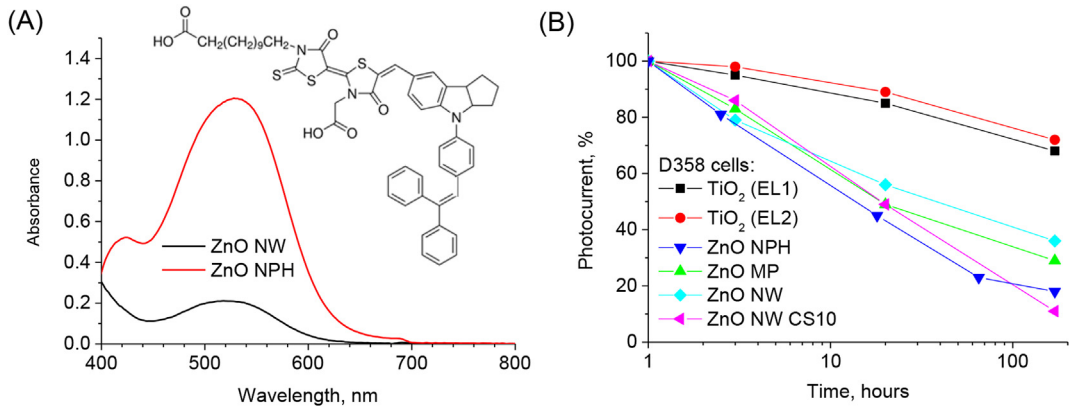

Fig. 2. (A) Representative steady-state absorption of D358 on indicated ZnO films. The light scattered from the film was subtracted. The inset shows the structure of D358 dye. (B) Decrease of the photocurrent of the cells (stored in the dark) with time.

nanoparticles prepared by both gas phase (NPG) and hydrothermal (NPH) techniques (Table S1B). The difference between ZnO and TiO_2 materials is similar to our previous observation for D149-sensitized solar cells (3 times difference between ZnO and TiO_2 nanoparticles) [22,23]. The reason for this behavior for D149 cells was worse initial charge separation, and evidences for similar explanation for D358 cells will be brought in the next sections. Table S1 also reveals that TiO_2 cell with electrolyte EL2 (with LiI but without TBP) exhibits a well-known and expected behavior: V_{OC} is smaller (by 90 mV with respect to the cell with EL1), due to the positive shift of the potential of the conduction band, while J_{SC} becomes larger (17.5 vs. 13.0 mA/cm^2), due to larger electron injection driving force and more efficient charge separation. Slightly lower V_{OC} values for all ZnO cells with respect to TiO_2 ones can be explained by worse charge separation in the former samples, affecting both J_{SC} and V_{OC}.

We also checked how fast all D358 cells decrease their performance. Fig. 2B shows a decrease in the photocurrent (with respect to the initial one shown in Table S1 and measured 1 h after cell preparation). Similar to our previous report on D149 [23], we observed a much faster degradation of the J_{SC} in ZnO cells than in TiO_2 ones. For example, after 1 day stored in the dark it drops to 90% of its initial value for titania cells and to about 50% of its initial value for ZnO cells. Similar decrease is observed in all ZnO materials (NPH, MP, NW), so it does not depend on the photoanode morphology. Moreover, the degradation has been observed to be independent from the synthesis methods as well (ZnO NPG vs ZnO NPH, Fig. S1A). One of the possible explanations of the degradation might be the desorption of the dye in certain electrolytes [23,29,30]. However, as will be evidenced below, no contribution of free dyes in the electrolyte is observed in transient absorption studies. Therefore, after the desorption the dye molecules should attach again to the new places on the surface. Interestingly, the absorption spectrum of the cells do not change during the decrease in the photocurrent, and after sufficiently long time (2–3 months) J_{SC} of the cells drops to the 10–15% of its initial value, both for TiO_2 and ZnO materials.

The ZnO cells with TiO_2 coating showed very small photocurrents, probably due to the poor charge transfer between the two materials in longer (ms) time scales (see Tables S2–S4, Figs. S2–S5 and the characterization of such cells in SI). Moreover, in Fig. S1B we report the temporal photodegradation of the TiO_2-coated samples, which shows that this process is as fast as for bare ZnO cells (compare with Fig. 2B).

To compare time constants of dye regeneration in different D358 cells, transient absorption studies in ns–μs range were applied under excitation density of 1.3 mJ/cm^2 (532 nm, energy 0.5 mJ per pulse). We chose 670 nm as probe wavelength because it is close to the maximum absorption of the dye radical cation (see next section). A decay at this wavelength (examples shown in Fig. S6) is due to decrease in the population of radical cation, while the negative offset is due to the transient Stark shift originating from the electric field of electrons in nanoparticles [21]. In principle, the radical cation decay might reflect the regeneration dynamics as well as recombination (between electrons in metal oxide and dye) [31]. However, recombination dynamics strongly depend on the excitation intensity [32–34], while in our case the kinetics are hardly changed when pump pulses of energy 5 times smaller or 4 times higher were applied for TiO_2 cells (Fig. S6). Therefore, we can assume that only regeneration process is explored in this experiment [14].

The kinetics at 670 nm (after shifting residual offset to zero and normalization of the amplitudes) are shown in Fig. 3, while the fitted decay time constants (τ_{reg}) are presented in Table 1. The fastest time constants are observed for titania cells. Within these cells faster decay (τ_{reg} = 0.34 μs vs τ_{reg} = 0.57 μs) is observed for electrolyte without TBP. This observation can be explained by the recently claimed shifting of HOMO level potential of the dyes under the presence of potential-determining additives in electrolyte [35], recently confirmed by some of us [14]. With more positive shift in

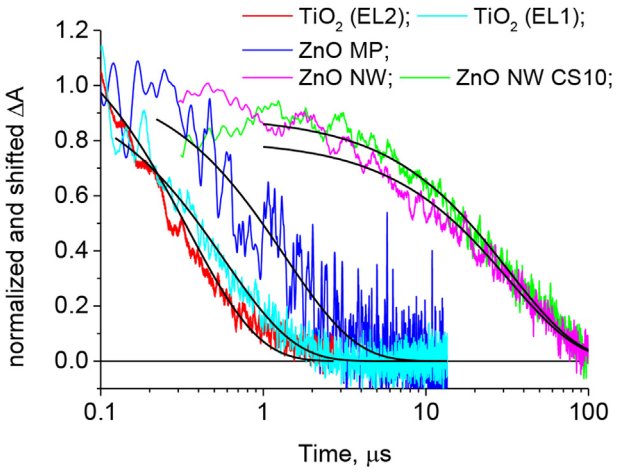

Fig. 3. Transient absorption kinetics probed at 670 nm (excitation 532 nm, 1.3 mJ/cm^2), attributed to dye regeneration. For better comparison, the kinetics are shifted to have the residual offset at zero and the amplitudes are normalized to 1. The black lines show the best fit using one-exponential function with the time constants given in Table 1.

the potential (EL2 vs. EL1) the driving force for dye regeneration becomes larger in the normal Marcus region. On the other hand, ZnO mesoporous cells exhibit about 3–4 times slower dye regeneration than titania cells in the same electrolyte (EL1). Similar slower regeneration was observed previously by us for D149-sensitized cells with ZnO nanoparticles from gas-phase methods, as well as for N719-sensitized cells with ZnO nanoparticles prepared by hydrothermal method [14,21]. Finally, a remarkably slow dye regeneration process is found for ZnO nanowire samples (one order of magnitude slower with respect to ZnO mesoporous cells).

3.2. Electron injection observed in femtosecond transient absorption

We started the femtosecond transient absorption studies with the reference measurements of D358 dye in ACN:tert-butanol (1:1) solution (the same as the one used for sensitization) in order to identify the transient states participating in the internal deactivation of the dye. The results obtained were similar to those found by us and other groups earlier for D149 dye [22,23,36–38]. Fig. S7 presents the results of global analysis in combined VIS and NIR ranges. The spectra associated with the fitted components represent the amplitudes of each pre-exponential factor at a certain wavelength (positive value indicates a decay of transient absorption signal, negative value – a rise of ΔA). The results show the participation of an initially excited Franck-Condon (FC) state (with maximum around 700 nm), which decays according to a time constant of around 300 fs. It should be commented that in our previous work [23] we noted such initial state as locally excited (LE) state, and that notation was not strictly correct because in the electronic transition the electron density is directly moved from donor part to acceptor part of the dye. After adoption of nuclear coordinates to the new electronic configuration, an intramolecular charge transfer (CT) state is formed, which suffers from solvation relaxation with time constants 2 and 23 ps. Additionally, a relaxed CT state (with maximum around 600 nm) is detected. This state decays with a 340 ps time constant, which is slightly faster than the corresponding decay observed for D149 in the same solvent mixture (420 ps) [23]. It should be also noted that in our notation CT name does not refer to the bound radical-electron pair (see below).

Transient absorption of the complete cells made with different nanostructures, as well as separated films sensitized with D358 (without electrolyte), were also measured. The measurements were performed 1–2 h after sample preparation to avoid degradation (Fig. S8). Figs. 4 and 5 present representative spectra for selected time delays between pump and probe pulses in VIS and NIR ranges, respectively.

The spectra are the combination of positive transient absorption from the species participating in the excitation and electron injection (FC and CT states of the dye, bound radical cation–electron complex, free radical-cation and electrons in semiconductor) and negative signals due to depopulation of the ground state of the dye (roughly between 500 and 600 nm) and transient Stark shift signals above 600 nm (which also contribute to positive signals for shorter wavelengths). The lack of some parts of depopulation bands in TiO_2 and Al_2O_3 samples in VIS range is due to the high absorbance of the samples in that region, which hinders the passing of probing light through the sample. Spectra for additional samples are shown in Figs. S9–S10. The results reported here for D358 dye and TiO_2 and ZnO NPH photoanodes are consistent with previous reports for the D149 dye [22,23]. As the D358 has a longer chain between electron donor and acceptor group and possess two COOH groups instead of one like the simpler D149 molecule, the present results point to the interesting conclusion that the different molecular structure of the dye does not influence significantly their early time photodynamics in DSSC.

The more efficient electron injection is, the higher the amplitudes of the final spectra (at 2.5 ns, Figs. 4 and 5) are, with respect to the initial ones. The characteristic bands of D358 radical cation (whose concentration is proportional to the number of injected electrons) lie at around 670 nm in the VIS range and 1300–1400 nm in the NIR range (Figs. 4A and 5A) [39]. In the NIR range it is a combined contribution of absorption of radical cation and electrons in TiO_2 or ZnO. Additionally, another measure of the efficiency of electron injection is the observation of the Stark shift signal, which is due to the presence of electric field generated by electrons in titania [21,39–42]. As more electrons are accumulated in the semiconductor, the larger the Stark shift becomes, and the negative signals in VIS range move further to the red (the highest shift is observed for TiO_2/EL2 sample – up to 660 nm) [21,39]. In the Al_2O_3 photoanode that we use as a reference, the electron injection is not possible due to the more negative position of the conduction band edge. However, contrary to the results for D358 in solution, there is a non-zero residual spectrum of D358 in Al_2O_3 films with the maximum at around 1100 nm (Fig. 5D). This could be assigned to the bound radical cation–electron complex. Hence, this is not a true injection of electrons, but the formation of an initial charge separation at the surface, that does not lead to the creation of a significant photocurrent and is subjected to geminate recombination. The possible explanation of the existence of such bound radical cation–electron complex might be the electron transfer, either to the very deep trap states below conduction band in alumina or to the trap states due to the presence of trace impurities in commercial Al_2O_3 nanopowder. Such spectra can be also recognized for all ZnO cells (Fig. 5B,C), indicating the existence of long-lived electron-dye cation pairs that do not appear in TiO_2. This effect has already been discussed in previous reports, and it is attributed to the larger dielectric constant of TiO_2 [1,14].

It should be emphasized that the reasons for the long-living bound complex of radical cation and electrons is completely different in Al_2O_3 and ZnO: in the first case the electrons are trapped because the position of the conduction band edge is too negative, while in the latter the complex exist due to electrostatic interaction, stronger than that in TiO_2 material [43–45]. This partially explains the worse relative photocurrent and smaller efficiency of charge injection and separation in ZnO samples with respect to titania ones. Interestingly, for ZnO films the final spectra in NIR are more like those of titania (main maximum at 1300–1400 nm, Fig. S10). This means that charge separation is better in fresh ZnO photoanodes without electrolyte than in complete cells. This is what we also recently observed for D149 [23]. Interestingly, during the fast degradation of the D358/ZnO cells, the amplitude of the residual NIR spectrum of the separated cations and electrons (with a maximum above 1200 nm) disappears, while the amplitude of the bound complex spectrum remains (Fig. S8). We observed similar changes in NIR spectrum for D149/TiO_2 cells,

Table 1
Regeneration time constant obtained in nanosecond transient absorption experiments. The time constants were obtained from one-exponential fits to the recorded transients at 670 nm (probe) upon excitation at 532 nm (1.3 mJ/cm^2).

Photoanode (electrolyte):	Time constant, μs
TiO_2 (EL2)	0.34
TiO_2 (EL1)	0.57
ZnO MP (EL1)	1.4
ZnO NW (EL1)	32
ZnO NW CS10 (EL1)	33

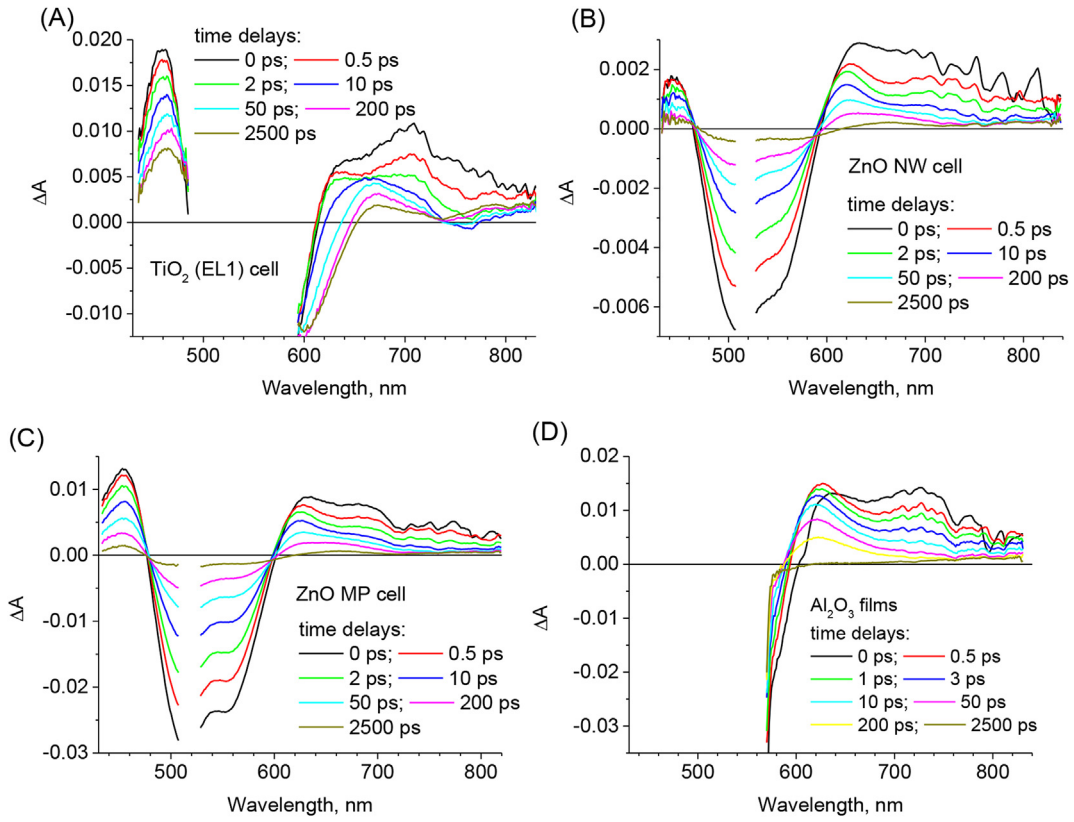

Fig. 4. Transient absorption spectra of (A) TiO_2 cell (with EL1), (B) ZnO NW cell, (C) ZnO MP cell and (D) Al_2O_3 film, all in VIS range for selected, indicated time delays between the pump (at 520 nm, 0.5 μJ) and probe pulses. See text for details about the origin of the different signals.

but for much slower cell degradation [23].

The global analysis of the cell and film samples was done by fitting 3 or 4 exponential functions (convoluted with IRF of the setup) to the transient absorption kinetics. The results (pre-exponential factor spectra of the fitted time constants) are shown in Figs. S11–S14. The time constants obtained represent the decay of initially excited (FC) state of D358 (amplitude spectra with maximum around 730 nm) and subsequent charge transfer (CT) state of D358 (amplitude spectra with maximum around 600 nm). The last component (>3 ns) in the global fit is a constant offset and is related to residual spectrum of radical cation and electrons. However, both states (FC and CT) decay in a non-exponential way so their fingerprints are "spread over" more than one time component. Therefore, the time scales of the FC and CT decays do not directly depend on the time constants of the fit, but rather on their relative contribution in particular pre-exponential spectra associated with these time constants. As an example, a comparison between the data for TiO_2/EL1 and TiO_2/EL2 cells is presented in SI (text and Fig. S15). Moreover, shorter time constants might indicate both faster electron injection or faster excited state self-quenching (probably singlet–singlet annihilation process) of the CT state [23].

All this makes the analysis and interpretation of the results quite complex, and we would like to propose a simpler approach for direct comparison of the most important parameter – electron injection efficiency – in different samples. First, the analysis is restricted to the NIR range, as we have shown that this region contains the fingerprints of both the dye excited state and the radical cation species. NIR transient spectra contain only the positive signals due to the absorption of transient species and they do not overlap with negative ground state depopulation (and stimulated emission) bands as well as the signals of transient Stark shift. The presence of the latter three types of signals in VIS region often makes the overall analysis more difficult. A more important advantage of doing the study in the NIR region is that the signal-to-noise ratio in transmission measurements of DSSC can often be better than that in the VIS region, due to the absence of the absorption of the dye. Furthermore, in the NIR there is no scattering of the nanostructure material (this is especially important for NW photoanodes). Next, only the first base kinetic vector obtained in singular value decomposition (SVD) analysis in the NIR range from 800 to 1500 nm is plotted to improve signal to noise ratio (the rest of the singular values are much smaller than the first one). It can be noted that such approach, based on first base kinetic vector of SVD, has been already proposed in the transient absorption studies of DSSC [46].

Fig. 6 and Fig.S16 present the 1st base kinetic vectors from SVD analysis for the cells and films studied in this work, which are probably the most conclusive part of the femtosecond measurements with respect to the comparison of different photoanodes. The initial signals are normalized to 1 to compare the samples of different stationary absorbance, and all samples presented in each plot were measured under the same pump pulse energy. The residual amplitude of the signal at 2–3 ns increases with the electron injection efficiency, although not proportionally. These values are compared in Table 2.

As can be seen, the residual amplitude for all ZnO cells (11–14%) is 2–3 times smaller than for TiO_2 (EL1) cells (32%, Fig. 5A), which correlates with the relative photocurrent (J_{SC}/N_{ph}) difference shown in Table S1A. As for the titania cells with electrolytes EL1 and EL2, the differences in the residual amplitude (78% vs 32%, 2.5 times, Fig. 5A) are much higher than the differences in the photocurrent (1.35 times). This could be probably explained by the fact that, as

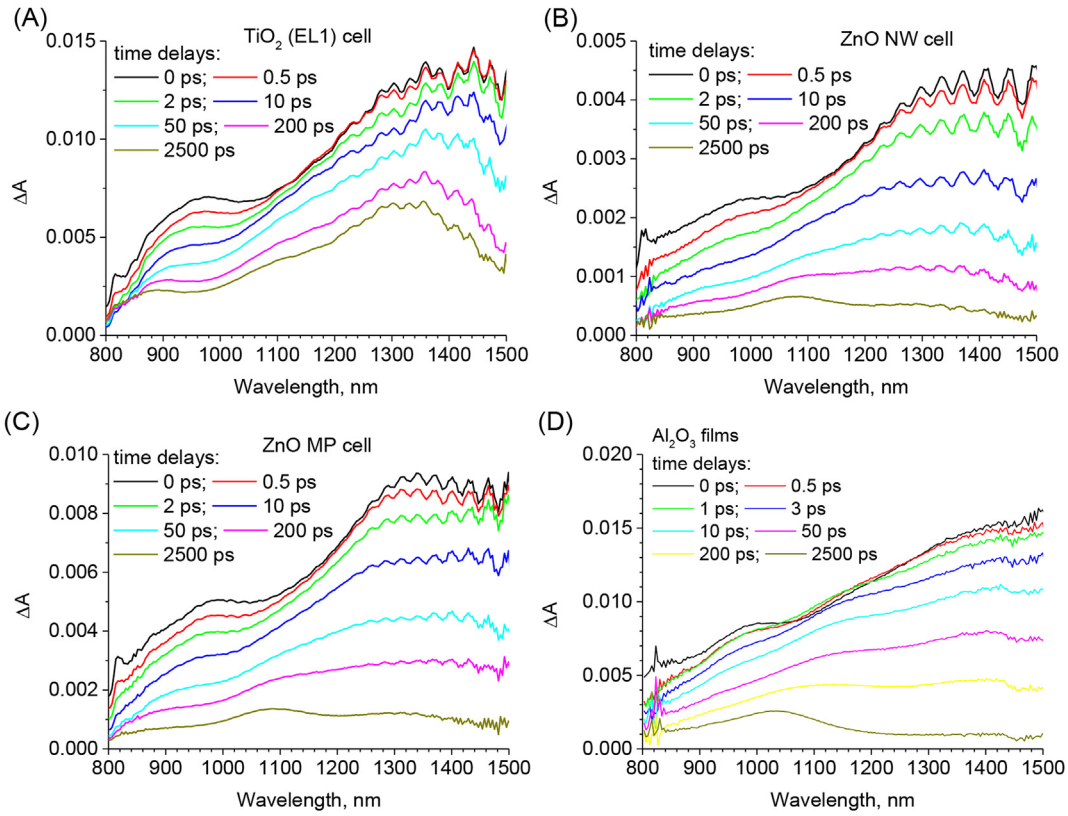

Fig. 5. Transient absorption spectra of (A) TiO_2 cell (with EL1), (B) ZnO NW cell, (C) ZnO MP cell and (D) Al_2O_3 film, all in NIR range for selected, included time delays between the pump (at 520 nm, 0.5 μJ) and probe pulses.

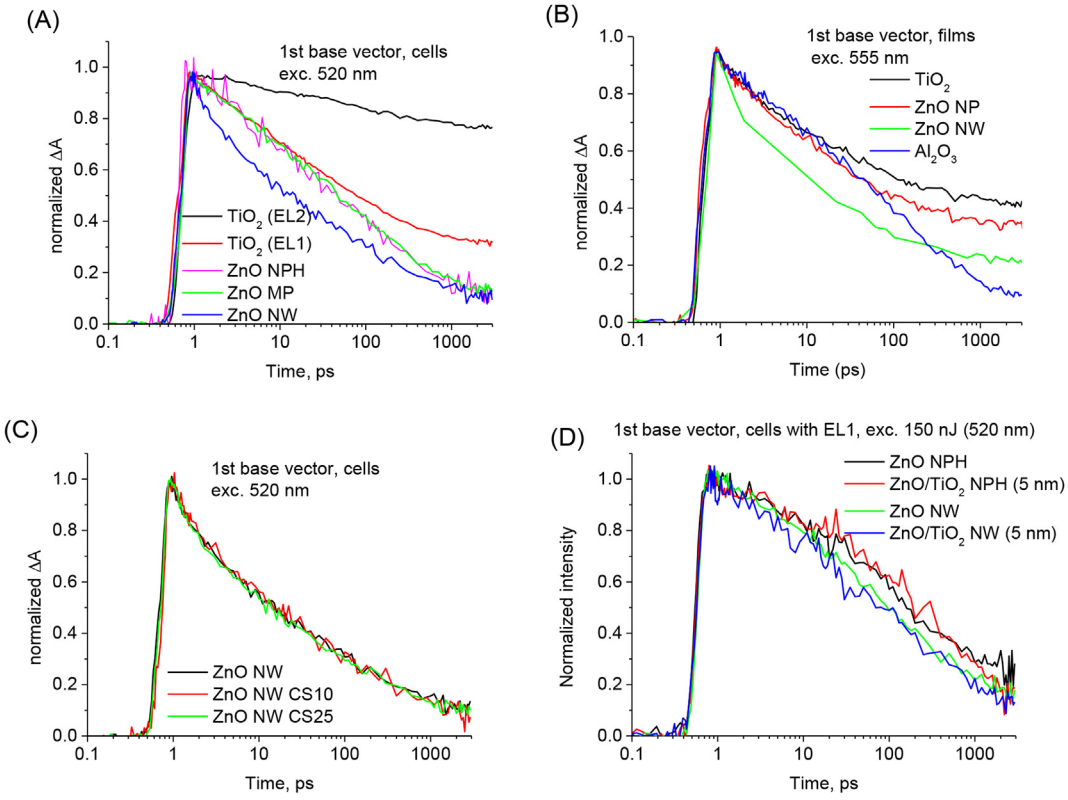

Fig. 6. The first base kinetic vector for indicated samples obtained after SVD global analysis in 800–1500 nm range. The excitation wavelength was 520 nm in figures A, C and D and 555 nm in figure B. The pump pulse energy was 500 nJ in A–C and 150 nJ in D.

Table 2
Ratio of the final amplitude to the initial amplitude in the NIR range of 1st base kinetic vectors from SVD analysis for different samples (cells and films). This ratio is a measure of the electron injection efficiency. For the same sample, more excited dyes (due to shorter excitation wavelength or higher pump fluence) results in smaller residual amplitudes.

Sample	Excitation wavelength, nm	Pump pulse fluence, nJ	Residual amplitude, %
TiO_2 cell (EL2)	520	500	78
TiO_2 cell (EL1)	520	2000	25
		500	32
		150	50
ZnO NPH cell	520	500	15
		150	22
ZnO NPH TiO_2 5 nm cell	520	150	18
ZnO MP cell	520	500	14
ZnO NW cell	520	500	11
		150	18
ZnO NW CS cell	520	500	11
ZnO NW TiO_2 5 nm cell	520	150	11
TiO_2 film	555	500	45
ZnO NPH film	555	500	34
	520	500	31
ZnO NW film	555	500	22
	520	500	17
ZnO NW CS film	520	500	17
Al_2O_3 film	555	500	10

discussed above, part of the FC state decay in TiO_2/EL2 cell takes place on the time scale shorter than IRF. Therefore, the ultrafast injection associated with this process quickly populates the radical cation state that already contributes to the initial signal in the 1st base vector. Therefore, the apparent decrease (from initial to residual values) in the kinetic vector is smaller.

The same analysis indicates that the decay of ZnO MP and ZnO NPH cells is the same (with ratio 14%, Fig. 6A), but that of ZnO NW is faster (with ratio 11%, Fig. 6A), probably due to the higher self-quenching of the dyes (see next section for further support of the self-quenching mechanism). The faster self-quenching might be explained by higher light scattering in NW than in NPH (Fig. S17), which results in more excited molecules under the same excitation fluence. This, in turn, implies closer average distance between excited dyes, since the dye coverage was reported to be similar for nanoparticles and nanowires [15]. ZnO NW CS10 and ZnO NW CS25 cells also have the same kinetics as the reference ZnO NW sample (Fig. 6C). The transient absorption signal decay is similar for "wet" (NPH) and "dry" (NPG) method of the ZnO nanoparticle preparation (Fig. S16D). Fig. 6D and S16A-B show the comparison of the kinetics in NIR range for ZnO/TiO_2 core–shell cells. As can be seen, contrary to expected improvement of TiO_2 shell, the decay of the TiO_2 coated samples is very similar to that of the reference cells, with the residual signal being even slightly smaller in the former than in the latter.

The above analysis was also applied to measurements in films (Fig. 6B and Fig. S16C). As already mentioned, the electron injection in ZnO NPH is better in films than in cells, which is in line with the 1st base vector plots (the residual signal in ZnO NPH film, 34%, is only slightly smaller than that of TiO_2 film, 45%). On the contrary, the electron injection efficiency in ZnO NW films and ZnO core–shell NW films (22%) is significantly worse than that in ZnO NPH film (Fig. S16C).

3.3. Details of the indoline dye deactivation scheme

In this section, we would like to discuss the electron injection route involving FC and relaxed CT states. We have proposed this mechanism in our recent work concerning solar cells made of the simpler indoline dye, D149 [23]. The results in this work confirm that it is also present in the case of the D358 dye. However, an alternative mechanism has been previously proposed for D149 [39,47], and for some all-organic dyes of other structures, but with similar spectral signatures of the transient states [48,49]. This mechanism postulates rapid electron injection (mainly <200 fs) from the dye to the metal oxide, followed by further spectral changes on the time scale of single or tens of picoseconds, and accompanied by an increase in transient Stark shift signal (explained by structural changes in the dye radical cation, movement of electrons and/or separation of initial radical-electron complex). We also include the bound radical-electron pair in our deactivation scheme, but just to explain the residual signal for ZnO and Al_2O_3 cells, important on the time scale of single ns after excitation. On the contrary, we think that the intermediate on picosecond time scale should be explained by the intramolecular excited CT state rather than the ground state of the radical cation (or bounded radical cation complex with electrons). This seems to be an important difference in both the understanding of electron injection for these kind of dyes and the interpretation of transient absorption results. Hence, we report here additional data and more experiments that further support our model. First, the spectral shape of the pre-exponential factor spectra in the VIS range (with maximum at around 600 nm) is similar on substrates enabling (TiO_2, ZnO) and blocking (Al_2O_3) injection, as well as that of CT state found in solution. We have already observed this for D149 dye [23], and the same works for D358 samples (Figs. S7, S11 and S13). The molecular LUMO orbital associated with CT state is probably slightly different in the isolated dye in solution compared to when the dye is attached to metal oxide, which can justify differences in NIR range [23]. The molecule on metal oxide is chemically bonded to Ti, Zn or Al atoms, so part of the electron charge in CT states can be shifted towards the metal oxide, having a more exciplex nature.

Next, we have observed (for D149 samples) that the decay of the intermediate depends on the coadsorbent concentration and the energy of the pump pulse, due to singlet–singlet annihilation between closely laying excited molecules [23]. The same effect is observed for D358 cells in the current studies (Fig. S18). Such self-quenching can only be explained by the process in excited states (CT state), not for ground state complex. For the latter, geminate recombination operates and it does not depend on the pump pulse intensity. Alternatively, the enhanced quenching could be explained by exceptionally fast recombination between free electrons and dye radical cation. Therefore, we made experiments under different negative bias applied to the working electrode and with very small pump energy (Fig. 7A). This changes the density of electrons in the metal oxide to a much larger extent than varying

pump fluence (Fig. S18).

As can be seen in Fig. 7A, no significant influence of the applied bias is observed. This proves that the kinetics in the picosecond range are not due to charge recombination. Another argument for the excited state nature of the observed intermediate is the fact that we have observed emission from the D149 dye occurring with the averaged time constant of about 100 ps [22,23]. In the emission experiment the excitation energy density was low, around 30 μJ/cm^2. So, one may argue that the emission comes from the same species as that initially observed in transient absorption experiment, but in the latter experiment, its lifetime becomes significantly shortened (<1 ps) due to enhanced self-quenching under higher pump energy density. Therefore, we made the transient absorption experiment with 10 times smaller pump fluence than that typically used (50 nJ, corresponding to density 100 μJ/cm^2). Choosing the proper probing wavelength at 605 nm (where FC and CT states decays induce opposite signal changes) we found that pump pulse energy hardly influences the lifetime of FC state, which is < 1 ps for both energies (Fig. 7B). Therefore, the observed longer emission must originate from the CT state, and its lifetime changes with different pump pulse intensity in transient absorption experiments due to self-quenching. Fig. 8 summarizes the most important points of the indoline dye deactivation scheme.

As shown in the previous section, TiO_2 coating of ZnO photoanodes did not bring the expected improvement of electron injection yield in femtosecond experiment (Fig. 6D). This indicates that dye self-quenching depends rather on the core material (ZnO) than on the thin shell (TiO_2) to which the dyes are directly attached. Therefore, most probably, the averaged parameters of the porous nanostructures are more important than the microscopic parameters in the vicinity of the dyes. The photophysics of the singlet–singlet annihilation process is based on energy transfer, whose rate, like in Förster mechanism, decreases with refractive index n of the medium as $1/n^4$. The size of the pores and nanostructures is much smaller than the light wavelength for energy transfer. Thus, the effective (averaged) refractive index should be responsible for the interaction between the dyes [50,51]. Such effective refractive index is hardly changed by thin shell coating and depends mainly on the core material. The refractive index at 600 nm is 2.6 for TiO_2 and 2.0 for ZnO. Assuming about 50% porosity of the nanomaterials filled with acetonitrile solvent (n = 1.3), the effective refractive index can be calculated as 2.0 for the TiO_2 photoanodes and 1.6 for the photoanodes with ZnO core. This, in turn, implies about 2 times difference in $1/n^4$ factor, which indicates two times higher rate of energy transfer in all ZnO materials, irrespective of the coating. Therefore, the lower refractive index of ZnO material with respect to that of TiO_2 might be another factor of the worse performance of ZnO cells. On the other hand, if our conclusions are correct, the use of ZnO photoanodes can be beneficial for DSSC systems with the so-called energy relay dyes. In this concept, the extra light harvesting is realized from the dyes that are diffusing in the electrolyte and interact with other dye attached to metal oxide due to Förster resonant energy transfer [52].

4. Conclusions

Several nanostructures of DSSC photoanodes made with ZnO and TiO_2 materials and sensitized with indoline D358 dye have been studied from the point of view of fast charge separation processes and device stability. Isolated photoanodes and fully working solar cells with liquid iodide-based electrolyte were investigated by time-resolved laser spectroscopy techniques in the time range from 100 fs to 100 μs. Dye regeneration was found to be slower in ZnO MP than in TiO_2 nanoparticles (3–4 times). The regeneration was even slower for ZnO NW, one order of magnitude below ZnO MP. The efficiency of electron injection in femtosecond transient absorption experiments was at least two times smaller for all ZnO photoanodes than for those with TiO_2 nanoparticles. The efficiency was also slightly smaller for ZnO NW with respect to ZnO NPH and ZnO MP, which is probably due to higher self-quenching of the dyes attached to nanowires. Modification of the ZnO NW with additional ZnO shell layers did not improve electron injection efficiency. Furthermore, all ZnO cells exhibited much faster degradation with time than TiO_2 cells.

The following findings are derived from our results:

A) Time-resolved laser spectroscopy studies of complete cells comparing several ZnO photoanode nanostructures: nanoparticles ("wet" NPH and "dry" NPG) nanowires (NW), electrodeposited mesoporous structures (MP) and core–shell nanostructures are reported for the first time, both in completed cells and in films.

B) A new proposed protocol proves to be successful to study the highly scattering DSSC cells with small signal to noise ratio in transient absorption experiment (e.g. NW cells). This is based on the global analysis in near-infrared range probing range (800–1500 nm) and the comparison of the base kinetic vectors from singular value decomposition analysis.

C) The solar cell samples without TBP additive in the electrolyte were studied. The comparison of the results to those of the

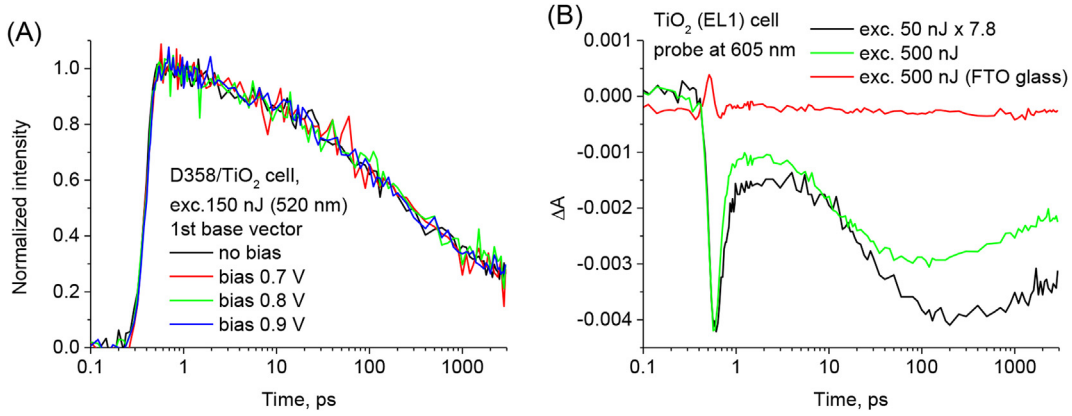

Fig. 7. (A) Dependence of the kinetics in NIR range on the applied voltage for TiO_2/EL1 cell. The 1st base vector from SVD in the range 800–1400 nm under excitation with 150 nJ pulse at 520 nm are shown. (B) Transient absorption kinetics at 605 nm for TiO_2/EL1 cell at different pump pulse fluence (a negligible contribution of the FTO substrate to the initial signal is also shown).

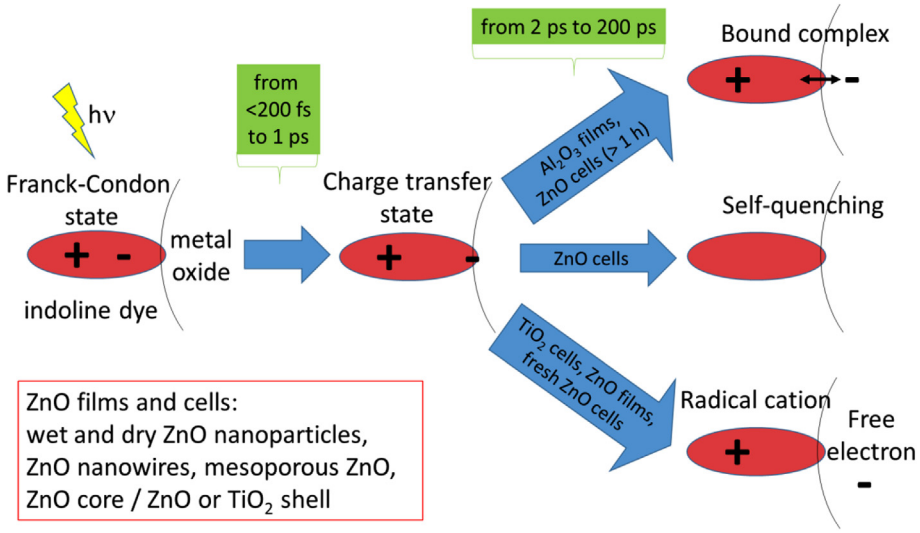

Fig. 8. Schematic deactivation scheme of indoline dye interacting with metal oxides in films and solar cells.

cells with TBP shows how the shift of the potential of dyes metal oxide conduction band and dye states influence the observed charge transfer dynamics.

D) This work reports the first time-resolved studies of indoline dye D358. Despite structural modifications, its photobehaviour in solution and when attached to metal oxide nanoparticles is similar, but not equivalent, to that of simpler D149 indoline dye.

E) Additional transient absorption experiments were performed (e.g. studies just after cell preparation, with different bias voltage, or at very low pump pulse intensity) to provide further evidence of the participation of dye relaxed charge transfer state in the deactivation on metal oxides. The electron injection from this excited state takes place on the time scale from several ps to several tens of ps. This lies in opposite to several recent reports on DSSC systems with all-organic dyes in which the presence of mainly sub-ps electron injection was postulated.

F) The transient absorption results of ZnO nanostructures with and without thin TiO_2 overlayers were compared for the first time. The similarity of the results indicate that the early-time photobehaviour of the dye depends more on the effective parameters (e.g. refractive index) of the photoanode structure than the material being in local contact with the dye.

Based on these findings, and taking into account previous contributions [14,22,23], we propose that the lower performance of ZnO cells with respect to those of TiO_2 materials (observed on the ultrafast and fast time scales below 100 μs) is a "universal" or "intrinsic" characteristic of ZnO materials when used as photoanodes, possibly affecting other classes of solar cells. First, the regeneration rate is observed to be slower for ZnO photoanodes. Second, the dye excited state decay in the emission measurements under small excitation energy is slower in ZnO than TiO_2 cells, which indicates the role of the difference in the density of acceptor states between ZnO and TiO_2. Furthermore, the transient absorption studies reveal higher contribution of bound radical cations–electron complexes in ZnO cells due to lower dielectric constant of this material. Moreover, with higher excitation energy more dominant role of self-quenching in the dye deactivation occurs for ZnO cells. As revealed in this contribution, this can be explained by higher energy transfer rate in ZnO cells due to the differences in refractive index between ZnO and TiO_2 – a parameter which has not been considered so far as important in the performance of ZnO material in photoanodes. Finally, we have found that different morphologies and synthetic methods of ZnO nanoporous photoanodes do not bring important differences in the photobehaviour of the attached indoline dyes. Therefore, most probably all three macroscopic parameters (density of acceptor states, dielectric constant and refractive index) contribute to the detrimental effect of using ZnO materials in solar cell photoanodes.

Acknowledgments

This work was supported by NCN (National Science Centre, Poland) under project 2012/05/B/ST3/03284 and MINECO (Ministerio de Economía y Competitividad, Spain) under proiects MAT2013-47192-C3-3-R and MAT2013-47192-C3-2-R. Financial support from the National Centre for Research and Development under research grant "Nanomaterials and their application to biomedicine", contract number PBS1/A9/13/2012 is also gratefully acknowledged. J. S. is a holder of a scholarship funded within Human Capital Operational Programme, European Social Fund. Dr. Gotard Burdziński is kindly acknowledged for helping with nanosecond transient absorption measurements.

Appendix A. Supplementary data

Supplementary data related to this article can be found at http://dx.doi.org/10.1016/j.matchemphys.2015.12.042.

References

[1] J.A. Anta, E. Guillen, R. Tena-Zaera, ZnO-based dye-sensitized solar cells, J. Phys. Chem. C 116 (2012) 11413–11425.
[2] J. Ajuria, I. Etxebarria, W. Cambarau, U. Muñecas, R. Tena-Zaera, J.C. Jimenoc, R. Pacios, Inverted ITO-free organic solar cells based on p and n semiconducting oxides. New designs for integration in tandem cells, top or bottom detecting devices, and photovoltaic windows, Energy Environ. Sci. 4 (2011) 453–458.
[3] J. You, L. Dou, K. Yoshimura, T. Kato, K. Ohya, T. Moriarty, K. Emery, C.-C. Chen, J. Gao, G. Li, Y. Yang, A polymer tandem solar cell with 10.6% power conversion efficiency, Nat. Commun. 4 (2013) 1446.
[4] D. Liu, T.L. Kelly, Perovskite solar cells with a planar heterojunction structure prepared using room-temperature solution processing techniques, Nat. Photonics 8 (2014) 133–138.
[5] D.Y. Son, J.H. Im, H.S. Kim, N.G. Park, 11% efficient perovskite solar cell based on ZnO nanorods: an effective charge collection system, J. Phys. Chem. C 118

(2014) 16567–16573.
[6] S. Mathew, A. Yella, P. Gao, R. Humphry-Baker, B.F.E. Curchod, N. Ashari-Astani, I. Tavernelli, U. Rothlisberger, M.K. Nazeeruddin, M. Grätzel, Dye-sensitized solar cells with 13% efficiency achieved through the molecular engineering of porphyrin sensitizers, Nat. Chem. 6 (2014) 242–247.
[7] N. Memarian, I. Concina, A. Braga, S.M. Rozati, A. Vomiero, G. Sberveglieri, Hierarchically assembled ZnO nanocrystallites for high-efficiency dye-sensitized solar cells, Angew. Chem.Int. Ed. 50 (2011) 12321–12325.
[8] E. Guillén, L. Peter, J.A. Anta, Electron transport and recombination in ZnO-based dye-sensitized solar cells, J. Phys. Chem. C 115 (2011) 22622–22632.
[9] M. Law, L.E. Greene, J.C. Johnson, R. Saykally, P. Yang, Nanowire dye-sensitized solar cells, Nat. Mater. 4 (2005) 455–459.
[10] S.H. Ko, D. Lee, H.W. Kang, K.H. Nam, J.Y. Yeo, S.J. Hong, C.P. Grigoropoulos, H.J. Sung, Nanoforest of hydrothermally grown hierarchical ZnO nanowires for a high efficiency dye-sensitized solar cell, Nano Lett. 11 (2011) 666–671.
[11] P. Labouchere, A.K. Chandiran, T. Moehl, H. Harms, S. Chavhan, R. Tena-Zaera, M.K. Nazeeruddin, M. Graetzel, N. Tetreault, Passivation of ZnO nanowire guests and 3D inverse opal host photoanodes for dye-sensitized solar cells, Adv. Energy Mater. 4 (2014) 1400217.
[12] T. Yoshida, J. Zhang, D. Komatsu, S. Sawatani, H. Minoura, T. Pauporté, D. Lincot, T. Oekermann, D. Schlettwein, H. Tada, D. Wöhrle, K. Funabiki, M. Matsui, H. Miura, H. Yanagi, Electrodeposition of inorganic/organic hybrid thin films, Adv. Func. Mater. 19 (2009) 17–43.
[13] M. Law, L.E. Greene, A. Radenovic, T. Kuykendall, J. Liphardt, P. Yang, ZnO–Al_2O_3 and ZnO–TiO_2 core–shell nanowire dye-sensitized solar cells, J. Phys. Chem. B 110 (2006) 22652–22663.
[14] J. Idígoras, G. Burdziński, J. Karolczak, J. Kubicki, G. Oskam, J.A. Anta, M. Ziółek, The impact of the electrical nature of the metal-oxide on the performance in dye-sensitized solar cells: new look at old paradigms, J. Phys. Chem. C 119 (2015) 3931–3944.
[15] E. Guillén, E. Azaceta, L.M. Peter, A. Zukal, R. Tena-Zaera, J.A. Anta, ZnO solar cells with an indoline sensitizer: a comparison between nanoparticulate films and electrodeposited nanowire arrays, Energy Environ. Sci. 4 (2011) 3400–3407.
[16] E. Guillén, E. Azaceta, A. Vega-Poot, J. Idígoras, J. Echeberría, J.A. Anta, R. Tena-Zaera, ZnO/ZnO core–shell nanowire array electrodes: blocking of recombination and impressive enhancement of photovoltage in dye-sensitized solar cells, J. Phys. Chem. C 117 (2013) 13365–13373.
[17] E. Azaceta, J. Idigoras, J. Echeberria, A. Zukal, L. Kavan, O. Miguel, H.J. Grande, J.A. Anta, R. Tena-Zaera, ZnO–ionic liquid hybrid films: electrochemical synthesis and application in dye-sensitized solar cells, J. Mater. Chem. A 1 (2013) 10173–10183.
[18] S. Ito, S.M. Zakeeruddin, R. Humphry-Baker, P. Liska, R. Charvet, P. Comte, M.K. Nazeeruddin, P. Péchy, M. Takata, H. Miura, S. Uchida, M. Grätzel, High-efficiency organic-dye-sensitized solar cells controlled by nanocrystalline-TiO_2 electrode thickness, Adv. Mater. 18 (2006) 1202–1205.
[19] J. Yang, P. Ganesan, J. Teuscher, T. Moehl, Y.J. Kim, C. Yi, P. Comte, K. Pei, T.W. Holcombe, M.K. Nazeeruddin, J. Hua, S.M. Zakeeruddin, H. Tian, M. Grätzel, Influence of the donor size in D–pi–A organic dyes for dye-sensitized solar cells, J. Am. Chem. Soc. 136 (2014) 5722–5730.
[20] Y. Wu, M. Marszalek, S.M. Zakeeruddin, Q. Zhang, H. Tian, M. Grätzel, W. Zhu, High-conversion-efficiency organic dye-sensitized solar cells: molecular engineering on D–A–pi-A featured organic indoline dyes, Energy Environ. Sci. 5 (2012) 8261–8272.
[21] G. Burdziński, J. Karolczak, M. Ziółek, Dynamics of local stark effect observed for a complete D149 Dye-sensitized solar cell, Phys. Chem. Chem. Phys. 15 (2013) 3889–3896.
[22] J. Sobuś, G. Burdziński, J. Karolczak, J. Idígoras, J.A. Anta, M. Ziółek, Comparison of TiO_2 and ZnO solar cells sensitized with an indoline dye: time-resolved laser spectroscopy studies of partial charge separation processes, Langmuir 30 (2014) 2505–2512.
[23] J. Sobuś, J. Karolczak, D. Komar, J.A. Anta, M. Ziółek, Transient states and the role of excited state self-quenching of indoline dyes in complete dye-sensitized solar cells, Dyes Pigments 113 (2015) 692–701.
[24] K. Premaratnea, G.R.A. Kumaraa, R.M.G. Rajapakseb, M.L. Karunarathnea, Highly efficient, optically semi-transparent, ZnO-based dye-sensitized solar cells with Indoline D-358 as the dye, J. Photochem. Photobiol. A Chem. 229 (2012) 29–32.
[25] N.M. Gómez-Ortíz, J. Idígoras, E. Guillén, A. Hernández, A. Sastre-Santos, F. Fernández-Lázaro, J.A. Anta, G. Oskam, Influence of dye chemistry and electrolyte solution on interfacial processes at nanostructured ZnO in dye-sensitized solar cells, J. Photochem. Photobiol. A Chem. 264 (2013) 26–33.
[26] A.G. Vega-Poot, M. Macías-Montero, J. Idígoras, A. Borrás, A. Barranco, A.R. Gonzalez-Elipe, F.I. Lizama-Tzec, G. Oskam, J.A. Anta, Mechanisms of electron transport and recombination in ZnO nanostructures for dye-sensitized solar cells, ChemPhysChem 15 (2014) 1088–1097.
[27] R. Tena-Zaera, J. Elias, C. Lévy-Clément, I. Mora-Seró, Y. Luo, J. Bisquert, Electrodeposition and impedance spectroscopy characterization of ZnO nanowire arrays, Phys. Status Solidi A 205 (2008) 2345–2350.
[28] J. Bisquert, Theory of the impedance of electron diffusion and recombination in a thin layer, J. Phys. Chem. B 106 (2002) 325–333.
[29] T.L. Bahers, F. Labat, T. Pauporte, I. Ciofini, Effect of solvent and additives on the open-circuit voltage of ZnO-based dye-sensitized solar cells: a combined theoretical and experimental study, Phys. Chem. Chem. Phys. 12 (2010) 14710–14719.
[30] E. Guillén, J. Idígoras, T. Berger, J.A. Anta, C. Fernández-Lorenzo, R. Alcántara, J. Navas, J. Martín-Calleja, ZnO-based dye solar cell with pure ionic-liquid electrolyte and organic sensitizer: the relevance of the dye–oxide interaction in an ionic-liquid medium, Phys. Chem. Chem. Phys. 13 (2011) 207–213.
[31] F. Li, J.R. Jennings, Q. Wang, Determination of sensitizer regeneration efficiency in dye-sensitized solar cells, ACS Nano 7 (2013) 8233–8242.
[32] S.A. Haque, Y. Tachibana, R.L. Willis, J.E. Moser, M. Grätzel, D.R. Klug, J.R. Durrant, Parameters influencing charge recombination kinetics in dye-sensitized nanocrystalline titanium dioxide films, J. Phys. Chem. B 104 (2000) 538–547.
[33] J. Nelson, S.A. Haque, D.R. Klug, J.R. Durrant, Trap-limited recombination in dye-sensitized nanocrystalline metal oxide electrodes, Phys. Rev. B 63 (2001) 205321.
[34] A.V. Barzykin, M. Tachiya, Mechanism of charge recombination in dye-sensitized nanocrystalline semiconductors: random flight model, J. Phys. Chem. A 106 (2002) 4356–4363.
[35] X. Yang, S. Zhang, K. Zhang, J. Liu, C. Qin, H. Chen, A. Islam, L. Han, Coordinated shifts of interfacial energy levels: insight into electron injection in highly efficient dye-sensitized solar cells, Energy Environ. Sci. 6 (2013) 3637–3645.
[36] P.W. Lohse, J. Kuhnt, S.I. Druzhinin, M. Scholz, M. Ekimova, T. Oekermann, T. Lenzer, K. Oum, Ultrafast photoinduced relaxation dynamics of the indoline dye D149 in organic solvents, Phys. Chem. Chem. Phys. 13 (2011) 19632–19640.
[37] M. Fakis, P. Hrobárik, E. Stathatos, V. Giannetas, P. Persephonis, A time resolved fluorescence and quantum chemical study of the solar cell sensitizer D149, Dyes Pigments 96 (2013) 304–312.
[38] A. El-Zohry, B. Zietz, Concentration, Solvent, Effects on the excited state dynamics of the solar cell dye D149: the special role of protons, J. Phys. Chem. C 117 (2013) 6544–6553.
[39] K. Oum, P.W. Lohse, O. Flender, J.R. Klein, M. Scholz, T. Lenzer, J. Duc, T. Oekermannz, Ultrafast dynamics of the indoline dye D149 on electrodeposited ZnO and sintered ZrO_2 and TiO_2 thin films, Phys. Chem. Chem. Phys. 14 (2012) 15429–15437.
[40] U.B. Cappel, S.M. Feldt, J. Schöneboom, A. Hagfeldt, G. Boschloo, The influence of local electric fields on photoinduced absorption in dye-sensitized solar cells, J. Am. Chem. Soc. 132 (2010) 9096–9101.
[41] A. Fattori, L.M. Peter, H. Wang, H. Miura, F. Marken, Fast hole surface conduction observed for indoline sensitizer dyes immobilized at fluorine-doped tin oxide-TiO_2 surfaces, J. Phys. Chem. C 114 (2010) 11822–11828.
[42] M. Pastore, F. De Angelis, Computational modeling of stark effects in organic dye-sensitized TiO_2 heterointerfaces, J. Phys. Chem. Lett. 2 (2011) 1261–1267.
[43] A. Furube, R. Katoh, T. Yoshihara, K. Hara, S. Murata, H. Arakawa, M. Tachiya, Ultrafast Direct, Indirect Electron-Injection, Processes in a photoexcited dye-sensitized nanocrystalline zinc oxide film: the importance of exciplex intermediates at the surface, J. Phys. Chem. B 108 (2004) 12583–12592.
[44] D. Stockwell, Y. Yang, J. Huang, C. Anfuso, Z. Huang, T. Lian, Comparison of electron-transfer dynamics from coumarin 343 to TiO_2, SnO_2, and ZnO Nanocrystalline thin films: role of interface-bound charge-separated pairs, J. Phys. Chem. C 114 (2010) 6560–6566.
[45] T.L. Bahers, M. Rerat, P. Sautet, Semiconductors used in photovoltaic and photocatalytic devices: assessing fundamental properties from DFT, J. Phys. Chem. C 118 (2014) 5997–6008.
[46] D. Kuang, S. Ito, B. Wenger, C. Klein, J.E. Moser, R. Humphry-Baker, S.M. Zakeeruddin, M. Grätzel, High molar extinction coefficient heteroleptic ruthenium complexes for thin film dye-sensitized solar cells, Adv. Func. Mater. 128 (2006) 4146–4154.
[47] E. Rohwer, C. Richter, N. Heming, K. Strauch, C. Litwinski, T. Nyokong, D. Schlettwein, H. Schwoerer, Ultrafast photodynamics of the indoline Dye D149 adsorbed to porous ZnO in dye-sensitized solar cells, ChemPhysChem 14 (2013) 132–139.
[48] K. Oum, O. Flender, P.W. Lohse, M. Scholz, A. Hagfeldt, G. Boschloo, T. Lenzer, Electron and hole transfer dynamics of a triarylamine-based dye with peripheral hole acceptors on TiO_2 in the absence and presence of solvent, Phys. Chem. Chem. Phys. 16 (2014) 8019–8029.
[49] S.G. Bairu, E. Mghanga, J. Hasan, S. Kola, V.J. Rao, K. Bhanuprakash, L. Giribabu, G.P. Wiederrecht, R. da Silva, L.G.C. Rego, G. Ramakrishna, Ultrafast interfacial charge-transfer dynamics in a donor–π–acceptor chromophore sensitized TiO_2 nanocomposite, J. Phys. Chem. C 117 (2014) 4824–4835.
[50] R.S. Meltzer, S.P. Feofilov, B. Tissue, H.B. Yuan, Dependence of fluorescence lifetimes of Y_2O_3:Eu31 nanoparticles on the surrounding medium, Phys. Rev. B 60 (1999) 14012–14015.
[51] M.L. Debasu, D. Ananias, A.G. Macedo, J. Rocha, L.D. Carlos, Emission-decay curves, energy-transfer and effective-refractive index in Gd2O3:Eu3+ nanorods, J. Phys. Chem. C 115 (2011) 15297–15303.
[52] B.E. Hardin, E.T. Hoke, P.B. Armstrong, J.H. Yum, P. Comte, T. Torres, J.M.J. Fréchet, M.K. Nazeeruddin, M. Grätzel, M.D. McGehee, Increased light harvesting in dye-sensitized solar cells with energy relay dyes, Nat. Photonics 3 (2009) 406–411.

SUPPORTING INFORMATION

for

Effect of different photoanode nanostructures on the initial charge separation and electron injection process in dye sensitized solar cells: a photophysical study with indoline dyes.

Jesús Idígoras [1], Jan Sobuś [2,3], Mariusz Jancelewicz [2], Eneko Azaceta [4], Ramon Tena-Zaera [4], Juan A. Anta [1] and Marcin Ziółek [3]*

[1]*Nanostructured Solar Cells Group, Department of Physical, Chemical and Natural Systems, Universidad Pablo de Olavide, Ctra. Utrera, km 1,ES-41013 Seville, Spain*

[2]*NanoBioMedical Centre, Adam Mickiewicz University, Umultowska 85, 61-614 Poznan, Poland.*

[3]*Quantum Electronics Laboratory, Faculty of Physics, Adam Mickiewicz University in Poznań, Umultowska 85, 61-614 Poznan, Poland.*

[4]*Materials Division, IK4-CIDETEC, Parque Tecnológico de San Sebastián, Paseo Miramón 196, Donostia-San Sebastián, 20009, Spain.*

Table S1.

Parameters of the studied D358 cells: absorbance of the films in air (A_{max}), open circuit voltage (V_{OC}) short circuit current (J_{SC}) fill factor (FF), calculated number of absorbed photons (N_{ph}) and relative photocurrent (J_{SC}/N_{ph}). N_{ph} was calculated for each sample based on the absorption spectra and AM1.5G data. However, it should be noted that light scattering effect was not included in the calculation of N_{ph}. The data in part (A) were obtained in one series of experiment under irradiation with LED lamp, while those in part (B) were obtained in another series, for which 1 Sun conditions were simulated by Xe lamp.

(A)

Photoanode (electrolyte)	ZnO NPH (EL1)	ZnO MP (EL1)	ZnO NW (EL1)	TiO_2 (EL1)	TiO_2 (EL2)
A_{max}	1.2	0.9	0.3	~4.0	~4.0
V_{OC}, mV	720	690	680	760	670
J_{SC}, mA/cm^2	5.1	3.3	2.0	13.0	17.5
FF	0.55	0.60	0.40	0.65	0.65
N_{ph}, $\times 10^{16}$, s^{-1}cm^{-2}	6.8	6.2	3.2	9.0	9.0
J_{SC}/N_{ph}, $\times 10^{-16}$ mAs	0.75	0.53	0.63	1.44	1.94

(B)

Photoanode, (electrolyte)	ZnO NPH (EL1)	ZnO NPG (EL1)
A_{max}	1.5	0.35
Layer thickness, μm	3.5	1
Cell area, cm^2	0.16	0.81
Deposition method	screen printing	spin coating
V_{OC}, mV	690	680
J_{SC}, mA/cm^2	4.2	1.7
FF	0.55	0.50
η, %	1.6	0.5
N_{ph}, $\times 10^{16}$, s^{-1}cm^{-2}	7.3	3.4
J_{SC}/N_{ph}, $\times 10^{-16}$ mAs	0.58	0.50

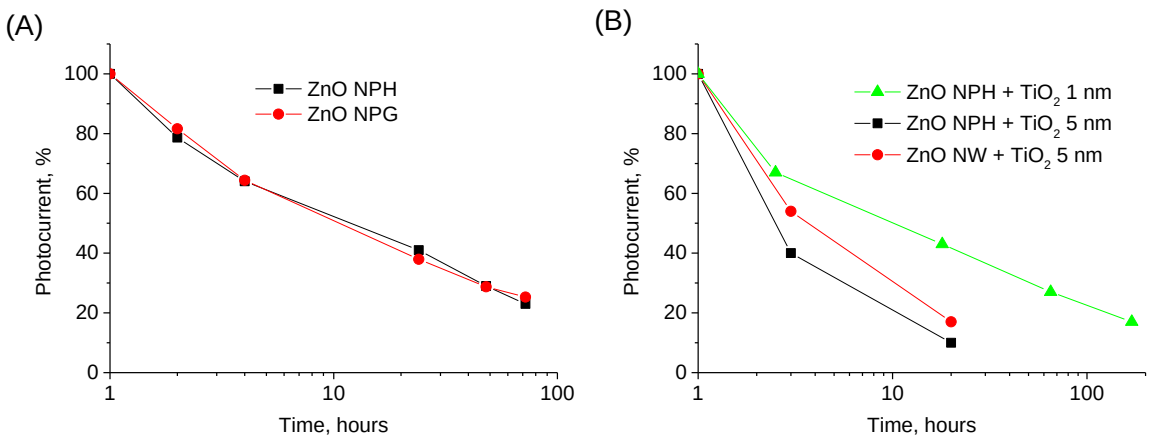

Figure S1. (A) The decrease of the photocurrent for the D358 cells with ZnO nanoparticles prepared by hydrothermal (NPH) and gas phase (NPG) methods (stored in the dark) with time. The parameters of the cells used in this experiment are given in Table S1B. (B) Decrease of the photocurrent of the TiO_2-coated cells (stored in the dark) with time.

TiO_2 coating of the ZnO materials

The main advantage of TiO_2 material over all ZnO structures for D358-sensitized solar cells is better electron injection efficiency and better stability of the devices. Therefore, we decided to check whether these properties depend more on the core material or on the outer layer of the nanostructures. To do so, ZnO NW and ZnO NPH photoanodes were coated with TiO_2 layers by ALD technique. The growth rate was typically 0.5 Å/cycle for TiO_2 on the planar surface. The growth per cycle has been controlled by measuring the films thickness on Si-wafer reference substrates placed in the reactor. As evidenced in Figure S2, this method gave a continuous coating of the thickness of about 5 nm for 100 cycles. We have also checked the effect of smaller thickness (20 cycles resulting in approximately 1 nm TiO_2 layer).

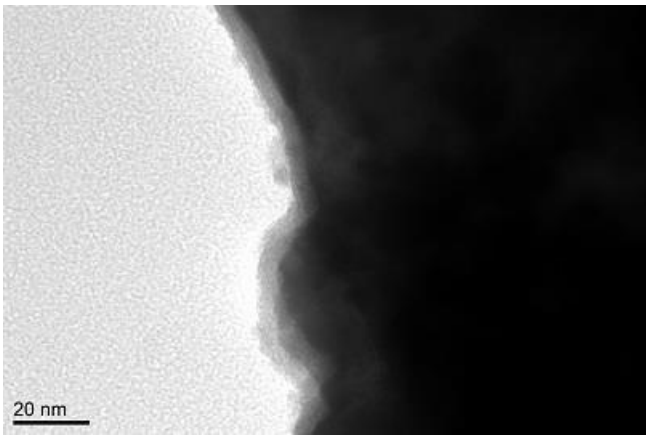

Figure S2. TEM picture of TiO_2 coating of ZnO NW (ALD method, 100 cycles, shell of about 5 nm thickness). Samples for TEM imaging were prepared as follows. Active part of the photoanode was scratched off the glass substrate and dispersed in ethanol using sonication for 1h. Afterwards, two drops of solution were applied to the TEM grid, followed by evaporation of the solvent using diaphragm pump for 1h. Images were taken using Jeol JEM-1400 microscope with LaB6 source and accelerating voltage of 120kV.

Table S2 collects the photovoltaic parameters of the cells under 1 Sun illumination. The exemplary current-volatge curves of the different cells are presented in Figure S3A. As can be seen, for both ZnO nanoparticles and nanowires, the TiO_2 coating yielded significantly lower photocurrents than for the reference, uncoated cells. For electrolyte EL1, J_{SC} of TiO_2-coated (5 nm) sample is only 14% for NPH and 7% for NW with respect to the reference bare samples. Lower photocurrents are also reflected in IPCE spectra (Figure S3B). Interestingly, both V_{OC} and

fill factor of the cells with TiO_2 shell increases. However, these improvements are not enough to compensate low J_{SC} values and the cell total efficiencies are 6-8 times smaller than those of uncoated counterparts. High V_{OC} suggest that low photocurrents of ALD-treated cells could be due to too negative shift of the potential of the conduction band. Thus, the cells filled with electrolyte EL2 (without TBP, resulting in lowering of V_{OC}) were checked (Table S2). The performance of such cells was still lower, although some improvement was observed (the efficiency of the TiO_2-coated ZnO NW cells was only 4 times smaller than that of uncoated ZnO NW). The most probable reason for small photocurrents in TiO_2-coated cells is that there is very poor charge transfer between titania shell and ZnO core. Therefore, the injected electrons are only transported through TiO_2 layer, and its contact with the electrode is limited. Indeed, for smaller TiO_2 layer thickness (1 nm) the photocurrent is even smaller (Table S2).

Table S2.

Photovoltaic parameters of the TiO_2 coated and the reference ZnO cells: open circuit voltage (V_{OC}), short circuit current (J_{SC}), fiil factor *(FF*) and total efficiency (η) under irradiation of 1 Sun. J_{SC} was measured 1 h after cell preparation.

Photoanode, electrolyte	ZnO NPH EL1	ZnO NPH + TiO_2 1nm EL1	ZnO NPH + TiO_2 5nm EL1	ZnO NW EL1	ZnO NW + TiO_2 5 nm EL1	ZnO NW EL2	ZnO NW + TiO_2 5 nm EL2
V_{OC}, mV	720	570	790	620	800	490	590
J_{SC}, mA/cm^2	4.4	0.3	0.6	2.0	0.13	1.2	0.23
FF	0.57	0.59	0.72	0.39	0.55	0.53	0.57
η, %	1.8	0.1	0.3	0.5	0.06	0.3	0.08

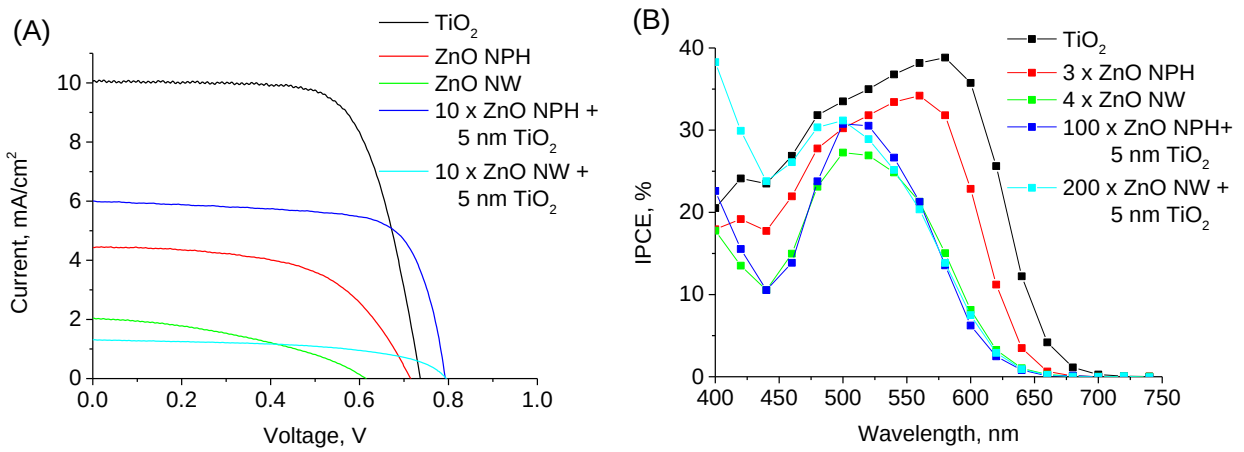

Figure S3. (A) Current-voltage curves of the indicated samples. The photocurrent of the ZnO cells coated with TiO_2 layer are multiplied by 10. (B) IPCE spectra of the indicated samples. The shape of IPCE reflects the different absorbance of the cells (high for nanoparticles of TiO_2 and ZnO, low for ZnO NW).

Further confirmation of our explanation comes from the additional cell characterization by electrochemical impedance spectroscopy and photocurrent decays spectra. The impedance data were fitted with the equivalent circuit for DSSC which yields the charge transfer resistance (R_{ct}) and chemical capacitance (C_μ) in the oxide-electrolyte interface. These two parameters exhibit exponential behavior for applied bias voltages around V_{OC}. The fits of the exponential function to R_{ct} and C_μ dependence on the applied voltage gives the recombination reaction order (parameter m) and trap energy distribution below the conduction band (parameter α), respectively (Figure S4). They are collected in Table S3 for the experiments in the dark and under 1 Sun illumination. In line with previous findings [1, 2], the dependence of the capacitance on applied voltage is much weaker for uncoated ZnO materials than for TiO_2 nanoparticles (small α values). However, for ZnO cells with TiO_2 coating the values of the parameter α substantially increase towards those of TiO_2 cells. Next, recombination resistance is much higher (an order of magnitude in the dark and even more under 1 Sun) for TiO_2 coated samples than for the reference ones (both bare ZnO and bare TiO_2, see Figure S4). This behavior is similar to the previous findings for ZnO/ZnO core-shell photoanodes and might explain high V_{OC} of the TiO_2 coated samples [3]. Smaller recombination is also revealed in the values of m parameter (Table S3). They nicely correlate with fill factor of the cells (especially under 1 Sun) – the smaller is

recombination order, the better fill factor is. Blocking of the recombination might be also an indication of poor charge transport between ZnO and TiO_2 layer – thus the charges externally applied to the photoanode recombine harder with the electrolyte. Interestingly, the recombination resistance under 1 Sun for bare ZnO cells decreases (because the Fermi level is shifted due to the injected electrons), but it is almost not changed when illumination is added to TiO_2 coated cells (see Figure S4). This means that the shift in Fermi level in TiO_2 shell is not "seen" in ZnO core.

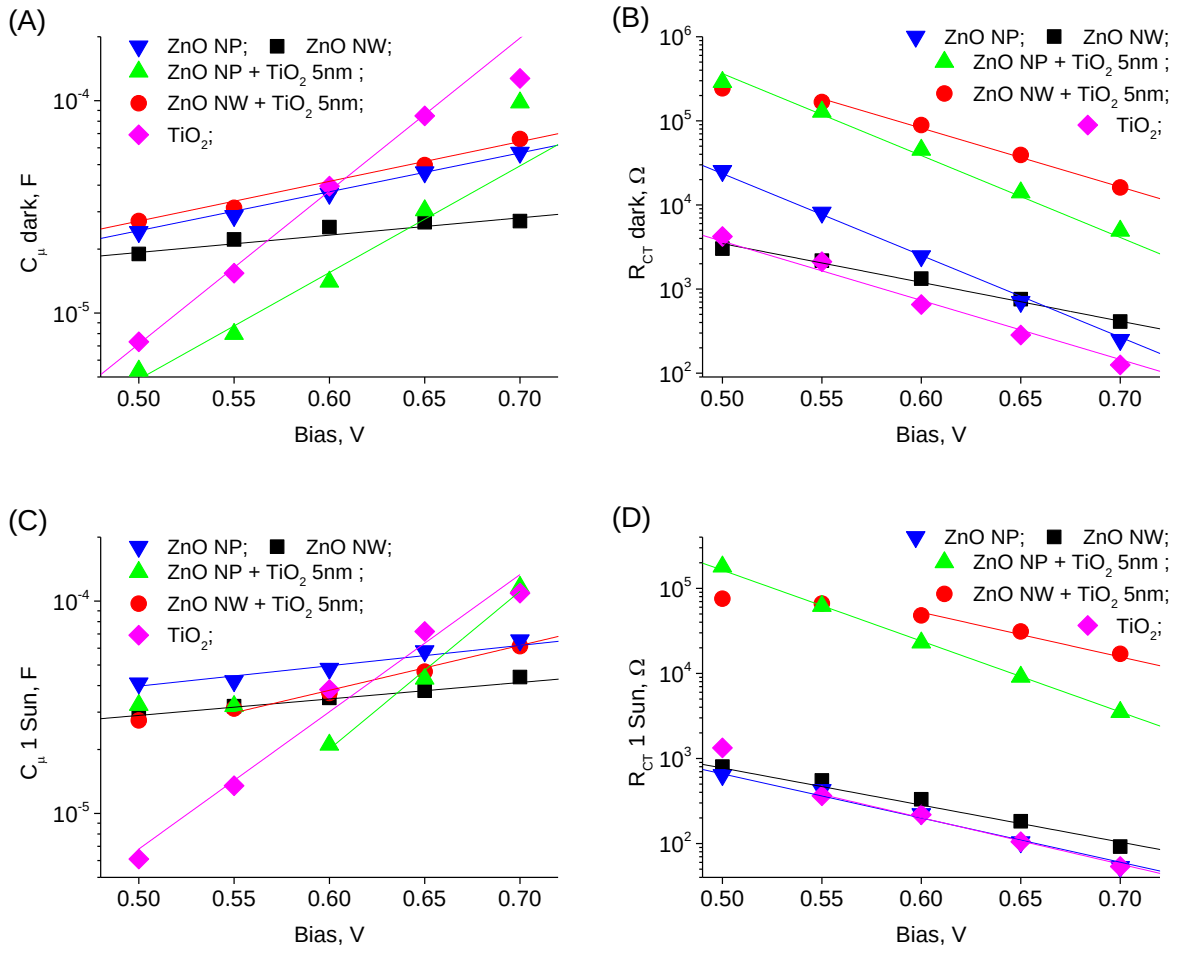

Figure S4. Plots of (A,C) chemical capacitance and (B,D) charge transfer resistance as a function of applied bias voltage obtained from electrochemical impedance measurements by fitting equivalent circuit for DSSC to the studied cells. The lines show the fit of the following functions with the indicated fitted parameters: (A,c) $C_\mu = C_0 \exp(\alpha\, Ve/kT)$, where α represents trap energy distribution below the conduction band; (B,D) $R_{ct} = R_0 \exp(-Ve/m\, kT)$, where m represents the empirical estimation of the reaction order in sublinear recombination kinetics. Plots (A,B) show results in the dark, while plots (C,D) – under 1 Sun illumination.

Table S3.

The parameters α (trap energy distribution below the conduction band) and *m* (reaction order in recombination kinetics) obtained from the fit of the following functions: $C_\mu = C_0 \exp(\alpha\, Ve/kT)$ and $R_{ct} = R_0 \exp(-Ve/m\, kT)$ for the indicated cells in the dark and under 1 Sun illumination.

Sample:	α (dark)	α (1 Sun)	*m* (dark)	*m* (1 Sun)
ZnO NPH	0.11	0.06	1.7	3.2
ZnO NPH TiO_2 5 nm	0.26	0.42	1.7	2.0
ZnO NW	0.05	0.05	3.6	3.9
ZnO NW TiO_2 5nm	0.11	0.13	2.4	3.2
TiO_2	0.43	0.38	2.4	3.1

The photocurrent decays measured under 0 V bias reveal the transport of injected electrons from the TiO_2 shell to the electrode. The results of such experiment is shown in Figure S5, and the averaged transport times are collected in Table S4. This experiment directly shows that the electron transport in each ZnO photoanode (NW and NPH) becomes an order of magnitude slower when TiO_2 shell is applied. We think that this is the strongest proof of poor electron transfer between TiO_2 and ZnO in the studied cells. By the way, the data also shows that the electron transport in ZnO nanowires is much faster than the one in the sintered nanoparticles layer. It should be also noted that the transport times are longer than those measured close to V_{OC} (for example by IMPS technique) since the photocurrent decay times are measured under 0 V bias. However, we observed similar behavior (significantly longer decays for TiO_2 coated cells than those of uncoated reference cells) at biases 0.6 V, but the temporal resolution was worse in those experiments.

Table S4.

Half-decays of the photocurrent presented in Figure S5.

Sample:	half decay, ms
ZnO NPH	24
ZnO NPH TiO_2 1 nm	620
ZnO NPH TiO_2 5 nm	860
ZnO NW	5
ZnO NW TiO_2 5nm	40
TiO_2	9

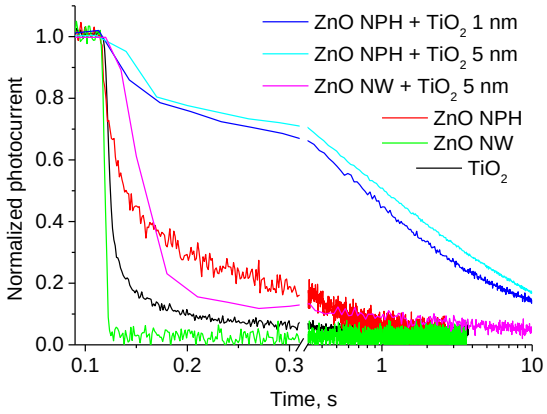

Figure S5. Photocurrent decays of the indicated samples at 0 V bias voltage. The excitation light (at 500 nm) intensity was 0.7 mW/cm^2.

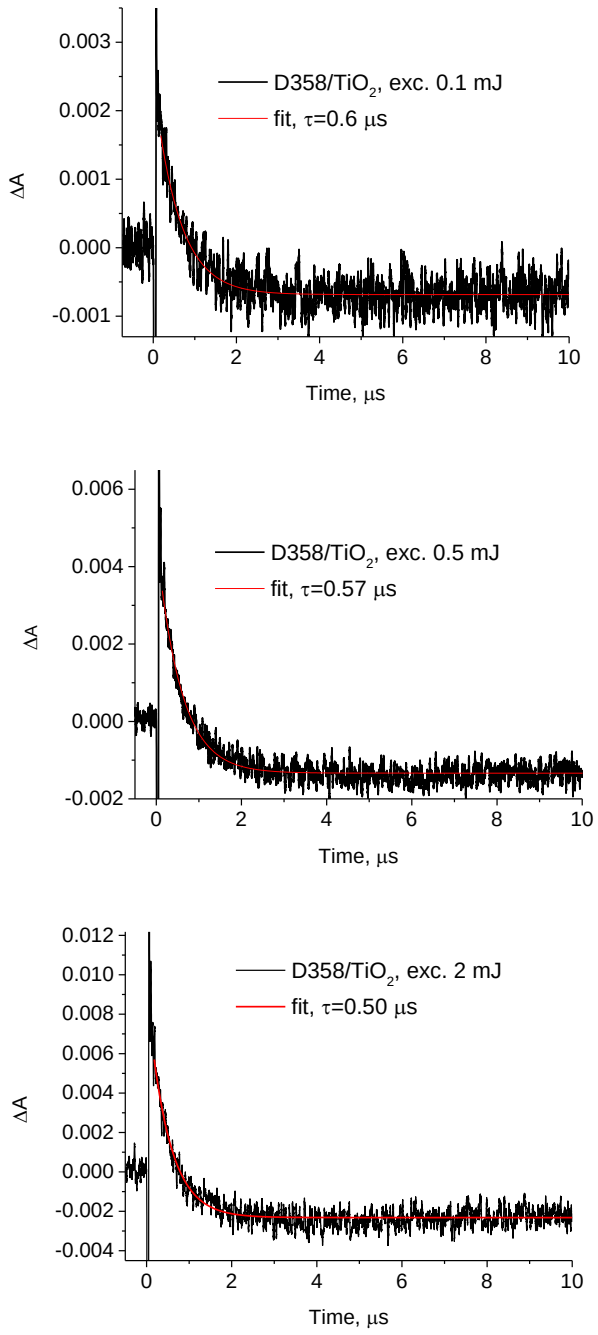

Figure S6. Transient absorption kinetics probed at 670 nm for TiO_2 (EL1) cells under different indicated pump pulse energy (excitation wavelength 532 nm). The red line shows the best fit using one-exponential function with the time constants given in Table S5.

Table S5.

Time constants obtained from one-exponential fit of the kinetics probed at 670 nm upon excitation at 532 nm with different pulse energies for TiO_2 (EL1) cell.

Pump energy	Time constant, μs
0.1 mJ	0.60
0.5 mJ	0.57
2.0 mJ	0.50

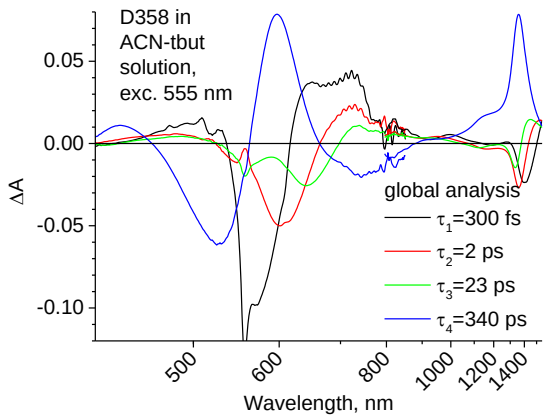

Figure S7. Pre-exponential factor spectra of the components with time constants given in the inset obtained by multi-exponential global fit for transient absorption of D358 dye in solution.

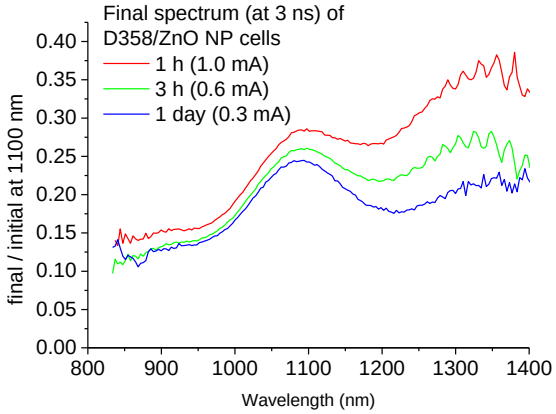

Figure S8. Changes in the final spectrum of the ZnO NPH cell as a function of time after cell preparation (and indicated decreasing J_{SC}). The signal is normalized so that the amplitude of initial spectrum is 1 at probing wavelength of 1100 nm. The residual signal correlates with the rapid decay of the photocurrent (see also Figure 2B). So, it is important to compare the ZnO cells of the same freshness, like we did.

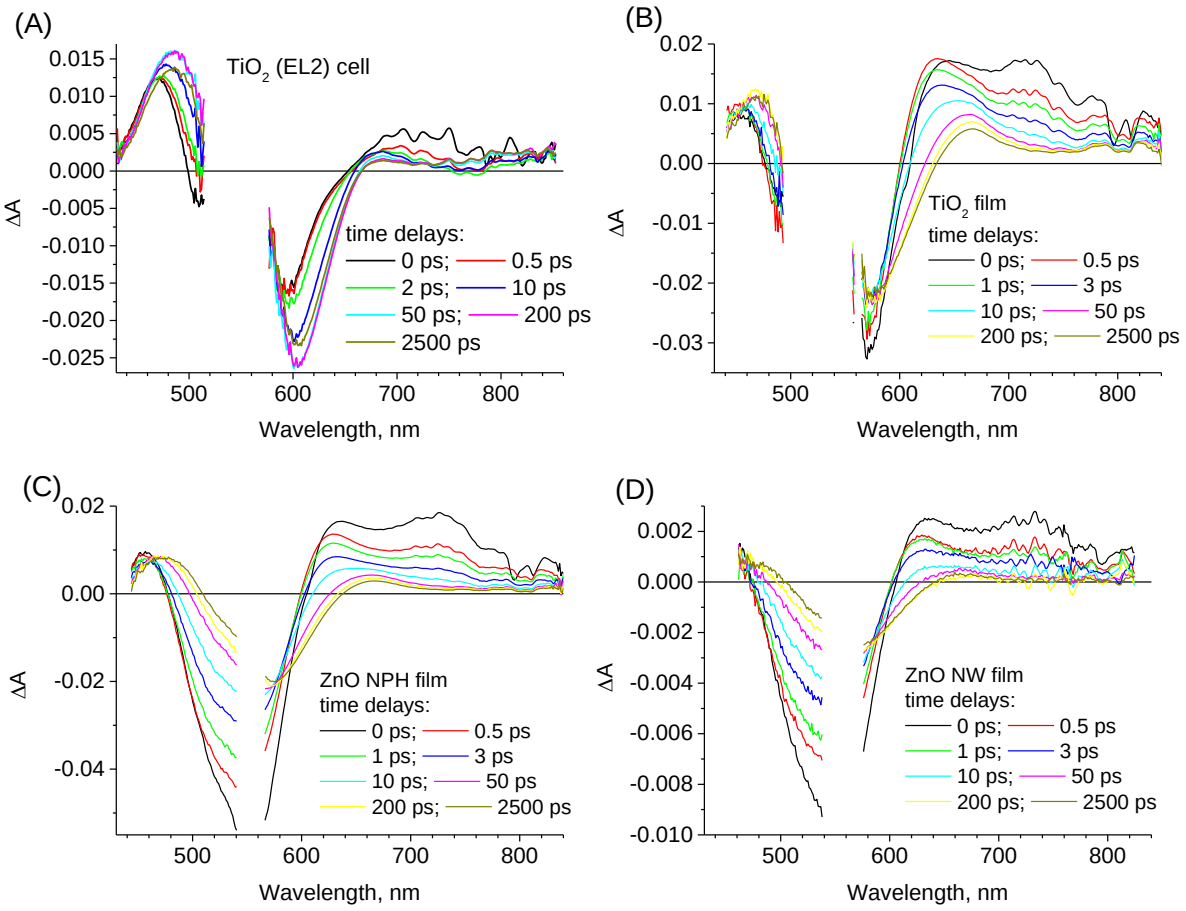

Figure S9. Transient absorption spectra of the indicated samples in VIS range for selected time delays between the pump (0.5 μJ) and probe pulses.

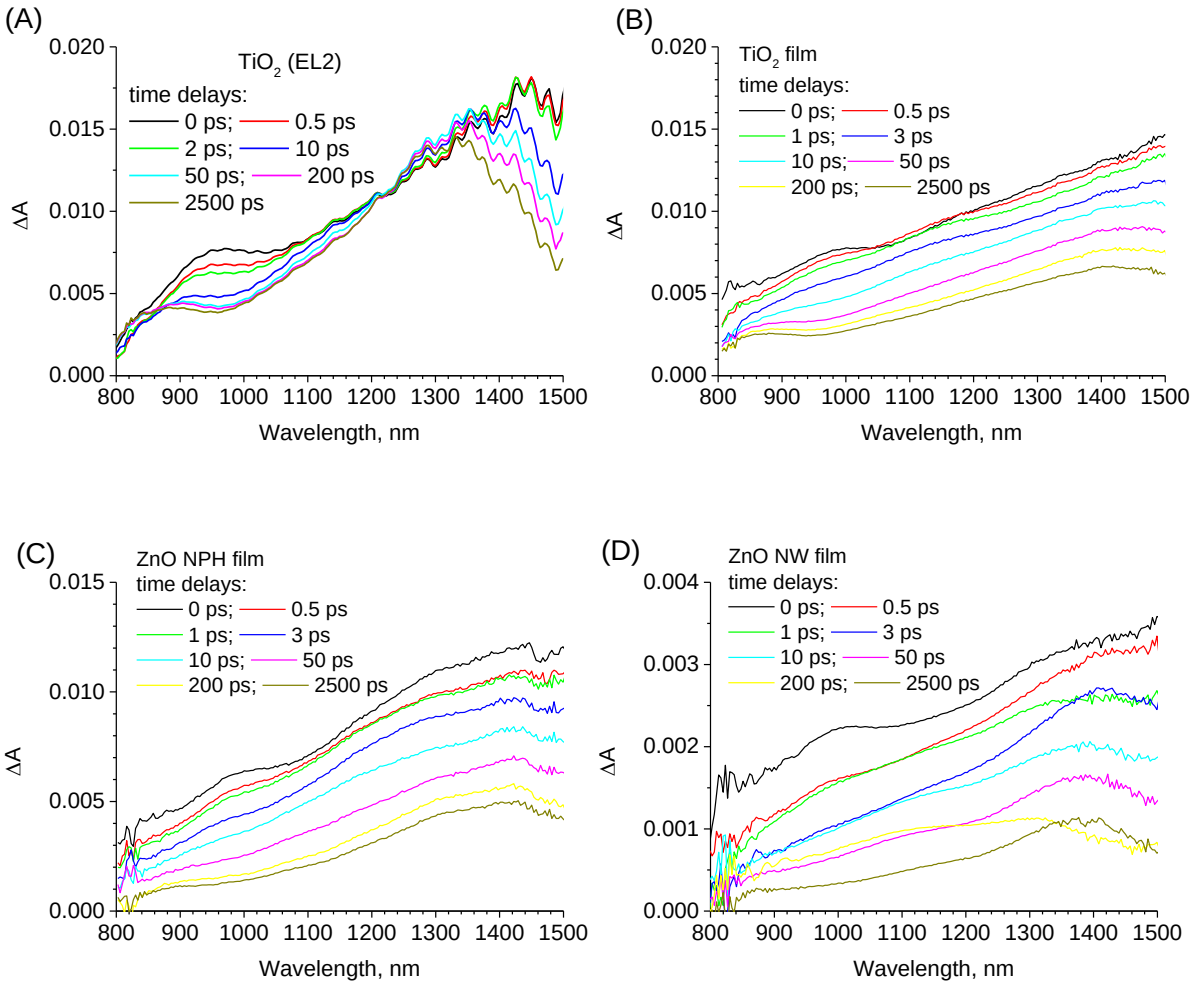

Figure S10. Transient absorption spectra of the indicated samples in NIR range for selected time delays between the pump (0.5 μJ) and probe pulses.

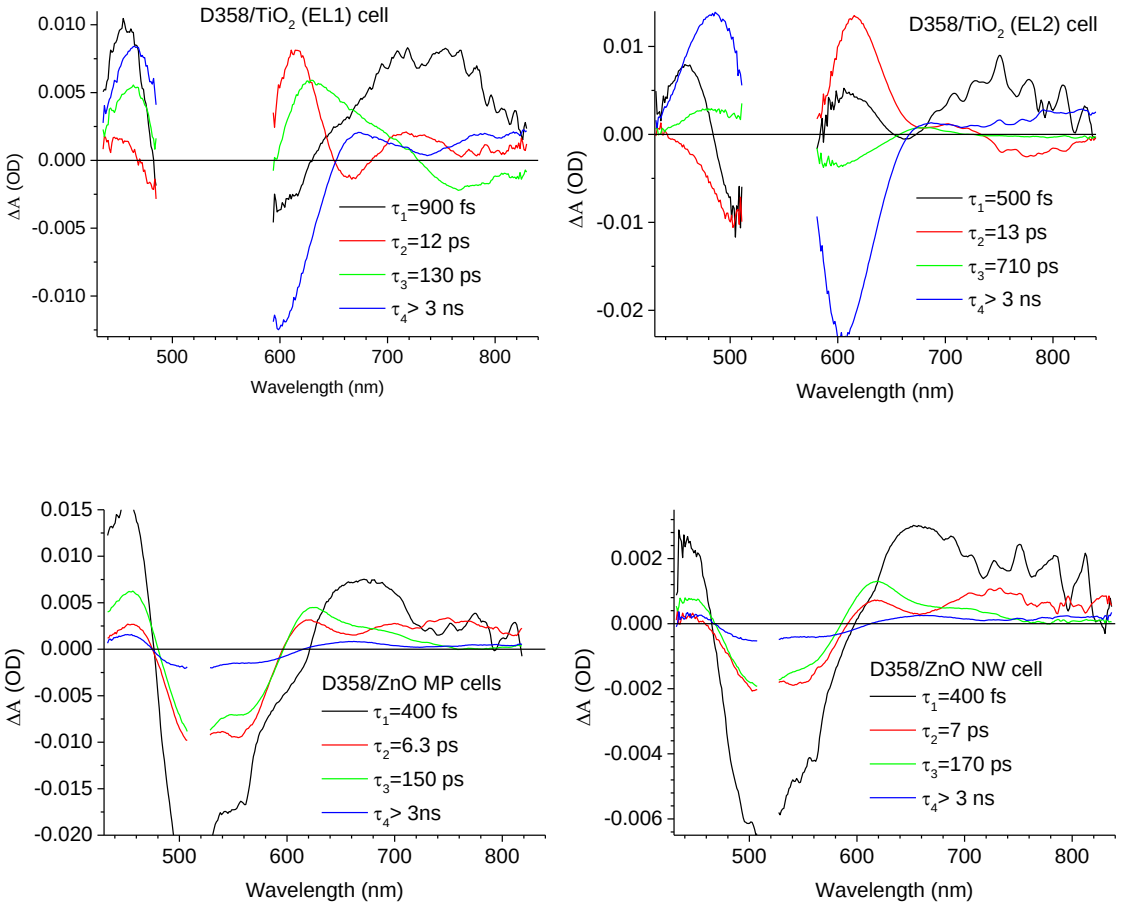

Figure S11. Pre-exponential factor spectra of the components with time constants given in the inset obtained by multi-exponential global fit of transient absorption in VIS range of the indicated cells.

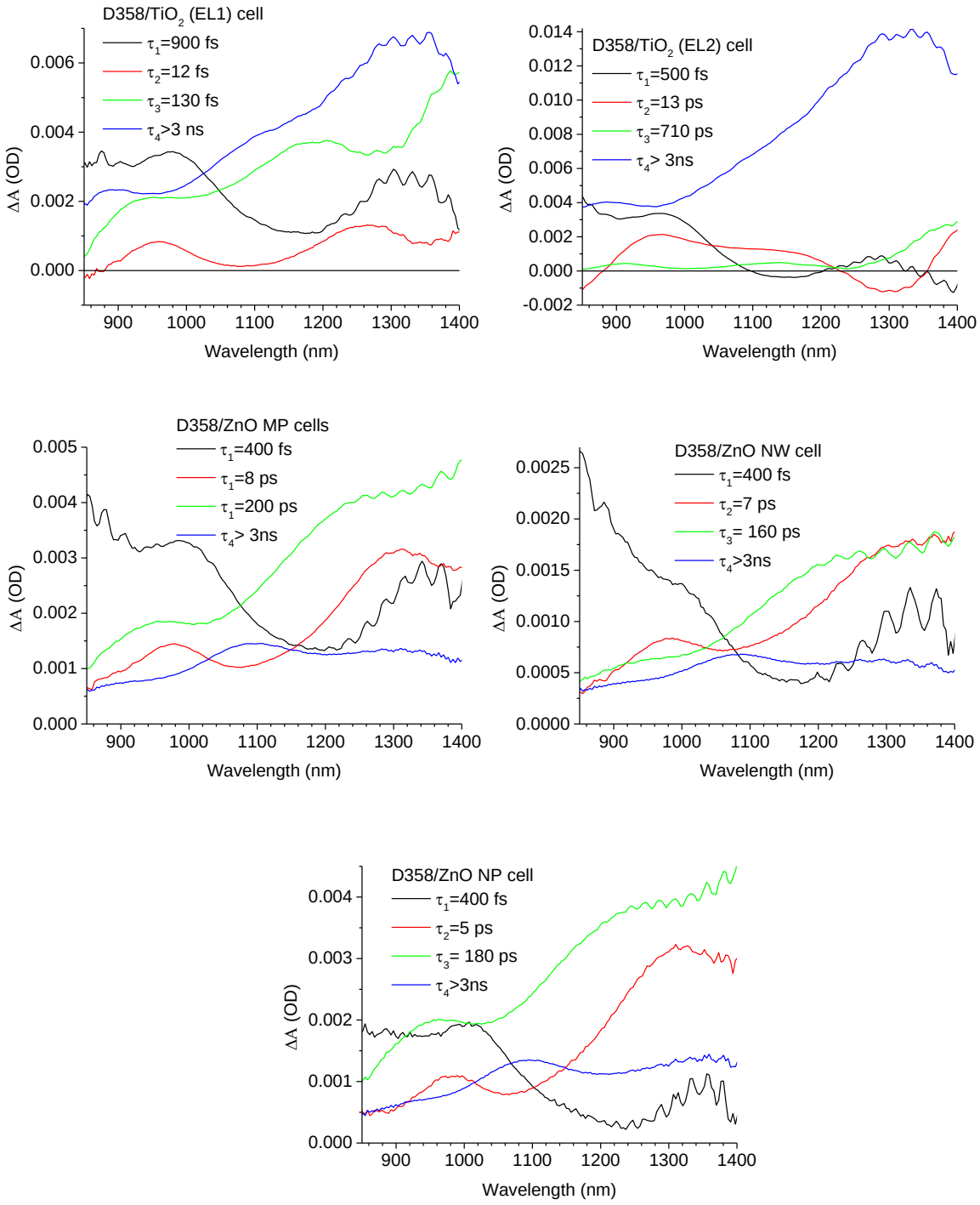

Figure S12. Pre-exponential factor spectra of the components with time constants given in the inset obtained by multi-exponential global fit of transient absorption in NIR range of the indicated cells.

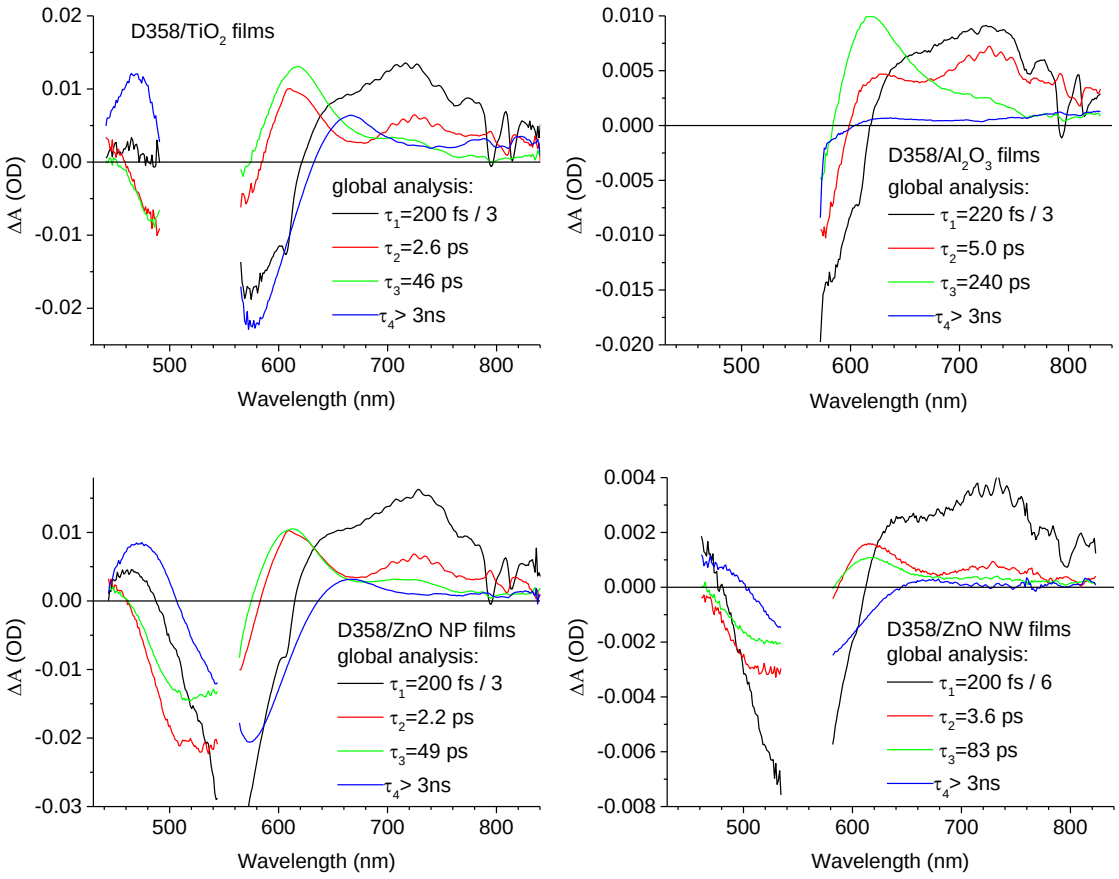

Figure S13. Pre-exponential factor spectra of the components with time constants given in the inset obtained by multi-exponential global fit of transient absorption in VIS range of the indicated film samples. The amplitude of the fastest component (τ_1=0.2 ps) is decreased by a factor of 3 because the fitting procedure makes it larger due to the convolution with comparable IRF.

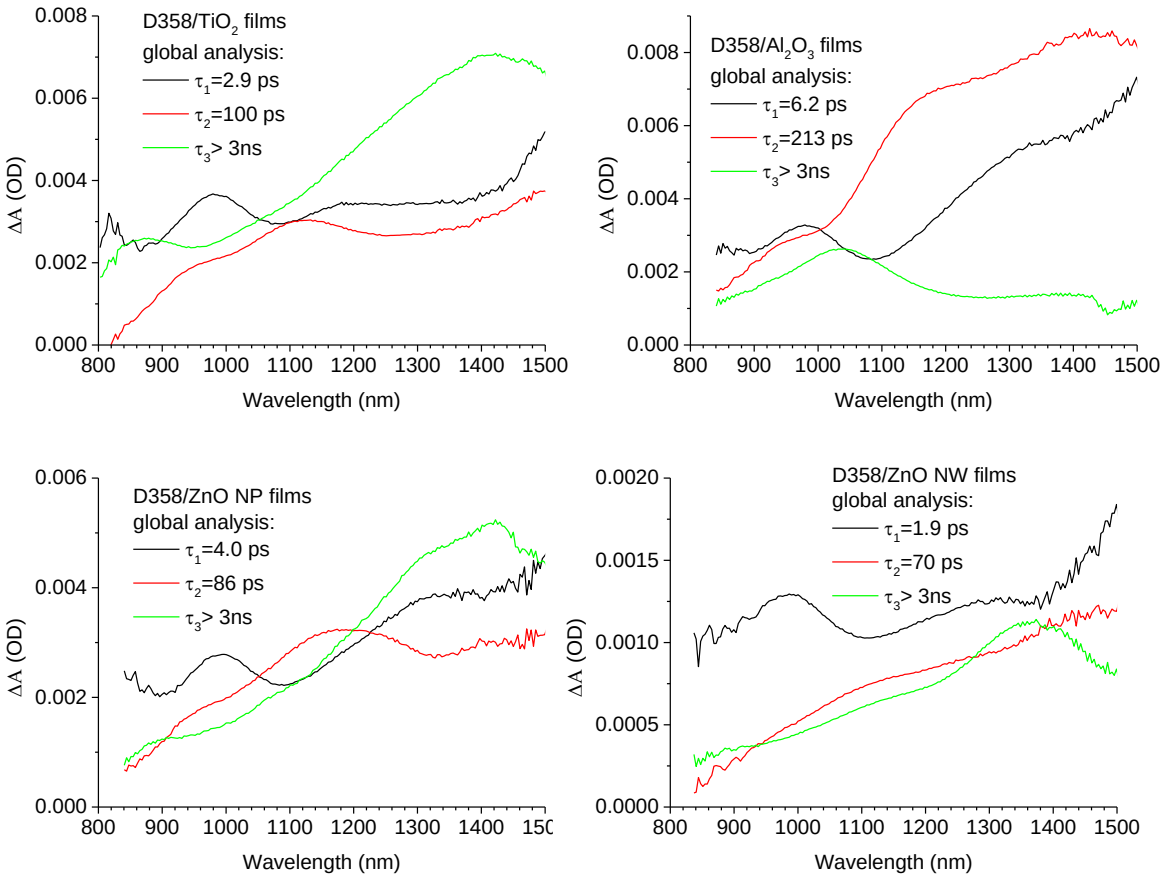

Figure S14. Pre-exponential factor spectra of the components with time constants given in the inset obtained by multi-exponential global fit of transient absorption in NIR range of the indicated film samples.

Electrolyte effect in femtosecond transient absorption

The example of the influence of better efficiency of electron injection on the transient absorption results is the comparison between the data for TiO_2/EL1 and TiO_2/EL2 cells. In the latter case the electrolyte does not contain TBP additive, which results in the commonly observed shift of the conduction band edge towards smaller energies and an increase of the injection rate due to either higher density of acceptor states in titania or higher dye-semiconductor electronic coupling [4]. In our transient absorption studies the resulting higher efficiency of electron injection in TiO_2/EL2 sample is directly reflected in the final spectra (e.g. at 2.5 ns, Figure 4A vs. S9A and Figure 5A vs. S10A), which have higher amplitude in NIR range and higher contribution of Stark shift in the VIS range (positive amplitudes in 480-520 nm range, negative amplitudes in 550-660 nm range) with respect to TiO_2/EL1. The dynamics of the excited states decay can also be observed in the kinetics at single wavelength, however, there is no probing wavelength at which only one state contributes to the transient absorption signal. Figure S15 presents the comparison of the transient absorption decay at 730 nm, where the contribution of FC state dominates: it decays significantly faster in EL2 than EL1. In the global analysis (Figures S11, S12) the decay of FC state (maximum of decay amplitude at 730 nm) contributes to the spectra of τ_1=0.9 ps and τ_2=12 ps components for TiO_2/EL1 cell and only to that of τ_1=0.5 ps component for TiO_2/EL2 cell. Moreover, the amplitudes of τ_1 component are smaller for TiO_2/EL2 than TiO_2/EL1 cell, which suggests that significant part of FC decay in electrolyte EL2 takes place on the time scale shorter than IRF of our setup (<150 fs). Similarly, the decay of CT state (maximum of decay amplitude at 600 nm) contributes to the spectra of τ_2=12 ps and τ_3=130 ps components for TiO_2/EL1 cell and only to that of τ_2=13 ps component for TiO_2/EL2 cells, being apparently faster.

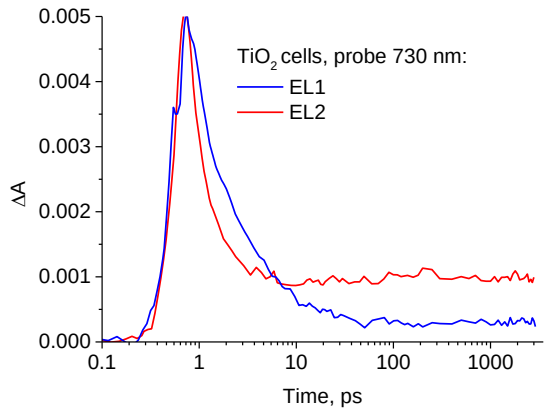

Figure S15. Comparison of the transient absorption kinetics of TiO_2 cells with different electrolytes measured at 730 nm (pump 520 nm, 500 nJ).

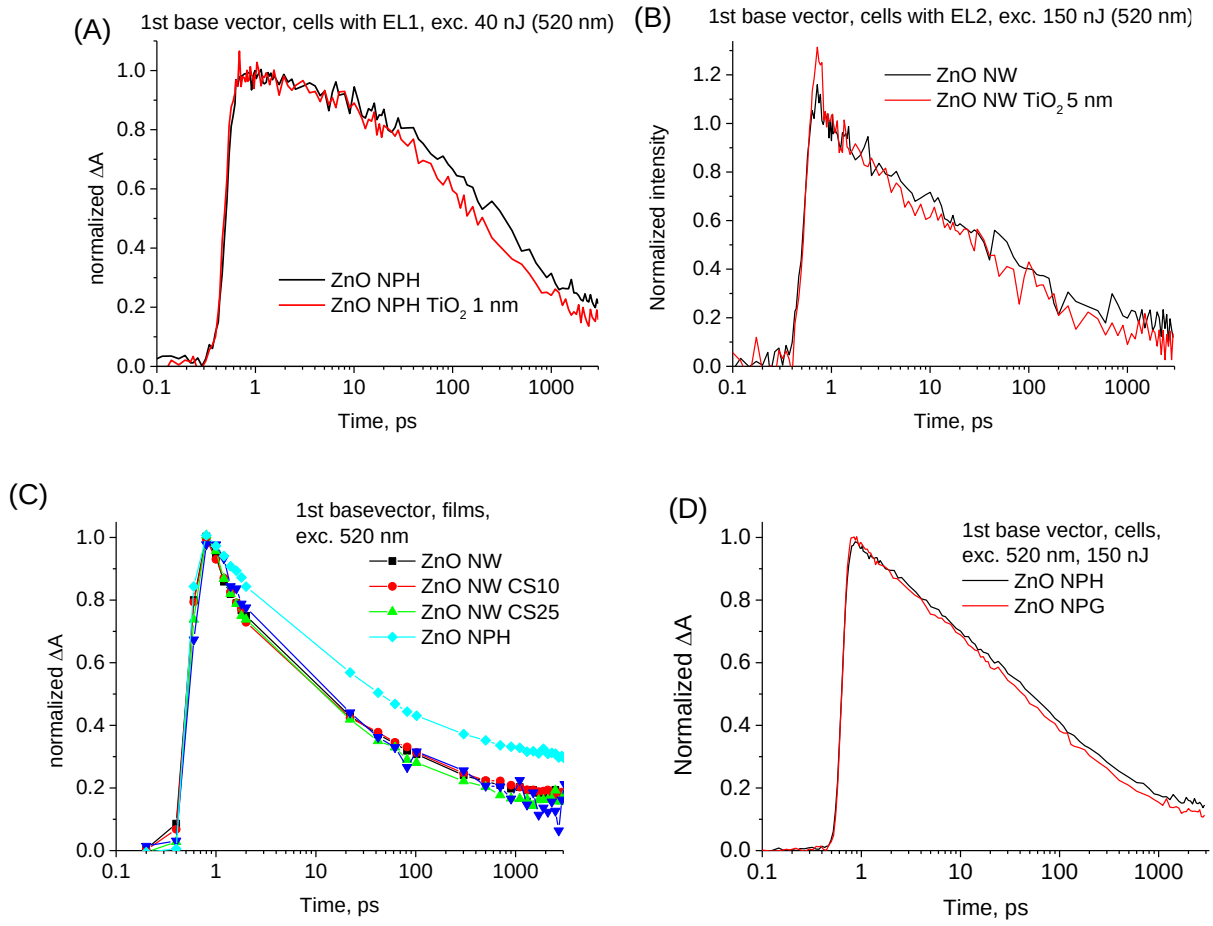

Figure S16. The first base kinetic vector of indicated samples obtained after SVD global analysis in 800-1400 nm range. The excitation wavelength was at 520 nm.

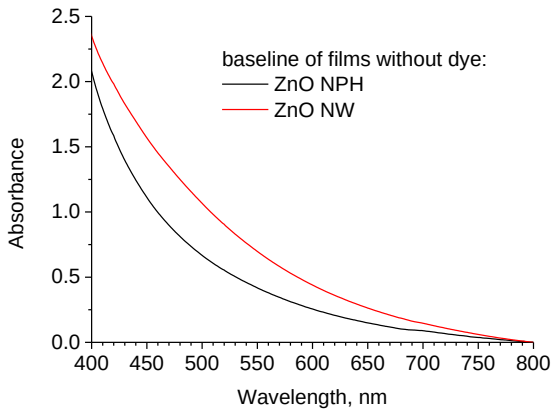

Figure S17. A baseline of the stationary absorption (in the transmission configuration) of ZnO NPH and ZnO NW showing higher scattering of the latter. It should be noted that the nanoparticle photoanodes in this study do not contain the scattering layer of larger particles.

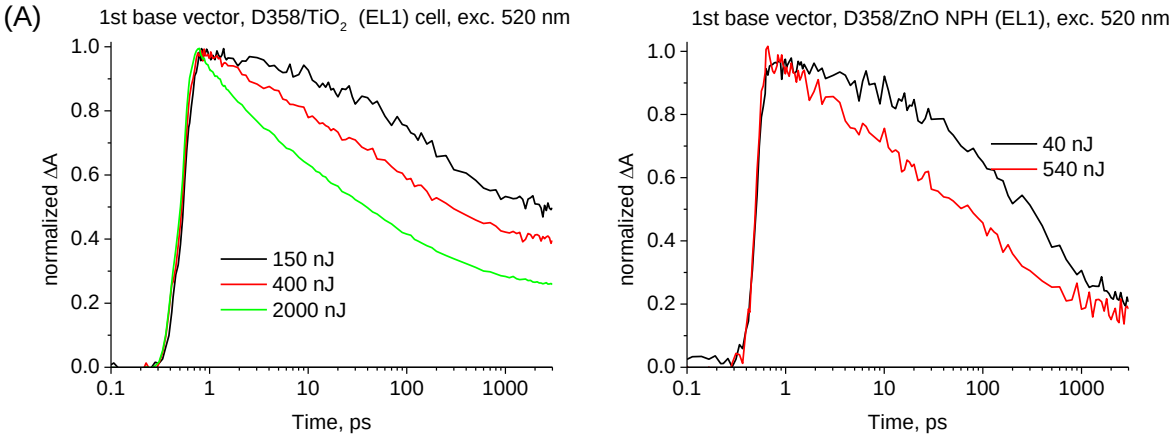

Figure S18. Effect of the excitation energy on TiO_2 and ZnO cells. Note that larger self-quenching occurring for higher pump pulse intensity results also in smaller residual population of radical cation (at 3 ns).

References:

[1] E. Guillén, L. Peter, J.A. Anta, Electron Transport and Recombination in ZnO-Based Dye-Sensitized Solar Cells, J. Phys. Chem. C, 115 (2011) 22622-22632.

[2] J.A. Anta, E. Guillén, R. Tena-Zaera, ZnO-Based Dye-Sensitized Solar Cells, J. Phys. Chem. C, 116 (2012) 11413-11425.

[3] E. Guillén, E. Azaceta, A. Vega-Poot, J. Idígoras, J. Echeberría, J.A. Anta, R. Tena-Zaera, ZnO/ZnO Core−Shell Nanowire Array Electrodes: Blocking of Recombination and Impressive Enhancement of Photovoltage in Dye-Sensitized Solar Cells, J. Phys. Chem. C, 117 (2013) 13365-13373.

[4] X. Yang, S. Zhang, K. Zhang, J. Liu, C. Qin, H. Chen, A. Islam, L. Han, Coordinated Shifts of Interfacial Energy Levels: Insight Into Electron Injection in Highly Efficient Dye-Sensitized Solar Cells, Energy Environ. Sci., 6 (2013) 3637-3645.

Factors affecting the performance of champion silyl-anchor carbazole dye revealed in the femtosecond to second studies of complete ADEKA-1 sensitized solar cells.

Jan Sobuś [1,2], Błażej Gierczyk [3], Gotard Burdziński [2],
Mariusz Jancelewicz [1], Anders Hagfeldt
and Marcin Ziółek[2]

[1]*NanoBioMedical Centre, Adam Mickiewicz University, Umultowska 85, 61-614 Poznan, Poland.*

[2]*Quantum Electronics Laboratory, Faculty of Physics, Adam Mickiewicz University in Poznań, Umultowska 85, 61-614 Poznan, Poland.*

[3]*Faculty of Chemistry, Adam Mickiewicz University, Umultowska 89b, 61-614, Poznan, Poland*

Abstract

The record laboratory efficiencies of dye-sensitized solar cells have been recently reported using an alkoxysilyl-anchor dye, ADEKA-1 (over 14%). In this work we use time resolved techniques to study the impact of key preparation factors (dye synthesis route, addition of co-adsorbent, use of cobalt-based electrolytes of different redox potential, creation of insulating Al_2O_3 layers and molecule capping passivation of the electrode) on the partial charge separation efficiencies in ADEKA-1 solar cells. We have observed that unwanted fast recombination of electrons from titania to the dye, probably associated with the orientation of the dyes on the titania surface, plays a crucial role in the performance of the cells. This recombination, taking place on the sub-ns and ns time scales, is suppressed in the best dye synthesis methods and upon addition of the co-adsorbent. Capping treatment significantly reduces the charge recombination between titania and electrolyte, improving the electron lifetime from tens of ms to hundreds of ms, or even to single seconds. Similar increase in electron lifetime is observed for homogenous Al_2O_3 over-layers on titania nanoparticles, however, in this case the total solar cells photocurrent is decreased due to smaller electron injection yield. Our studies should be important for broader use of very promising silyl-anchor dyes and the further optimization and development of dye-sensitized solar cells.

1. Introduction

Dye-sensitized solar cells (DSSC) [1-4] represent one of the most important emerging photovoltaic technologies, which – thanks to potential inexpensiveness – have a real chance to become an alternative to the hitherto used relatively expensive solar panels, dominated by inorganic silicon cells and thin film cells (mainly CIGS). Thanks to the specific properties of DSSC such as good efficiency under moderate sunlight intensity, possibility of making semi-transparent systems and possibility of using dyes of different absorption bands, they can be used in rooms, in decorations or on building façades, (i.e. in the so-called BIPV: building-integrated photovoltaics). However, their widespread use requires improvement of the DSSC efficiency (the highest certified one is 11.9% [5]). Another important problem is the stability of DSSC devices.

Total charge separation in DSSC, whose quantum yield determines the maximum current flowing in the solar cell, involves a few partial processes: electron injection from the dye to the semiconductor (usually titania) nanostructure, the regeneration of the oxidized dye, and charge collection from the nanostructured photoanode [1, 3-4]. To ensure quantum yields of charge separation close to 100%, some excess energy is needed for particular partial processes that have to compete with the undesired pathways of charge transfer. However, the greater the excess energy (energy loss), the lower the voltage of the open circuit (Voc). The value of this voltage, along with the photocurrent intensity, determines the actual efficiency of the solar cell [1, 6]. For many years the dominant systems were the DSSC with ruthenium dyes and an iodide electrolyte (containing the pairs I^-/I_3^-, whose redox reaction mechanism is multi-electron), in which effective process of dye regeneration required particularly large driving force [7-9]. Recently, alternative electrolytes based on cobalt ions (with single-electron redox pair Co^{2+}/Co^{3+}) have been developed, whose redox level is energetically lower (has more positive potential) [10-12]. The use of these electrolytes in combination with organic dyes without ruthenium content, has led to higher Voc values of the solar cells at similar values of photocurrent, which has brought laboratory efficiencies of DSSC using porphyrin dyes as high as up to 13% [13-14]. Calculations suggest that the use of cobalt-based electrolytes and optimization of all parameters should theoretically bring the DSSC efficiency of almost 18% (at the total energy loss reduced to 0.6 eV relatively to 0.75 eV for iodide electrolytes) [6]. However, in the systems with cobalt electrolytes, the common problem is a fast process of undesirable recombination of electron from the conduction band, which

enforces the use of special methods for insulation of metal oxide nanoparticles from the electrolyte, for the majority of dyes.

At this point the novel family of the dyes with silyl anchoring groups have been proposed by Japanese researchers to be employed as sensitizers in DSSC [15-19]. It has been shown that the covalent bond made by the alkoxysilyl groups on the surface of the metal oxide nanoparticles (Si-O-Ti), is much stronger than that made by the traditional carboxylic groups (C-O-Ti). Owing to this property, it was possible to apply the passivation of the metal oxide surface by few rather strong acids (called multi-capping) that fill the voids between the dye molecules and block the access of the cobalt electrolyte to the metal oxide nanoparticles. This method could not be applied for the systems with dyes comprising carboxylic groups because it resulted in the detachment of dye molecules from the nanoparticles surface [16]. Moreover, silyl-anchor dyes exhibit remarkable stability and resistance to water in DSSC devices [16].

The best dye of this new family so far turned to be ADEKA-1, a silyl modification of popular carbazole sensitizer MK2 [20-23]. For ADEKA-1 used alone the best efficiency of DSSC was 12.5% [16], and in combination with SFD-5 (another silyl-anchor dye, absorbing in more short-wavelength range of solar spectrum) the efficiency increased to 12.8% [18], while in co-sensitization with LEG4 (a carboxy-anchor dye with triphenylamine electron donor group) the best efficiency exceeded 14% [19]. According to our knowledge, this is actually a record reported laboratory efficiency of DSSC. Therefore, it is quite likely that the dyes with silyl anchoring groups in combination with cobalt electrolytes can instigate revival of DSSC technology.

On the other hand, however, the studies of DSSC employing silyl-anchor dyes have not been undertaken in other laboratories so far. One of the reasons might be difficulties with the proper dye synthesis. Moreover, no fundamental characterisation of the dyes with silyl anchoring groups is available. This problem needs thorough fundamental research that would bring information on the interaction of the dyes with metal oxide nanoparticles so that the design of new DSSC would be more effective. In particular, to the best of our knowledge, no time-resolved studies have been performed for the dyes with silyl anchoring groups.

Therefore, in this work we employ time-resolved laser spectroscopy and electrochemical impedance spectroscopy to study the dynamics of charge transfer in complete solar cells sensitized with ADEKA-1 dye on the time scale from 200 fs to several seconds. We investigate the influence of several optimization procedures (employed for DSSC

sensitized with ADEKA-1 [16]) on the partial charge separation efficiencies. These additional treatments are: the incorporation of co-adsorbent, the use of cobalt-based electrolytes of different redox potential, creation of insulating Al_2O_3 layers and molecule capping passivation of the electrode. Moreover, we report, with much more details, the route for the most efficient (and free from polymerization problems) synthesis of ADEKA-1 and related alkoxysilyl-anchor dyes.

2. Experimental

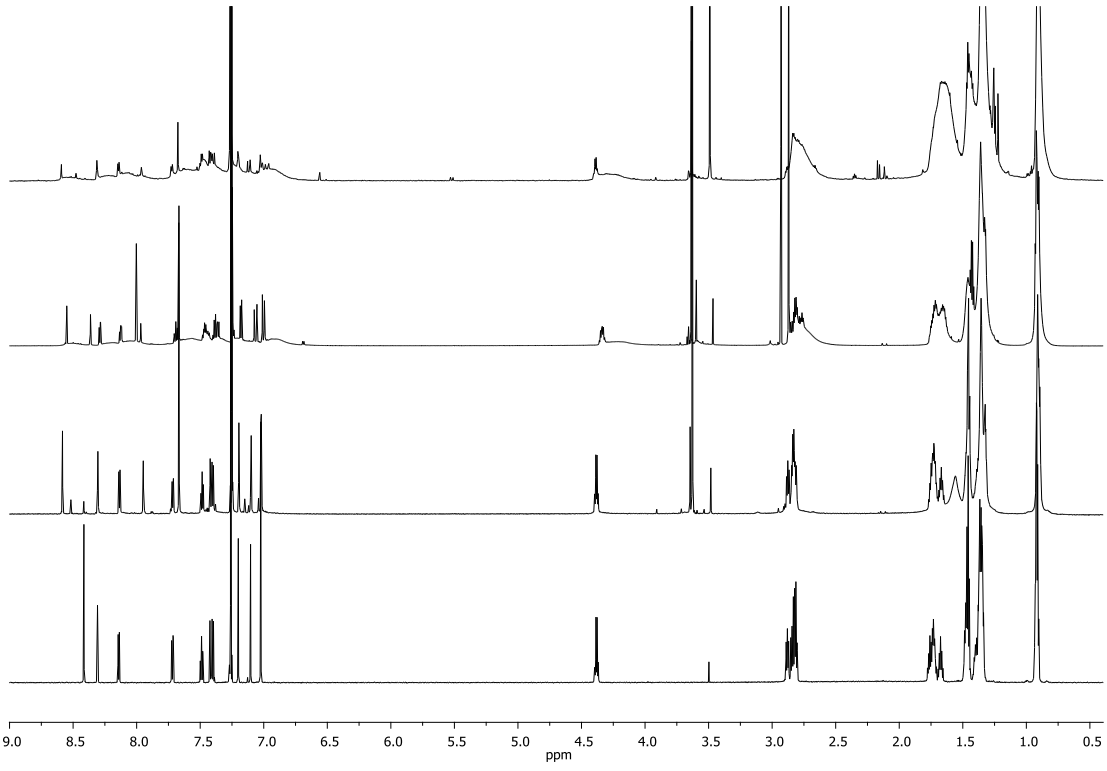

Fig. 1. ADEKA-1 dye structure (top) and ^{1}H NMR spectra of (from the bottom): MK2, ADEKA-1, and partially polymerized ADEKA-1 samples (*ca.* 30 and 5 % of monomer, respectively) in $CDCl_3$ (bottom).

2.1 Dye synthesis

2.1.1 Chemical compounds and apparatus used

All solvents were dried with molecular sieves (3Å, 20% m/v). Reactions were made in flame-dried glassware under argon atmosphere. Dimethylformamide (DMF) was allowed to stand over CaH_2 for 24 h and distilled under reduced pressure immediately prior the use.

^{1}H and ^{13}C NMR spectra were recorded at 298 K on Agilent DD2 800 spectrometer, operating at frequencies 799.926 and 201.162 MHz, respectively, equipped with $^{1}H[^{13}C/^{15}N]$ triple resonance probe (90° pulse width: ^{1}H – 13.6 μs; ^{13}C – 6.9 μs). The samples concentration was 0.01 M. 1D spectra were recorded using standard one-pulse sequence (*s2pul*), 2D experiments were made using standard sequences with gradient pulses (gCOSY, gHMQCAD, gHMBCAD). The ^{13}C NMR spectra were recorded with broadband ^{1}H decoupling. Elementary analyses were made on a Vario EL III analyzer. FT-IR spectra were recorded on a Bruker IFS 66s spectrometer in KBr disc (1 mg in 200 mg KBr).

2.1.2 Synthesis process

To a stirred solution of 100 mg of MK2 dye (0.105 mmol) in 2 mL of chloroform, solution of 14.6 mg oxalyl chloride (0.115 mmol) in the same solvent (200 μL) was added, followed by addition of 100 μL of DMF. After 1 h the mixture was cooled to 0°C and the solutions of 4-(trimethoxysilyl)aniline (22.3 mg, 0.105 mmol) and ethyldiisopropylamine (27.1 mg, 0.210 mmol) in chloroform (200 μL) were added. The mixture was then mixed for 2 h at room temperature. After that the solvent was evaporated, the solid residue was dissolved in 1 mL of chloroform and 50 mL of methanol was added. The solid, blackish product was filtered off, washed with methanol and dried in vacuum. Yield 110 mg (91 %). ^{1}H NMR ($CDCl_3$): δ 8.59 (1H, s; H-29); 8.31 (1H, d, 1.7 Hz; H-8); 8.14 (1H, d, 7.4 Hz; H-5); 7.96 (1H, s; H-46); 7.72 (1H, dd, 8.4 & 1.7 Hz; H-10); 7.68 (4H, s; H-33 & 34); 7.49 (1H, dd, 8.1 & 7.5 Hz; H-3); 7.42 (1H, d, 8.1 Hz; H-2); 7.41 (1H, d, 8.4 Hz; H-11); 7.26 (1H, t, 7.4 Hz; H-4); 7.20 (1H, s; H-14); 7.11 (1H, s; H-26); 7.03 (1H, s; H-18 or H-22); 7.02 (1H, s; H-18 or H-22); 4.39 (2H, q, 7.3 Hz; H-44); 3.64 (9H, s; H-36); 2.86 (8H, m; H-38); 1.71 (8H,m; H-39); 1.46 (16H, m; H-40 & 41); 1.46 (3H, t, 7.3 Hz; H-45); 1.34 (8H, m; H-42); 0.91 (12H, m; H-43). ^{13}C NMR ($CDCl_3$): δ 155.54 (C-31); 151.4 (C-30); 144.8 (C-25); 143.6 (C-13); 142.7 (C-29); 140.9 & 143.3 (C-17 & 21); 140.8 (C-16); 140.4 (C-1); 139.6 (C-12); 135.9 (C-34); 135.4 & 136.8 (C-20 & 24); 129.8 (C-27); 129.2 (C-28); 128.9 & 129.1 (C-19 & 23); 129.0 & 128.3 (C-18 & 22); 128.5 (C-15); 127.4 (C-26); 126.0 (C-3); 125.7 (C-32 & 35); 125.4 (C-9); 125.1 (C-14);

123.9 (C-10); 123.4 (C-7); 122.8 (C-6); 120.6 (C-5); 119.5 (C-33); 119.1 (C-4); 117.9 (C-37); 117.6 (C-29); 108.8 & 108.7 (H-2 & H-11); 50.9 (C-36); 37.7 (C-44); 28.0-32.0 (C-38, 39, 40 & 41); 22.6 (C-42); 14.1 (C-43); 13.6 (C-45). IR (KBr): 3440, 3415, 2928, 2852, 2195, 1683, 1569, 1513, 1491, 1418, 1315, 1196, 1085, 825, 801, 724 cm^{-1}. Elemental analysis: calc. C 69.93; H 7.27; N 3.65; S 11.15; found C 70.02; H 7.35; N 3.59; S 11.05.ADEKA-1 structure and atom numbering are shown in Figure 1. ^{1}H-^{13}C HSQC and IR spectra are shown in Figures S1-S2 (in the Supporting Information).

2.2 Cell preparation

2.2.1 Preparation of the photoanode

Glass plates of the size 16x14 mmol were cut from the FTO glass sheet (Solar 4 mmol thickness, 10Ω/sq, Nippon Sheet Glass, Japan). They were cleaned using the solution of 2g Degonex detergent in 1 l of water in ultrasonic bath for 45 minutes. Afterwards, they were further purified by treatment in a UV-O3 system (Model No. 256–220 , Jelight Company, Inc.) for 15 min. Next they were submerged in 40 mmol aqueous solution of $TiCl_4$ for 40 minutes in 70 °C, followed by rinsing in water and ethanol. Subsequently, an approximately 8 μm thick layer of mesoporous titania was deposited by screen printing twice (54T, Estal Mono, Schweiz. Seidengazefabrik, AG, Thal) the commercially available screen printing pastes (30NR-D or 18NR-T, Dyesol) with 8 minute paste settling on 125 °C hotplate after the first print. No scattering layer was used, since it would prohibit transient absorption studies. After printing and verifying thickness by the needle profilometry, the photoanodes were again subjected to $TiCl_4$ treatment described before with concentration lowered to 20 mmol. Finally, the electrodes with the TiO_2 pastes were gradually heated under an airflow at 125 °C for 5 min, 325 °C for 5 min, at 375 °C for 5 min, at 450 °C for 15 min, and at 500 °C for 15 min.

2.2.2 Counter electrode preparation

Counter electrodes were prepared by cutting 18x14 mm plates from the FTO covered glass sheet (LOF Industries, TEC 15 Ω/sq, 2.2 mm thickness) and had 1 mm conical holes sand-blasted in them. Afterwards there were cleaned in water, acetone and dried. Heating to 400 °C for 30 minutes in order to remove any organic contamination left was followed by drop-wise deposition of 80 μL of solution of graphene nanoplatelets (1 mg per 2 mL of acetone). Upon drying in low humidity conditions it left a uniform carbon layer on the glass surface.

2.2.3 Dye deposition

Prior to dye deposition the photoanodes were dried in 400 °C for 30 minutes to remove any residual water or other contaminants. Unless otherwise indicated the dye solution had concentration of 0.2 mmol, the solvent used was toluene (dyes without co-adsorbent) or 9:1 mixture of toluene and acetonitrile (dyes with co-adsorbent). The dyes used were MK2 (Sigma) and ADEKA-1 (synthesis route described in previous paragraphs). The co-adsorbent used was isooctyltrimethoxysilane (OTMS, Sigma Aldrich) with concentration of 0.1 or 0.2 mmol. Working electrodes were placed in the dye solution and stored in 5 °C for 16-20 hours to enable full absorption of the dye.

2.2.4 Cell assembly

Both electrodes were connected together using a polymer seal (25 μm Surlyn, Meltronix, Solaronix SA) with conducting surfaces facing inwards. They were then filled with electrolyte through the holes in the counter electrode and sealed with the cover glass on top. The electrolyte consisted of 0.25 mol Co^{2+}Bis(trifluoromethane)sulfonimide (TFSI), 0.035 mol of Co^{3+}TFSI, 0.1M of LiTFSI and 0.5M tertbutylpyridine (TBP). Cobalt redox couple used was cobalt-phenantroline (Co-Phen) in most cases (if not stated otherwise). For comparison, some cells were prepared with cobalt-bypyridine complexes (Co-Bpy).

2.2.5 ALD and capping treatment

In some of the cells additional preparation steps were involved in order to make core shell structures or incorporate the capping treatment. Alumina shell was deposited on the photoanodes before submerging them in the dye using Atomic Layer Deposition (ALD) technique. It was performed using R-200 reactor (Picosun) with deionized water and trimethylaluminium as oxygen and aluminium sources respectively. The length of the deposition (0.1 s or 2 s) and purge (3 s or 8 s) steps of the cycle turned out to be of high importance as will be describe in further chapters. Capping treatment was performed by sequentially dipping the photoanodes in the appropriate solutions and rinsing them with toluene, just after taking them out from a dye and right before cell assembly. All capping solutions had 1 mmol concentration in 1:1 toluene:acetonitrile solvent. For single capping (SC) treatment the electrode was submerged in heptanoic acid solutions for 30 minutes. For

multi capping treatment it was dipped in n-octadecyl succinic acid for 10 minutes, n-hexadecyl malonic acid for 10 minutes, tetradecylphosphonic acid for 5 minutes, octylphosphonic acid for 5 minutes, heptanoic acid for 10 minutes and finally ethylphosphonic acid for 5 minutes.

2.3 Cell characterization

A current-voltage characterization of the solar cell was performed with a potentiostat (model M101 with frequency response analyzer FRA32M module, Autolab) coupled to a photoelectric spectrometer equipped with the option of solar simulator (Instytut Fotonowy – Photon Institute, Poland). The sunlight conditions were simulated by a Xe lamp with AM 1.5 G spectral filter and intensity adjusted to 100 mW/cm^2 using a calibrated silicon cell (RR-74, Rera Systems). It was used to obtain characteristics of the cells subjected to transient absorption measurements. Part of the current voltage characterization was done on a solar simulator equipped with a 450 W xenon lamp (Model No. 81172, Oriel) calibrated by using a reference Si photodiode equipped with an IR-cutoff filter (KG-3, Schott) as well (cells to be later analyzed by EIS). Electrochemical impedance spectroscopy (EIS) measurements were performed using SP-300 potentiostat (BioLogic) over the range from 0.1 Hz to 7 MHz spread in 80 measuring points distributed evenly on the logarithmic frequency scale. The obtained curves were analyzed using the ZView software using transport line element [24]. More information about the voltage range and equivalent circuits is presented in the Supplementary Information.

All transient absorption studies were performed for fully assembled, working solar cells (the same as those characterized in current-voltage measurements). The setup for ultrafast broadband transient absorption has been described before (Helios spectrometer, Ultrafast Systems, and Spectra Physics laser system) [25]. The pump pulses were set at 500 nm and the IRF (pump-probe cross correlation function) was about 250 fs (FWHM). The pump pulse energy of 60 nJ corresponds to energy density of about 30 $\mu J/cm^2$. The transient absorption measurements were performed in the spectral range of 450-850 nm and in the time range of up to 3 ns. The nanosecond flash photolysis setup was based on Q-switched Nd:YAG laser and a 150 W xenon arc lamp as the excitation and the probing light sources, respectively [26]. The pump pulse wavelength was set at 532 nm and the energy was set at 0.15 mJ (energy density of about 300 $\mu J/cm^2$).

The global analysis of the transient absorption data was performed using Surface Explorer software (Ultrafast Systems) and Asufit program [27] for ultrafast transient absorption and nanosecond flash photolysis, respectively. Both programs fit a multi-exponential function (convoluted with IRF) to either the kinetic vectors of a selected number of singular values (Surface Explorer) or to the kinetic traces for all analysed wavelengths (Asufit). As a result of the analysis the characteristic time constants were obtained as well as the wavelength-dependent amplitudes associated with them (also called decay associated difference spectra or pre-exponential factor spectra).

3. Results and discussion

3.1 Effect of the synthesis route

The synthetic procedure for ADEKA-1 published previously [16] is questionable in several aspects. First, the authors have reported using water during work-up of the reaction mixture, i.e. extraction of polar byproducts with this solvent. It is well known, that alkoxysilane derivatives are highly unstable in hydrolytic conditions [28-29]. In the presence of water they undergo polycondensation (*via* silanol intermediate). This process is faster in the presence of ionic substances in water. In consequence, the use of this procedure results in a mixture of ADEKA-1 and polymeric products formed during its polycondensation. Depending on the time of shaking with water and on its amount the organic layer contains a mixture of monomeric and polymeric form of the dye or even only polymer (Figure 1). The authors of the discussed procedure used column chromatography on silica to purify the product. The second well known aspect of alkoxysilane chemistry is the tendency of these compounds to reacting with surface of silica (and other oxide materials) [30-32]. The presence of silanol groups on the SiO_2 surface results in immobilization of SiOR containing molecules linked *via* SiOSi bond formation. This interaction strongly decreases the yield of the product. If the elution of the dye is carried out slowly, almost 100% of the monomer is covalently bonded to the silica. The fast elution allows separation of the expected fraction, however reduces its purity. Working up of the reaction mixture according to the procedure published previously results in isolation of minute amount of ADEKA-1 (5-10 mg). The last questionable information is the composition of eluent. The authors have used a mixture of chloroform-hexane (1:1 v/v). Both ADEKA-1 and MK2 dyes do not move on silica in this solvent system. The use of pure diethyl ether, acetonitrile, chloroform-methanol (1:1) or

chloroform-acetone (1:2) is needed to elute ADEKA. Resulting upgraded synthesis process is described in experimental section.

During the process of optimization several batches of ADEKA-1 were obtained, with different content of the polymerized version of the dye (ranging from monomer only through 50/50 monomer/polymer mixture to the fully polymerized batch). The polymer content was verified by NMR in all cases. For simplicity, the samples will be named (here and in the rest of the text) according to the monomer content, eg. "60%m" means the sample consisting of 60% of monomer and 40% of polymer. The cells made with the following samples were investigated: 100%m, 100%m_old (the same sensitizing solution kept for more than 2 months), 60%m, 50%m and 0%m. The differences in the monomer content can be also observed in the normalized stationary absorption spectra in toluene by examination of the local absorption minimum around 423 nm (Figure S3). A clear minimum is present for pure monomer synthesis (both in fresh and aged solutions), while the spectrum of fully polymerized dye (0%m) doesn't exhibit the characteristic minima. Moreover it turned out that the polymerized dye has its absorption maximum slightly moved to the shorter wavelength, while the absorption tail is extended to the red. For equal mixture of monomer and polymer, the absorption spectrum is more similar to 100%m, but the minimum at 423 nm is flattened.

3.2. General trends observed in transient absorption

While it is hard to compare the absolute efficiencies of the all cells prepared with those dye, and electrode treatment variants, as they were assembled in two different laboratories and conditions, a measure of checking the dye performance can be utilized based on transient absorption data. A simple way to test the relative efficiency of the charge separation occurring up to 3 ns (time window of the ultrafast transient absorption setup) is a comparison of the normalized kinetics probed at 750 nm. As previously reported by us for the reference MK2 dye [33], the combined spectrum of dye radical cation and electrons in titania has a maximum close to this wavelength. On the other hand, the initial signal (just after excitation) is proportional to the population of the singlet excited state of the dye. Therefore, the magnitude of the signal left after the 3 ns (ratio of the final to initial amplitude) shows the amount of the charge carriers that got successfully separated and did not recombine with the dye molecule itself. The selected, representative kinetics for different ADEKA-1 cells (as well as the reference kinetics for MK2 cell) are presented in Figure 2A. As can be seen, there is a large

variety of the residual amplitude for different ADEKA-1 cells, and only the best configurations match the efficiency obtained for MK2 cell.

It should be noted that the above analysis reflects the initial charge separation efficiency with respect to the number of absorbed photons, so it cannot be directly correlated with Jsc of the cells having different number of absorbed dyes. The global solar cell parameter that accounts for the differences in light absorption is total absorbed photon to current efficiency (APCE). This parameter was estimated by dividing the number of the photons absorbed by the dye (obtained from integration of stationary absorption spectrum of the sensitized electrode, with subtracted spectrum of unloaded one, taking into account the photon flux from AM1.5G data) by the photocurrent of the full working device.

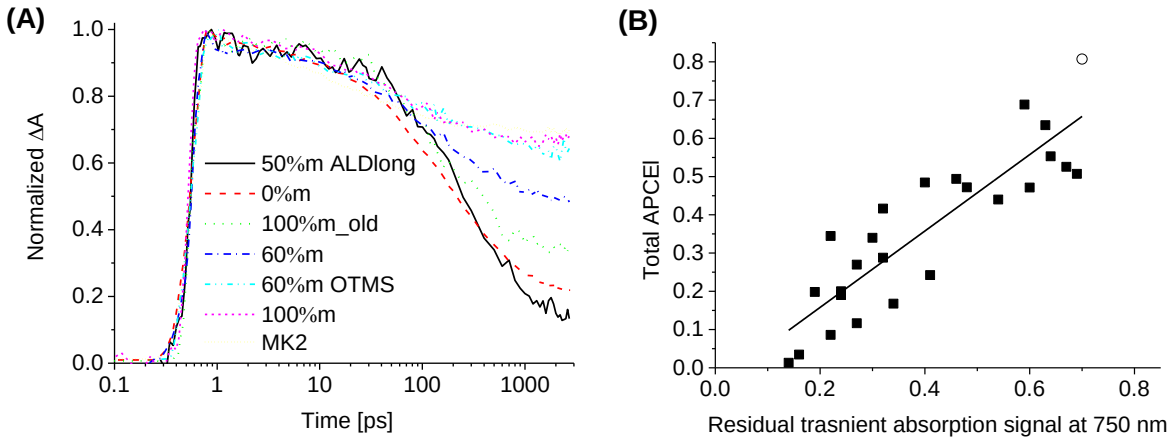

Figure 2. Kinetic of transient absorption traces at 750 nm of various cells sensitized with ADEKA-1 dye **(A)** and total APCE of the various cells plotted versus the relative amplitude of residual signal at 750 nm in transient absorption experiment measured after 3 ns after sample excitation **(B)**. The detailed parameters (various versions of ADEKA-1 dye, surface treatments and addition (or lack) of OTMS co-adsorbent) of the cells shown in Figure (B) are presented in Table S1.

As is shown on Figure 2B and in Table S1, the amplitude of the residual signal at 750 nm well corresponds to the total APCE of the device, independently of the dye series, coadsorbent addition and surface treatments (described in further chapters). The MK2 dye is being used as a reference here due to its high efficiency on this timescale. If it can be matched by ADEKA-1 on the ultrafast timescale, the alkoxysilane bonding provides ways to prevent transport recombination on the longer timescales and improve voltage of the device (as will be shown later on). Judging from Figure 2 and Table S1 one can see that the fully polymerized ADEKA-1 dye gives the lowest efficiency. The cells from the aged synthesis

(100%m_old) fares not much better. The best efficiency on the ultrafast timescales is obtained for the fresh pure monomer synthesis.

More detailed information can be obtained by the global analysis of the transient absorption spectra. The analysis was performed in a similar way to that recently reported by us for MK2 cells [33]. The transient absorption spectra are decomposed using 4 time constants plus an offset constant in the time window of an experiment. The pre-exponential factor spectra of the fitted components are shown in Figure 3 for selected samples. The first three components were similar for all cells, so for a better comparison between different cells their average values (0.2 ps, 3 ps and 40 ps) were used in the final fitting. The fourth, sub-ns component (in the range of several hundred ps) was left a variable one. The fastest component (0.2 ps) is comparable to the IRF of the setup and it contains significant contribution of coherent artifacts that occur during pump-probe overlap [34], so for the clarity of the presentation it is omitted from the graphs. The two shortest components (0.2 and 3 ps) are attributed to the electron injection process from the excited dyes. As can be seen in Figure 3, the pre-exponential factor spectra of 3 ps component are usually negative in the range from 600 to 750 nm, which probably indicates the rise of the population of dye radical cation and trapped electrons in titania [33], as well as a decay of the stimulated emission from the excited state of the dye.

Longer components (40 ps and sub-ns) should be probably assigned to the fast recombination between the injected electrons and the dyes [33, 35-38]. We think that the factors driving such recombination can be similar to those recently reported DSSCs with porphyrin dyes [39-40]. As has been shown, the fast recombination rates are directly dependent on the dye molecule orientation (tilt angle) on the surface, with perpendicular molecules having longest recombination times [40]. To account for the observed features, the recombination mechanism “through space” was proposed rather than “through bonding”, the former favoring recombination in the configurations with the electron donor part of the dye closer to the titania surface. Similarly to our previous assignment for MK2 [33], the 40 ps component represents the recombination between the electrons injected to the trap states (yet to be successfully separated) and the dye. This recombination process occurs probably through the dye bonding. For all ADEKA-1 cells the amplitude of 40 ps component mirrors somehow the 3 ps one, and their relative ratio is rather independent from the cell efficiency. On the contrary, the “sub-ns” and constant offset components vary a lot for the cells of different performance. Therefore, we think that the sub-ns component represents the

recombination with the dye through the empty space between the titania and the absorbing part of the dye molecule. Since it competes with the constant offset signal of the successfully separated oxidized dyes and charge carriers, its low amplitude and red shift is mostly beneficial for the successful charge separation.

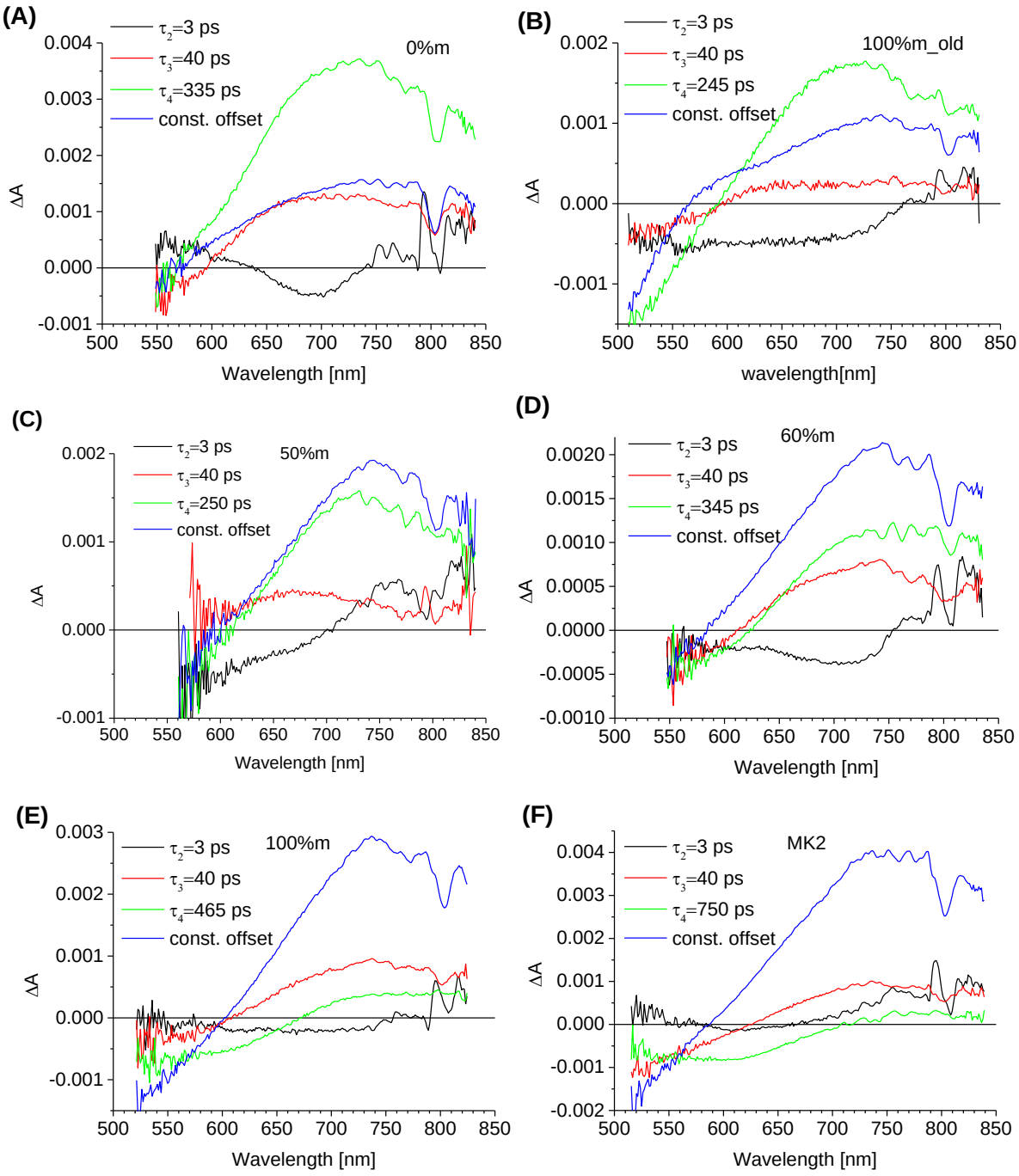

Figure 3. Wavelength dependent amplitudes of the indicated time constants obtained from global analysis of transient absorption spectra of full cells sensitized with various versions of ADEKA-1 (with the spectra of reference MK2 dye included): (A) 0%m, (B) 100%m_old, (C) 50%m, (D) 60%m, (E) 100%m and (F) MK2.

It is clearly visible from Figure 3 that the polymerized version (0%m) has the highest amplitude of the sub-ns signal compared to the blue residual one. The aged dyes also exhibits higher sub-ns signal than the constant offset one. At the moment, we do not have a clear explanation why the old 100%m solution gives much worse performance then the fresh one, since both stationary absorption (Figure S3) and NMR analysis do not reveal any differences in the signals of ADEKA. One explanation might be that the dye can suffer from isomerization with time which facilities worse orientation on nanoparticle surface and thus higher recombination. Moving to the 50%m and 60%m synthesis, the recombination signal is suppressed successfully and increasing the monomer content by 10% makes the recombination signal even lower and extends it characteristic time by 100 ps. Optimized synthesis process (100%m) results in the lowest amplitude of the sub-ns component and the position where its spectrum changes the sign from negative to positive (intersection with $\Delta A=0$ line) shifts as far as 670 nm. The red shift of the negative amplitude in the sub-ns component in efficient cells might be due to the Stark shift effect [26, 41-42]. As more electrons are fully separated in better cells, they create larger electric field on the nanoparticle surface, which leads to enhanced negative signal due to the Stark shift of dye absorption band. Another possibility is that in better cells the orientation of molecules is more perpendicular to the surface, which makes the direction of ADEKA-1 dipole moment change better aligned with electric field direction, and in turn also enhances Stark shift effect [26, 41-42].

Selected fully assembled cells were also probed with transient absorption measurements in ns-μs timescale. Resulting kinetics were analyzed using global fitting multi-exponential function and the resultant time constants with the wavelength-dependent amplitudes (associated with teach time constant) are shown in Figure 4 (A-C). Besides the 3 components shown in the figures, an additional 20 ns component (IRF of the setup) was also used in the fit to account for the scattered light. Two shorter components (around 200 ns and 3.5 - 4 μs) represent the decay of the oxidized dye molecules (radical cation) due to dye regeneration (by electrolyte) and electron-dye recombination. Their spectra can be divided to a positive part, which is an effect of absorption of oxidized dye, and a negative part representing disappearing absorption of the ground state of dye molecules (bleach signal) Stark shift effect. The longest time, having positive amplitude over all wavelengths, represents electrons in titania.

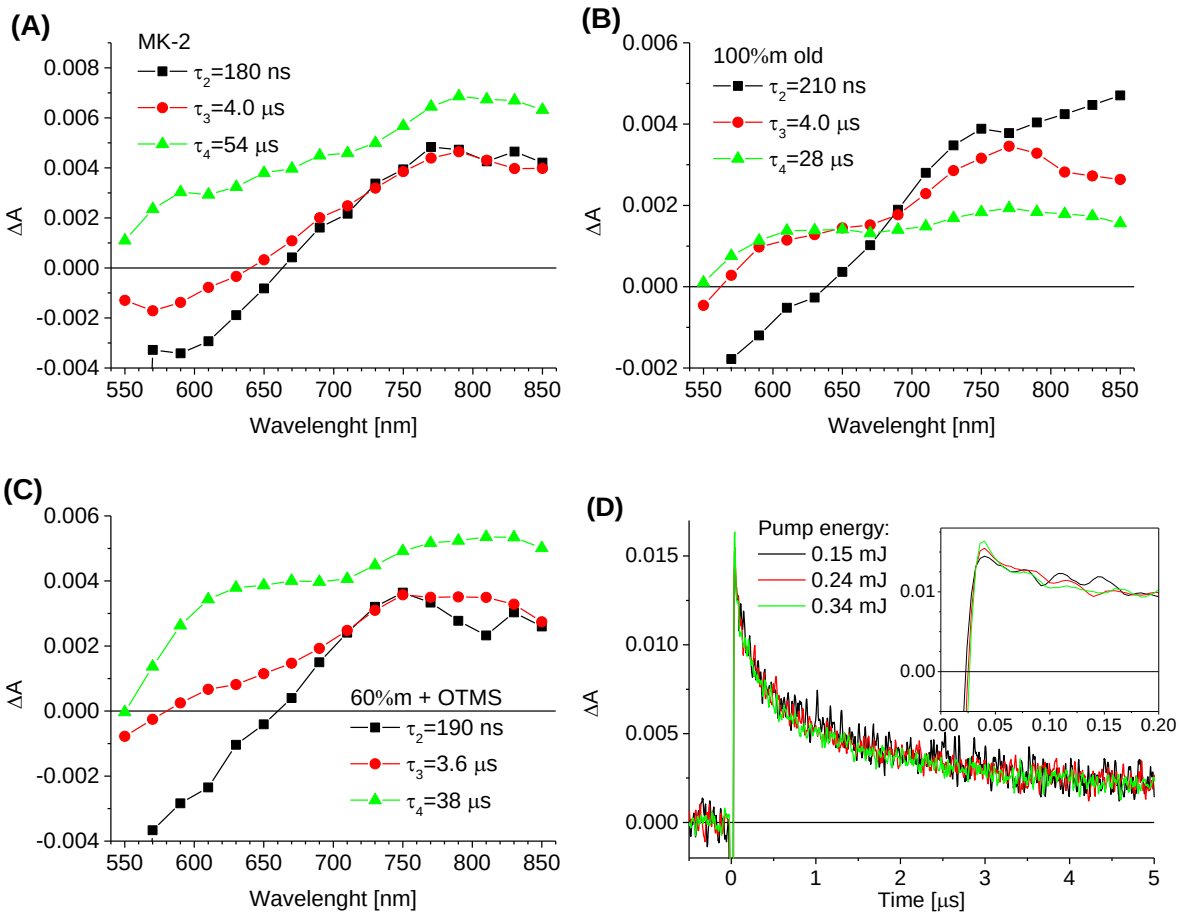

Figure 4. (A-C) Wavelength-dependent amplitudes with the indicated time constants obtained from the global fit to the flash photolysis results of the MK2 and ADEKA-1 cells. (D) Kinetics at 7500 nm obtained in flash photolysis experiments for ADEKA-1 cell and the indicated pump pulse energies. The inset shows the magnified initial signal.

The results for reference MK2 cells (Figure 4A) are similar to our previous report [33], but in that work we resolved one averaged short component (about 1 μs), assigned to dye regeneration dynamics. Here we find that this component should be rather divided into the two contributions (200 ns and 4 μs) of slightly different pre-exponential factor spectra. Most probably, the faster one contains significant part of electron-dye recombination, which might be a continuation of the sub-ns recombination observed in ultrafast transient experiments (lowering the performance of the solar cell). Indeed, for ADEKA-1 cell of worse efficiency (Figure 4B, old solution) the contribution of the 200 ns component is higher than that in the better cell (Figure 4C), while the amplitude of the final component (due to the electrons left in titania) is lower in the former than in the letter cell. Moreover, the effect of the pump pulse intensity investigated for the kinetics at 750 nm (Figure 4D) confirms this assignment. As a

result of higher pump intensity (thus higher population of injected electrons and oxidized dyes per nanoparticle) the contribution of fast component increases (as expected for the recombination process), while the dynamics of the middle, microsecond component is unchanged. Therefore, the latter can be assigned exclusively to dye regeneration process.

To summarize this part, we have observed that fast recombination plays a crucial role in the performance of the solar cells with ADEKA-1 dye. The unwanted dye recombination, probably associated with the orientation of the dyes on the titania surface, takes place on the sub-ns and ns time scales. Its amount is correlated with the photocurrent of the cells corrected for the number of absorbed dyes (total APCE). The dyes with higher content of monomers give smaller recombination and better performance. Enhanced recombination in ADEKA-1 compared to the reference MK2 dye can be probably explained by higher electronic coupling between dye and titania (due to different anchoring groups) and/or additional molecule rotation possibilities present in the extended anchoring group of ADEKA-1. In the next sections, the influence of other factors on the recombination dynamics will be presented, which are: the effect of different position of the redox couple potential, the addition of co-adsorbent, capping treatment and the effect of alumina protection layer. Besides the fs-µs laser spectroscopies, the electrochemical impedance spectroscopy will be also employed to test the charge separation dynamics occurring on longer time scales.

3.3 Effect of different cobalt complex (Co-phen vs Co-bpy)

For selected MK2 and ADEKA-1 cells we have checked the effect of changing the electrolyte redox pair from cobalt-phenenatroline to cobalt-bypyridine. The reason was to check the effect of shifting the position of electrolyte redox potential (from 0.62V vs NHE for Co-phen to 0.56 V vs NHE for Co-bpy) on the observed charge separation dynamics. The macroscopic parameters were affected in the way analogous to that frequently reported: for more positive redox potential the Voc of the cell increases, but at some point the Jsc start to decrease due to not sufficiently fast dye regeneration. Photovoltaic parameters of example set of MK2 cells are presented in Table S2. As can be seen, use of Co-phen instead of Co-bpy yields on average 23 mV higher voltage at the expense of 1.2 mA/cm^2 lower photocurrent. Similar effects were observed for ADEKA-1 cells (in a few configurations for which the redox couple effect was measured): lower Voc by about 20-30 mV and higher Jsc by about 10-20%, when Co-phen is replaced with Co-bpy.

Within the experimental error, no differences were observed between the ultrafast transient absorption results of the cells filled with the two cobalt electrolytes, both for MK2 and ADEKA-1. This could be expected as the position of the electrolytes redox potential should not influence either electron injection or electron-dye recombination dynamics. On the contrary, nanosecond flash photolysis measurements revealed the difference in the dye regeneration time constant. For MK2 cells, middle component in the global analysis (see previous section and Figure 4) was equal to 4 μs for Co-phen and 3 μs for Co-bpy. Similar shortening of the regeneration kinetics was observed for ADEKA-1 cells: the averaged time constants decreased from 3.5 μs for Co-phen to 2.5 μs for Co-bpy. For both dyes the effect can be attributed to larger driving force for the dye regeneration process when bypyridine redox complex is used with respect to the phenenatroline one. On the one hand, the differences in the fitted time constants between both Co complexes are not large. However, having in mind the discovered fast recombination (occurring partially on the time scales shorter than regeneration dynamics), even small improvements in regeneration time constant might be responsible for the evident increase in Jsc of the cells.

3.4 Impact of addition of the coadsorbent

A common method used to improve the efficiency of the device is addition of the coadsorbent to the dye solution. It is absorbed on the surface of the oxide between the dye molecules, resulting in decrease in dye agglomeration and higher average distance between dye molecules, which in turn reduces the energy transfer between them [43-44]. It can also help in arranging the dye molecules perpendicularly to the oxide surface, which reduces the recombination through space, which was previously reported for porphyrin dyes [39-40]. Figure 5 shows the global analysis spectrum of the 50%m and 60%m cells after the addition of OTMS as a co-adsorbent. Indeed, the sub-ns recombination component is heavily reduced and the residual one (constant offset) is improved in both cases (compare with Figures 3 without of the same synthesis series but without OTMS). Moreover, the sub-ns spectrum is moved a little to the red and the characteristic time is vastly increased. This most likely indicates that absorption of OTMS molecules on titania surface takes up empty spaces between dye molecules and prevents their “tiling” on the surface, consequently reducing recombination. The overall positive impact of the addition of OTMS on the sub-ns processes is also reflected by the higher residual signal of the kinetic at 750 nm for the samples containing OTMS, compared to their counterparts without it (e.g. Figure 2A for 60%m).

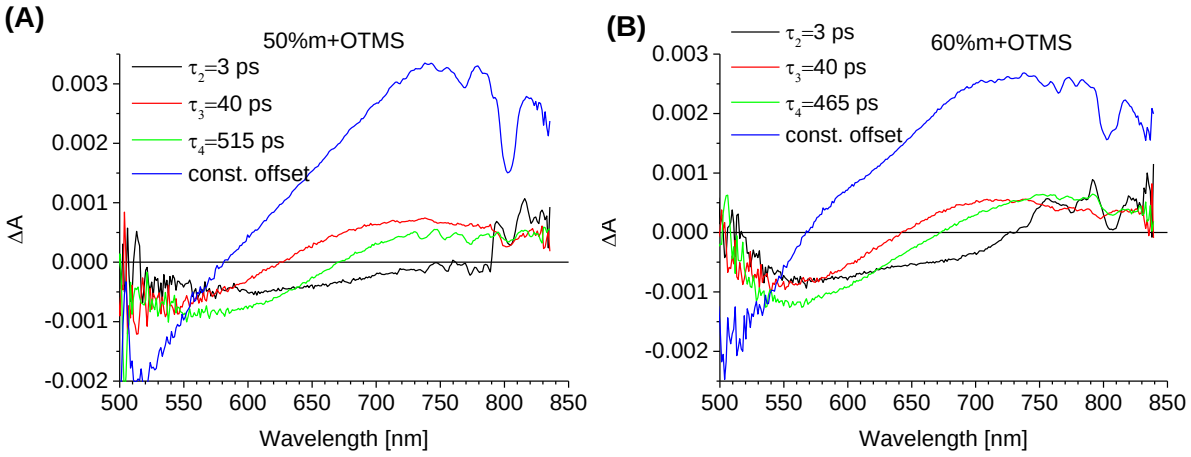

Figure 5. Wavelength dependent amplitudes of the indicated time constants obtained from global analysis of transient absorption spectra of full cells sensitized with ADEKA-1 dye and addition of OTMS: (A) 50%M, (B) 60%M. These figures can be compared to those of the corresponding samples without OTMS presented in Figures 3C and D.

The improvement in the charge separation efficiency comes at the expense of the absorbance of the sample. The absorbance and number of absorbed photons was compared for the photoanodes sensitized with the dye solutions with and without addition of the OTMS. Resulting spectra can be seen in Supporting information (Fig. S4). Both the maximum absorbance of the electrode and number of absorbed photons is reduced upon addition of OTMS in both cases, as expected. Moreover, it also blue-shifts the absorbance maximum from 512 nm to 487 nm in the cell sensitized with 50%m dye and from 509 nm to 499 nm in the cell sensitized with 60%m one.

Looking at the performance of the cells (Table 1) one can see that the current loss from the use of OTMS is bigger than it should be expected from the loss of absorbed photons. Voltage on the other hand is slightly increased, despite photocurrent drop. The underlying reasons were investigated by the electrochemical impedance spectroscopy. As can be seen in Figure 6A, while the charge transfer resistance is the same in both cases, the transport resistance is slightly increased upon addition of OTMS, which indicates possible lower charge collection efficiency (calculated as a ratio of charge transfer resistance over the sum of transport and charge transfer resistance) being explanation for lower current. Chemical capacitance shifts by about 20mV to the higher potential (Figure 6B). Being the representation of the number of occupied trap states in titania it is a good estimation of relative conduction band movement. It shows that OTMS may act similarly to TBP, moving the conduction band towards more negative potentials by 20 mV and consequently improving

Voc by that amount. Combining the Voc change from the CB shift (+20 mV) with the expected loss from the lower photocurrent (-12 mV) one obtains +8 mV shift, which well agrees with experimentally observed shift of +5 mV. No notable changes in the ideality factor of the device or trap state density were observed.

Table 1. Comparison of the photovoltaic parameters of ADEKA-1 cells with and without addition of OTMS to the dye solution (and also without TBP in the electrolyte) - short circuit current density (Jsc), open circuit voltage (Voc), fill factor (FF) and sunlight conversion efficiency (Eff).

Name	Jsc [mA/cm2]	Voc [mV]	FF	Eff. [%]
without OTMS with TBP	6.57	757	0.768	3.85
with OTMS with TBP	5	762	0.772	2.97
with OTMS without TBP	8.5	628	0.695	3.71

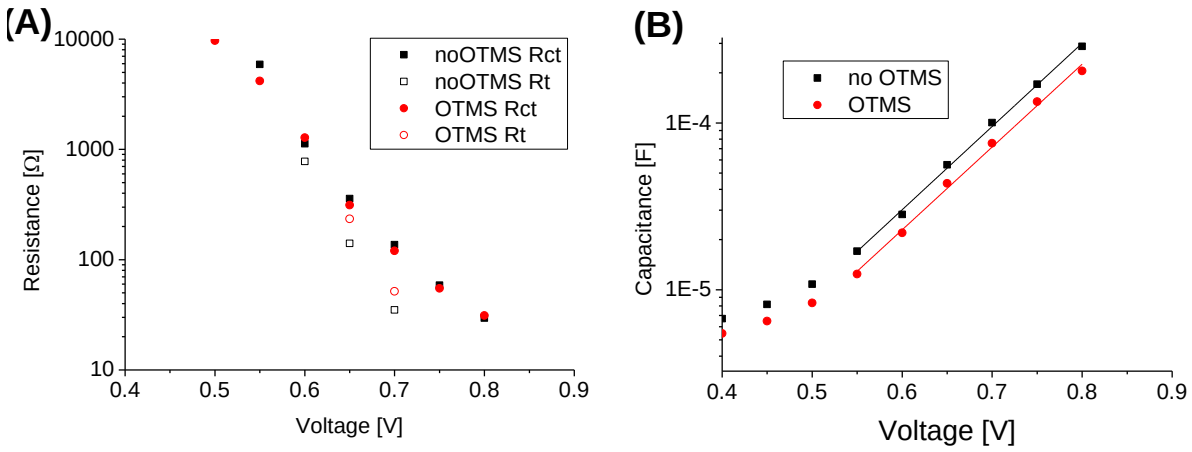

Figure 6. Charge transfer resistance, transport resistance (A) and chemical capacitance (B) of ADEKA-1 cells with and without addition of OTMS.

3.5 Effect of ALD and capping

Electrochemical impedance spectroscopy was also used to determine the impact of the capping process (single and multi-capping was analyzed) and alumina shell created by ALD process on the efficiency of the charge transport, occurring on the timescale from ms to s. Two series of data were obtained, one showing the effect of alumina layer and another for the capping treatment. Photovoltaic parameters of these cells are gathered in Table 2. Slight discrepancies in the parameters of the reference samples in both series come from the difference in the TiO_2 paste used (30NR-D for cells with capping treatment and 18NR-T for

cells with ALD treatment). Nevertheless, all the samples in the single data set were prepared using the same materials and conditions. In the Figure 7 one can see the data gathered for the cells created with the photoanodes subjected to the ALD treatment with varying thickness of the alumina shell. First big impact of the alumina shell is the decreasing photocurrent with the increase in thickness of the shell. It is attributed to lower injection efficiency caused by the unfavorable energy levels in Al_2O_3. Another noticeable effect of the ALD treatment is the rise in the charge transfer resistance with the increasing thickness of the shell (Rct), while the transport resistance (Rt) remains mostly intact (a). It is expected fact, since the position of the energy levels of alumina prevents the back-transfer of electrons to electrolyte. At the same time, preparation by ALD ensures that titania layer is mostly intact (so is charge transport through the nanoparticle network), thus transport resistance is unchanged. The capacitance of the mesoporous layer stays unchanged as well (b). Increase in the charge transfer resistance combined with the constant capacitance leads to much longer electron lifetimes in the cells with alumina shell (c). With the increasing thickness of the blocking layer up to 1.5 order of magnitude lifetime extension can be achieved, resulting in over 60 mV improvement in Voc. However, looking at the charge collection efficiency diagram (d) even 0.2 nm thickness is enough to obtain over 90% charge collection efficiency at the voltage corresponding to maximum power point and thicker layers can push efficiency up to 98% (at the great expense of current, though).

Capping treatment yields, in many ways, similar results, even though the blocking mechanism is slightly different. The obtained data are combined in Figure 8. Again, creation of the blocking layer at the surface of the nanoparticles, that prevents recombination, results in large increase of charge transfer resistance (a). This time, however, instead of prohibiting the electrons' access to the titania surface, the molecules of electrolyte suffered from the blocked pathway of getting close to the oxide's surface (due to the existence of the capping layer). Looking at the chemical capacitance, it seems that the capping treatment affects the surface of titania in the opposite way than TBP or OTMS and shifts the CB edge by approximately 30 mV in case of single capping and 55 mV in case of multi capping away from the excited level of the dye. While lifetime is increased by almost one order of magnitude with the use of single capping (c), the increased transport resistance counters that positive effect and makes the charge collection efficiency remains similar to the one in uncapped case (d). Multi capping, on the other hand, not only increases the carrier lifetime by

almost 2 orders of magnitude, but also yields over 95% charge collection efficiency. Moreover, the voltage and current density of the cell is significantly improved as well.

Additional parameters, namely diode ideality factor, dark current density, trap distribution and volumetric density of trap states below conduction band, were extracted as well, giving more insight into the effect of surface treatment. These results are gathered in Table 3. It is evident that both kinds of treatment lead to the improvement of ideality factor m and reduction of dark current, thus improving Voc of the device (at the same current). The trap distribution parameter α is lowered by the treatment in both cases. When it comes to alumina shell it may be attributed to the shell having higher conduction band edge. With the trap states maintaining their position and averaged CB moved closer to the dye's excited state, the distribution of traps with regard to the band edge is stretched, which is described by lower α parameter. Similar effect is observed in the case of cells subjected to the capping treatment, the exact mechanism however is unknown. Number of states below CB remains unchanged, which is expected due to no impact of those processes on the titania underneath.

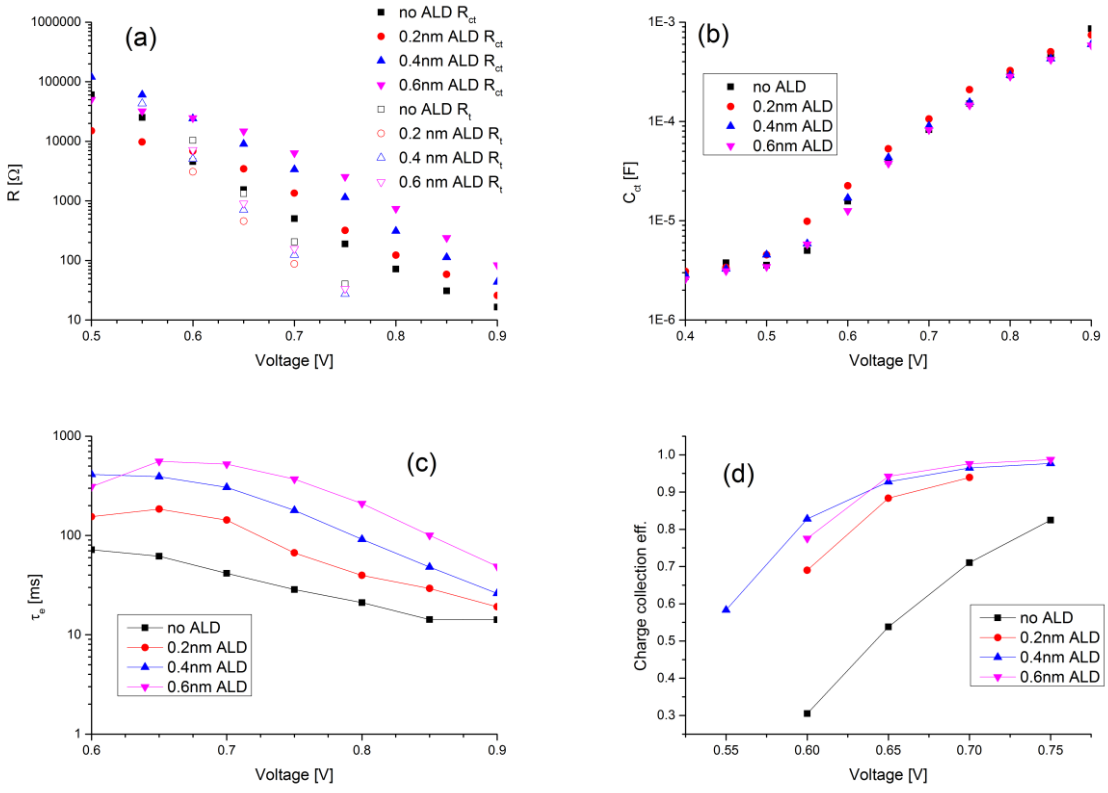

Figure 7. Parameters obtained from the EIS measurement for cells subjected to ALD treatment - charge transfer and transport resistance (a), charge transfer capacitance (b), electron lifetime (c) and charge collection efficiency (d).

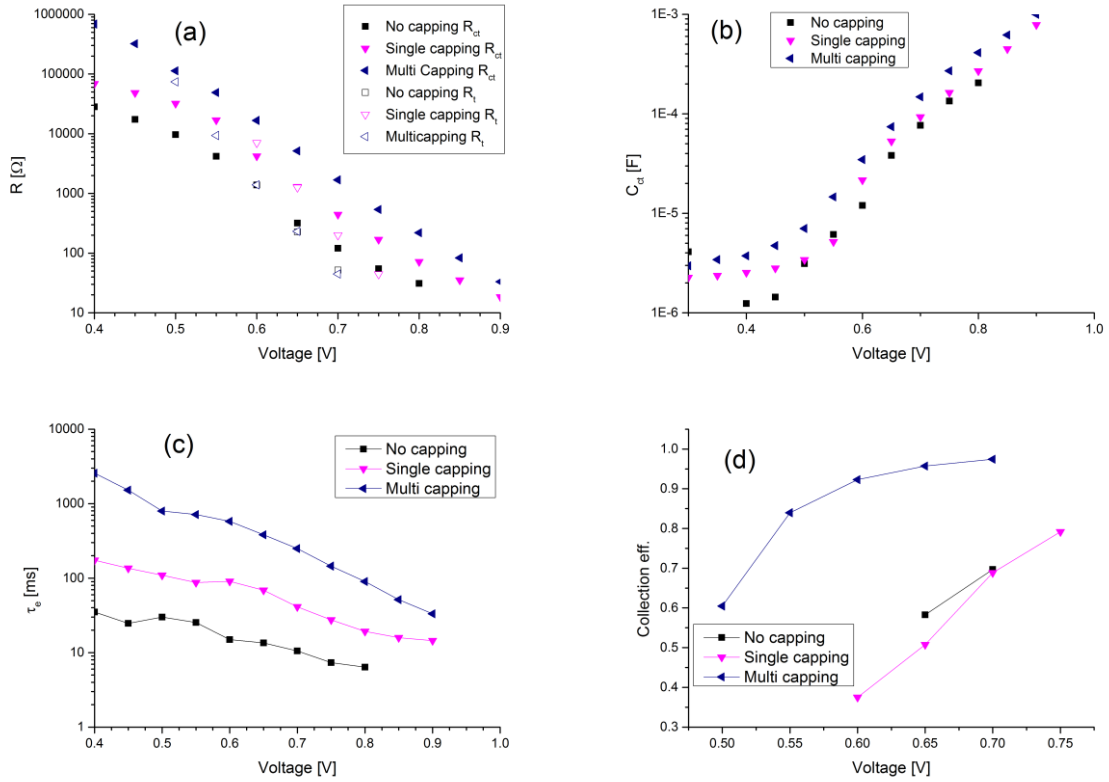

Figure 8: Parameters obtained from the EIS measurement for cells subjected to capping treatment - charge transfer and transport resistance (a), charge transfer capacitance (b), electron lifetime (c) and charge collection efficiency (d).

Table 2. Main photovoltaic parameters of the characterized cells - short circuit current density (Jsc), open circuit voltage (Voc), fill factor (FF) and sunlight conversion efficiency (Eff).

	Jsc [mA/cm2]	Voc [mV]	FF	Eff. [%]
No ALD	3.67	768	0.76	2.18
ALD 0.2 nm	3.2	815	0.781	2.05
ALD 0.4 nm	2	835	0.788	1.35
ALD 0.6 nm	1.84	837	0.776	1.2
No capping	5	762	0.77	2.97
Single capping	4.87	804	0.781	3.06
Multi capping	6.6	867	0.755	4.31

Table 3. Calculated ideality factor (m), dark current density (j0), trap distribution parameter (α) and volumetric density of trap states below conduction band (NL) for obtained cells.

	m	j0[mA/cm2]	α	NL[1/cm3]
No ALD	2.18	1.42E-06	0.30	2.56E+20
ALD 0.2 nm	2.01	1.98E-07	0.26	2.54E+20
ALD 0.4 nm	1.83	1.73E-08	0.26	2.51E+20
ALD 0.6 nm	1.89	1.52E-08	0.27	2.51E+20
No capping	1.99	1.21E-06	0.36	2.66E+20
Single capping	1.96	1.93E-07	0.28	2.54E+20
Multi capping	1.91	5.99E-08	0.27	2.58E+20

The type of the treatment affect the stationary absorption of the cells (Fig. S5). ALD treatment has lesser effect on the total absorption. Initially it even increases by little bit, yet with increase of thickness the volume of additional material leads to decrease in surface area and consequence worse dye deposition. The capping treatment consisting of additional dipping in solution several times after dye deposition leads to dye dissolving (however to much lesser extent with ADEKA-1 than MK2, where capping treatment led to higher loss in current and no voltage difference) lowering the absorption of the photoanode and consequently number of absorbed photons. There is little to no additional shift of absorption maxima vs the cells just with addition of OTMS, they stay around 490 nm.

Impact of the various kinds of surface treatment on the ultrafast behavior of the cells was checked using transient absorption spectroscopy. The effect of ALD is discussed in the next section. Multi capping sometimes increases the residual signal at 750 nm, and sometimes slightly decreases it compared to cells with just OTMS present (Table S1). The positive action for the early time behavior is observed in “bad” performing cells, while the opposite is found for “good” cells (sensitized with fresh solutions of high monomer-content and with OMTS) As described earlier, OTMS is probably acting as a mean to straighten up the dye molecules perpendicularly to the surface and capping may act in similar way, just not as efficiently. In the cells with sub-optimal dye orientation, it helps to make dye molecules more perpendicular to the surface, thus reducing recombination and improving the final signal. In the cells with optimal orientation, capping treatment may cause slight unbalance in the system, marginally lowering the final signal.

3.6 Importance of ALD parameters

One crucial thing that we discovered was the importance of the settings of ALD utilized in photoanode preparation. Impact of these parameters has recently been investigated for planar structures [45]. However, one must remember that it takes much longer time for the precursor to penetrate and react with entire mesoporous photoanode, than it would take with the planar substrate, so no direct transition of reaction parameters can be applied. Depending on whether the deposition time was long enough or not, two opposite impacts on cells' performance are observed. All the cells presented in previous chapters were prepared using the deposition time long enough to form uniform monolayer in each cycle. Nevertheless, in order to investigate the effect of partial ALD coating cells were prepared with the same number of ALD cycles (with expected thickness of the shell equal to 1 nm) but differing deposition and purge times. One method labeled "short" with 0.1 s deposition time and 3 s purge time and another labeled "long" with 2 s deposition time and 8 s purge time was used. Results of the cells treated in both ways, together with reference, are presented in Table 4.

Table 4. Photovoltaic performance of cells prepared with "short" and "long" ALD methods - short circuit current density (Jsc), open circuit voltage (Voc), fill factor (FF) and sunlight conversion efficiency (Eff).

Name	Jsc [mA/cm2]	Voc [mV]	FF	Eff. [%]
50%m+ OMTS	6.3	717	0.48	2.52
50%m+OMTS+1nm_shortALD	8.6	728	0.48	3.01
50%m+OMTS+1nm_longALD	0.2	917	0.80	0.12

As can be seen, the "short" short ALD rises the obtained photocurrent with no difference in the fill factor and the voltage increase of the magnitude that can be attributed solely to current increase. Longer, "long" deposition on the other hand cuts the photocurrent almost entirely, hugely increasing voltage and fill factor instead. The first behavior can be explained if we assume that under insufficient time to form a continuous uniform monolayer during the first deposition cycle, next layers prefer to grow on the already created alumina islands instead of holes with titania. This way an alumina shell with pinholes is being created. We believe that the electrons are injected through those pinholes, so there is no big difference in the efficiency of this process. The alumina islands between dye molecules act similarly to the capping molecules, blocking the transport recombination and increasing charge collection

efficiency. As a result, higher photocurrent is observed. The reported improvement of the cell properties upon depositing oxide shells from solution could probably be explained by the same mechanism [16]. Letting the deposition proceed with the time needed to form a full layer ("long" ALD route) creates an uniform barrier that seems to block injection and recombination alike. The electrons are probably injected not into titania but into very deep trap states in alumina, rest may form surface states that recombine through space with dye molecule. As a result, the photocurrent is very low, but the voltage is enhanced. For such low photocurrent and dark current also suppressed the fill factor is increased significantly. No significant difference between the two deposition routes was observed by stationary absorption measurements.

Effect of both deposition routes on the ultrafast processes in the fully assembled cells was checked by the global analysis of the femtosecond transient absorption measurements (Figure 9). "Short" ALD method, similarly to the capping treatment, has no significant effect on the ultrafast processes. It shortens the characteristic time of special recombination but keeps its amplitude low, well below the residual signal. "Long" ALD on the other hand has a very profound recombination (sub-ns component) signal and low residual (constant offset) signal, which confirms the proposed blockade of injection and spatial recombination of the charges from created surface states. These observations are further supported by residual signal in the kinetics from Figure 2A. It can be observed there that the "long" ALD treatment result in a huge drop in final kinetic amplitude.

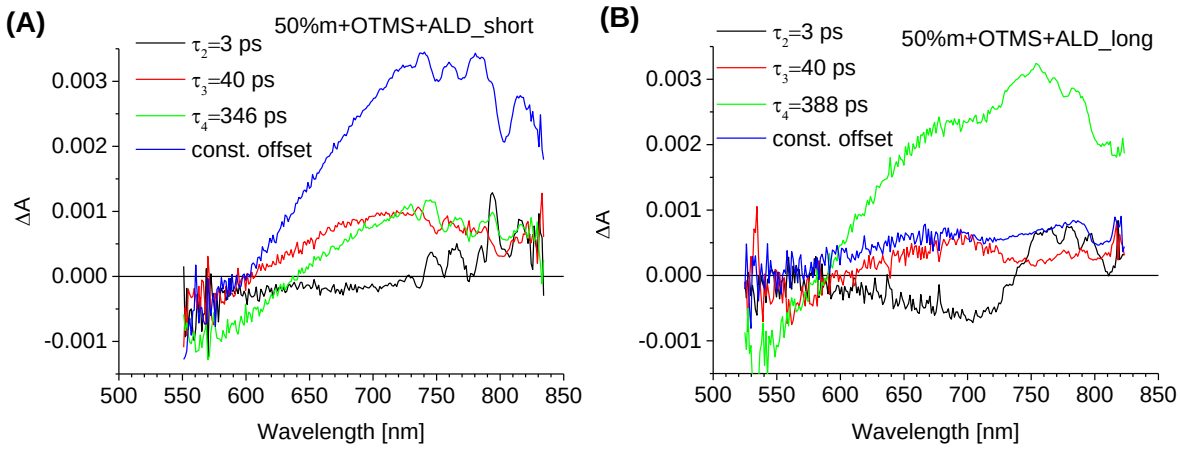

Figure 9. Wavelength dependent amplitudes of the indicated time constants obtained from global analysis of transient absorption spectra of the cells prepared with "short" ALD treatment (A) and "long" ALD treatment (B), both for 1 nm layers. They should be compared to Figure 5A.

4. Conclusions

The dynamics of charge transfer in complete solar cells sensitized with very efficient silyl-anchor ADEKA-1 dye, and with different preparation parameters, was studied on the time scale from 200 fs to several seconds.

The most important conclusions arise from the transient absorption spectroscopy results in the fs-ps regime. In this work we have shown that there is a time component in the global analysis of these spectra, associated with the ultrafast spatial recombination between dye molecule and oxide surface with characteristic time of hundreds of picoseconds (sub-ns), that can be directly connected with the photon to current conversion efficiency. With its increase in amplitude, the number of successfully injected electrons falls down, directly affecting the performance of the whole device. We have proved that in the case of ADEKA-1 dye increase in the degree of polymerization leads to increase of this unwanted recombination, so for the best devices pure monomer is desirable. We have also devised a new, optimized synthesis process for ADEKA-1 dye providing pure monomer compound with high yield. Addition of the co-adsorbent (OTMS) was found to decrease the unwanted sub-ns component as well, probably by reorientation of the tilt of dye molecules on the surface of the oxide. Creation of the uniform alumina shell led to the hampered electron injection, with the sub-ns component's amplitude significantly increased.

Secondly, flash photolysis measurements have shown that there is also a connection between performance of the device and relative amplitude of the shortest component of (assigned to sub-μs electron recombination) and longest (assigned to electron population left), with the dominance of the latter being indication of well performing device. It has also been confirmed that Co- phenenatroline redox shuttle yields higher voltages than Co- bypyridine one, but at the expense of the photocurrent drop, being result of slightly slower (3.5 μs vs. 2.5 μs) dye regeneration.

Next, electrochemical impedance spectroscopy has provided information about slightly increased transport resistance and minute conduction band shift occurring after addition of OTMS. We have also investigated impact of the surface treatments on charge collection efficiency by this method. Both molecular capping and creation of insulating Al_2O_3 layers was found to increase the lifetime of electrons significantly and rise charge collection efficiency over 90%. Moreover, the capping treatment causes slight (up to 55 mV) shift in conduction band in the opposite direction compared to OTMS and results in increases in the

voltage and photocurrent. ALD on the other hand causes voltage and fill factor increases, but at the expense of the photocurrent drop.

Finally, we have underlined the importance of the parameters used during the atomic layer deposition of alumina shell, which may lead to disparate results, affecting the properties of the device in an unexpected way.

We believe that these results will enable the better understanding of alkoxysilyl dyes and lead to development of better DSSCs in general.

Acknowledgements

This work was supported by NCN (National Science Centre, Poland) under project 2012/05/B/ST3/03284. J. S. is a holder of a scholarship funded within Human Capital Operational Programme, European Social Fund. Katarzyna Pydzińska is kindly acknowledged for the help with the preparation and characterization of one series of ADEKA-1 cells.

References

[1] Hagfeldt, A.; Boschloo, G.; Sun, L.; Kloo, L.; Pettersson, H., Dye-Sensitized Solar Cells. Chem. Rev. **2010,** 110, 6595-6663.
[2] Grätzel, M., Photoelectrochemical Cells. Nature **2001,** 414, 338-344.
[3] Grätzel, M.; Durrant, J. R., Dye-Sensitised Mesoscopic Solar Cells. In Nanostructured and Photoelectrochemical Systems for Solar Photon Conversion, Archer, M. D.; Nozik, A. J., Eds. Imperial College Press: 2008; pp 503-536.
[4] Kalyanasundaram, K., Dye-Sensitized Solar Cells. EPFL press: 2010.
[5] www.nrel.gov/ncpv, National Center for Photovoltaics. National Renewable Energy Laboratory (NREL)
[6] Sobuś, J.; Ziółek, M., Optimization of Absorption Bands of Dye-Sensitized and Perovskite Tandem Solar Cells Based on Loss-in-Potential Values. Phys. Chem. Chem. Phys. **2014,** 16, 14116-14126.
[7] O'Regan, B.; Grätzel, M., A Low-Cost, High-Efficiency Solar Cell Based on Dye-Sensitized Colloidal Tio2 Films. Nature **1991,** 353, 737-740.
[8] Nazeeruddin, M. K.; De Angelis, F.; Fantacci, S.; Selloni, A.; Viscardi, G.; Liska, P.; Ito, S.; Takeru, B.; Grätzel, M., Combined Experimental and Dft-Tddft Computational Study of Photoelectrochemical Cell Ruthenium Sensitizers. J. Am. Chem. Soc. **2005,** 127, 16835-16847.
[9] Yu, Q.; Wang, Y.; Yi, Z.; Zu, N.; Zhang, J.; Zhang, M.; Wang, P., High-Efficiency Dye-Sensitized Solar Cells: The Influence of Lithium Ions on Exciton Dissociation, Charge Recombination, and Surface States. ACS Nano **2010,** 4, 6032-6038.
[10] Feldt, S. M.; Wang, G.; Boschloo, G.; Hagfeldt, A., Effects of Driving Forces for Recombination and Regeneration on the Photovoltaic Performance of Dye-Sensitized Solar Cells Using Cobalt Polypyridine Redox Couples. J. Phys. Chem. C **2011,** 115, 21500-21507.

[11] Zhou, D.; Yu, Q.; Cai, N.; Bai, Y.; Wang, Y.; Wang, P., Efficient Organic Dye-Sensitized Thin-Film Solar Cells Based on the Tris(1,10-Phenanthroline)Cobalt(Ii/Iii) Redox Shuttle. Energy Environ. Sci. **2011,** 4, 2030-2034.
[12] Pazoki, M.; Lohse, P. W.; Taghavinia, N.; Hagfeldt, A.; Boschloo, G., The Effect of Dye Coverage on the Performance of Dye-Sensitized Solar Cells with a Cobalt-Based Electrolyte. Phys. Chem. Chem. Phys. **2014,** 16, 8503-8508.
[13] Yella, A.; Lee, H.-W.; Tsao, H. N.; Yi, C.; Chandiran, A. K.; Nazeeruddin, M. K.; Diau, E. W.-G.; Yeh, C.-Y.; Zakeeruddin, S. M.; Grätzel, M., Porphyrin-Sensitized Solar Cells with Cobalt (Ii/Iii)–Based Redox Electrolyte Exceed 12 Percent Efficiency. Science **2011,** 334, 629-634.
[14] Mathew, S.; Yella, A.; Gao, P.; Humphry-Baker, R.; Curchod, B. F. E.; Ashari-Astani, N.; Tavernelli, I.; Rothlisberger, U.; Nazeeruddin, M. K.; Grätzel, M., Dye-Sensitized Solar Cells with 13% Efficiency Achieved through the Molecular Engineering of Porphyrin Sensitizers. Nat. Chem. **2014,** 6, 242-247.
[15] Kakiage, K.; Tokutome, T.; Iwamoto, S.; Kyomen, T.; Hanaya, M., Fabrication of a Dye-Sensitized Solar Cell Containing a Mg-Doped Tio2 Electrode and a Br3/Br Redox Mediator with a High Open-Circuit Photovoltage of 1.21 V. Chem. Comm. **2013,** 49, 179.
[16] Kakiage, K.; Aoyama, Y.; Yano, T.; Otsuka, T.; Kyomen, T.; Unno, M.; Hanaya, M., An Achievement of over 12 Percent Efficiency in an Organic Dye-Sensitized Solar Cell. Chem. Comm. **2014,** 50, 6379-6381.
[17] Matta, S. K.; Kakiage, K.; Makuta, S.; Veamatahau, A.; Aoyama, Y.; Yano, T.; Hanaya, M.; Tachibana, Y., Dye-Anchoring Functional Groups on the Performance of Dye-Sensitized Solar Cells: Comparison between Alkoxysilyl and Carboxyl Groups. J. Phys. Chem. C **2014,** 118, 28425-28434.
[18] Kakiage, K.; Aoyama, Y.; Yano, T.; Oya, K.; Kyomen, T.; Hanaya, M., Fabrication of a High-Performance Dye-Sensitized Solar Cell with 12.8% Conversion Efficiency Using Organic Silyl-Anchor Dyes. Chem. Comm. **2015,** 51, 6315-6317.
[19] Kakiage, K.; Aoyama, Y.; Yano, T.; Oya, K.; Fujisawa, J.-i.; Hanaya, M., Highly-Efficient Dye-Sensitized Solar Cells with Collaborative Sensitization by Silyl-Anchor and Carboxy-Anchor Dyes. Chem. Comm. **2015,** 51, 15894-15897.
[20] Koumura, N.; Wang, Z.-S.; Mori, S.; Miyashita, M.; Suzuki, E.; Hara, K., Alkyl-Functionalized Organic Dyes for Efficient Molecular Photovoltaics. J. Am. Chem. Soc. **2006,** 128, 14256-14257.
[21] Murakami, T. N.; Koumura, N.; Uchiyama, T.; Uemura, Y.; Obuchi, K.; Masaki, N.; Kimurac, M.; Mori, S., Recombination Inhibitive Structure of Organic Dyes for Cobalt Complex Redox Electrolytes in Dye-Sensitised Solar Cells. J. Mater. Chem. A **2013,** 1, 792-798.
[22] Kashif, M. K.; Axelson, J.; Duffy, N. W.; Forsyth, C. M.; Chang, C. J.; Long, J. R.; Spiccia, L.; Bach, U., A New Direction in Dye-Sensitized Solar Cells Redox Mediator Development: In Situ Fine-Tuning of the Cobalt(Ii)/(Iii) Redox Potential through Lewis Base Interactions. J. Am. Chem. Soc. **2012,** 134, 16646-16653.
[23] Hara, K.; Wang, Z.-S.; Cui, Y.; Furube, A.; Koumura, N., Long-Term Stability of Organic–Dye-Sensitized Solar Cells Based on an Alkyl-Functionalized Carbazole Dye. Energy Environ. Sci. **2009,** 2, 1109-1114.
[24] Fabregat-Santiago, F.; Garcia-Belmonte, G.; Mora-Seró, I.; Bisquert, J., Characterization of Nanostructured Hybrid and Organic Solar Cells by Impedance Spectroscopy. Phys. Chem. Chem. Phys. **2011,** 13, 9083-9118.

[25] Idigoras, J.; Burdziński, G.; Karolczak, J.; Kubicki, J.; Oskam, G.; Anta, J. A.; Ziółek, M., The Impact of the Electrical Nature of the Metal-Oxide on the Performance in Dye-Sensitized Solar Cells: New Look at Old Paradigms. J. Phys. Chem. C **2015,** 119, 3931-3944.
[26] Burdziński, G.; Karolczak, J.; Ziółek, M., Dynamics of Local Stark Effect Observed for a Complete D149 Dye-Sensitized Solar Cell. Phys. Chem. Chem. Phys. **2013,** 15, 3889-3896.
[27] Katilius, E.; Hindorff, J.; Woodbury;, N. Asufit Program Available at www.public.asu.adu/~Laserweb/Asufit/Asufit.html.
[28] Brochier Salon, M.-C.; Naceur Belgacem, M., Hydrolysis-Condensation Kinetics of Different Silane Coupling Agents. Phosphorus, Sulfur, and Silicon **2011,** 186, 240-254.
[29] McNeil, K. J.; DiCaprio, J. A.; Walsh, D. A.; Pratt, R. F., Kinetics and Mechanism of Hydrolysis of a Silicate Triester, Tris(2-Methoxyethoxy)Phenylsilane. J. Am. Chem. Soc. **1980,** 102, 1859-1865.
[30] Van Der Voorta, P.; Vansanta, E. F., Silylation of the Silica Surface a Review. J. Liq. Chromatogr. Relat. Technol. **1996,** 19, 2723-2752.
[31] Goodwin, J. W.; Harbron, R. S.; Reynolds, P. A., Functionalization of Colloidal Silica and Silica Surfaces Via Silylation Reactions. Colloid Poly. Sci. **1990,** 268, 766-777.
[32] Deschner, T.; Liang, Y.; Anwander, R., Silylation Efficiency of Chorosilanes, Alkoxysilanes, and Monosilazanes on Periodic Mesoporous Silica. J. Phys. Chem. C **2010,** 114, 22603-22609.
[33] Sobuś, J.; Kubicki, J.; Burdziński, G.; Ziółek, M., Carbazole Dye-Sensitized Solar Cells Studied from Femtoseconds to Seconds—Effect of Additives in Cobalt- and Iodide-Based Electrolytes. ChemSusChem **2015,** 8, 3118-3128.
[34] Lorenc, M.; Ziółek, M.; Naskręcki, R.; Karolczak, J.; Kubicki, J.; Maciejewski, A., Artifacts in Femtosecond Transient Absorption Spectroscopy. Appl. Phys. B-Lasers Opt. **2002,** 74, 19.
[35] Zhang, X.-H.; Ogawa, J.; Sunahara, K.; Cui, Y.; Uemura, Y.; Miyasaka, T.; Furube, A.; Koumura, N.; Hara, K.; Mori, S., Alternation of Charge Injection and Recombination in Dye-Sensitized Solar Cells by the Addition of Nonconjugated Bridge to Organic Dyes. J. Phys. Chem. C **2013,** 117, 2024-2031.
[36] Wiberg, J.; Marinado, T.; Hagberg, D. P.; Sun, L.; Hagfeldt, A.; Albinsson, B., Distance and Driving Force Dependencies of Electron Injection and Recombination Dynamics in Organic Dye-Sensitized Solar Cells. J. Phys. Chem. B **2010,** 114, 14358-14363.
[37] Piatkowski, P.; Martin, C.; di Nunzio, M. R.; Cohen, B.; Pandey, S.; Hayse, S.; Douhal, A., Complete Photodynamics of the Efficient Yd2-O-C8-Based Solar Cell. The Journal of Physical Chemistry C **2014,** 118, 29674-29687.
[38] Huang, W.-K.; Cheng, C.-W.; Chang, S.-M.; Lee, Y.-P.; Diau, E. W.-G., Synthesis and Electron-Transfer Properties of Benzimidazole-Functionalized Ruthenium Complexes for Highly Efficient Dye-Sensitized Solar Cells. Chem. Comm. **2010,** 46, 8992-8994.
[39] Imahori, H.; Kang, S.; Hayashi, H.; Haruta, M.; Kurata, H.; Isoda, S.; Canton, S. E.; Infahsaeng, Y.; Kathiravan, A.; Pascher, T.; Chábera, P.; Yartsev, A. P.; Sundström, V., Photoinduced Charge Carrier Dynamics of Zn-Porphyrin-Tio2 Electrodes: The Key Role of Charge Recombination for Solar Cell Performance. J. Phys. Chem. A **2011,** 15, 3679-3690.
[40] Ye, S.; Kathiravan, A.; Hayashi, H.; Tong, Y.; Infahsaeng, Y.; Chabera, P.; Pascher, T.; Yartsev, A. P.; Isoda, S.; Imahori, H.; Sundström, V., Role of Adsorption Structures of Zn-Porphyrin on Tio2 in Dye-Sensitized Solar Cells Studied by Sum Frequency

Generation Vibrational Spectroscopy and Ultrafast Spectroscopy. J. Phys. Chem. C **2013,** 117, 6066-6080.
[41] Ardo, S.; Sun, Y.; Staniszewski, A.; Castellano, F. N.; Meyer, G. J., Stark Effects after Excited-State Interfacial Electron Transfer at Sensitized Tio2 Nanocrystallites. J. Am. Chem. Soc. **2010,** 132, 6696-6709.
[42] Cappel, U. B.; Feldt, S. M.; Schöneboom, J.; Hagfeldt, A.; Boschloo, G., The Influence of Local Electric Fields on Photoinduced Absorption in Dye-Sensitized Solar Cells. J. Am. Chem. Soc. **2010,** 132, 9096-9101.
[43] Sobuś, J.; Karolczak, J.; Komar, D.; Anta, J. A.; Ziółek, M., Transient States and the Role of Excited State Self-Quenching of Indoline Dyes in Complete Dye-Sensitized Solar Cells. Dyes Pigments **2015,** 113, 692-701.
[44] Martín, C.; Ziółek, M.; Douhal, A., Ultrafast and Fast Charge Separation Processes in Real Dye-Sensitized Solar Cells. J. Photochem. Photobiol. C: Photochem. Rev. **2016,** 26, 1-30.
[45] Iatsunskyi, I.; Coy, E.; Viter, R.; Nowaczyk, G.; Jancelewicz, M.; Baleviciute, I.; Załęski, K.; Jurga, S., Study on Structural, Mechanical, and Optical Properties of Al2o3–Tio2 Nanolaminates Prepared by Atomic Layer Deposition. J. Phys. Chem. C **2015,** 119, 20591-20599.

Supporting information

for

Factors affecting the performance of champion silyl-anchor carbazole dye revealed in the femtosecond to second studies of complete ADEKA-1 sensitized solar cells.

NMR Spectra

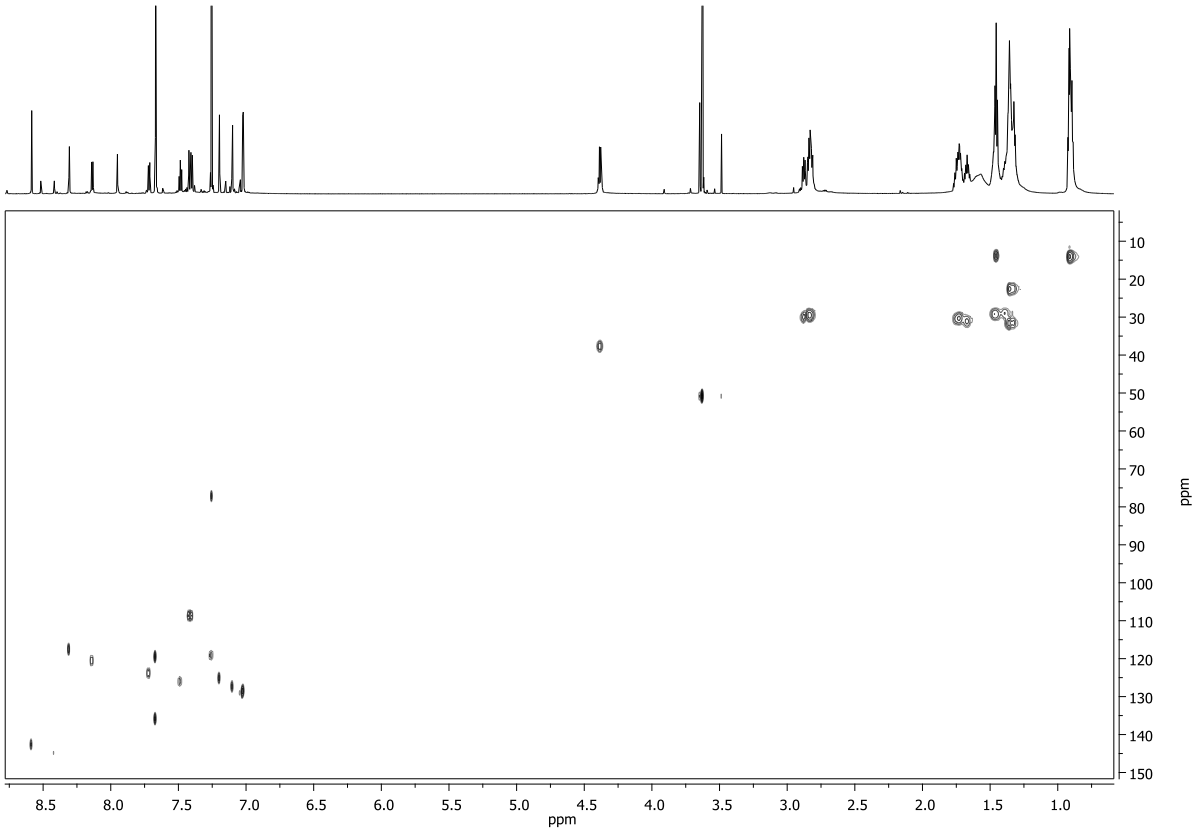

Figure S1. ^{1}H-^{13}C HSQC spectrum of ADEKA-1 in $CDCl_3$

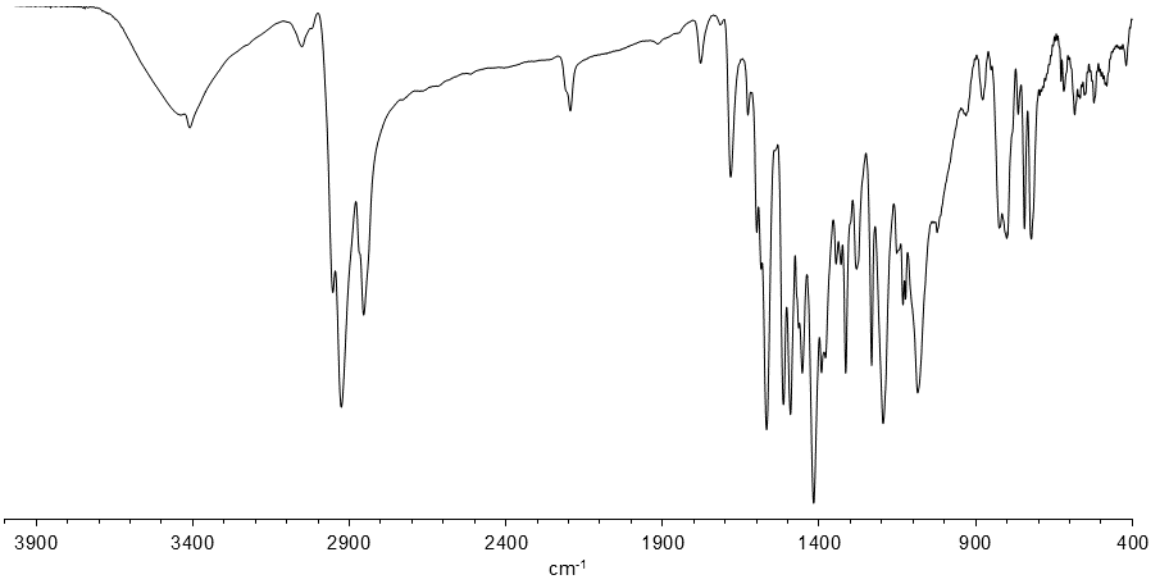

Figure S2. IR spectrum of ADEKA-1 (KBr disc, 1 mg of ADEKA-1 in 200 mg of KBr)

Stationary spectra

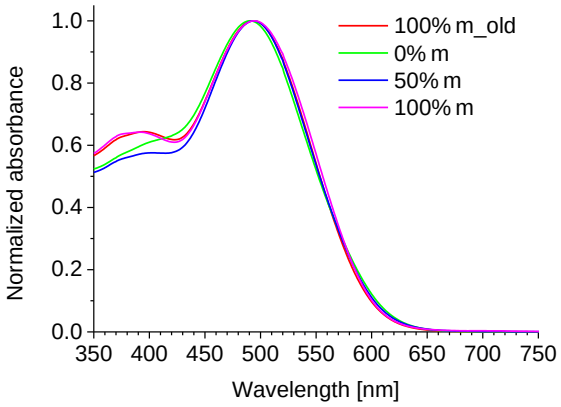

Figure S3. Normalized stationary absorption spectra of ADEKA-1 dye in toluene with different degree of polymerization.

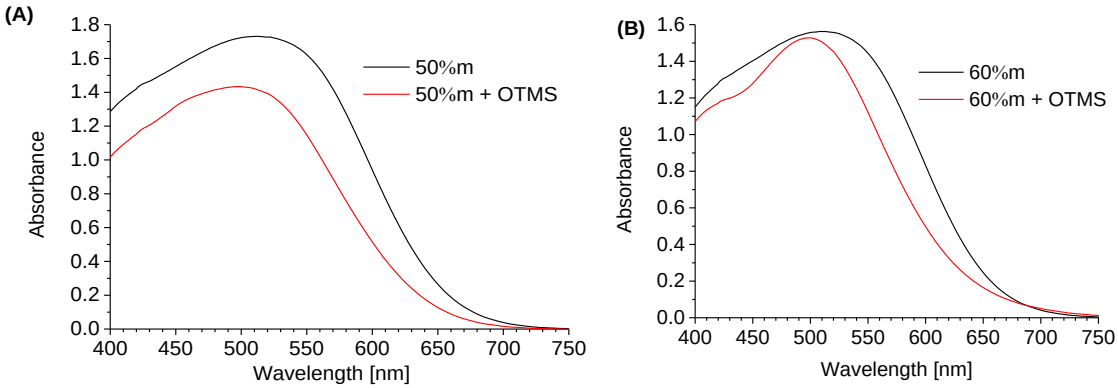

Figure S4. Stationary spectra and number of absorbed photons of the films sensitized with the ADEKA-1 dye: 50%m (A) and 60%m (B both) with and without addition of OTMS.

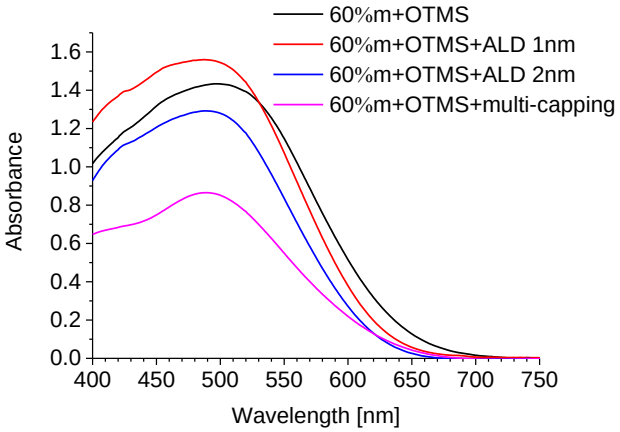

Figure S5. Stationary absorption spectra of photoanodes sensitized with ADEKA dye + OTMS with different additional surface treatment.

Cell parameters

Table S1.

Photovoltaic parameters of representative cells constituting Fig. 4B - photocurrent density (J_{SC}), open circuit voltage (V_{OC}), fill factor (FF) , efficiency (Eff), corrected photoconversion efficiency (Total APCE), number of absorbed photons (Nph), absorbance of the cells close to the maximum (at 500 nm, A_{max}) and the amplitude of the normalized residual signal of kinetic at 750 nm (S_{res}, after 3 ns).

Cell	V_{OC} [V]	FF	J_{SC} [$mAcm^{-2}$]	Eff [%]	Nph [$s^{-1}m^{-2}$]	Total APCE	S_{res}	A_{max}
MK2	0.72	0.45	11.24	3.64	8.70E+20	0.81	0.70	1.51
100%m_old+OTMS	0.70	0.46	3.60	1.16	5.40E+20	0.42	0.32	0.71
100%m_old+OTMS+ALDshort_1nm	0.62	0.37	2.16	0.50	5.00E+20	0.27	0.27	0.58
100%m_old+OTMS +multi capping	0.67	0.61	2.95	1.19	3.80E+20	0.48	0.40	0.48
100%m_old+OTMS +ALDlong_1nm	0.85	0.59	2.28	1.14	7.20E+20	0.20	0.19	1.22
0%m	0.61	0.52	1.17	0.37	8.50E+20	0.09	0.22	1.56
0%m+OTMS	0.61	0.66	1.27	0.51	6.80E+20	0.12	0.27	1.04
50%m	0.74	0.54	7.35	2.92	9.30E+20	0.49	0.46	1.70
50%m+OTMS	0.72	0.50	6.57	2.39	8.10E+20	0.51	0.69	1.43
50%m+OTMS+multi capping	0.70	0.59	4.22	1.75	6.00E+20	0.44	0.54	0.85
50%m+OTMS+ALDshort_1nm	0.73	0.48	8.59	3.02	7.80E+20	0.69	0.59	1.40
50%m+OTMS+ALDlong_1nm	0.92	0.80	0.16	0.12	7.60E+20	0.01	0.14	1.54
60%m	0.72	0.50	6.87	2.44	9.10E+20	0.47	0.48	1.56
60%m+OTMS	0.70	0.55	7.43	2.87	8.40E+20	0.55	0.64	1.50
60%m+OTMS+multi capping	0.69	0.66	4.83	2.20	6.40E+20	0.47	0.60	0.90
100%m	0.71	0.54	6.98	2.70	8.30E+20	0.53	0.67	1.32

Table S2.

Photovoltaic performance of the MK2 cells prepared to check differences between Co-bpy and Co-phen electrolyte - photocurrent density (Jsc), open circuit voltage (Voc), fill factor (FF) and efficiency. In this case a scattering layer was added during the electrode preparation.

	Co-bpy				Co-phen			
Cell no.	Jsc[mA/cm2]	Voc[mV]	FF	Eff. [%]	Jsc[mA/cm2]	Voc[mV]	FF	Eff.[%]
1	14.26	811	0.58	6.86	13.55	827	0.65	7.37
2	15.15	810	0.61	7.63	14.01	827	0.67	7.80
3	14.80	797	0.66	7.93	13.06	830	0.66	7.28
4	14.73	810	0.64	7.75	13.55	837	0.70	8.03
Averaged	**14.73**	**807**	**0.62**	**7.54**	**13.54**	**830**	**0.67**	**7.62**

Impedance

All the impedance measurements were carried out on the Bio-logic SP-300 potentiostat over the range from 0.1Hz to 7MHz in 80 measuring points distributed evenly on the logarithmic frequency scale. The voltage range used differed depending on sample Voc, yet typically it was spanning from 0V to 0.9V in 50mV increments. Obtained data was analyzed by the ZView software using different equivalent circuits for high, medium and low voltage regimes (Figure S6). At high voltages the TiO_2 is conductive (Rt=0), current flows entirely through it meaning RC element corresponding to FTO is negligible. There is also Warburg diffusion element present , which can be neglected at lower voltages. Upon lowering voltage transport resistance appears and therefore transport line element has to be used. At low voltages TiO_2 is insulating and all the charge transport goes through FTO-electrolyte interface and electrolyte-counter electrode interface. Diode ideality factor, dark current density, trap distribution and volumetric density of trap states below conduction band were calculated from the exponential fit of the Rct and Cct parameters as described elsewhere [S1]. Conduction band shift (originating from the capping layer or coadsorbent addition) was estimated based on voltage shift needed to overlap Cct curves of the cells being compared.

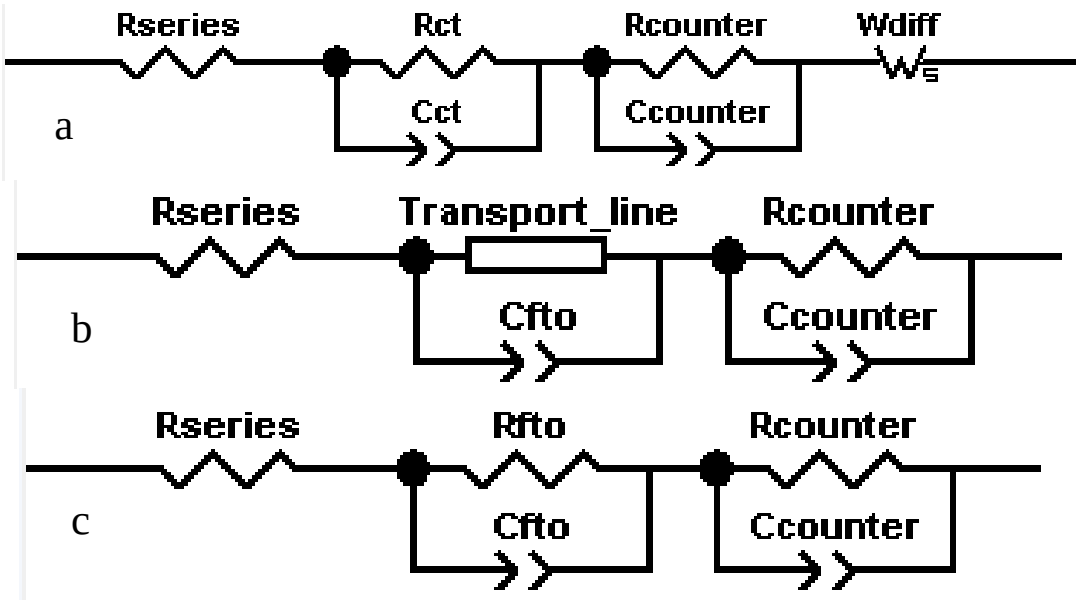

Figure S6. Equivalent circuits for high (a), medium (b) and low(c) voltage regimes.

[S1] Fabregat-Santiago, F.; Garcia-Belmonte, G.; Mora-Seró, I.; Bisquert, J., Characterization of Nanostructured Hybrid and Organic Solar Cells by Impedance Spectroscopy. Phys. Chem. Chem. Phys. **2011,** 13, 9083-9118.

Statements of the co-authors

Poznań, 13.01.2016

mgr inż. Jan Sobuś
Zakład Elektroniki Kwantowej
Wydział Fizyki UAM
jansob@amu.edu.pl

Oświadczenie

Jako autor rozprawy doktorskiej chciałbym określić mój wkład w proces przygotowania publikacji naukowych, które tworzą moją rozprawę.

Pierwszą grupą prac są prace eksperymentalne:

1. *Comparison of TiO_2 and ZnO Solar Cells Sensitized with an Indoline Dye: Time-Resolved Laser Spectroscopy Studies of Partial Charge Separation Processes,* **Jan Sobuś**, Gotard Burdziński, Jerzy Karolczak, Jesus Idígoras, Juan A. Anta and Marcin Ziółek, Langmuir, **30** (2014) 2505–2512
2. *Transient states and the role of excited state self-quenching of indoline dyes in complete dye-sensitized solar cells,* **Jan Sobuś**, Jerzy Karolczak, Dariusz Komar, Juan A. Anta and Marcin Ziółek, Dyes and Pigments, **113** (2015) 692-701
3. *Carbazole Dye- Sensitized Solar Cells Studied from Femtoseconds to Seconds —Effect of Additives in Cobalt and Iodide-Based Electrolytes,* **Jan Sobuś**, Jacek Kubicki, Gotard Burdziński and Marcin Ziółek, ChemSusChem, **8** (2015) 3118–3128
4. *Effect of different photoanode nanostructures on the initial charge separation and electron injection process in dye sensitized solar cells: a photophysical study with indoline dyes,* Jesús Idígoras, **Jan Sobuś**, Mariusz Jancelewicz, Eneko Azaceta, Ramon Tena-Zaera, Juan A. Anta and Marcin Ziółek, Materials Chemistry and Physics, **170** (2016) 218-228

Mój udział w tych publikacjach polegał na konstrukcji ogniw (za wyjątkiem pracy 4, gdzie przygotowałem tylko część z nich), pomiarach i analizie krzywych prądowo-napięciowych, pomiarach i analizie widm IPCE, pomiarach i analizie przy pomocy spektroskopii impedancyjnej oraz spektroskopii UV-VIS. Wykonałem również zdjęcia SEM do prac 1 i 3 oraz TEM do pracy 4. W pracy 1 uczestniczyłem w pomiarach i analizie wyników fotolizy błyskowej. We wszystkich powyższych pracach brałem udział w dyskusji wyników, pisałem fragmenty manuskryptów oraz dokonywałem ich korekty.

W ramach rozprawy doktorskiej przygotowana została również praca teoretyczna:

5. *Optimization of absorption bands of dye-sensitized and perovskite tandem solar cells based on loss-in-potential values,* **Jan Sobuś** and Marcin Ziółek, Phys. Chem. Chem. Phys., **16** (2014) 14116-14126

Mój udział w tej pracy to zaprojektowanie i implementacja w języku C algorytmu pozwalającego wyznaczać optymalne parametry ogniw tandemowych, wygenerowanie przy jego pomocy rezultatów numerycznych oraz dyskusja wyników, pisanie części manuskryptu i jego korekta.

Częścią rozprawy doktorskiej jest też jeszcze nie opublikowana praca, obecnie będąca w formie gotowego manuskryptu w trakcie korekt u współautorów:

6. *Factors affecting the performance of champion silyl-anchor carbazole dye revealed in the femtosecond to second studies of complete ADEKA-1 sensitized solar cells.* **Jan Sobuś,** Błażej Gierczyk, Gotard Burdziński, Mariusz Jancelewicz, Anders Hagfeldt and Marcin Ziółek, paper in preparation: finalized and sent to co-authors for corrections.

W pracy tej moim udziałem były konstrukcja ogniw oraz badania i analiza wyników pomiarów krzywych prądowo-napięciowych, spektroskopii impedancyjnej i spektroskopii UV-VIS. Dodatkowo przeprowadziłem badania przy pomocy femtosekundowej spektroskopii absorpcji przejściowej i dokonałem analizy ich wyników. Uczestniczyłem też w dyskusji wyników oraz napisałem większość manuskryptu.

Z poważaniem

Jan Sobuś

Poznań, dnia 12.01.2016

Dr. hab. Marcin Ziółek, prof. UAM
Wydział Fizyki
Uniwersytet im. Adama Mickiewicza w Poznaniu
ul. Umultowska 85, 61-614 Poznań
e-mail: marziol@amu.edu.pl

Oświadczenie o współautorstwie w publikacjach

W związku z rozprawą doktorską mgr. inż. Jana Sobusia, którego jestem promotorem, składam następujące oświadczenie dotyczące mojego współautorstwa w publikacjach z jego udziałem.

Pierwsza grupa dotyczy prac eksperymentalnych, przedstawionych w następujących publikacjach:

[1] J. Sobuś, G. Burdziński, J. Karolczak, J. Idígoras, J. A. Anta, M. Ziółek, *Comparison of TiO_2 and ZnO Solar Cells Sensitized with an Indoline Dye: Time-Resolved Laser Spectroscopy Studies of Partial Charge Separation Processes*, Langmuir, **30** (2014) 2505.

[2] J. Sobuś, J. Karolczak, D. Komar, J. A. Anta, M. Ziółek, *Transient states and the role of excited state self-quenching of indoline dyes in complete dye-sensitized solar cells*, Dyes & Pigments, **113** (2015) 692.

[3] J. Sobuś, J. Kubicki, G. Burdziński, M. Ziółek, *Carbazole Dye-Sensitized Solar Cells Studied from Femtoseconds to Seconds—Effect of Additives in Cobalt- and Iodide-Based Electrolytes*, ChemSusChem **8** (2015) 3118.

[4] J. Idígoras, J. Sobuś, M. Jancelewicz, E. Azaceta, R. Tena-Zaera, J. A. Anta, M. Ziółek, *Effect of different photoanode nanostructures on the initial charge separation and electron injection process in dye sensitized solar cells: A photophysical study with indoline dyes*, Mater. Chem. Phys. **170** (2016) 218.

Mój udział w powyższych publikacjach polegał na wykonywaniu i analizie pomiarów metodą femtosekundowej absorpcji przejściowej, częściowej analizie pomiarów wykonanych za pomocą nanosekundowej fotolizy błyskowej, dyskusji wyników i pisaniu znacznej części manuskryptu. Jestem również autorem głównych koncepcji tych prac.

Drugą grupę stanowi praca obliczeniowo-teoretyczna:

[5] J. Sobuś, M. Ziółek, *Optimization of absorption bands of dye-sensitized and perovskite tandem solar cells based on loss-in-potential values,* Phys. Chem. Chem. Phys., **16** (2014) 14116.

W tym przypadku jestem również autorem koncepcji pracy, brałem udział w dyskusji wyników i pisaniu części manuskryptu.

Ponadto, do rozprawy doktorskiej mgr. inż. Jana Sobusia postanowiliśmy dołączyć gotowy manuskrypt, który wprawdzie nie stanowi jeszcze opublikowanej pracy, ale został przez nas niedawno przygotowany i wysłany do poprawek pozostałym współautorom. Manuskrypt ten stanowi efekt ostatnich 9 miesięcy pracy Jan Sobusia, zawiera również ważne i ciekawe wyniki związane z tematem jego rozprawy doktorskiej.

[6] J. Sobuś, B. Gierczyk, G. Burdziński, M. Jancelewicz, A. Hagfeldt (+ ewentualnie inne osoby z jego grupy), M. Ziółek, *Factors affecting the performance of champion silyl-anchor carbazole dye revealed in the femtosecond to second studies of complete ADEKA-1 sensitized solar cells,* manuskrypt wysłany do korekty współautorów.

Mój udział w powyższej pracy polegał na zaproponowaniu ogólnej koncepcji pracy, pomocy Janowi Sobusiowi przy wykonywaniu pomiarów metodą femtosekundowej absorpcji przejściowej, udziale przy dyskusji wyników, analizie wyników nanosekundowej fotolizy błyskowej i pomocy przy pisaniu manuskryptu. Przedstawię również wkład pozostałych współautorów: dr. hab. Błażej Gierczyk wykonał syntezę i charakterystykę badanego w pracy barwnika; dr. hab. Gotard Burdziński wykonał pomiary metodą nanosekundowej fotolizy błyskowej; dr Mariusz Jancelewicz wykonał pokrycie części elektrod warstwą Al_2O_3 metodą ALD; przygotowanie składników fotoogniw (elektrody), konstrukcja części z nich i pomiary metodą spektroskopii impedancyjnej zostały wykonane przez Jana Sobusia podczas stażu w grupie prof. Andersa Hagfeldta w ośrodku EPFL w Lozannie.

Z poważaniem,

M. Ziółek

Marcin Ziółek

dr hab. Gotard Burdziński, prof. UAM
Zakład Elektroniki Kwantowej
Wydział Fizyki UAM
tel. wew. 5017
gotardb@amu.edu.pl

Poznań, 5.01.2016

Oświadczenie o moim udziale w publikacjach mgra inż. Jana Sobusia

Mój wkład naukowy do wymienionych poniżej prac naukowych [1-2] jest bardzo skromny. Byłem odpowiedzialny za pomoc przy realizacji pomiarów kinetyk absorpcji przejściowej na spektrometrze nanosekundowym w zakresie UV-vis. Miałem też możliwość zapoznania się z pierwszą wersją tych manuskryptów i zaproponowania drobnych poprawek.

[1] J. Sobuś, G. Burdziński, J. Karolczak, J. Idígoras, J. A. Anta, M. Ziółek, Comparison of TiO2 and ZnO Solar Cells Sensitized with an Indoline Dye: Time-Resolved Laser Spectroscopy Studies of Partial Charge Separation Processes, Langmuir, 30 (2014) 2505.

[2] J. Sobuś, J. Kubicki, G. Burdziński, M. Ziółek, Carbazole Dye-Sensitized Solar Cells Studied from Femtoseconds to Seconds—Effect of Additives in Cobalt- and Iodide-Based Electrolytes, ChemSusChem 8 (2015) 3118.

Z poważaniem

dr hab. Gotard Burdziński

Jacek Kubicki
Wydział Fizyki
Uniwersytet im. Adama Mickiewicza w Poznaniu
ul. Umultowska 85
61-614 Poznań
jacek.kubicki@amu.edu.pl
618295016

Poznań, 5 stycznia 2016

Oświadczenie

Oświadczam, że mój udział w pracy J. Sobuś, J. Kubicki, G. Burdziński, M. Ziółek, *Carbazole Dye-Sensitized Solar Cells Studied from Femtoseconds to Seconds—Effect of Additives in Cobalt- and Iodide-Based Electrolytes*, ChemSusChem 8 (2015) 3118 związany był z pomiarami szybkości wstrzykiwania elektronów do półprzewodnika oraz szybkości zaniku stężenia elektronów w półprzewodniku. W tym celu przygotowałem femto-sekundowy spektrometr pracujący w zakresie średniej podczerwieni, wykonałem pomiary korzystając z dostarczonych mi baterii oraz wykonałem wstępną analizę numeryczną tych wyników.

Jacek Kubicki

Poznań, dnia 11.01.2016

Dr. hab. Marcin Ziółek
Wydział Fizyki
Uniwersytet im. Adama Mickiewicza w Poznaniu
ul. Umultowska 85
61-614 Poznań
e-mail: marziol@amu.edu.pl

Oświadczenie o współautorstwie ś. p. dr. Dariusza Komara

Z powodu śmierci dr. Dariusza Komara oświadczam, jako autor korespondencyjny poniższej pracy, że był on współautorem następującej publikacji:

J. Sobuś, J. Karolczak, D. Komar, J. A. Anta, M. Ziółek, *Transient states and the role of excited state self-quenching of indoline dyes in complete dye-sensitized solar cells*, Dyes & Pigments, **113** (2015) 692.

Jego udział w powstaniu tej publikacji polegał na napisaniu programu do dopasowania zaników fluorescencji do funkcji tzw. rozciągniętego eksponensa (*stretched exponential function*). Analiza wyników emisyjnych badanych w tej publikacji fotoogniw wykonana była z wykorzystaniem tego programu.

Z poważaniem,

M. Ziółek

Marcin Ziółek

Dr Jerzy Karolczak

Wydział Fizyki UAM

Ul. Umultowska 85, 61-614 Poznań

Poznań, 11-01-2016

OŚWIADCZENIE

Jako współautor poniższych prac oświadczam, że brałem udział w ich realizacji a mój wkład polegał na przygotowaniu i zaadaptowaniu układu pomiarowego laserowego spektrometru emisyjnego do badań czasów zaniku fluorescencji metodą skorelowanego w czasie liczenia pojedynczych fotonów opierającego się na technice pomiaru czasów zaniku metodą odbiciową. W obu pracach wykonywałem pomiary oraz obliczenia czasów zaniku procesów zachodzących w barwnikowych bateriach słonecznych tworzonych na bazie nanokryształów tlenku tytanu oraz różnego rodzaju barwników organicznych.

A) J. Sobuś, G. Burdziński, J. Karolczak, J. Idígoras, J. A. Anta, M. Ziółek, Comparison of TiO2 and ZnO Solar Cells Sensitized with an Indoline Dye: Time-Resolved Laser Spectroscopy Studies of Partial Charge Separation Processes, Langmuir, 30 (2014) 2505.

B) J. Sobuś, J. Karolczak, D. Komar, J. A. Anta, M. Ziółek, Transient states and the role of excited state self-quenching of indoline dyes in complete dye-sensitized solar cells, Dyes & Pigments, 113 (2015) 692.

Z wyrazami szacunku

Jerzy Karolczak

Poznań, dn. 13.01.2016

Dr Mariusz Jancelewicz
Centrum NanoBioMedyczne UAM
ul. Umultowska 85
61-614 Poznań

Oświadczenie o współautorstwie

Oświadczam, że jestem współautorem następującej publikacji:

Jesús Idígoras, Jan Sobuś, Mariusz Jancelewicz, Eneko Azaceta, Ramon Tena-Zaera, Juan A. Anta, Marcin Ziołek, "Effect of different photoanode nanostructures on the initial charge separation and electron injection process in dye sensitized solar cells: A photophysical study with indoline dyes", Materials Chemistry and Physics 170 (2016) 218-228.

Mój udział w powyższej pracy polegał na osadzeniu warstw dwutlenku tytanu (TiO_2) na podłożach szklanych przy użyciu techniki ALD (Atomic Layer Deposition).

M. Jancelewicz

Department of Physical, Chemical, and Natural Systems
Carretera de Utrera Km 1
41013 Seville
SPAIN

Juan Antonio Anta
Professor of Physical Chemistry
E-mail: anta@upo.es

Tel: (+34) 954 34 9314
Fax.: (+34) 954 34 98 14

January 6, 2016

Co-author Statement

I declare that I am the co-author of the following publications

1. J. Sobuś, G. Burdziński, J. Karolczak, J. Idígoras, J. A. Anta, M. Ziółek, Comparison of TiO_2 and ZnO Solar Cells Sensitized with an Indoline Dye: Time-Resolved Laser Spectroscopy Studies of Partial Charge Separation Processes, Langmuir, 30 (2014) 2505. o ignored
2. J. Sobuś, J. Karolczak, D. Komar, J. A. Anta, M. Ziółek, Transient states and the role of excited state self-quenching of indoline dyes in complete dye-sensitized solar cells, Dyes & Pigments, 113 (2015) 692. o ignored
3. J. Idígoras, J. Sobuś, M. Jancelewicz, E. Azaceta, R. Tena-Zaera, J. A. Anta, M. Ziółek, Effect of different photoanode nanostructures on the initial charge separation and electron injection process in dye sensitized solar cells: A photophysical study with indoline dyes, Mater. Chem. Phys. DOI:10.1016/j.matchemphys.2015.12.042

My contribution to them consisted in providing sample materials (ZnO), supervision of my former Ph.D student (also co-author of publications 1 and 3), and participation in the data analysis, interpretation of the results and final writing and proof-reading of the manuscripts.

With best regards,

NOMBRE ANTA MONTALVO JUAN ANTONIO - NIF 05275588D

Firmado digitalmente por NOMBRE ANTA MONTALVO JUAN ANTONIO - NIF 05275588D
Nombre de reconocimiento (DN): c=ES, o=FNMT, ou=FNMT Clase 2 CA, ou=500740773, cn=NOMBRE ANTA MONTALVO JUAN ANTONIO - NIF 05275588D
Fecha: 2016.01.06 11:24:10 +01'00'

Juan Antonio Anta

San Sebastián, January 08, 2015

Dr. Eneko Azáceta Muñoz
Junior researcher in Nanomaterials Unit
IK4-CIDETEC, Parque Tecnológico de San Sebastián
Paseo Miramón, 196
20009 Donostia - San Sebastián
e-mail: eazaceta@cidetec.es

Co-author Statement

I declare that I am the co-author of the publication:

Jesús Idígoras, Jan Sobuś, Mariusz Jancelewicz, Eneko Azaceta, Ramon Tena-Zaera, Juan A. Anta, Marcin Ziołek, "Effect of different photoanode nanostructures on the initial charge separation and electron injection process in dye sensitized solar cells: A photophysical study with indoline dyes", Materials Chemistry and Physics 170 (2016) 218e228.

My contribution consisted of carrying out the deposition and physico-chemical characterization of ZnO nanostructures. I also contributed to the analysis and discussion of the data of the whole collaborative study.

Signature

San Sebastián, January 08, 2015

Dr. Ramón Tena-Zaera
Head of Nanomaterials Unit
IK4-CIDETEC, Parque Tecnológico de San Sebastián
PaseoMiramón, 196
20009 Donostia - San Sebastián
e-mail: rtena@cidetec.es,

Co-author Statement

I declare that I am the co-author of the publication:

Jesús Idígoras, Jan Sobuś, Mariusz Jancelewicz, Eneko Azaceta, Ramon Tena-Zaera, Juan A. Anta, Marcin Ziołek, "Effect of different photoanode nanostructures on the initial charge separation and electron injection process in dye sensitized solar cells: A photophysical study with indoline dyes", Materials Chemistry and Physics 170 (2016) 218e228.

My contribution consisted of conceiving and supervising the deposition and physico-chemical characterization of the ZnO nanostructures. I also contributed to the analysis and discussion of the data of the whole collaborative study.

Signature

Department of Physical, Chemical, and Natural Systems
Carretera de Utrera Km 1
41013 Seville
SPAIN

Jesús Idígoras
Postdoctoral Research
E-mail: jaidileo@upo.es

January 8, 2016

Co-author Statement

I declare that I am the co-author of the following publications:

1. J. Sobuś, G. Burdziński, J. Karolczak, **J. Idígoras**, J. A. Anta, M. Ziółek, *Comparison of TiO_2 and ZnO Solar Cells Sensitized with an Indoline Dye: Time-Resolved Laser Spectroscopy Studies of Partial Charge Separation Processes*, Langmuir, 30 (2014) 2505. o ignored

2. **J. Idígoras**, J. Sobuś, M. Jancelewicz, E. Azaceta, R. Tena-Zaera, J. A. Anta, M. Ziółek, *Effect of different photoanode nanostructures on the initial charge separation and electron injection process in dye sensitized solar cells: A photophysical study with indoline dyes*, Mater. Chem. Phys. DOI:10.1016/j.matchemphys.2015.12.042

My contribution to them consisted in providing sample materials (ZnO and TiO_2), and participation in the data analysis, interpretation of the results and final writing and proof-reading of the manuscripts.

With best regards,

Jesús Idígoras